

3698

LIBRARY

JNCASR  
539.6 P05



3698

JNCASR

Acc  
No. 3698

LIBRARY

# Phase Behaviour of Linear Molecular Crystals in Bulk and on Graphite : A Molecular Dynamics Simulation Study

A Thesis

Submitted For the Degree of  
**DOCTOR OF PHILOSOPHY**  
in the Faculty of Science

by

**M. Krishnan**



CHEMISTRY AND PHYSICS OF MATERIALS UNIT  
JAWAHARLAL NEHRU CENTRE FOR ADVANCED SCIENTIFIC RESEARCH  
(A DEEMED UNIVERSITY)  
Bangalore – 560 064, India

APRIL 2005

539.6

POS

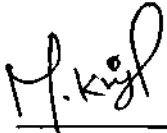
*Dedicated to my parents*



## DECLARATION

I hereby declare that the matter embodied in the thesis entitled “**Phase Behaviour of Linear Molecular Crystals in Bulk and on Graphite : A Molecular Dynamics Simulation Study**” is the result of investigations carried out by me at the Chemistry and Physics of Materials Unit, Jawaharlal Nehru Centre for Advanced Scientific Research, Bangalore, India under the supervision of Prof. S. Balasubramanian and that it has not been submitted elsewhere for the award of any degree or diploma.

In keeping with the general practice in reporting scientific observations, due acknowledgement has been made whenever the work described is based on the findings of other investigators. Any omission that might have occurred by oversight or error of judgement is regretted.



---

M. Krishnan

## CERTIFICATE

I hereby certify that the matter embodied in this thesis entitled “**Phase Behaviour of Linear Molecular Crystals in Bulk and on Graphite : A Molecular Dynamics Simulation Study**” has been carried out by Mr. M. Krishnan at the Chemistry and Physics of Materials Unit, Jawaharlal Nehru Centre for Advanced Scientific Research, Bangalore, India under my supervision and that it has not been submitted elsewhere for the award of any degree or diploma.



---

Prof. S. Balasubramanian  
(Research Supervisor)

## ACKNOWLEDGEMENTS

It is my pleasure to thank my research supervisor Prof. S. Balasubramanian for giving me an opportunity to explore the interesting area of research on computational materials science. I am extremely thankful to him for teaching me the molecular dynamics simulations and for his guidance, support, and encouragement right from the beginning of this project. I sincerely acknowledge the academic freedom that I enjoyed in his group and the advices and the suggestions at various stages of the work. I also thank him for providing me excellent computing resources without which the project would not have been successful. The research training that I received from him will surely help me in approaching even more complex problems that I may pursue in the coming years.

I thank Prof. C.N.R. Rao, F.R.S, Chairman, CPMU, for research support and for being a source of inspiration for me. I am grateful to him for sharing his research experiences and for narrating us the motivating scientific anecdotes at various occasions in JNCASR.

I also would like to thank Nehru Centre for providing me an excellent research facilities, stimulating research ambience, and for the financial support.

I express my sincere thanks to all the faculty members of CPMU and TSU for the fruitful discussions I had with them and for the courses they offered. I am particularly thankful to Prof. Swapan K. Pati (TSU, JNCASR) and Prof. S. Yashonath (SSCU, IISc) for showing interest in my academic advancements and for their caring words.

I am grateful to Sagar Sen and Preston Moore for the visualization program.

I have enjoyed the company and friendship of my present and past lab mates : Moumita

Saharay, Subrata Pal, Sagar Sen, B.L. Bhargava, Saswati, Manish C.M., Sunil Kumar, J. Sarkar, MDK, A. Verma, and Swarna. Special thanks are due to Moumita Saharay for cheerful company and for making the figures given in the introduction section of this thesis.

I thank all the staff members of JNCASR for their constant help.

I thank JNCASR and CDAC for computational facilities.

I acknowledge CSIR, India for a Senior Research Fellowship and all my friends in JNC, and IISc for their help.

Finally, I am thankful to my father and family members for their continued support and encouragement.

# Preface

The thesis entitled "**Phase Behaviour of Linear Molecular Crystals in Bulk and on Graphite: A Molecular Dynamics Simulation Study**" presents the results of investigations on linear molecular crystals under varied conditions of temperature and pressure. Classical molecular dynamics (MD) simulations were employed to characterize the microscopic structure, energetics and the dynamics of these systems while the vibrational properties were studied using normal mode analysis (NMA) and other methods.

Characteristic features of chain molecules and their properties in condensed phases are introduced in Chapter 1. A comprehensive survey of earlier studies on molecular crystals is presented. This chapter ends with a detailed description of the method of our choice, the molecular dynamics technique.

Chapter 2 covers the results obtained from the isothermal-isobaric MD simulations on the thermal behaviour of crystalline poly(ethylene oxide) (PEO). The possibility of a new, solid phase of PEO has been explored. This phase has been characterized to be partially disordered, with a loss of long-range, in-plane orientational correlations between molecules. Across the premelting transition, the PEO oligomers continue to be oriented along the *c*-axis of the crystal with the retention of short-range helical conformational order. Interesting dynamical changes across this transition that results in sliding diffusion and helical oscillations of the chains have been studied.

Results on the vibrational properties of crystalline PEO explored using NMA and from the MD trajectory are provided in Chapter 3. An efficient algorithm to obtain the elements of the Hessian matrix arising out of complex macromolecular interactions is provided. Visual analyses of atomic displacements and group theoretical methods were employed to assign the vibrational features to specific modes. The model predictions on the PEO vibrations in the solid state compare well with experiment.

Chapter 4 presents a study on the high-pressure behaviour of crystalline *n*-heptane using isothermal-isobaric molecular dynamics simulations. Structural and conformational changes associated with the solid-liquid transition upon decompression and within the solid phase with increasing pressure have been explored. Although the solid-liquid tran-

sition has clear signatures such as the formation of *gauche* defects along the molecular backbone, the simulations do not show any sign for a solid-solid transition at high pressures. However, interesting changes in the environment around methyl groups and in their dynamics are observed. These have been substantiated by calculations of the vibrational density of states obtained from a normal mode analysis and from the simulation trajectory.

Coverage dependent structural changes exhibited by ultrathin films of *n*-hexane adsorbed on graphite have been investigated in Chapter 5. Employing simulations that do not impose any particular periodicity on the adsorbed layer, the results of the present investigations are compared to neutron diffraction experiments. A structural transition from a uniaxially incommensurate lattice to a fully commensurate structure, on increasing the coverage from a monolayer to trilayer was observed. Additional simulations that employ regular periodic boundary conditions have also been performed to confirm the results.

Chapter 6 provides the outcome of investigations on the thermal behaviour of ultrathin *n*-heptane films physisorbed on graphite using constant temperature MD simulations. An uniaxially commensurate monolayer (UCM), an uniaxially commensurate bilayer (UCB) and a fully commensurate bilayer (FCB) of *n*-heptane have been studied in order to distinguish the contributions from coverage and in-plane density to the process of melting. The calculated intermolecular energy per molecule shows that the FCB structure is more stable than the UCB structure, consistent with x-ray and neutron scattering experiments. In all these systems, disordering processes in the solid state involves a fraction of molecules rotating about their backbone axes, in agreement with scanning tunneling microscopy studies. The molecules present in the uniaxially commensurate structures (UCM and UCB) were found to be facile to rotate about their long axes, causing these adlayers to melt at lower temperatures compared to the fully commensurate structure. The importance of conformational defects for the melting of these quasi-two dimensional systems has also been explored. A quantitative analysis of axial rotations of molecules present in the first adsorbed layer of FCB yields an average angle of rotation of  $40^\circ$ , in excellent agreement with x-ray and neutron scattering experiments.

# Nomenclature

- MD : Molecular Dynamics
- NMA : Normal Mode Analysis
- PE : Poly(Ethylene)
- PEO : Poly(Ethylene Oxide)
- PTFE : Poly(TetraFluoroEthylene)
- POM : Poly(OxyMethylene)
- NMR : Nuclear Magnetic Resonance
- DSC : Differential Scanning Calorimetry
- UAM : United Atom Model
- AAM : All Atom Model
- PME : Particle Mesh Ewald
- TCF : Time Correlation Function
- SOC : Single Occupancy Cell
- TAM : Transverse Acoustic Mode
- LAM : Longitudinal Acoustic Mode
- $\mathbf{r}_i$  : Position vector of  $i^{\text{th}}$  atom
- $\mathbf{p}_i$  : Momentum of  $i^{\text{th}}$  atom
- $m_i$  : Mass of  $i^{\text{th}}$  atom

- $\mathbf{F}_i$  : Force acting on the  $i^{\text{th}}$  atom
- $H$  : Hamiltonian of a classical system
- $N$  : Total number of particles present in a system
- $V$  : Volume
- $P$  : Pressure
- $E$  : Total energy of a system
- $T$  : Temperature
- $\mu$  : Chemical potential
- $\Gamma$  : Phase space vector
- $f(\Gamma)$  : Phase space distribution function
- $\Omega(N, V, E)$  : Microcanonical partition function
- NPT-F : Isothermal-isobaric simulations with fully flexible cell
- NPT-I : Isothermal-isobaric simulations with isotropically flexible cell
- NVT : Isothermal simulations
- $h$  : Planck's constant
- $\eta_i$  : Thermostat 'position'
- $p_{\eta_i}$  : Thermostat 'momentum'
- $Q_i$  : Thermostat 'mass'
- $N_f$  : Number of degrees of freedom
- $\bar{\mathbf{p}}_g$  : The cell variable momentum matrix
- $\bar{\mathbf{P}}_{int}$  : Pressure tensor of the system
- $\tilde{\mathbf{h}}$  : Cell matrix
- $\tilde{\mathbf{I}}$  : Identity matrix
- $k_B$  : Boltzmann constant



# Contents

<b>Acknowledgements</b>	<b>v</b>
<b>Preface</b>	<b>vii</b>
<b>Nomenclature</b>	<b>ix</b>
<b>1 Introduction</b>	<b>1</b>
1.1 Linear Molecules . . . . .	1
1.2 Chain Molecules in Condensed Phases . . . . .	5
1.3 Phase Behaviour of Molecular Crystals . . . . .	8
1.4 Theoretical Studies . . . . .	16
1.5 Molecular Dynamics . . . . .	17
1.5.1 Constant Temperature Molecular Dynamics :	
Nosé-Hoover Chains Method . . . . .	19
1.5.2 Isothermal-Isobaric Molecular Dynamics :	
Fully Flexible Cell . . . . .	21
1.5.3 Interaction Potential . . . . .	23
1.5.4 Molecular Models . . . . .	24
1.5.5 Long-range Forces . . . . .	25
1.5.6 Reversible Reference System Propagation Algorithm . . . . .	29
1.5.7 Time Correlation Functions (TCF): . . . . .	33

1.6	Free Energy Calculations . . . . .	34
1.7	Limit of Metastability . . . . .	37
1.8	Codes Developed and Used . . . . .	38
	<b>Bibliography</b>	<b>41</b>
<b>2</b>	<b>Thermal Evolution of Conformation, Structure, and Dynamics in Crystalline Poly(Ethylene Oxide)</b>	<b>55</b>
2.1	Introduction . . . . .	55
2.2	Simulation Details . . . . .	60
2.3	Results and Discussion . . . . .	64
2.3.1	Structure . . . . .	66
2.3.2	Dynamics . . . . .	85
2.4	Conclusions . . . . .	92
	<b>Bibliography</b>	<b>97</b>
<b>3</b>	<b>Vibrational Dynamics of Solid Poly(Ethylene Oxide)</b>	<b>103</b>
3.1	Introduction . . . . .	103
3.2	Simulation Details . . . . .	105
3.2.1	Normal Mode Analysis (NMA) . . . . .	108
3.3	Results and Discussion . . . . .	110
3.4	Conclusions . . . . .	120
3.5	Appendix 1 . . . . .	121
3.5.1	Hessian from the torsional interaction . . . . .	122
3.5.2	Hessian from the Coulomb interaction . . . . .	124
	<b>Bibliography</b>	<b>127</b>
<b>4</b>	<b><i>n</i>-Heptane Under Pressure: Structure and Dynamics from Molecular</b>	

<b>Simulations</b>	<b>131</b>
4.1 Introduction . . . . .	131
4.2 Simulation Details . . . . .	132
4.3 Results and Discussion . . . . .	136
4.3.1 Crystal structure, Volume, and Energetics . . . . .	136
4.3.2 Structure around terminal group . . . . .	138
4.3.3 Conformation . . . . .	147
4.3.4 Dynamics . . . . .	148
4.4 Conclusions . . . . .	166
<b>Bibliography</b>	<b>169</b>
<b>5 Structure of Solid Monolayers and Multilayers of <i>n</i>-Hexane on Graphite</b>	<b>173</b>
5.1 Introduction . . . . .	173
5.1.1 <i>n</i> -Alkanes on Graphite Surface . . . . .	173
5.1.2 <i>n</i> -Hexane on Graphite . . . . .	174
5.2 Simulation Details . . . . .	176
5.3 Results and Discussion . . . . .	183
5.4 Conclusions . . . . .	193
<b>Bibliography</b>	<b>195</b>
<b>6 Phase Behaviour of Ultrathin Crystalline <i>n</i>-Heptane Films on Graphite: An Atomistic Simulation Study</b>	<b>199</b>
6.1 Introduction . . . . .	199
6.2 Details of Simulation . . . . .	202
6.3 Results and Discussion . . . . .	204
6.3.1 Energetics . . . . .	204
6.3.2 Density profile . . . . .	206

6.3.3	Orientation of molecular zig-zag plane . . . . .	211
6.3.4	Torsional distribution . . . . .	216
6.3.5	Defect Density . . . . .	219
6.3.6	Defect-Defect correlation . . . . .	221
6.4	Conclusions . . . . .	223
	<b>Bibliography</b>	<b>227</b>
	<b>List of Publications</b>	<b>231</b>

# Chapter 1

## Introduction

### 1.1 Linear Molecules

Long chain or linear molecules are common in our daily lives and play key roles in many areas of science and technology. A variety of substances such as oil, soaps, detergents, and plastics are constituted of such molecules. In addition, macromolecules of biological importance such as DNA, RNA, proteins are essential components for the very existence of our life. These factors justify the vast amount of scientific activity initiated in recent years to understand various aspects of such macromolecular systems [1–11].

The atoms in a chain molecule are covalently bonded in concatenated sequence thus giving rise to its structural framework. Depending on the nature of chemical constituents, such molecules exhibit diverse conformations ranging from linear zigzag to helical structure. For example, polyethylene (PE) (molecular formula :  $(-\text{CH}_2-)_n$ ) adopts a planar zigzag structure while poly(ethylene oxide) (PEO)  $(-\text{C}_2\text{H}_4\text{O}-)_n$ , and poly (tetrafluoroethylene) (PTFE)  $(-\text{CF}_2-)_n$  adopt a helical conformation [10,11]. Figure 1.1 depicts the molecular structure of some of these molecules. The thermodynamic, hydrodynamic, physical and mechanical properties of such molecular materials can be explained by their structure in the solid state [1–3]. For instance, the mechanical properties of polyethylene can be significantly changed by altering its structure by external stimulus. This property

has been heavily exploited in polymer drawing and other engineering applications [4]. Conformation is important in other contexts too. The biological activity of a protein is influenced by its conformation. Having established the strong relationship between the

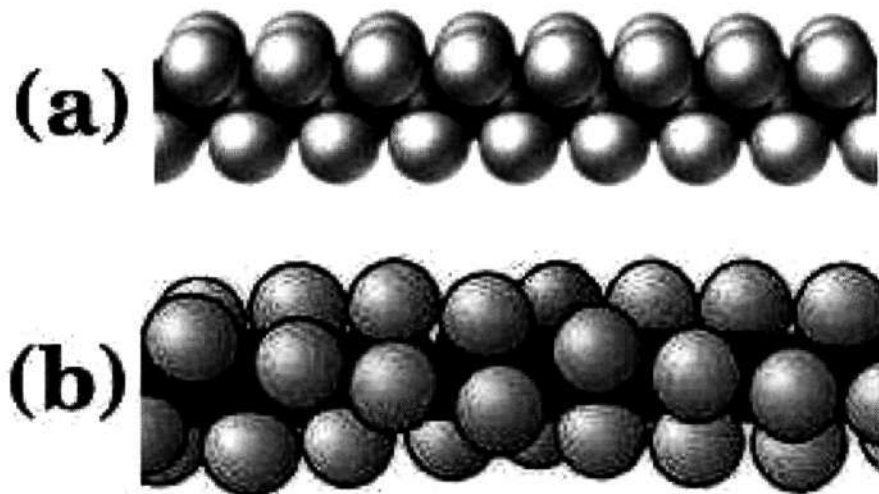


Figure 1.1: Molecular structure of (a) linear zigzag poly(ethylene) and (b) helical poly(tetrafluoroethylene) is shown. The carbon atoms are shown in black while hydrogens in poly(ethylene) and fluorines in poly(tetrafluoroethylene) are indicated by grey spheres.

molecular structure and the properties, it is important to learn how such chain molecules could change their structure. A schematic diagram of a linear molecule is provided in Figure 1.2. Variables known as internal coordinates which define the molecular structure are also given in Figure 1.2. The three principal internal coordinates are bond lengths, bend angles, and dihedral angles, which are illustrated in Figure 1.2. Although bond stretching and angle bending modes are invariably present in these molecules, the overall structure of a molecule is not affected by excitations of such modes. Thus, the potential energy surface that characterizes these internal coordinates can be thought of as a harmonic well with minima at their equilibrium values. A characteristic feature of such long-chain molecules is their ability to rotate about bonds, leading to diverse molecular conformations. At this point, one should note the subtle difference between the terms, *configuration* and *conformation*. Although both are related to spatial arrangement of atoms, configurations

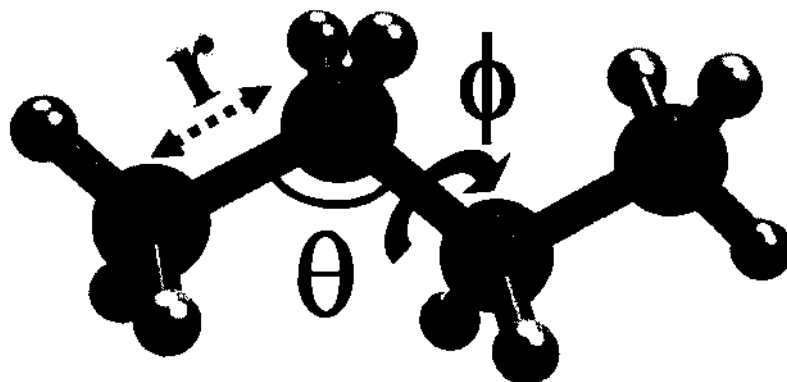


Figure 1.2: Molecular structure of  $n$ -butane. The black spheres represent carbons while grey spheres stand for hydrogens. The internal coordinates such as instantaneous bond length ( $r$ ), bend angle ( $\theta$ ), and the dihedral angle ( $\phi$ ) are also shown.

generated solely by rotation about bonds of the molecular framework are called conformations. Note that the configuration of a molecule can also be changed by bond-stretching, angle-bending and other non-bonded interactions. These configurations cannot be called as conformations.

An understanding of conformation in  $n$ -alkanes has a long history. Very early investigations on the thermodynamic properties of  $n$ -alkanes using statistical mechanical calculations showed large deviation of the calculated values from experimental results [12]. These calculations assumed free rotation of C-C bonds. Following this, Pitzer and co-workers suggested the existence of potential barrier to rotation about the C-C bond [13–15]. The calculations carried out with this assumption yielded results on the thermodynamics that were in close agreement with experiments. Interestingly, electron diffraction [16] and Raman spectroscopy [17] measurements provided strong evidences for the presence of barrier to the rotation of the C-C bond. Thus, conformational studies have become an important tool in understanding the structure and properties of flexible chain molecules [18, 19]. In Figure 1.3, we show the torsional potential energy surface associated with the rotation of the central C-C bond of butane to explain the different conformational states. The conformational state with the lowest energy at  $\phi=180^\circ$  is called the '*trans*'-conformation. The other two minima at  $60^\circ$  and  $300^\circ$  are called '*gauche*'-conformations. In the *trans*

state the methyl groups are as far apart as possible while in the *gauche* state they are relatively closer. Thus, in the *gauche* state the molecule experiences steric strain. Accordingly, the *gauche* conformers are of higher energy than the *trans* state. In what follows, the term 'conformational defect' refers to the conformational state corresponding to the local minimum of the torsional potential energy surface. It is also to be noted that the energy required for a molecule to change its conformation is more than an order of magnitude lesser than that is required to break a bond. It is to be noted that each conformation has distinct physical properties and show different spectral features. The transition from one conformational state to another can be thermally activated at room temperature. Having said that, it is important to highlight the difficulties associated with the characterization of conformational states of chain molecules. As the number of torsional angles increases linearly with the number of atoms present in a molecule, the accessible conformational space for a long-chain molecule becomes rather large. Even if we restrict the rotational

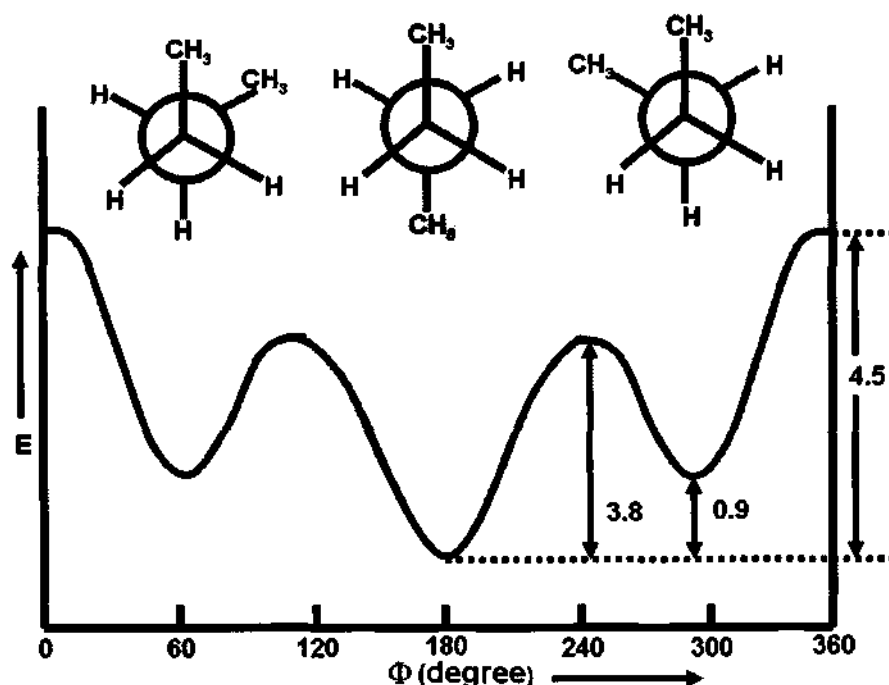


Figure 1.3: The torsional potential associated with the rotation about the central C-C bond in *n*-butane. The energy values are given in kilocalories. The Newman projections of different conformational states of *n*-butane are also shown.



angles for a given bond to a set of  $P$  discrete values, there exists  $PQ$  number of conformations for a molecule with  $Q$  bonds. Thus, exploring the conformational space of a long-chain molecule is a non-trivial task.

Another interesting property of a chain molecule is its dynamics. The atomic motions in a chain molecule vary from localized vibrational motion, with periods around a few femtoseconds, to conformational excitations happening in the timescale of few picoseconds, and collective relaxations in which a significant fraction of the atoms in a molecule take part [20]. Thus, the existence of wide spectrum of relaxational modes reflects the rich dynamics exhibited by such molecules.

## 1.2 Chain Molecules in Condensed Phases

Long-chain molecules in condensed phases experience intermolecular interactions in addition to intramolecular interactions. The competition between intra- and intermolecular interactions can influence its conformational order. In the molten state, these molecules exhibit conformational defects. Upon cooling the melt, the system undergoes two interesting ordering processes: (i) molecular nucleation (ii) crystal nucleation. The mechanism by which the chain molecules adopt an ordered conformational state in the crystalline phase is called *molecular nucleation*. In molecular nucleation, the chains extend spatially so as to attain the lowest energy conformation and thereby acquiring intrachain regularity. The ground state for polyethylene and  $n$ -alkanes is the *all-trans* planar zigzag while for PTFE, PEO, and poly(oxymethylene) (POM) the helical conformation is the ground state [10, 11]. Thus, conformational defects are almost eliminated during the process of molecular nucleation. Since the number of accessible conformational states is very large for chain molecules, the process of molecular nucleation is a slow process. In crystal nucleation, such structurally regular molecules rearrange so as to maximize interactions between atoms in adjacent chains. This results in increased interchain correlations leading to a high degree of packing. Since the requirement of intramolecular regularity is essential

for chain molecular crystallization, molecular nucleation precedes crystal nucleation while cooling from the melt. In Figure 1.4, we show the behaviour of crystalline PTFE at three different temperatures to explain the concept of molecular and crystal nucleation [21]. In the molten state (Figure 1.4c), PTFE exhibits large number of conformational defects and vanishingly small interchain correlations. Upon cooling, these molecules acquire low energy helical conformation but still with poor interchain correlations (Figure 1.4b). Further cooling gives rise to an ordered crystalline state with optimum interchain packing as shown in Figure 1.4a. In order to make a connection between molecular nucleation and

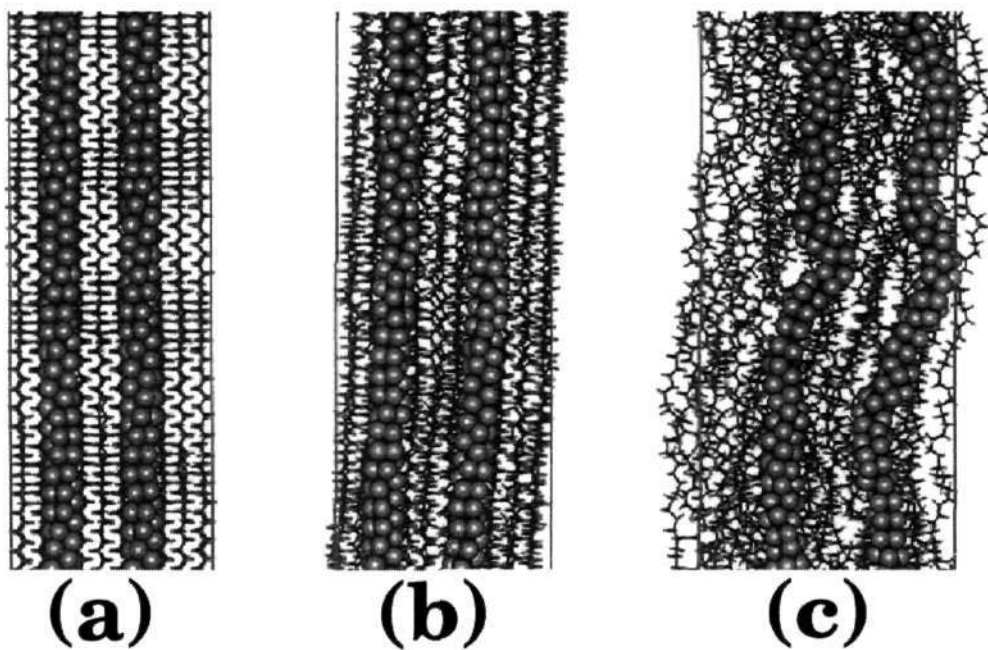


Figure 1.4: A schematic representation of (a) crystalline, (b) partially crystalline, and (c) disordered liquid phase of PTFE is shown. Two selected chains are shown in a space-filling ball representation while the rest are depicted in stick representation [From Ref [21]].

crystal nucleation, the concept of crystallization of chain molecules is briefly explained here. Chain molecules can form crystals but not under all circumstances. Slow cooling from the molten state enables the chain molecules to rearrange, thus leading to lamellar crystals, where the molecules are oriented approximately perpendicular to the plane of the lamella. The rest of the discussion pertains to the molecular structure and morphology of

polymer crystals. The molecules in the crystalline phase can be either extended or folded depending upon its molecular mass [23, 24]. Low molecular mass samples generally form extended-chain crystals while high molecular mass samples inevitably form folded-chain crystals. Figure 1.5 provides a schematic representation of folded and extended chain crystals.

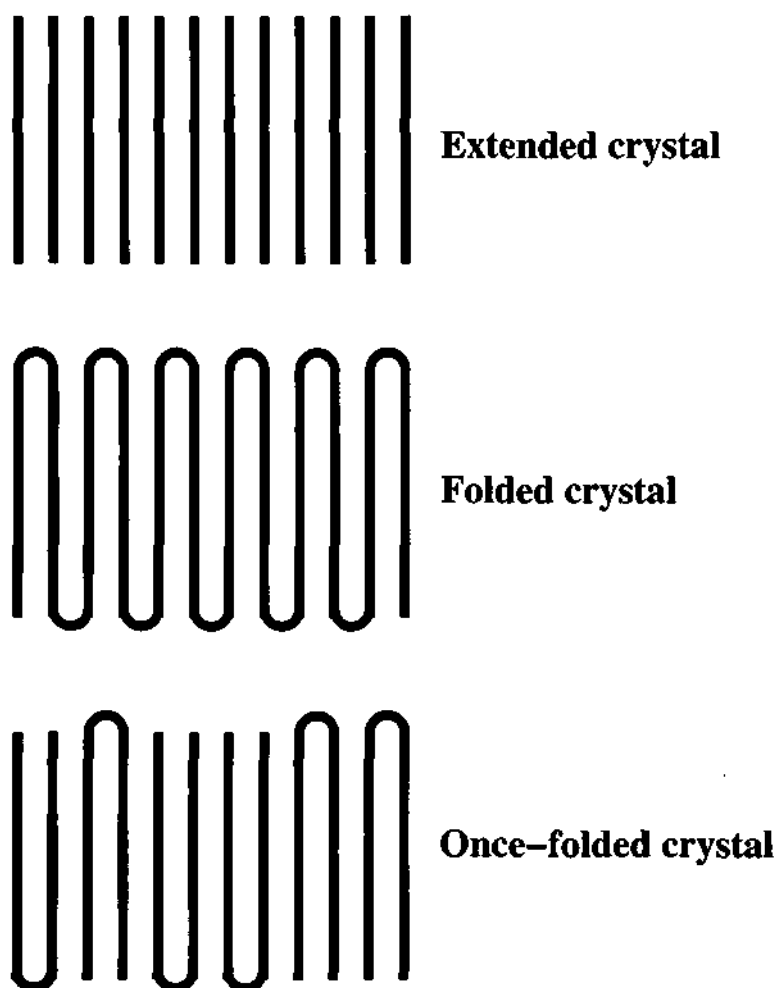


Figure 1.5: Schematic diagram of extended, folded, and once-folded polymeric chains in the crystalline state is shown.

The crystal would have a lower free energy if the molecules were completely extended with no folds. The formation of folded-chain crystals suggests that crystallization of such molecules is strongly affected by kinetic factors such as heating rate and crystallization

temperature. Thus, the folded-chain crystals are metastable form of the extended-chain crystals. Experimental techniques such as optical microscopy, electron microscopy, small angle X-ray diffraction, and neutron scattering methods have played a vital role in understanding the morphological aspects of these crystals. Despite the considerable attention paid on folded-chain crystals, a comprehensive understanding of the structure of the folds and processes leading to their formation is still lacking. Small angle X-ray diffraction and optical microscopy experiments have concluded that these lamellae are homogeneous and contain only integer fold (IF) structures and that the end groups are rejected onto the lamellar surfaces [4, 22]. Crystallization conditions, structural regularity of the molecules, their flexibility and length determine the regularity and the nature of the folds. The molecular mechanisms responsible for chain folding and unfolding, the relative stability of folded-chain crystals compared to the extended-chain form are some of the interesting issues that are of current interest [22–27].

### 1.3 Phase Behaviour of Molecular Crystals

The structural and conformational properties of these elongated molecules in condensed phases can be altered by thermodynamic variables such as temperature and pressure. It is well documented in the literature that a variety of chain molecules exhibit polymorphic transitions in the crystalline phases [1, 2, 11, 28–30]. These polymorphs can differ in the way molecules are packed. Also, such transitions can result in interesting dynamics in the solid state [31–37]. In general, activation energies for dynamical events in crystals are larger compared to liquids. A large number of sophisticated experimental techniques have been employed to study interesting structural and associated dynamical changes in the solid state. These include X-ray diffraction [38–51], calorimetry [46, 52–62], neutron scattering [31–34, 63–65], solid-state Nuclear Magnetic Resonance (NMR) [66–78], infrared [62, 79] and Raman spectroscopy [80–82], and dielectric spectroscopy [52]. It is difficult to provide a comprehensive survey of phase behaviour of molecular crystals. Here, we

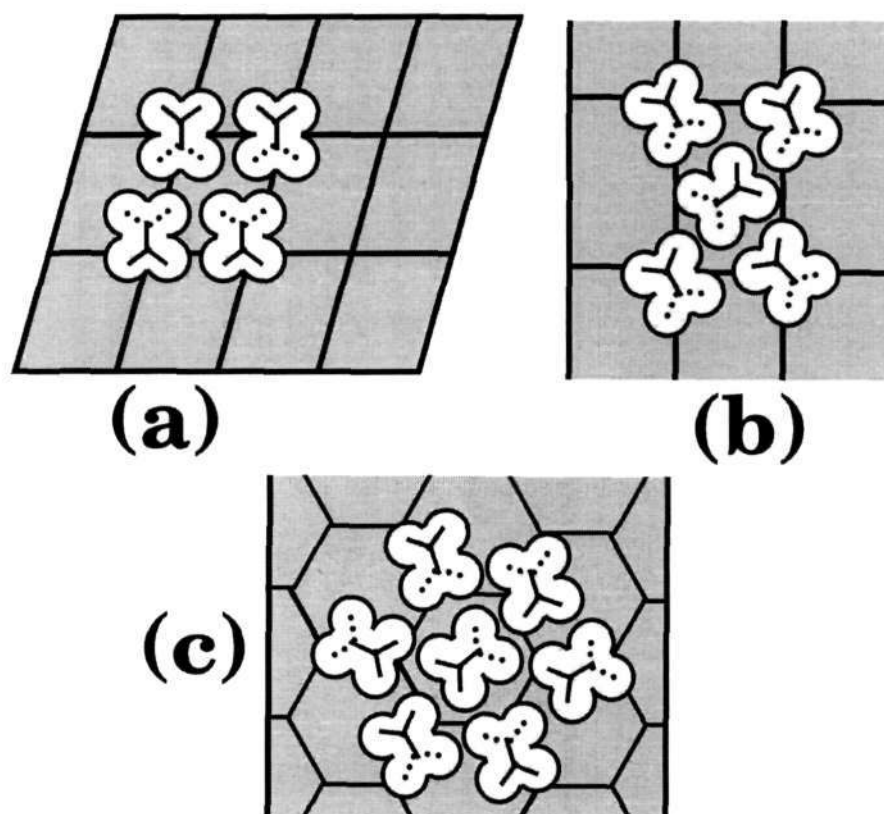


Figure 1.6: **Hydrocarbon chain packing in the solid state. (a) triclinic subcell with an oblique two dimensional lattice (b) orthorhombic perpendicular subcell with a rectangular two dimensional lattice and (c) hexagonal subcell with a hexagonal two dimensional lattice [Adopted from Ref. [1]].**

showcase such studies on two molecular crystals. These are crystals of  $n$ -alkanes and PTFE. Interestingly, these two molecular crystals exhibit all the interesting features that are relevant for our study.

$n$ -alkanes exhibit a rich phase behaviour. They are prototypical systems consisting almost all the essential features of long-chain molecules. Their studies in recent years have led to an understanding of the mechanism of polymer crystallization and melting [83–85]. Also,  $n$ -alkanes are the essential component of lipids and surfactants [1]. Interestingly, crystal structure studies of  $n$ -alkanes have shed new light into the structure and packing of nearly all lipids containing long aliphatic chains. In view of the similarities between chain packing in normal alkanes and that in aliphatic lipids, an investigation of the phase behaviour of  $n$ -alkanes have gained renewed interest in recent years [90–95]. Also, substi-

tuted *n*-alkanes find applications in chemical industries and in living systems. *n*-alkanes adopt the all-trans conformation in the crystalline state. This means that all the C-C bonds in a molecule are in the trans conformational state, giving rise to a zigzag topology to its backbone. Based on the molecular packing, crystals of *n*-alkanes are broadly classified into two categories: (i) dense crystalline phase in which chains are tightly packed with specific chain-chain interactions (ii) rotator phase wherein partial rotation of molecular backbone or of the CH<sub>2</sub> groups exists that results in loose packing of chains. The subcell of tightly packed crystals of *n*-alkanes can have either triclinic or orthorhombic form while that of rotator phase takes a hexagonal shape as shown in Figure 1.6.

Note that these polymorphs possess very similar energies thus making their characterization rather difficult. Earlier X-ray studies on *n*-alkane crystals have unambiguously identified these phases [38–41]. The structure factor obtained from these studies can distinguish the nonspecific crystalline packing from specific chain packing. As shown in Figure 1.7, the structure factor corresponding to the crystal with tight chain packing exhibit splitting of peaks while that of the rotator phase has a single relatively broad peak. The liquid state is characterized by a broad scattering fringe centered at 4.5–4.7 Å while hexagonal subcell gives a single symmetrical diffraction profile centered around 4.2 Å. Note that the two dimensional rectangular lattice that result in pseudo-hexagonal packing gives a shoulder or second peak at around 4.1 Å. The temperature dependence of the mean volume of CH<sub>2</sub> groups and the surface area per chain perpendicular to the chain axis also exhibit signatures corresponding to the thermally induced transitions between these polymorphs. Results obtained from such an analysis on a series of odd-alkanes are shown in Figure 1.8. The discontinuous change in these quantities at low temperature signifies the orthorhombic perpendicular to hexagonal transition while that at higher temperature is due to melting. The enthalpic changes associated with these transitions can be measured quantitatively through differential scanning calorimetry (DSC) experiments. The DSC traces show a premelting enthalpic peak together with the one that is associated with

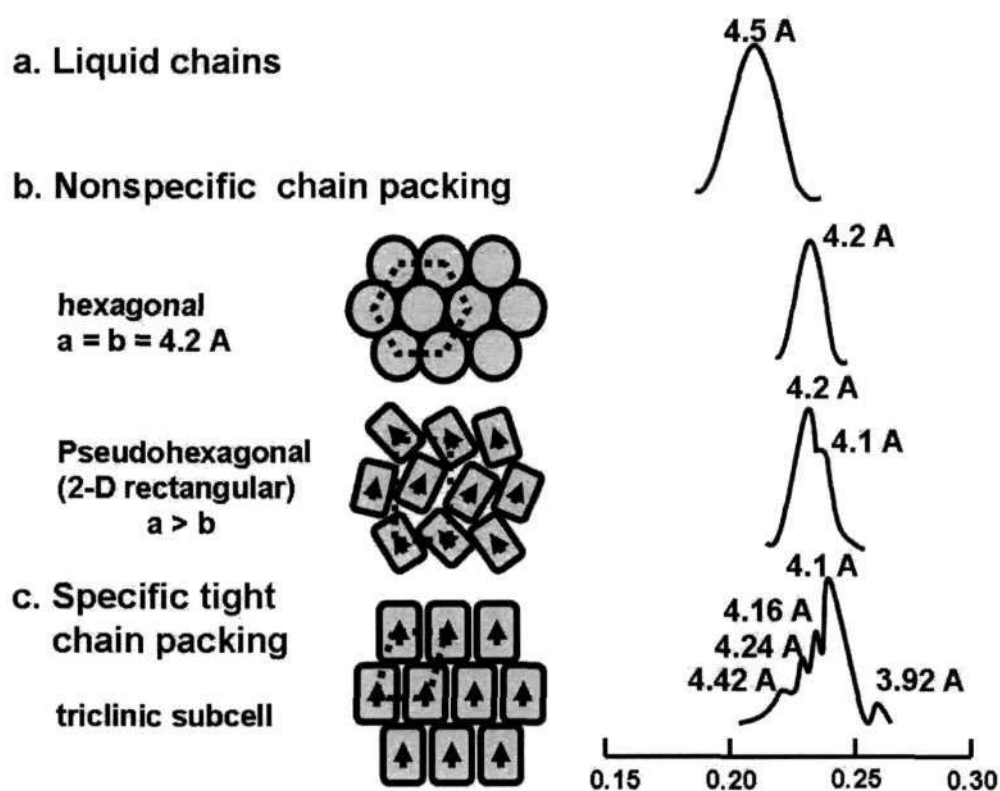


Figure 1.7: The structure factor obtained from X-ray diffraction from liquid, nonspecific crystalline chain packing and specific chain packing. (a) The liquid state is characterized by a broad scattering fringe centered at 4.5-4.7 Å. (b) Nonspecific crystalline packing gives two rather similar patterns. The hexagonal gives a single symmetrical diffraction centered about 4.2 Å, while pseudo-hexagonal packing (rectangular lattice) gives a shoulder or second peak at 4.1 Å. (c) Specific chain packing gives a large number of spacings related to the specific chain-chain interactions [Adopted from Ref. [1]].

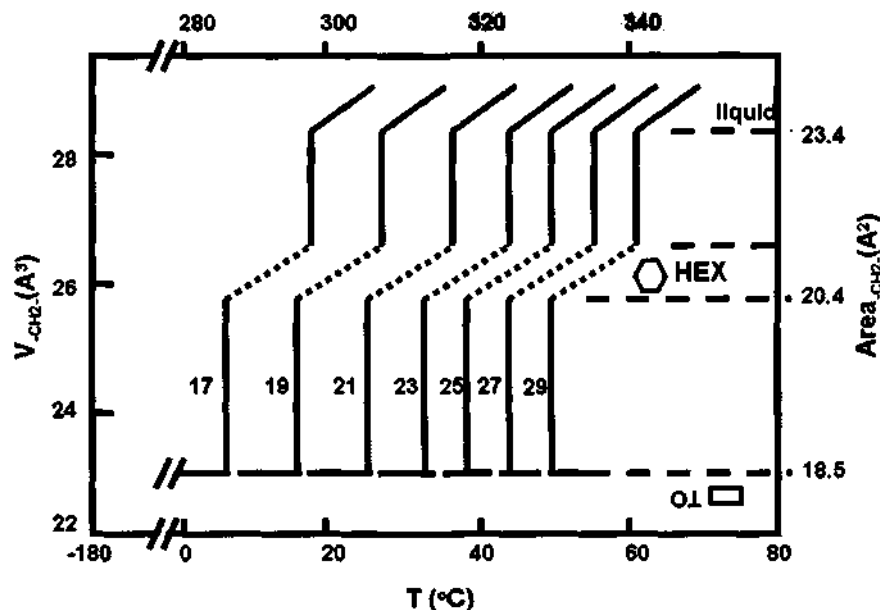


Figure 1.8: The volume of the  $-\text{CH}_2-$  group as a function of temperature for odd-numbered normal hydrocarbons undergoing an orthorhombic to hexagonal transition and hexagonal-to-liquid transition. The corresponding areas of the  $-\text{CH}_2-$  group is also given on the right [Adopted from Ref. [1]].

the melting as shown in Figure 1.9. The effect of temperature on the interchain packing in solid  $n$ -alkanes has been investigated by Ryckaert and Klein using molecular dynamics simulations [96]. They have modeled  $n$ -alkanes as all-atom infinite chains with flexible backbones. They have provided molecular level insight into the temperature induced disordering and associated translational and rotational diffusion of molecules in the solid state. They have also characterized the structure and dynamics of a bilayer of  $n$ -alkane tricosane ( $\text{C}_{23}\text{H}_{48}$ ) in both the crystalline and pseudohexagonal rotator phases close to the phase transition [97]. They have found that in the crystalline phase the chains adopt *all-trans* conformation while conformational defects were found in the rotator phase. Also, in the rotator phase, molecules undergo rotational jumps and longitudinal translation motion. Further simulation studies carried out by them to characterize the rotator phases of solid  $n$ -alkanes are consistent with experiments and also provide microscopic information about the nature of these phases [98,99]. X-ray scattering studies on  $n$ -alkanes carried



out by Sirota et al have shown that there exists five different rotator phases which can be distinguished by distortions and tilts of the molecules [100]. Existence of these rotator phases have also been confirmed by calorimetric studies [101]. These phases show large thermal expansion and compressibility suggesting that their heat capacity is dominated by anharmonic effects [102]. Spectroscopic measurements have shown that there are substantial number of chain-end *gauche* defects in the rotator phases. The concentration of such defects increases with increasing temperature [62, 103]. The enthalpy of melting at the rotator-liquid, rotator-rotator, and crystal-rotator transitions have also been characterized in the literature [55, 90, 91]. It would be instructive to know whether odd-even effect exists in rotator phases. It is known that the even *n*-alkanes form triclinic crystals while odd *n*-alkanes crystallize in orthorhombic form. This indicates that odd-even effect signif-



Figure 1.9: DSC trace of an odd-alkane, heptadecane (C<sub>17</sub>) is shown. The peak at 10°C represents the transition from a tightly packed orthorhombic crystal to a pseudo-hexagonally packed crystal. The peak at 21°C signifies the melting transition. Both transitions are sharp with enthalpies of 2.5 and 9.2 kcal/mol, respectively [Adopted from Ref. [1]].

icantly affects the way in which molecules pack in the crystal. It has been shown that the distinction between odd- $n$  and even- $n$ -alkanes vanishes in the rotator phases [100]. Thus, it is natural to expect the odd-even effect to appear across the rotator-crystal transition. The result obtained from such an investigation has demonstrated that the odd-even effect is absent both in the crystal-rotator and rotator-liquid transitions while it is present in rotator-crystal transition [93].

Another noteworthy feature of  $n$ -alkanes is their ability to show surface freezing effect. Sirota and co-workers have investigated the surface structure of chain molecular melts and their mixtures using a variety of experimental techniques including X-ray and surface tension measurements [104–111]. They have extensively worked on normal alkanes and alcohols. Their results show that  $n$ -alkanes exhibit surface freezing, whereby a single crystalline monolayer is formed at the surface of the isotropic bulk liquid and it coexists with the liquid at temperatures up to 3° C above the bulk freezing temperature. These crystalline monolayers also exhibit polymorphism. Although liquid crystals exhibit such surface ordering phenomenon, they show liquid-like behaviour in the plane perpendicular to the long-axis of the molecules. In contrast,  $n$ -alkanes form a fully ordered crystalline phase on the surface of its melt.

Another system of interest that has relevance to this thesis is poly(tetra fluoroethylene) (PTFE). The molecular formula of PTFE is  $(-\text{CF}_2)_n$ . It can be thought of as polyethylene with hydrogens replaced by a much heavier fluorine atoms. Note that the van der Waals radius of hydrogen is 1.1-1.2 Å while that of fluorine is 1.47 Å [112]. In PE, the hydrogen atoms attached to next near neighbor carbon atoms are separated by a distance of  $\sim 2.54$  Å which is greater than the van der Waals diameter of hydrogen atoms. Thus, in the planar zigzag configuration of PE the hydrogen atoms attached to next near neighbor carbon atoms are not in contact but separated by a distance. Since these hydrogens are well separated from each other, the planar zigzag configuration minimizes the steric interactions thus making it a stable structure of PE. Note that the 1-3

carbon distance is the same for PE and PTFE. Had the conformation of PTFE been the same as PE, the fluorine atoms attached to next near neighbor carbon atoms would be separated by a distance of  $\sim 2.54\text{\AA}$  only, which is less than the van der Waals diameter of fluorine. Thus, the steric interactions between these larger fluorine atoms destabilizes the planar zigzag configuration and forces the PTFE chain to adopt a helical conformation [42, 43]. Thus the helical structure of a fluoroalkane chain is due to the inherent property of an isolated molecule. Since the experimental characterization of the structure and the rotational angles for different conformational isomers of a longer fluoro carbon chain (where the number of carbons greater than or equal to 4) is rather difficult, if not impossible, the relative contribution of inter- and intra-molecular effects in stabilizing the helical conformation in the condensed phase is not unambiguous. Although *ab initio* calculations have shown that the helicity observed in the condensed phases is mainly due to intramolecular interactions, the relative energies of different conformational isomers are highly sensitive to the basis set size and the level of correlation effects [113, 114]. An analysis of X-ray diffraction [42, 43], spectroscopic [115], NMR [116–119], and calorimetric [120–123] data on PTFE has yielded the phase diagram shown in Figure 1.10. The low temperature solid phase, Phase II, is an ordered crystalline structure with triclinic symmetry. The molecules adopt helical conformation with a pitch of 13 carbon atoms per  $180^\circ$  turn of the backbone. Upon heating, between 292K and 303K, unwinding of helical chains occurs in the crystal leading to a new solid phase called Phase IV. This phase possesses an overall hexagonal symmetry and the pitch of the molecular helix is increased to 15 carbon atoms per  $180^\circ$  twist. Upon a further increase in temperature, the emergence of a thermally stable, partially disordered, new crystalline phase called Phase I is observed. In this phase, the chains are oriented parallel to each other and are hexagonally packed. This phase is thermally stable from room temperature up to the melting point of PTFE (around 600K). It has been shown by X-ray diffraction studies that the long-range orientational order of  $\text{CF}_2$  groups is absent in this phase [43]. The

high thermal stability of Phase I has been attributed to the disordering of  $\text{CF}_2$  groups. PTFE also exhibits an orientationally ordered *all-trans* high pressure solid phase called Phase III.

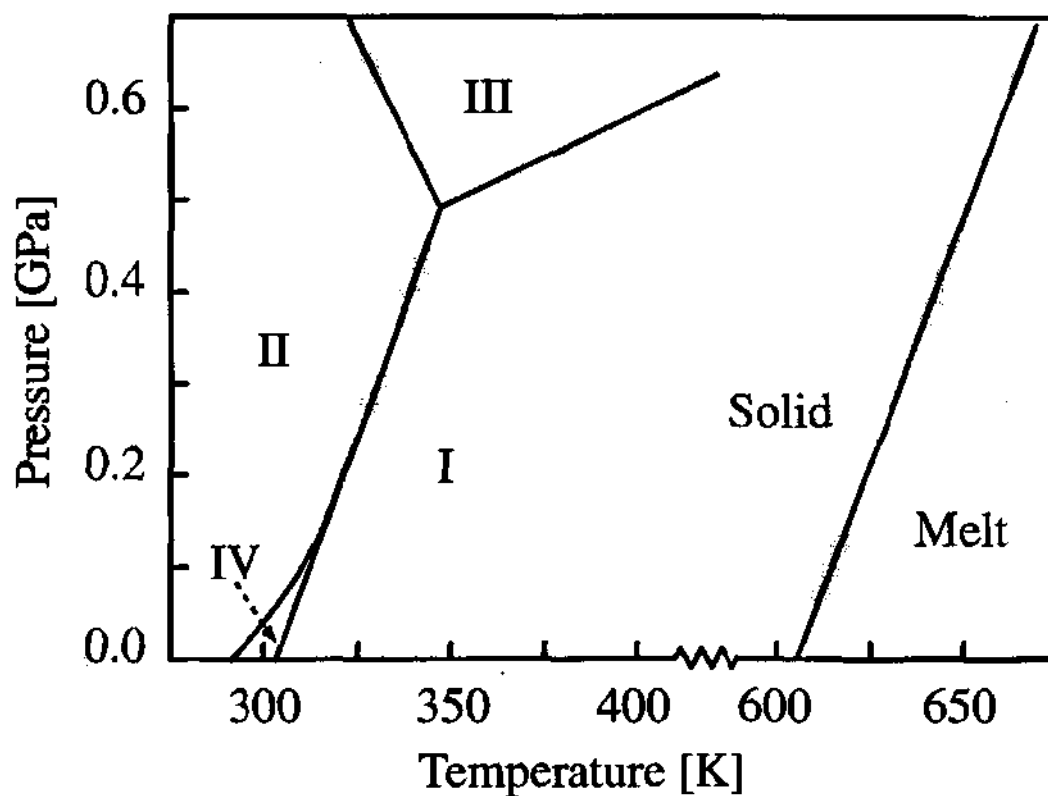


Figure 1.10: Phase Diagram of PTFE [From Ref. [21]].

## 1.4 Theoretical Studies

Various theoretical methods exist to explore the phase diagram of simple and complex molecular systems. In this section, a brief introduction to some of them is provided. Detailed descriptions of other methods can be found in Ref. [124]. As stated above, we restrict ourselves to case studies of *n*-alkanes and PTFE.

## 1.5 Molecular Dynamics

Molecular dynamics (MD) is one of the computer simulation methods that has wide spectrum of applications in many branches of physics, chemistry, biology and chemical engineering. It has become an inevitable tool to understand the microscopic structure and dynamics of diverse systems such as crystals, simple and complex liquids, macromolecular assemblies, biomolecules and glassy materials. It is also used to model interfacial phenomena and to study the dynamics of molecules in confined environment [124–130]. The system of interest is modelled to consist of  $N$  classical particles which interact via an empirical potential. The microscopic time evolution of this classical many-body system is dictated by Newton's equations of motion. In the following, we assume that the system is represented in Cartesian coordinates. Let  $\mathbf{r}_1, \mathbf{r}_2, \dots, \mathbf{r}_N$  denote the positions of these particles and  $\mathbf{p}_1, \mathbf{p}_2, \dots, \mathbf{p}_N$  represent their momenta. We write the equations of motion using the Hamiltonian formulation. Let  $H(\mathbf{r}_1, \mathbf{r}_2, \dots, \mathbf{r}_N, \mathbf{p}_1, \mathbf{p}_2, \dots, \mathbf{p}_N)$  be the Hamiltonian of a system of  $N$  particles interacting with each other via the potential,  $U(\mathbf{r}_1, \mathbf{r}_2, \dots, \mathbf{r}_N)$ .

Thus,

$$H(\mathbf{r}_1, \mathbf{r}_2, \dots, \mathbf{r}_N, \mathbf{p}_1, \mathbf{p}_2, \dots, \mathbf{p}_N) = \sum_{i=1}^N \frac{\mathbf{p}_i^2}{2m_i} + U(\mathbf{r}_1, \mathbf{r}_2, \dots, \mathbf{r}_N) \quad (1.1)$$

The Hamilton's equations of motion of this system is given as

$$\begin{aligned} \dot{\mathbf{r}}_i &= \frac{\partial H}{\partial \mathbf{p}_i} = \frac{\mathbf{p}_i}{m_i} \\ \dot{\mathbf{p}}_i &= -\frac{\partial H}{\partial \mathbf{r}_i} = \mathbf{F}_i \end{aligned}$$

where  $\mathbf{F}_i$  denotes the force acting on the  $i^{\text{th}}$  atom,  $m_i$  is its mass. These coupled equations of motion need to be integrated numerically to obtain the  $\mathbf{r}_i$  and  $\mathbf{p}_i$  as a function of time, given their initial values. Note that in the Hamiltonian formulation, the set of positions and momenta of particles describe the microscopic state of the system. Thus, if we represent the state of this classical system as a point in the  $6N$  dimensional space

that is formed by the set of positions and momenta (i.e.,  $\mathbf{r}_1, \mathbf{r}_2, \dots, \mathbf{r}_N, \mathbf{p}_1, \mathbf{p}_2, \dots, \mathbf{p}_N$ ), the Hamilton's equations of motion describes the time evolution of this point in this space. This hyperspace formed by the  $6N$  components of particle positions and momenta is called *phase space*. Let  $N$ ,  $V$ ,  $P$ ,  $E$ ,  $T$ , and  $\mu$  represent the number of particles, volume, pressure, total energy, temperature, and chemical potential of a system, respectively. By keeping some of these thermodynamic quantities as constant, one can characterize different statistical ensembles. For example, a system maintained at constant  $N$ ,  $V$ , and  $E$  gives rise to microscopic states belonging to the microcanonical ensemble which is often denoted as the NVE ensemble. The equilibrium phase space distribution function corresponding to this ensemble is given as,

$$f(\Gamma) = \frac{1}{N!h^{3N}\Omega(N, V, E)}\delta(H(\Gamma) - E) \quad (1.2)$$

where  $\Omega(N, V, E)$  is the microcanonical partition function defined as,

$$\Omega(N, V, E) = \frac{1}{N!h^{3N}} \int \delta(H(\Gamma) - E) d\Gamma \quad (1.3)$$

This expression suggests that the systems in the microcanonical ensemble are uniformly distributed on a constant energy hypersurface of phase space. The ensemble average of a physical observable  $A(\Gamma)$  can be written as,

$$\langle A \rangle = \frac{\int d\Gamma A(\Gamma) f(\Gamma)}{\int d\Gamma f(\Gamma)} \quad (1.4)$$

The difference between MD simulation and the statistical mechanical approach is as follows: In MD, the time evolution of a system is monitored and the properties are averaged over time while in statistical mechanics, properties are averaged over a collection of identical systems called ensemble (time evolution is not necessary). The ergodic hypothesis suggests that the time average and the ensemble average are equal provided the system is

allowed to visit all accessible points in phase space. Thus, the basic aim of MD simulation is to design equations of motion such that the system of interest will evolve in phase space and eventually generate the desired phase space distribution function dictated by the required ensemble. Since Hamilton's equations conserve the Hamiltonian (i.e. the total energy) of a system of constant  $N$  and  $V$ , the dynamical trajectory of the system obeying these equations will generate a set of states on the constant energy hypersurface in phase space as dictated by the microcanonical ensemble. Although simple, MD simulations in NVE ensemble do not mimic the experimental situation realistically. Experiments are, in general, performed either at constant temperature or constant pressure conditions. Thus a new set of equations of motion has to be devised that will generate microscopic states in the canonical ensemble (i.e. NVT ensemble) or the isothermal-isobaric ensemble (i.e. NPT ensemble). Since Hamilton's equations of motion fail to generate microscopic states in such ensembles, one needs to use non-Hamiltonian dynamics. The following discussion provides an overview of non-Hamiltonian dynamics. The basic idea of this approach is to assume that the system of interest is coupled with external influence such as a heat bath (thermostat) or a mechanical piston (barostat) so as to keep its temperature or pressure constant. In this approach, the phase space of the system is extended by introducing additional dynamical variables that describe the time evolution of thermostat and/or barostat.

### 1.5.1 Constant Temperature Molecular Dynamics :

#### Nosé-Hoover Chains Method

The extended system method was originally proposed by Andersen to perform constant temperature and/or constant pressure molecular dynamics simulations [131]. In constant temperature simulations, the particles were allowed to change their velocities by stochastic collisions. The distribution of the velocities of the particles which collided is chosen to reproduce the canonical ensemble. This method results in a discontinuous phase space

trajectory due to sudden change of the velocities by collisions. Following this approach, Nosé proposed a method to generate canonical distribution from equations of motion obtained from an extended Hamiltonian [132, 133]. These equations were constructed so as to generate smooth, deterministic, and time-reversible phase space trajectories. Later, Hoover modified the Nosé's equations that resulted in a non-Hamiltonian set of equations called the Nosé-Hoover equations [134]. It is later shown that the Nosé-Hoover dynamics is not ergodic for small or stiff systems. To circumvent the problems associated with Nosé-Hoover dynamics, Martyna *et al* proposed a set of non-Hamiltonian equations of motion to generate the canonical ensemble [135–137]. In this method called the Nosé-Hoover chain (NHC) dynamics method, a system at constant  $N$  and  $V$  is attached to a chain of  $M$  thermostats. Thus, the thermostat variables  $\eta_1, \eta_2, \dots, \eta_M$  and their conjugate momenta  $p_{\eta_1}, p_{\eta_2}, \dots, p_{\eta_M}$  describe the state of the heat source/sink attached to the system. The dynamics of the system and the chain of thermostats in the extended phase space is controlled by the following equations of motion:

$$\begin{aligned}
 \dot{\mathbf{r}}_i &= \frac{\mathbf{p}_i}{m_i} \\
 \dot{\mathbf{p}}_i &= -\frac{\partial U}{\partial \mathbf{r}_i} - \frac{p_{\eta_1}}{Q_1} \mathbf{p}_i \\
 \dot{\eta}_1 &= \frac{p_{\eta_1}}{Q_1} \\
 \dot{p}_{\eta_1} &= \sum_{i=1}^N \frac{\mathbf{p}_i}{m_i} \cdot \mathbf{p}_i - N_f k_B T - \frac{p_{\eta_2}}{Q_2} p_{\eta_1} \\
 \dot{p}_{\eta_i} &= \frac{p_{\eta_{i-1}}^2}{Q_{i-1}} - k_B T - \frac{p_{\eta_{i+1}}}{Q_{i+1}} p_{\eta_i} \quad i = 2, \dots, M-1 \\
 \dot{p}_{\eta_M} &= \frac{p_{\eta_{M-1}}^2}{Q_{M-1}} - k_B T
 \end{aligned} \tag{1.5}$$



where  $-\frac{\partial U(\mathbf{r}_i)}{\partial \mathbf{r}_i}$  represents the force on particle  $i$  due to all the other particles in the system and  $N_f$  is the number of degrees of freedom. Equations (1.5), known as the Nosé-Hoover chain (NHC) or MTK equations, have the conserved energy:

$$H' = \sum_{i=1}^N \frac{\mathbf{p}_i^2}{2m_i} + U(\mathbf{r}) + \sum_{i=1}^M \frac{p_{\eta_i}^2}{2Q_i} + N_f k_B T \eta_1 + \sum_{i=2}^M k_B T \eta_i \quad (1.6)$$

and can be shown to generate the canonical partition function.

## 1.5.2 Isothermal-Isobaric Molecular Dynamics :

### Fully Flexible Cell

In the isothermal-isobaric ensemble MD, the volume of the simulation cell is allowed to vary so as to keep the average internal pressure equal to the external set pressure. The volume of the cell can change either isotropically without changing its shape [131] or anisotropically with change of shape [138–140]. Parrinello *et al* have employed this method to investigate the  $\alpha \leftrightarrow \beta$  phase transition in AgI [141]. At low temperature AgI has the wurtzite structure in which the iodide ions form a hcp lattice and the silver ions are tetrahedrally coordinated to each iodine and show no self-diffusion. Upon heating AgI to 420 K, it undergoes a structural change from  $\beta$  to  $\alpha$  phase. The  $\alpha$  phase is called the superionic phase in which iodine ions form a bcc lattice and silver ions are mobile. This structural change and associated mobility of silver ions were successfully demonstrated by this isothermal-isobaric simulation. Also, such MD simulations have been used to study the polymorphic transitions exhibited by variety of materials [142–154]. We have employed the recently proposed equations of motion that generate microscopic states in the isothermal-isobaric ensemble for characterizing some of the systems dealt with in this thesis. We describe here the NPT simulation of a fully flexible cell (NPT-F simulation). The non-Hamiltonian equations of motion that generate microscopic states in the NPT-F ensemble can be written as [136, 137, 155],

$$\begin{aligned}
\dot{\mathbf{r}}_i &= \frac{\mathbf{p}_i}{m_i} + \frac{\tilde{\mathbf{p}}_g}{W} \mathbf{r}_i \\
\dot{\mathbf{p}}_i &= \mathbf{F}_i - \frac{\tilde{\mathbf{p}}_g}{W} \mathbf{p}_i - \frac{1}{N_f} \frac{\text{Tr}(\tilde{\mathbf{p}}_g)}{W} \mathbf{p}_i - \frac{p_\eta}{Q} \mathbf{p}_i \\
\dot{\tilde{\mathbf{h}}} &= \frac{\tilde{\mathbf{p}}_g \tilde{\mathbf{h}}}{W} \\
\dot{\tilde{\mathbf{p}}}_g &= V(\tilde{\mathbf{P}}_{\text{int}} - \tilde{\mathbf{P}}) + \frac{1}{N_f} \sum_{i=1}^N \frac{\mathbf{p}_i^2}{m_i} \tilde{\mathbf{I}} - \frac{p_\eta}{Q} \tilde{\mathbf{p}}_g \\
\dot{\eta} &= \frac{p_\eta}{Q} \\
\dot{p}_\eta &= \sum_{i=1}^N \frac{\mathbf{p}_i^2}{m_i} + \frac{\text{Tr}(\tilde{\mathbf{p}}_g^t \tilde{\mathbf{p}}_g)}{W} - (N_f + d^2) k_B T
\end{aligned} \tag{1.7}$$

where  $\tilde{\mathbf{h}}$  is the cell matrix,  $V = \det[\tilde{\mathbf{h}}]$  is the volume of the cell,  $\tilde{\mathbf{I}}$  is the identity matrix,  $\text{Tr}(\tilde{\mathbf{p}}_g^t \tilde{\mathbf{p}}_g)$  is the sum of the squares of all the elements of  $\tilde{\mathbf{p}}_g$ , the cell variable momentum matrix,  $\tilde{\mathbf{p}}_g^t$  is the transpose of  $\tilde{\mathbf{p}}_g$ , and  $\tilde{\mathbf{P}}_{\text{int}}$  is the pressure tensor of the system given by

$$\tilde{\mathbf{P}}_{\text{int}} = \frac{1}{V} \left[ \sum_{i=1}^N \frac{\mathbf{p}_i \mathbf{p}_i}{m} + \sum_{i=1}^N \mathbf{r}_i \mathbf{F}_i - \frac{\partial U}{\partial \tilde{\mathbf{h}}} \tilde{\mathbf{h}}^t \right] \tag{1.8}$$

Equations (1.7) have the conserved energy

$$H' = H(\mathbf{p}, \mathbf{r}, V) + \frac{\text{Tr}(\tilde{\mathbf{p}}_g^t \tilde{\mathbf{p}}_g)}{2W} + \frac{p_\eta^2}{2Q} + (N_f + d^2) k_B T \eta + P \det(\tilde{\mathbf{h}}) \tag{1.9}$$

and can be shown to generate the partition function

$$\Delta(N, P, T) = \int d\tilde{\mathbf{h}} e^{-\beta P \det(\tilde{\mathbf{h}})} Q(N, \tilde{\mathbf{h}}, T) [\det(\tilde{\mathbf{h}})]^{1-d} \tag{1.10}$$

### 1.5.3 Interaction Potential

The success of atomistic simulations depends critically on the quality of the model used for the molecular structure and the potential of interaction. The total potential energy of a molecular system can be written as a sum of valence interactions between bonded atoms and interactions between non-bonded atoms through space. The valence energy can be written as a sum of bonded two, three, and four body interactions. Each bond in our model is treated as a classical harmonic spring with a force constant  $K_b$  and equilibrium bond length  $r_0$ . Similarly, the angle between bonds meeting at a given atom can also be allowed to vary harmonically around its equilibrium value. The spring constant and the equilibrium bend angle are denoted as  $K_\theta$  and  $\theta_0$ , respectively. The torsional energy is represented in cosine power series of the dihedral angle. The non-bonded interactions consist of both electrostatic and van der Waals contributions. We have used exponential-6 potential to model van der Waals interaction between non-bonded atoms. Thus, the total potential energy of a general system can be written as,

$$\begin{aligned}
 U(\{\mathbf{r}\}) = & \frac{1}{2} \sum_{ij}^{\text{bonded}} K_r^{ij} (r_{ij} - r_{ij}^0)^2 + \frac{1}{2} \sum_{ijk}^{\text{bonded}} K_\theta^{ijk} (\theta_{ijk} - \theta_{ijk}^0)^2 \\
 & + \sum_{ijkl}^{\text{bonded}} \sum_{n=0}^6 a^n \cos^n \phi_{ijkl} + \frac{1}{4\pi\epsilon_0} \sum_i^N \sum_{j>i}^N \frac{q_i q_j}{r_{ij}} \\
 & + \sum_i^N \sum_{j>i}^N \left[ A_{ij} e^{-B_{ij} r_{ij}} - \frac{C_{ij}}{r_{ij}^6} \right] \tag{1.11}
 \end{aligned}$$

where  $i$ ,  $j$ ,  $k$ , and  $l$  denote atom indices,  $q_i$  and  $q_j$  are the partial charges of  $i^{\text{th}}$  and  $j^{\text{th}}$  atom respectively,  $\epsilon_0$  is the permittivity of free space,  $K_r^{ij}$  and  $K_\theta^{ijk}$  are the stretching and bending force constants respectively,  $\phi_{ijkl}$  is the dihedral angle, and  $r_{ij}$  is the interatomic distance between atoms  $i$  and  $j$ . The last two terms in Eq.1.11 are applicable to interaction sites separated by more than three bonds in a molecule and to every pair of sites belonging to different molecules. The interaction parameters involved in Eq.1.11 are determined either based on experimental studies or from *ab initio* quantum chemical calculations.

For instance, X-ray diffraction studies on molecular crystals can give equilibrium bond lengths and bond angles while spectroscopic measurements can provide force constants required for valence interactions. As far as torsional parameters are concerned, vibrational spectroscopic techniques like infra-red and Raman scattering have played a vital role in determining these quantities. Since the vibrational spectrum is sensitive to conformational changes, one can get the population of different conformers and thereby calculate the height of the barrier that separates different conformational states. The work presented in this thesis employs interaction potentials developed by others and that documented in the literature.

#### 1.5.4 Molecular Models

Macromolecular simulations can be conducted using two approaches: ones using an United Atom Model (UAM) or those using an All-Atom Model (AAM). In the UAM, a set of few atoms are replaced by a single pseudoatom which constitute the sites of interaction of the molecule. In contrast, AAM models consider every atom of the molecule to be explicitly present. The UAM and AAM of *n*-butane is shown Figure 1.11. Note that for a system having  $N$  interaction sites, the number of non-bonded interactions scales as  $N^2$ . Replacement of a set of atoms by a single pseudoatom greatly decreases the number of interaction sites and thus UAM reduces the computational time required to calculate the energy and forces, significantly. MD simulations with UAM can be used to generate long trajectories of macromolecular systems. Although UAM works well for low density phases such as gases and liquids, it is not an appropriate choice for simulations of crystalline solids and dense liquids [98]. In such systems, steric interactions between the individual atoms play a non-trivial role in the equilibrium structure and dynamics. Also, alkanes within UAM have a smaller moment of inertia than one with AAM [156,157]. This may influence their dynamics significantly. All-atom models have successfully been used to explore the melting and phase behaviour of such dense systems [158–160]. In light of this, we have

used all-atom models for all the crystals dealt with in this thesis.

### 1.5.5 Long-range Forces

Some of the pair interaction potentials  $U(r_{ij})$ , where  $r_{ij}$  is the distance between the atoms  $i$  and  $j$ , decay no faster than  $r_{ij}^{-d}$  where  $d$  is the dimensionality of the system. Forces arising from such interatomic potentials are called long-range forces. For example, the Coulombic interaction between two point charges separated by a distance  $r$  in three dimensional space is

$$U(r) = \frac{1}{4\pi\epsilon_0} \frac{q_i q_j}{r} \quad (1.12)$$

In MD simulations, one often finds difficulty in handling such long-range forces for the following reasons: Significant contribution of the potential energy exists even for distances greater than half of the box length ( $L$ ). This implies that the standard method of truncating the potential at  $L/2$  will lead to erroneous results. Also, spherical truncation of the

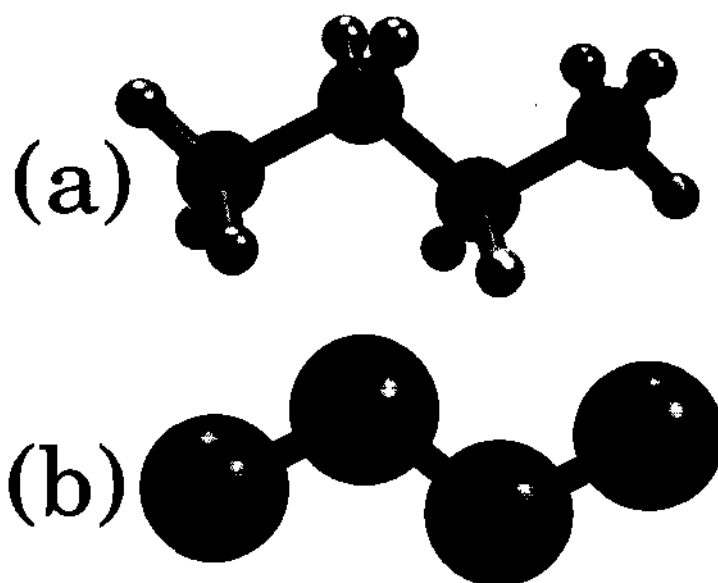


Figure 1.11: (a) All-atom and (b) united atom representation of *n*-butane - In (a), black spheres denote carbons while grey spheres represent hydrogens ; In (b), both methyl and methylene groups are shown by black spheres.

potential may give rise to a non-neutral interaction sphere due to the imbalance between the positive and negative charges within it. This can cause artifacts in the simulation and methods to remove such effects are reported to be sensitive to system size. Thus, truncation of the potential is not the proper way of handling long-range forces. Also, the Coulomb sum is conditionally convergent. These reasons necessitate new methods. Among such methods, the Ewald summation technique and an efficient implementation called particle mesh Ewald are widely used. Since these techniques have been used to simulate some of the systems covered in this thesis, we provide here a brief introduction to these methods.

### Ewald Sum :

Consider a periodic system of  $N$  point charges  $q_1, q_2, \dots, q_N$  located at positions  $\mathbf{r}_1, \mathbf{r}_2, \dots, \mathbf{r}_N$  respectively, in a box defined by lattice vectors  $\mathbf{a}_1, \mathbf{a}_2,$  and  $\mathbf{a}_3$ . Since these lattice vectors need not be orthogonal to each other, this method can be applied to the simulation of non-cubic boxes also. The net charge in the simulation box is assumed to be zero such that the system as a whole is electrically neutral. The charges in this periodic system interact via the Coulombic potential. Note that a point charge  $q_i$  located at position  $\mathbf{r}_i$  interacts with other charges  $q_j$  (with  $j \neq i$ ) located at  $\mathbf{r}_j$  as well as with all of their periodic images at positions  $\mathbf{r}_j + n_1\mathbf{a}_1 + n_2\mathbf{a}_2 + n_3\mathbf{a}_3$  for all integers  $n_1, n_2,$  and  $n_3$ . The point charge  $q_i$  can also interact with its own periodic images located at  $\mathbf{r}_i + n_1\mathbf{a}_1 + n_2\mathbf{a}_2 + n_3\mathbf{a}_3$  for all integers  $n_1, n_2,$  and  $n_3$  except  $n_1 = n_2 = n_3 = 0$ . The total electrostatic potential energy of the system is given as

$$U_{\text{coul}}(\{\mathbf{r}\}) = \left(\frac{1}{2}\right) \frac{1}{4\pi\epsilon_0} \sum'_{\mathbf{n}} \sum_{i=1}^N \sum_{j=1}^N \frac{q_i q_j}{r_{\mathbf{n}ij}} \quad (1.13)$$

where  $r_{\mathbf{n}ij} = |\mathbf{r}_i - (\mathbf{r}_j + n_1\mathbf{a}_1 + n_2\mathbf{a}_2 + n_3\mathbf{a}_3)|$  and the sum over  $\mathbf{n}$  indicates summation over all periodic boxes (including the  $\mathbf{n}=0$  (i.e.  $n_1 = n_2 = n_3 = 0$ ), the central box) and sums over  $i$  and  $j$  are over atoms in the box. The prime on the summation over boxes indicates that the self-interactions (i.e.  $i=j,$  and  $\mathbf{n}=0$ ) are omitted. The basic aim of the Ewald

summation technique is to split the Coulombic sum given in Eq. 1.13 into short- and long-range components. This break-up can be achieved by introducing a convergence function  $\phi(r)$  in the interaction potential. Using this function, one can rewrite Eq. 1.13 as follows [127, 130]:

$$\begin{aligned}
 U_{coul}(\{\mathbf{r}\}) &= \left(\frac{1}{2}\right) \frac{1}{4\pi\epsilon_0} \sum_{\mathbf{n}}' \sum_{i=1}^N \sum_{j=1}^N \frac{q_i q_j}{r_{nij}} \phi(r_{nij}) \\
 &+ \left(\frac{1}{2}\right) \frac{1}{4\pi\epsilon_0} \sum_{\mathbf{n}}' \sum_{i=1}^N \sum_{j=1}^N \frac{q_i q_j}{r_{nij}} (1 - \phi(r_{nij}))
 \end{aligned} \quad (1.14)$$

The convergence function,  $\phi(r)$ , should be selected such that it should decay rapidly to zero as  $r$  increases, and  $\phi(0)$  should be unity. Thus, the presence of  $\phi(r)$  allows the first sum to converge in real space for distances less than  $r_{cut}$ , the real space interaction cutoff. A suitable choice of  $\phi(r)$  can be made such that the second term of  $U_{coul}(\{\mathbf{r}\})$  can be made convergent in the reciprocal space. The complementary error function,  $erfc(r)$ , which is defined as

$$erfc(r) = 1 - \sqrt{\frac{2}{\pi}} \int_0^r e^{-x^2} dx \quad (1.15)$$

where  $\zeta$  is the convergent parameter, has all the desired properties of the convergence function. Note that the parameter  $\zeta$  provides an additional handle to fine tune the range of convergence. By selecting  $erfc(\zeta r)$  as a convergence function, one can rewrite Eq. 1.14 as,

$$\begin{aligned}
 U_{coul}(\{\mathbf{r}\}) &= \left(\frac{1}{2}\right) \frac{1}{4\pi\epsilon_0} \sum_{\mathbf{n}}' \sum_{i=1}^N \sum_{j=1}^N \frac{q_i q_j}{r_{nij}} erfc(\zeta r_{nij}) \\
 &+ \left(\frac{1}{2}\right) \frac{1}{4\pi\epsilon_0} \sum_{\mathbf{n}}' \sum_{i=1}^N \sum_{j=1}^N \frac{q_i q_j}{r_{nij}} erf(\zeta r_{nij})
 \end{aligned} \quad (1.16)$$

where we have used the fact that  $erfc(\zeta r) + erf(\zeta r) = 1$ . The Ewald parameter  $\zeta$  can be fine tuned such that the first term in Eq. 1.16 is converged for distances less than  $r_{cut}$ . The

Fourier transform of the the second sum in Eq. 1.16, which is still long-ranged, can be evaluated in reciprocal space as a rapidly converging sum over reciprocal lattice vectors. Note that the self-interaction energy and the contribution coming from the bonded atoms should be subtracted out from the reciprocal term of the Ewald sum. Thus, the total Coulombic energy can be written as

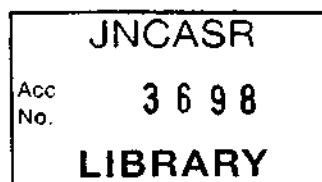
$$\begin{aligned}
 U_{coul}(\{\mathbf{r}\}) &= U_{real} + U_{reci} - U_{self} - U_{bonded} \\
 &= \frac{1}{4\pi\epsilon_0} \sum_{i=1}^N \sum_{j>i}^N \frac{q_i q_j}{r_{ij}} \text{erfc}(\zeta r_{ij}) + \frac{1}{2V\epsilon_0} \sum_{\mathbf{k}\neq 0} \frac{e^{-\frac{k^2}{4\zeta^2}}}{k^2} \left| \sum_{j=1}^N q_j e^{-i\mathbf{k}\cdot\mathbf{r}_j} \right|^2 \\
 &\quad - \frac{\alpha}{4\pi^{\frac{3}{2}}\epsilon_0} \sum_{j=1}^N q_j^2 - \frac{1}{4\pi\epsilon_0} \sum_i^N \sum_{j>i}^{bonded} \frac{q_i q_j}{r_{ij}} \text{erf}(\zeta r_{ij}) \quad (1.17)
 \end{aligned}$$

Here the third term is the self-energy term which has to be subtracted from the total reciprocal energy. Since atoms belonging to the same molecule are allowed to interact via the non-bonded part of the potential if they are separated by more than three bonds, these interactions also should be subtracted from reciprocal part of the Coulombic potential. The last term in Eq. 1.17 takes care of this. Although neutral systems have been considered here for the sake of simplicity, the Ewald summation technique can be applied to non-neutral systems also.

### Particle Mesh Ewald :

Although Ewald summation method has been used extensively in computer simulation of various systems, the computational cost associated with this method becomes too large for larger systems. The direct application of Ewald summation is an  $O(N^2)$  computational problem which can be reduced to  $O(N^{\frac{3}{2}})$  by suitable tuning of Ewald parameters. Particle Mesh Ewald (PME) is one of the methods to reduce the computational cost and makes the calculation to be of  $O(N \ln N)$  [161–164]. In PME, the Ewald screening parameter





is adjusted such that the contribution to the real space part of the Ewald sum by atom pairs that are separated by a distance greater than a specified cutoff is negligible. PME differs from regular Ewald summation method in the way in which the reciprocal part is evaluated. In PME, the system of interest is replaced by a mesh and the charge of one particle is distributed between its nearest mesh points. The reciprocal space energy and the force due to this term are evaluated at each grid point and stored into arrays at the beginning of the simulation. The reciprocal space contribution to the electrostatic potential is expressed as a convolution of grid based charge distribution and a "smearing function". Since the convolution of two functions in real space can be expressed as their product in reciprocal space, one can use Fast Fourier Transformation (FFT) to perform such reciprocal space products. Higher order interpolation scheme is used to compute the reciprocal space contribution to the electrostatic energy distributed for a given configuration of charged ions based on the values stored at grid points. The accuracy of PME method depends on the choice of the order of interpolation scheme and the grid spacing.

### 1.5.6 Reversible Reference System Propagation Algorithm

Despite its success in obtaining macroscopic quantities from the time evolution of microscopic states of the system, MD simulations of large molecular systems with many degrees of freedom often turns out to be a computationally demanding task. The main bottleneck in the simulation of complex molecular systems is the presence of high-frequency intramolecular motions that restrict the time step needed to integrate the equations of motion numerically. In a standard MD method, the slowly varying intermolecular forces are also calculated at every time step along with the rapidly varying intramolecular forces. Note that within a few time steps, the intermolecular forces would not have changed much. Thus, the total trajectory length that can be generated from such MD simulations is severely limited by the expensive calculations of intermolecular energy and forces at every time step. Multiple time step methods, in general are efficient in handling such cases.

539.6  
P05

They employ a small timestep to integrate the fast degrees of freedom and a larger step for the slow ones. The Reversible Reference system propagation algorithm (r-RESPA) developed by Tuckerman *et al* is one of the multiple time step methods that takes care of the separation of time scales present in the dynamics of macromolecules [165]. In r-RESPA, the fast and the slow modes are integrated with different time steps thus making the integration scheme more efficient to generate long time trajectories. Similarly, the intermolecular potential can be split into long- and short-range part and these can be evaluated with different time steps. This algorithm enables us to study interesting phenomena of complex macromolecular systems that are beyond the reach of single time step MD simulations. The beauty of the r-RESPA method is that it preserves the time reversal symmetry inherent in the equations of motion. A brief introduction to the implementation of r-RESPA for macromolecular systems is as follows: The treatment provided here is based on Ref. [166]. The time evolution of any classical system in phase space is given as

$$\Gamma(t) = e^{i\mathbf{L}t}\Gamma(0) \quad (1.18)$$

where  $\Gamma(t)$  and  $\Gamma(0)$  are phase space variables of the system at times  $t$  and  $t=0$ , respectively. Here, the operator  $e^{i\mathbf{L}t}$  is called the classical time evolution operator and  $i\mathbf{L}$  is the Liouville operator which is defined as,

$$\begin{aligned} i\mathbf{L} &\equiv [\dots, \mathbf{H}] \\ &= \sum_{i=1}^N \left( \dot{\mathbf{r}}_i \frac{\partial}{\partial \mathbf{r}_i} + \mathbf{F}_i(\{\mathbf{r}\}) \frac{\partial}{\partial \mathbf{p}_i} \right) \end{aligned} \quad (1.19)$$

where  $\mathbf{F}_i$  is the total force acting on  $i^{th}$  atom. For a macromolecular system, this force can be decomposed as,

$$\mathbf{F}_i = \mathbf{F}_i^{stretch} + \mathbf{F}_i^{bend} + \mathbf{F}_i^{torsion} + \mathbf{F}_i^{vdw} + \mathbf{F}_i^{Coul} \quad (1.20)$$

Here,  $\mathbf{F}_i^{stretch}$ ,  $\mathbf{F}_i^{bend}$ ,  $\mathbf{F}_i^{torsion}$ ,  $\mathbf{F}_i^{vdw}$ , and  $\mathbf{F}_i^{Coul}$  are the force acting on the  $i^{th}$  atom due to bond stretching, angle bending, torsion, van der Waals and Coulombic interactions respectively. Note that  $\mathbf{F}_i^{vdw}$  and  $\mathbf{F}_i^{Coul}$  arise from non-bonded interactions while the other forces are due to bonded atoms. Since the number of non-bonded interactions is relatively large, computation of the forces due to such interactions is the most time consuming part of MD simulations. In order to reduce the computational burden, we can divide the non-bonded forces into long- and short-range by using a switching function  $S(r)$  which is defined as,

$$S(r) = \begin{cases} 1 & r < r_c - \Delta r \\ 1 + R^2(2R - 3) & r_c - \Delta r \leq r \leq r_c \\ 0 & r_c < r \end{cases} \quad (1.21)$$

where  $R \equiv (r - (r_c - \Delta r)) / \Delta r$ ,  $r$  is the interatomic distance,  $r_c$  is the short-range cutoff, and  $\Delta r$  is the healing length. In the following treatment, we omit the subscript  $i$  from the forces as it is not going to affect the generality of the results. Thus, one can write the non-bonded forces,  $\mathbf{F}_{nb}$ , as,

$$\mathbf{F}_{nb} = \mathbf{F}_{nb}^{long} + \mathbf{F}_{nb}^{short} \quad (1.22)$$

with

$$\begin{aligned} \mathbf{F}_{nb}^{short} &= S(r)\mathbf{F}_{nb} \\ \mathbf{F}_{nb}^{long} &= (1 - S(r))\mathbf{F}_{nb} \end{aligned} \quad (1.23)$$

The Liouville operator can be split into four parts,

$$\mathbf{L} = \mathbf{L}_1 + \mathbf{L}_2 + \mathbf{L}_3 + \mathbf{L}_4 \quad (1.24)$$

such that

$$\begin{aligned}
 \mathbf{L}_1 &= \dot{\mathbf{r}} \frac{\partial}{\partial \mathbf{r}} + \mathbf{F}^{stretch} \frac{\partial}{\partial \mathbf{p}} \\
 \mathbf{L}_2 &= (\mathbf{F}^{bend} + \mathbf{F}^{torsion}) \frac{\partial}{\partial \mathbf{p}} \\
 \mathbf{L}_3 &= \mathbf{F}_{nb}^{short} \frac{\partial}{\partial \mathbf{p}} \\
 \mathbf{L}_3 &= \mathbf{F}_{nb}^{long} \frac{\partial}{\partial \mathbf{p}}
 \end{aligned}$$

It is to be noted that the stretching modes are the fastest degrees of freedom while the long range part of the non-bonded interaction is the slowest among all. Keeping that in mind, we rewrite the evolution equation as

$$\Gamma(t) = \mathbf{G}(t)\Gamma(0) \quad (1.25)$$

where  $\mathbf{G}(t)$  is given as,

$$\begin{aligned}
 \mathbf{G}(t) \equiv e^{i\mathbf{L}_4 t/2} [e^{i\mathbf{L}_2 \tau_3/2} \{e^{i\mathbf{L}_2 \tau_2/2} (e^{i\mathbf{L}_1 \tau_1})^{n_1} e^{i\mathbf{L}_2 \tau_2/2}\}^{n_2} \\
 e^{i\mathbf{L}_2 \tau_3/2}]^{n_3} e^{i\mathbf{L}_4 t/2}
 \end{aligned} \quad (1.26)$$

This evolution operator allows the bond stretching modes to evolve with a time step of  $\tau_1$  while angle bending and torsional degrees of freedom are sampled with a time step of  $\tau_2$ . Similarly, the short range non-bonded interaction forces are integrated with a time step of  $\tau_3$  while that of long-range part are evolved in steps of  $t$ . These time steps are related to each other through the following equations,

$$\begin{aligned}
 \tau_3 &= \frac{t}{n_3} \\
 \tau_2 &= \frac{t}{n_2 n_3} \\
 \tau_1 &= \frac{t}{n_1 n_2 n_3}
 \end{aligned} \quad (1.27)$$

where  $n_1$ ,  $n_2$ , and  $n_3$  are integers. For the molecules considered in this thesis, the C-H stretching is the fastest mode and a timestep of at least 0.5 fs is needed to integrate it. Thus, we have used an outer time step,  $t = 4$  fs with  $n_1 = n_2 = n_3 = 2$  which gives rise to 0.5 fs for the C-H stretch.

### 1.5.7 Time Correlation Functions (TCF):

The MD trajectory thus generated by solving the equations of motion that characterize the desired ensemble can be used to study the vibrational and the transport properties of the system. This can be achieved by examining the correlation between the dynamical quantities and the time dependence of such correlations. Time correlation functions give unambiguous microscopic insight into the dynamics of the system. Experimentally measurable transport coefficients such as diffusion constant, viscosity, thermal conductivity, and others, which are accessible from non-equilibrium MD, can also be calculated from equilibrium simulations [167,168]. This can be achieved using the linear response theory which relates these transport coefficients to the time integral of the TCF of some dynamical variable. For instance, the diffusion coefficient is related to the time integral of the velocity auto-correlation function (VACF) as follows,

$$D = \frac{k_B T}{m} \int_0^{\infty} C(t) dt \quad (1.28)$$

where  $C(t) = \frac{\langle \mathbf{v}(t) \cdot \mathbf{v}(0) \rangle}{\langle \mathbf{v}(0) \cdot \mathbf{v}(0) \rangle}$  is the normalized VACF. Moreover, the vibrational density of states of a system can also be obtained by Fourier transforming the VACF. The power spectrum  $C(\omega)$  is defined as

$$C(\omega) = \int_{-\infty}^{\infty} C(t) e^{-i\omega t} dt. \quad (1.29)$$

The power spectrum thus obtained has valuable information on the different vibrational modes present in the system and is directly proportional to the vibrational density of

states (VDOS).

## 1.6 Free Energy Calculations

The relative stability of different phases of a system at a given thermodynamic state-point is determined by their free energies. The chemical potential of two coexisting phases are equal. Thus, for an exploration of the phase diagram or phase equilibria of a system, a determination of the free energy of the system at different thermodynamic state points is a prerequisite. The free energy of a system in a canonical ensemble is given as [167],

$$F = -k_B T \ln \left( \frac{1}{h^{3N} N!} \int \int e^{-\beta H(\mathbf{r}, \mathbf{p})} d\mathbf{r} d\mathbf{p} \right) \quad (1.30)$$

where  $h$  is the Planck's constant.

One of the earliest methods of calculating the free energy was proposed by Widom and is called the particle insertion scheme [169,170]. This method uses the relation between excess chemical potential to the change in total energy associated with a random insertion of an additional particle in an equilibrium  $N$ -particle system. This relation is given as

$$\mu_{ex} = -k_B T \ln \int \langle e^{-\beta \Delta U} \rangle_N d\mathbf{r} \quad (1.31)$$

where  $k_B$  is the Boltzmann constant,  $T$  is temperature, and  $\Delta U$  is the change in energy due to an additional particle insertion. The symbol  $\langle \dots \rangle_N$  denotes an ensemble average over many configurations of the equilibrated  $N$  particle system. This ensemble average can be calculated from Monte Carlo or molecular dynamics simulations. This method performs poorly for high density fluids and solid phases as the probability of accepting the inserted particle becomes very small at high densities. Such methods cannot be used directly for molecular systems of moderate densities as the acceptance probability becomes negligibly small. Also, the the solid-fluid phase transition is first order and exhibits a high degree

of hysteresis effects. This is due to computational "kinetic effects" such as equilibration times and extent of sampling that makes the path connecting these high density phases irreversible. Thus, standard thermodynamic integration methods also fail for these studies as they require a reversible path (isotherms or isochores) connecting the system from one thermodynamic state to another of known free energy. For example, usually the ideal gas is considered as a reference state for the calculation of free energy of a fluid phase. Note that the free energy of an ideal gas can be calculated analytically. Thus, one can generate isotherms of this fluid system using Monte Carlo or molecular dynamics simulations and calculate the free energy at a given density by integrating along an isotherm to zero density where the system behaves as an ideal gas of known free energy. For a solid, a reversible path at constant density can be constructed by connecting to a low temperature harmonic solid of known free energy. The free energy difference between these two states are obtained by calculating the average internal energy from simulations and integrating it along the isochore. The systems for which a solid-solid transition occurs along the isochore or systems that are not harmonic solids at low temperatures cannot be studied by this method. In order to surmount these problems, various methods to study the free energy of any solid have been proposed. These methods construct an artificial reversible path connecting the system of interest and an artificial system of known free energy. This reversible path is called artificial because only the intermolecular interactions are varied without varying the thermodynamic state variables such as temperature, density along this path. One of the earliest of such methods is called single-occupancy-cell (SOC) method introduced by Hoover and Ree and was applied to study the melting of hard-sphere and hard-disk solids [171,172]. In this method, an artificial solid is constructed such that the center of each particle in an  $N$ -particle system is confined to its own cell of volume  $V/N$ . The collision of particles with the walls of the SOC and collision with neighboring particles are the two kinds of interactions that allow the particles in the artificial solid to be confined inside its own SOC. The artificial solid is constructed such

that at high densities its properties are the same as a perfect solid. At low densities, the collisions of the particles with the walls of the SOC become dominant thus preventing the melting of the artificial solid. The free energy of the solid can be obtained by computing

$$F_{solid}(V_2) - F_{art\ solid}(V_1) = - \int_{V_1}^{V_2} P(V) dV \quad (1.32)$$

at constant temperature. Here,  $F_{art\ solid}(V_1)$  stands for free energy of the artificial solid. It has been pointed out that the path connecting the solid and artificial solid phase is not quite reversible as it passes through a weak first-order transition [173]. Frenkel and Ladd proposed a new method in which a reversible path is constructed between the solid under consideration and the Einstein crystal with the same structure [174]. In the Einstein crystal, the particles are coupled harmonically to their equilibrium lattice positions. The Hamiltonian of the solid can be written as,

$$\begin{aligned} H(\lambda) &= H_0 + \lambda V(\mathbf{r}) \\ &= H_0 + \lambda \sum_{i=1}^N (\mathbf{r}_i - \mathbf{r}_i^0)^2 \end{aligned} \quad (1.33)$$

where  $\mathbf{r}_i^0$  is the equilibrium lattice position of  $i^{th}$  atom,  $\mathbf{r}_i$  is its instantaneous position,  $V(\mathbf{r})$  is the potential energy of the Einstein crystal,  $\lambda$  is the coupling constant, and  $\mathbf{r} = \{\mathbf{r}_1, \mathbf{r}_2, \dots, \mathbf{r}_N\}$  denotes the complete set of atomic coordinates. The differential of free energy with respect to  $\lambda$  can be shown as,

$$\begin{aligned} \frac{\partial F}{\partial \lambda} &= -K_B T \frac{\partial}{\partial \lambda} \ln \int \dots \int e^{-\beta(H_0 + \lambda V(\mathbf{r}))} d\mathbf{r}^N \\ &= \langle V(\mathbf{r}) \rangle_\lambda \end{aligned} \quad (1.34)$$

Where the brackets  $\langle \dots \rangle_\lambda$  represents an ensemble average calculated for a particular value of  $\lambda$ . By integrating this equation with respect to  $\lambda$ , we can relate the free energy of the



solid and that of a crystal with spring constant  $\lambda$  as

$$F(\lambda = 0) = F(\lambda) - \int_0^\lambda \langle V(\mathbf{r}) \rangle_\lambda d\lambda \quad (1.35)$$

Such free energy methods have been used to characterize the phase behaviour of both model systems and the realistic mimic of relatively smaller molecular systems such as  $\text{N}_2$  [175–177],  $\text{CO}_2$  [178], and  $\text{N}_2\text{O}$  [179]. While considerable efforts were made to understand the gas-liquid equilibrium of chain molecular systems [159, 180, 181], improvements in the methodology have enabled in recent years to explore the solid-fluid phase behaviour too [158].

## 1.7 Limit of Metastability

Along the pathway to thermodynamic equilibrium, kinetic effects such as heating or cooling rate, crystallization or freezing conditions and others could lead the system to metastable states. These states are thermodynamically less stable than the equilibrium phase but more stable than unstable states. For metastable states,

$$\frac{dF}{d\phi} = 0$$

$$\frac{d^2F}{d\phi^2} > 0$$

where  $F$  is the thermodynamic free energy and  $\phi$  is an order parameter. Metastable states are stable with respect to small fluctuations but the system trapped in such a state can eventually reach the global free energy minima where the equilibrium state of the system is located. Understanding the mechanism by which the system evolves from the metastable state to the equilibrium phase and the rate associated with this transition has interesting applications in chemical industries and in living systems [182]. It was

proposed by Ostwald that the transformation from one stable state to another proceeds via a sequence of metastable states and follows a stage of increasing stability [183]. It is known that superheating a liquid above its boiling point or supercooling it below its freezing point gives rise to a metastable liquid state. For example, water at atmospheric pressure can be supercooled to  $-41^{\circ}\text{C}$  and superheated to  $302^{\circ}\text{C}$  [182]. Thus, in order to make a system to go into a metastable phase, it should not be allowed to sample the more stable configurations. The concept of metastability is not limited to liquid state alone. A crystalline solid can be superheated well above its equilibrium melting point. It is known that the process of melting starts at grain boundaries and at the free surfaces of crystals. Thus by avoiding the presence of free surfaces and grain boundaries, one can superheat a crystal well above its equilibrium melting point. There has been lot of interest on understanding the limit of stability of metastable phases of superheated crystals [184–187]. Heating rate, among other parameters, plays a dominant role in determining the limit of metastability. In MD simulations, free surfaces are removed by the application of periodic boundary conditions. Also, the heating rates employed in such simulations are many orders of magnitude higher than that achieved in experiments. Calorimetry experiments [188] generally employ heating rates that range from 0.5 to 30 K/min while in MD simulations it can range from 1 K/fs to 1 K/ns. These factors clearly suggest that metastable phases are inevitable in such simulations. Although it is true, one can reduce the limit of metastability in MD simulations by introducing lattice and conformational defects [189].

## 1.8 Codes Developed and Used

The bulk MD simulations reported in this thesis were performed using the PINY\_MD code [190] while the phase behaviour studies of *n*-alkanes physisorbed on the basal plane of graphite were carried out using the NEMD code [191]. For the characterization of vibrational features of molecular crystals dealt with in this thesis, we have developed

a code that uses the method of normal mode analysis. The structure, thermodynamic, and dynamical properties reported here were all calculated using codes developed during the course of this research work. All the calculations reported here were performed on the Beowulf clusters built in our group as well as on the parallel computers available in the central computing facilities of Jawaharlal Nehru Centre for Advanced Scientific Research (JNCASR), India. We have also used the computing resources of the national super-computing facility provided by Centre for Development of Advanced Computing (CDAC), India. In Table 1.1, we give a list of computers used and their descriptions.

Name of the Computer	Description	Service Provider
Kamadhenu	8-node Beowulf cluster	Our Group (JNCASR)
Bheema	10-node Beowulf cluster	Our Group (JNCASR)
Bella	Compaq ES40, 4 processors	JNCASR
Bevu	Compaq ES40, 4 processors	JNCASR
HP1, HP2, HP3, HP4	Hewlett-Packard K260 servers, 3 processors each	JNCASR
PARAM PADMA super computer	IBM-SP servers	CDAC

Table 1.1: List of computers used in this research work and their descriptions



# Bibliography

- [1] D.M. Small, *The Physical Chemistry of Lipids: From Alkanes to Phospholipids* (Plenum, New York, 1986).
- [2] A.I. Kitaigorodskii, *Molecular Crystals and Molecules* (Academic Press, New York, 1973).
- [3] J. Lascombe, *Dynamics of Molecular Crystals* (Elsevier, Amsterdam, 1986).
- [4] G. Strobl, *The Physics of Polymers* (Springer, New York, 1997).
- [5] A.Y. Grosberg, and A.R. Khokhlov, *Giant Molecules, Here, There and Everywhere* (Academic Press, San Diego, CA, 1997).
- [6] J.H. Fuhrhop, and J. Köning, *Membranes and Molecular Assemblies : The Synekinetic Approach* (The Royal Society of Chemistry, Cambridge, 1994).
- [7] M. Rubinstein, and R.H. Colby, *Polymer Physics* (Oxford University Press, New York, 2004).
- [8] E. Kissa, *Fluorinated Surfactants : Synthesis, Properties, and Applications* (Surfactant Science Series, Vol. 50) (Marcel Dekker, Inc., New York, 1994).
- [9] D. Attwood, and A.T. Florence, *Surfactant Systems : Their Chemistry, Pharmacy, and Biology* (Chapman and Hall, London, 1983).
- [10] H. Tadokoro, *Polymer* **25**, 147 (1984)

- 
- [11] B. Wunderlich, M. Möller, J. Grebowicz, and H. Baur, *Adv. Polymer Sci.* **87**, 50 (1988).
- [12] L.S. Kassel, *J. Chem. Phys.* **4**, 276 (1936).
- [13] J.D. Kemp, and K.S. Pitzer, *J. Chem. Phys.* **4**, 749 (1936).
- [14] K.S. Pitzer, *J. Chem. Phys.* **5**, 469 (1937).
- [15] K.S. Pitzer, *J. Chem. Phys.* **5**, 473 (1937).
- [16] J.Y. Beach, and K.J. Palmer, *J. Chem. Phys.* **6**, 639 (1938).
- [17] S. Mizushima, Y. Morino, and M. Takeda, *J. Chem. Phys.* **9**, 826 (1941).
- [18] M.S. Newman, *Steric Effects in Organic Chemistry* (John Wiley & Sons, Inc., New York, 1956).
- [19] S.I. Mizushima, *Structure of Molecules and Internal Rotation* (Academic Press, Inc., 1954).
- [20] A.K. Mazur, *J. Phys. Chem. B* **102**, 473 (1998).
- [21] M. Sprik, U. Röthlisberger, and M.L. Klein, *Mol. Phys.* **97**, 355 (1999); *J. Phys. Chem. B.* **101**, 2745 (1997).
- [22] C.P. Buckley, and A.J. Kovacs, in *Structure of Crystalline Polymers* (Ed. I.H. Hall, Elsevier-Applied Science, London, 1984, pp. 261).
- [23] J.M. Schultz, *Polymer Crystallization : The Development of Crystalline Order in Thermoplastic Polymers* (Oxford University Press, New York, 2001).
- [24] L. Mandelkern, *Crystallization of Polymers* (Vol. 1, Cambridge University Press, 2002).
- [25] D.M. Sadler, and G.H. Gilmer, *Polymer* **25**, 1446 (1984).

- 
- [26] H. Meyer, and F. Müller-Plathe, *J. Chem. Phys.* **115**, 7807 (2001).
- [27] H. Meyer, and F. Müller-Plathe, *Macromolecules* **35**, 1241 (2002).
- [28] J.A. Sauer, and A.E. Woodward, *Revs. Mod. Phys.* **32**, 88 (1960).
- [29] P. Schmidt, B. Schneider, J. Baldrian, L. Terlemezyan, M. Mihailov, and B. Ivanova, *Polymer* **28**, 217 (1987).
- [30] G. Ungar, *Polymer* **34**, 2050 (1993).
- [31] J.D. Barnes, *J. Chem. Phys.* **58**, 5193 (1973).
- [32] G. Strobl, B. Ewen, E.W. Fischer, and W. Piesczek, *J. Chem. Phys.* **61**, 5257 (1974).
- [33] B. Ewen, E.W. Fischer, W. Piesczek, and G. Strobl, *J. Chem. Phys.* **61**, 5265 (1974).
- [34] B. Ewen, and D. Richter, *J. Chem. Phys.* **69**, 2954 (1978).
- [35] A. Chiba, A. Hasegawa, K. Hikichi, and J. Furuichi, *J. Phys. Soc. Japan* **21**, 1777 (1966).
- [36] M. Yamamoto, and K. Hikichi, *J. Polym. Sci., Part C* **15**, 93 (1966).
- [37] M.M. Dorio, and J.C.W. Chien, *Macromolecules* **8**, 734 (1975).
- [38] A. Müller, *Proc. R. Soc. London Ser. A* **127**, 417 (1930).
- [39] A. Müller, *Proc. R. Soc. London Ser. A* **127**, 514 (1932).
- [40] A. Müller, *Nature (London)* **164**, 1002 (1949).
- [41] A. Müller, *Proc. R. Soc. London Ser. A* **207**, 101 (1951).
- [42] C.W. Bunn, and E.R. Howells, *Nature (London)* **174**, 549 (1954).
- [43] E.S. Clark, L.T. Muus, *Z. Kristallogr.* **117**, 119 (1962).

- 
- [44] I. Denicolo, J. Doucet, and A.F. Craievich, *J. Chem. Phys.* **78**, 1465 (1983).
- [45] H.B. Burgi, *Acta Cryst.*, **B45**, 383 (1989).
- [46] T. Yamamoto, K. Nozaki, and T. Hara, *J. Chem. Phys.* **92**, 631 (1990).
- [47] J.D. Dunitz, V. Shoemaker, and K.N. Trueblood, *J. Phys. Chem.* **92**, 856 (1988).
- [48] V. Chevallier, E. Provost, J.B. Bourdet, M. Bouroukba, D. Petitjean, and M. Dirand, *Polymer* **40**, 2121 (1999).
- [49] A.B. Herhold, H.E. King, E.B. Sirota, *J. Chem. Phys.* **116**, 9036 (2002).
- [50] D. Mondieig, V. Metivaud, H.A.J. Oonk, and M.A. Cuevas-Diarte, *Chem. Mat.* **15**, 2552 (2003).
- [51] D.M. Rein, L. Shavit, R.L. Khalfin, Y. Cohen, A. Terry, and S. Rastogi, *J. Polym. Sci. Part B - Polym. Phys.* **42**, 53 (2004).
- [52] J.D. Hoffman, *J. Chem. Phys.* **20**, 541 (1952).
- [53] C.M. Atkinson, M.J. Richarso, *Trans. Farad. Soc.* **65**, 1749 (1969).
- [54] S.L. Wang, K. Tozaki, H. Hayashi, S. Hosaka, and H. Inaba, *Thermochimica Acta* **408**, 31 (2003).
- [55] U. Domanska, and D. Wyrzykowskastankiewicz, *Thermochimica Acta* **179**, 265 (1991).
- [56] H.L. Finke, M.E. Gross, G. Waddington, and H.M. Huffman, *J. Amer. Chem. Soc.* **76**, 333 (1954).
- [57] T. Gorecki, S.P. Srivastava, G.B. Tiwari, C. Gorecki, and A. Zurawska, *Thermochimica Acta* **345**, 25 (2000).
- [58] C. Josefiak, A. Wurflinger, and G.M. Schneider, *Colloid Polym. Sci.* **255**, 170 (1977).



- [59] B. Koppitz, *Colloid Polym. Sci.* **252**, 999 (1974).
- [60] K. Takamizawa, Y. Nagao, D. Irii, and Y. Urabe, *Thermochimica Acta* **88**, 205 (1985).
- [61] G.W.H. Hohne, and K. Blankenhorn, *Thermochimica Acta* **238**, 351 (1994).
- [62] M. Maroncelli, H.L. Strauss, and R.G. Snyder, *J. Chem. Phys.* **82**, 2811 (1985).
- [63] R.G. Alamo, J.D. Londono, L. Mandelkern, F.C. Stehling, and G.D. Wignall, *Macromolecules* **27**, 411 (1994).
- [64] M. Bee, A. Renault, J. Lajzerowiczbonneteau, and M. Lebarscombe, *J. Chem. Phys.* **97**, 7730 (1992).
- [65] F. Guillaume, C. Sourisseau, and A.J. Dianoux, *J. Chem. Phys.* **93**, 3536 (1990).
- [66] S. Ishikawa, and I. Ando, *J. Mol. Struct.* **273**, 227 (1992).
- [67] S. Ishikawa, H. Kurosu, and I. Ando, *J. Mol. Struct.* **248**, 361 (1991).
- [68] S. Ishikawa, and I. Ando, *J. Mol. Struct.* **291**, 183 (1993).
- [69] E. Katoh, H. Kurosu, and I. Ando, *J. Mol. Struct.* **318**, 123 (1994).
- [70] T. Nakaoki, H. Nagano, and T. Yanagida, *J. Mol. Struct.* **699**, 1 (2004).
- [71] M.J. Stewart, W.L. Jarrett, L.J. Mathias, R.G. Alamo, and L. Mandelkern, *Macromolecules* **29**, 4963 (1996).
- [72] K.E. Russell, G. Wu, S. Blake, and R.D. Heyding, *Polymer* **33**, 951 (1992).
- [73] S. Kim, H. Kimura, S. Kuroki, and I. Ando, *Chem. Phys. Lett.* **367**, 581 (2003).
- [74] F. Imashiro, T. Maeda, T. Nakai, A. Saika, and T. Terao, *J. Phys. Chem.* **90**, 5498 (1986).

- 
- [75] T. Yamanobe, T. Sorita, T. Komoto, I. Ando, and H. Sato, *J. Mol. Struct.* **131**, 267 (1985).
- [76] C. Akita, T. Kawaguchi, F. Kaneko, H. Yamamoto, and M. Suzuki, *J. Phys. Chem.* **108**, 4862 (2004).
- [77] K. Kuwabara, F. Horii, and Y. Ogawa, *J. Mol. Struct.* **602**, 79 (2002).
- [78] K. Kuwabara, F. Horii, and Y. Ogawa, *J. Mol. Struct.* **569**, 55 (2001).
- [79] M.I. Bank, and S. Krimm, *J. Polym. Sci., Part A-2-Polym. Phys.* **7**, 1785 (1969).
- [80] K.H. Fiedler, S.L. Wunder, R.G. Priest, et al., *J. Chem. Phys.* **76**, 5541 (1982).
- [81] L. Kurelec, S. Rastogi, R.J. Meier, P.J. Lemstra, *Macromolecules* **33**, 5593 (2003).
- [82] J.M. Lagaron, *J. Mol. Struct.* **37**, 4101 (2002).
- [83] K. Esselink, P.A.J. Hilbers, and B.W.H. van Beest, *J. Chem. Phys.* **101**, 9033 (1994).
- [84] N. Waheed, M.S. Lavine, and G.C. Rutledge, *J. Chem. Phys.* **116**, 2301 (2002).
- [85] M.J. Ko, N. Waheed, M.S. Lavine, and G.C. Rutledge, *J. Chem. Phys.*, **121**, 2823 (2004).
- [86] T. Yamamoto, *Polymer* **45**, 1357 (2004).
- [87] P. Welch, and M. Muthukumar, *Phys. Rev. Lett.* **87**, 218302 (2001).
- [88] K. Fukao, and Y. Miyamoto, *Phys. Rev. Lett.* **79**, 4613 (1997).
- [89] C.M. Chen, and P.G. Higgs, *J. Chem. Phys.* **108**, 4305 (1998).
- [90] J. Doucet, I. Denicolo, A. Craievich, and A. Collet, *J. Chem. Phys.* **75**, 5125 (1981).
- [91] G. Ungar, *J. Phys. Chem.* **87**, 689 (1983).
- [92] A.F. Craievich, I. Denicolo, and J. Doucet, *Phys. Rev. B* **30**, 4782 (1984).

- 
- [93] E.B. Sirota, D.M. Singer, *J. Chem. Phys.* **101**, 10873 (1994).
- [94] P.K. Mukherjee, M. Deutsch, *Phys. Rev. B* **60**, 3154 (1999).
- [95] P.K. Mukherjee, *J. Chem. Phys.* **113**, 4472 (2000).
- [96] J.P. Ryckaert, and M. L. Klein, *J. Chem. Phys.* **85**, 1613, (1986).
- [97] J.P. Ryckaert, M. L. Klein, and I. R. McDonald, *Phys. Rev. Lett.* **58**, 698 (1987).
- [98] J.P. Ryckaert, I.R. McDonald, and M.L. Klein, *Mol. Phys.* **67**, 957 (1989).
- [99] J.P. Ryckaert, M.L. Klein, and I.R. McDonald, *Mol. Phys.* **83**, 439 (1994).
- [100] E.B. Sirota, H.E. King, Jr., D.M. Singer, and H.H. Shao, *J. Chem. Phys.* **98**, 5809 (1993).
- [101] E.B. Sirota, and D.M. Singer, *J. Chem. Phys.* **101**, 10873 (1994).
- [102] E.B. Sirota, D.M. Singer, and H.E. King, Jr., *J. Chem. Phys.* **100**, 1542 (1994).
- [103] W.L. Jarret, L.J. Mathias, R.G. Alamo, L. Mandelkern, and D.L. Dorset, *Macromolecules* **25**, 3468 (1992).
- [104] X.Z. Wu, E.B. Sirota, S.K. Sinha, B.M. Ocko, and M. Deutsch, *Phys. Rev. Lett.* **70**, 958 (1993).
- [105] E.B. Sirota, X.Z. Wu, B.M. Ocko, and M. Deutsch, *Phys. Rev. Lett.* **79**, 531 (1997).
- [106] B.M. Ocko, X.Z. Wu, E.B. Sirota, S.K. Sinha, O. Gang, and M. Deutsch, *Phys. Rev. E* **55**, 3164 (1997).
- [107] B.M. Ocko, E.B. Sirota, M. Deutsch, E. DiMasi, S. Coburn, J. Strzalka, S. Zheng, A. Tronin, T. Gog, and C. Venkataraman, *Phys. Rev. E* **63**, 032602 (2001).
- [108] X.Z. Wu, B.M. Ocko, H. Tang, E.B. Sirota, S.K. Sinha, and M. Deutsch, *Phys. Rev. Lett.* **75**, 1332 (1995).

- 
- [109] E. Sloutskin, E. B. Sirota, H. Kraack, B. M. Ocko, and M. Deutsch, *Phys. Rev. E* **64**, 031708 (2001).
- [110] O. Gang, B.M. Ocko, X.Z. Wu, E.B. Sirota, and M. Deutsch, *Phys. Rev. Lett.* **80**, 1264 (1998).
- [111] O. Gang, X.Z. Wu, B.M. Ocko, E.B. Sirota, and M. Deutsch, *Phys. Rev. E* **58**, 6086 (1998).
- [112] A. Bondi, *J. Phys. Chem.* **68**, 441 (1964).
- [113] D.A. Dixon, *J. Phys. Chem.* **96**, 3698 (1992).
- [114] G.D. Smith, R.L. Jaffe, and D.Y. Yoon, *Macromolecules* **27**, 3166 (1994).
- [115] G. Masetti, F. Cabassi, G. Morelli, and G. Zerbi, *Macromolecules* **6**, 700 (1973).
- [116] W.P. Slichter, *J. Polymer Sci.* **24**, 173 (1957).
- [117] D.W. McCall, D.C. Douglass, and D.R. Falcone, *J. Phys. Chem.* **71**, 998 (1967).
- [118] A.J. Vega, and A.D. English, *Macromolecules* **13**, 1635 (1980).
- [119] D.A. Lathrop, and K.K. Gleason, *Macromolecules* **26**, 4652 (1993).
- [120] V. Villani, and R. Pucciariello, *Colloid Polymer Sci.* **271**, 652 (1993).
- [121] H.W. Starkweather, P. Zoller, G.A. Jones, and A.J. Vega, *J. Polymer Sci., Polymer Phys. Edn* **20**, 751 (1982).
- [122] S.F. Lau, H. Suzuki, and B. Wunderlich, *J. Polymer Sci., Polymer Phys. Edn.* **22**, 379 (1984).
- [123] H.W. Starkweather, *Macromolecules* **19**, 1131 (1986).
- [124] D. Frenkel, and B. Smit, *Understanding Molecular Simulation* (Academic Press, San Diego, 1996).

- 
- [125] M.P. Allen, D.J. Tildesley, *Computer Simulation of Liquids* (Oxford, Clarendon, 1987).
- [126] G. Ciccotti, D. Frenkel, and I.R. McDonald, *Simulation of Liquids and Solids : Molecular Dynamics and Monte Carlo Methods in Statistical Mechanics* (North-Holland, Amsterdam, 1990).
- [127] J.P. Hansen in G. Ciccotti, and W.G. Hoover, *Molecular-Dynamics Simulation of Statistical-Mechanical Systems* (North-Holland, Amsterdam, 1986).
- [128] A.R. Leach, *Molecular Modelling : Principles and Applications* (Prentice Hall, Harlow, 2001).
- [129] A.K. Rappe, and C.J. Casewit, *Molecular Mechanics Across Chemistry* (University Science Books, Sausalito, 1997).
- [130] M.J. Field, *A Practical Introduction to Simulation of Molecular Systems* (Cambridge University Press, Cambridge, 1999).
- [131] H.C. Andersen, *J. Chem. Phys.* **72**, 2384 (1980).
- [132] S. Nosé, *Mol. Phys.* **52**, 255 (1984).
- [133] S. Nosé, *J. Chem. Phys.* **81**, 511 (1984).
- [134] W.G. Hoover, *Phys. Rev. A* **31**, 308 (1985).
- [135] G.J. Martyna, M.L. Klein, and M. Tuckerman, *J. Chem. Phys.* **97**, 2635 (1992).
- [136] G.J. Martyna, M.E. Tuckerman, D.J. Tobias, and M.L. Klein, *Mol. Phys.* **87**, 1117 (1996).
- [137] C.J. Mundy, S. Balasubramanian, K. Bagchi, M.E. Tuckerman, G.J. Martyna, and M.L. Klein, *Reviews in Computational Chemistry* **14**, 291 (1999).

- 
- [138] M. Parrinello and A. Rahman, *Phys. Rev. Lett.* **45**, 1196 (1980).
- [139] M. Parrinello and A. Rahman, *J. Appl. Phys.* **52**, 7182 (1981).
- [140] M. Parrinello and A. Rahman, *J. Chem. Phys.* **76**, 2662 (1982).
- [141] M. Parrinello, A. Rahman, and P. Vashishta, *Phys. Rev. Lett.* **50**, 1073 (1983).
- [142] G.S. Pawley, and G.W. Thomas, *Phys. Rev. Lett.* **48**, 410 (1982).
- [143] J.R. Ray, *J. Appl. Phys.* **53**, 6441 (1982).
- [144] S. Nosé, and M.L. Klein, *Phys. Rev. Lett.* **50**, 1207 (1983).
- [145] S. Nosé, and M.L. Klein, *J. Chem. Phys.* **78**, 6928 (1983).
- [146] R.W. Impey, S. Nosé, and M.L. Klein, *Mol. Phys.* **50**, 243 (1983).
- [147] S. Nosé, and M.L. Klein, *Mol. Phys.* **50**, 1055 (1983).
- [148] M. Parrinello, and A. Rahman, *J. Chem. Phys.* **80**, 860 (1984).
- [149] R.W. Impey, M.L. Klein, I.R. McDonald, *J. Chem. Phys.* **82**, 4690 (1985).
- [150] J.R. Ray, M.C. Moody, and A. Rahman, *Phys. Rev. B* **32**, 733 (1985).
- [151] R.W. Impey, M. Sprik, and M.L. Klein, *J. Chem. Phys.* **83**, 3638 (1985).
- [152] J.P. Ryckaert, and M.L. Klein, *J. Chem. Phys.* **85**, 1613 (1986).
- [153] D. Brown, and J.H.R. Clarke, *Macromolecules* **24**, 2075 (1991).
- [154] M. Wilson, F. Hutchinson, and P.A. Madden, *Phys. Rev. B* **65**, 094109 (2002).
- [155] G.J. Martyna, D.J. Tobias, M.L. Klein, *J. Chem. Phys.* **101**, 4177 (1994).
- [156] S. Leggetter, and D.J. Tildesley, *Mol. Phys.* **68**, 519 (1989).
- [157] F.Y. Hansen, J.C. Newton, and H. Taub, *J. Chem. Phys.* **98**, 4128 (1993).

- 
- [158] J.M. Polson, and D. Frenkel, *J. Chem. Phys.* **111**, 1501 (1999).
- [159] B. Chen, M.G. Martin, and J.I. Siepmann, *J. Phys. Chem. B* **102**, 2578 (1998).
- [160] D.J. Tobias, K. Tu, M.L. Klein, *J. Chim. Phys. Phys.-Chim. Biol.* **94**, 1482 (1997).
- [161] T. Darden, D. York, and L. Pedersen, *J. Chem. Phys.* **98**, 10089 (1993).
- [162] U. Essmann, L. Perera, M.L. Berkowitz, T. Darden, H. Lee, and L.G. Pedersen, *J. Chem. Phys.* **103**, 8577 (1995).
- [163] M. Deserno, and C. Holm, *J. Chem. Phys.* **109**, 7678 (1998).
- [164] M. Deserno, and C. Holm, *J. Chem. Phys.* **109**, 7694 (1998).
- [165] M. Tuckerman, B.J. Berne, and G.J. Martyna, *J. Chem. Phys.* **97**, 1990 (1992).
- [166] D.D. Humphreys, R.A. Friesner, and B.J. Berne, *J. Phys. Chem.* **98**, 6885 (1994).
- [167] D.A. McQuarrie, *Statistical Mechanics* (University Science Books, Sausakito, 2003).
- [168] B.J. Berne, and R. Pecora, *Dynamic Light Scattering : With Applications to Chemistry, Biology, and Physics* (John Wiley & Sons, Inc., New York, 1976).
- [169] B. Widom, *J. Chem. Phys.* **39**, 2808 (1963).
- [170] B. Widom, *J. Chem. Phys.* **86**, 869 (1982).
- [171] W.G. Hoover, and F.H. Ree, *J. Chem. Phys.* **47**, 4873 (1967).
- [172] W.G. Hoover, and F.H. Ree, *J. Chem. Phys.* **49**, 3609 (1968).
- [173] H. Ogura, H. Matsuda, T. Ogawa, N. Ogita, and U. Ueda, *Prog. Theor. Phys.* **58**, 419 (1977).
- [174] D. Frenkel, and A.J.C. Ladd, *J. Chem. Phys.* **81**, 3188 (1984).

- 
- [175] E. J. Meijer, D. Frenkel, R. A. LeSar, and A. J. C. Ladd, *J. Chem. Phys.* **92**, 7570 (1990).
- [176] B. Kuchta, K. Rohleder, R. D. Eppers, and J. Belak, *J. Chem. Phys.* **102**, 3349 (1995).
- [177] B. Kuchta, K. Rohleder, R. D. Eppers, and J. Belak, *J. Chem. Phys.* **106**, 6771 (1997).
- [178] B. Kuchta, and R. D. Eppers, *Phys. Rev. B* **47**, 14691 (1993).
- [179] B. Kuchta, and R. D. Eppers, *Phys. Rev. B* **45**, 5072 (1992).
- [180] B. Smit, S. Karaborni, and J. I. Siepmann, *J. Chem. Phys.* **102**, 2126 (1995).
- [181] M.G. Martin, and J.I. Siepmann, *J. Phys. Chem. B* **102**, 2569 (1998).
- [182] P.G. Debenedetti, *Metastable Liquids : Concepts and Principles* (Princeton University Press, Princeton, 1996).
- [183] S.Z.D. Cheng, and A. Keller, *Annu. Rev. Mater. Sci.* **28**, 533 (1998).
- [184] Z.H. Jin, P. Gumbsch, K. Lu, and E. Ma, *Phys. Rev. Lett.* **87**, 055703-1 (2001).
- [185] K. Lu, and Y. Li, *Phys. Rev. Lett.* **80**, 4474 (1998).
- [186] S.N. Luo, and T.J. Ahrens, *Appl. Phys. Lett.* **82**, 1836 (2003).
- [187] S.N. Luo, T.J. Ahrens, T. Cagin, A. Strachan, W.A. Goddard III, and D.C. Swift, *Phys. Rev. B* **68**, 134206 (2003).
- [188] C.P. Buckley, and A.J. Kovacs, *Colloid and Polym. Sci.* **254**, 695 (1976).
- [189] G.F. Velardez, S. Alavi, and D.L. Thompson, *J. Chem. Phys.* **119**, 6698 (2003).
- [190] M.E. Tuckerman, D.A. Yarne, S.O. Samuelson, A.L. Hughes, and G.J. Martyna, *Comp. Phys. Comm.* **128**, 333 (2000).



[191] NEMD code was developed by C.J. Mundy, S. Balasubramanian, and M.L. Klein.

## Chapter 2

# Thermal Evolution of Conformation, Structure, and Dynamics in Crystalline Poly(Ethylene Oxide)

### 2.1 Introduction

Poly(ethylene oxide) (PEO) is a flexible polar polymer with the molecular formula  $(-\text{CH}_2-\text{CH}_2-\text{O}-)_n$ . Low molecular weight PEO (with M.W. less than around 3000) is often functionalized with an alcohol group on one end and is called poly(ethylene glycol) or PEG. It is soluble both in water and in common organic solvents. The ethylene units are hydrophobic while the oxygens are hydrophilic. The competition between these interactions has given rise to its rich phase behaviour in aqueous solution [1–5]. Thus, it finds applications in a wide variety of situations, including as a dispersing agent for drugs [6], and to seed helical segments in proteins [7]. PEO exhibits remarkable drag-reducing properties in the flow of water through channels and also has the ability to reduce friction between surfaces [8, 9]. Thus, PEO has received growing attention and a wide variety of experimental and theoretical studies have been performed to understand its structural

and conformational properties in crystalline, molten state and in aqueous solution [10–17].

PEO itself is a solvent for salts in solid polymer electrolytic (SPE) systems [18,19]. The lack of a clear understanding of the conduction mechanism of ions in SPE's has spurred a large amount of research, both experimental and theoretical, on PEO:salt complexes [20–26]. It is widely believed that the conduction of ions is driven by the mobility of the host polymer [27]. With increase in the temperature, the ionic conductivity increases due presumably to thermally induced changes in the polymer dynamics [18].

Despite the wealth of studies on PEO:salt complexes, the exact phase behavior of crystalline PEO (or that of PEG) is unclear. We provide a brief overview of early experimental studies on the thermal behavior of solid PEO and PEG, so as to enable a better appreciation of our MD results to be presented in this chapter.

Based on their x-ray diffraction, IR, and Raman spectroscopic studies, Tadokoro *et al* proposed a molecular model for PEO [28,29]. Their model envisaged PEO as a uniform helical chain consisting of seven monomer units which turns twice in the fiber identity period. The average C-O and C-C torsional angles were  $188.15^\circ$  and  $64.58^\circ$ , thus leading to a *trans(t)-trans(t)-gauche(g)* conformational sequence. A wide distribution in the C-O torsional angle was observed, which implied a distortion of the helix. This distortion from a uniform (7/2) helix was imputed to strong intermolecular interactions in the crystalline lattice and to the flexibility of the ether backbone. However, the conformation was essentially a (7/2) helix and the *ttg* sequence was comparable to the one proposed for the uniform helix. In the crystal, the molecules are arranged such that a right-handed helical one is surrounded by four near neighbor molecules that are left-handed and vice versa.

Yoshihara *et al* have studied the temperature dependence of the polarized infrared spectra of PEO [30]. One of their interesting observations that is relevant to the present work is the splitting of the perpendicular bands of the spectra present at 947 and 844  $\text{cm}^{-1}$ , at low temperatures. The perpendicular 947  $\text{cm}^{-1}$  band was assigned to the symmetric rocking mode of methylene ( $\text{CH}_2$ ) groups and to the asymmetric stretching of COC

triplets. Similarly, the band at  $844\text{ cm}^{-1}$  was assigned to the asymmetric rocking mode of  $\text{CH}_2$  groups. It was found that the perpendicular bands (with the electric vector of the incident radiation being perpendicular to the long axis of the PEO chains) split at low temperatures, while the parallel bands do not. Based on the orientation of the sample with respect to the infrared beam, it can be deduced that the low temperature splittings are a consequence of dominant intermolecular interactions. A possible deduction is that the methylene groups perceive a different orientation of the neighbor shell at lower temperatures than in the room temperature solid.

Recently, Privalko *et al* have carried out magnetic susceptibility ( $\chi$ ) measurements of PEO over a range of molecular masses and temperatures [31]. The temperature dependence of  $\chi$  exhibited two discontinuous jumps, one at low temperature ( $T_1$ ) and the other at a slightly higher temperature ( $T_2$ ). The steep rise in  $\chi$  at  $T_2$  was accredited to the melting of PEO, while the jump at  $T_1$  was attributed to a solid-state transition of unspecified nature.

In order to understand the molecular motion that is characteristic of helical polymers, Hikichi and Furuichi performed nuclear magnetic resonance (NMR), dielectric, x-ray, and thermal expansion measurements on low molecular weight crystals of PEO [32]. These measurements were carried out in the temperature region between 90K and the melting point. The temperature dependence of the  $^1\text{H}$  NMR line width of the feature associated with the crystalline regions revealed a rapid narrowing at 270K, well below the melting point of the sample. Based on dielectric dispersion data and  $^1\text{H}$  NMR results, they speculated the possibility of rotational or oscillational motion about the helical axis of the molecule at 270K, i.e., in the crystalline phase of the sample.

Lang *et al* have employed differential scanning calorimetry (DSC) and spin-labeling technique to understand the solid state relaxations in PEO [33]. The DSC traces showed three endothermic peaks below the melting point. While two of them were associated with amorphous regions in the sample, the prominent peak at 263K was due to crys-

talline regions. They have proposed the possibility of a crystalline phase transition at this temperature.

The melting point of crystalline PEO is around 335K with a marginal dependence on molecular weight [34].

With this review of experimental data on the temperature dependence of the properties of crystalline PEO, we now examine the role of its morphology in these transitions. The crystal structure, crystallisation kinetics, and morphology of PEO have been extensively studied [35–39]. PEO crystallizes in a lamellar form and each lamella can contain extended or folded chains depending upon the molecular mass and the cooling rate of the sample. It has been known that samples with molecular mass less than 4000 form extended-chains (i.e., no folds), while polymer chains with higher molecular weights prefer to fold onto themselves within the lamellae, retaining their crystallinity. Small angle x-ray diffraction and optical microscopy experiments have concluded that the lamellae are homogeneous and contain only integer fold (IF) structures and that the end groups are rejected onto the lamellar surfaces [34, 35, 40]. The number of folds per molecule depends on the crystallization temperature and time.

A large number of calorimetry studies have been performed over the last three decades, both on extended and folded chain crystals of PEO [34, 41–48]. Early studies by Buckley and Kovacs have shown multiple endotherms for folded chain crystals [34, 41], which were interpreted to arise due to transitions from a folded chain of  $m$ -folds to one with  $(m-1)$  folds. This quantized reduction of the folds necessitates the existence of chain mobility below the melting point. The activation of molecular mobility too, should ideally be observed in a DSC experiment, although results on an extended chain crystal were not unambiguous on this issue. Buckley and Kovacs have observed only a low temperature tail or hump for such crystals below the melting endotherm and have ascribed it to polydispersity of the sample [42]. It could be possible that the activation energy associated with the increased mobility of the chains at a premelting temperature is smaller than what

could be detected in calorimetry. In addition, kinetics and the quality of the sample may hinder an accurate understanding of the thermodynamics of the crystalline sample.

Most computer simulations on PEO have focussed their attention on the amorphous sample, due primarily to interesting dynamics therein, and its relationship to ion mobility in such polymer matrices. The first successful attempt to understand the crystalline phase of PEO was made by Brown and coworkers [49, 50]. They proposed an interaction potential that could stabilize the crystal phase of PEO. This potential was later employed to model PEO melts [51, 52], and crystalline and amorphous PEO:NaI [53, 54] complexes. Similar efforts were also undertaken by Müller-Plathe and coworkers to understand the conformational properties of PEO in condensed phases [55] and to elucidate the ion conduction mechanism in amorphous PEO:LiI complexes [24]. MD simulations have also been employed by Smith and coworkers to elucidate the structure and dynamics of PEO-salt complexes [56] and aqueous PEO solutions [57], using a potential model derived from *ab initio* calculations [58].

To summarize, the experimental evidence on the existence of a premelting transition in low molecular weight poly(ethylene oxide) is unclear, and the phase behavior of crystalline PEO has not been explored using computer simulation methods. It is not far fetched to expect the widely accepted molecular mobility in the crystalline state to be associated with a premelting endotherm. Our aim is to investigate such premelting transitions and associated molecular mobility in the solid state and to provide microscopic insight into the molecular mechanism associated with such transitions in crystalline PEO. In the present study, we employ the interaction potential of Neyertz, Brown and Thomas [49], with the inclusion of flexible backbone and methylene groups [59, 60].

We have carried out isothermal-isobaric molecular dynamics simulations of monodisperse poly(ethylene oxide) of molecular weight 1220, between temperatures ranging from 300K to 930K. Experimental studies on the thermal behavior of PEO seem to exhibit signatures of a premelting transition around 270 to 300K. Note that these experiments have

employed a heating rate (5-15 degrees per minute) that is several orders of magnitude lower than the lowest rates that one can achieve in simulations. It is well documented that higher heating rates lead to superheating and would shift the transitions to higher temperatures [61,62]. The potential parameters employed in our simulations were successfully used by Brown and coworkers to stabilize the crystalline phase of PEO at 300K [49]. In light of these two reasons, we begin our simulations of crystalline PEO from 300K. Note that although free energy calculations [63,70] and improved Gibbs ensemble Monte Carlo studies can provide a precise location of transition points, one cannot capture the molecular mechanism of melting and the associated dynamical changes in the crystalline phase with these methods. It is the latter that motivates us to employ straightforward molecular dynamics simulations in this study.

## 2.2 Simulation Details

PEO crystallizes in a monoclinic lattice with the space group  $P2_1/a$  [29]. In Figure 2.1, we show the crystalline PEO unit cell. It consists of two right- and two left-handed helical chains each with seven  $-(C_2H_4O)-$  units. The cell parameters are  $a=8.05 \text{ \AA}$ ,  $b=13.04 \text{ \AA}$ ,  $c(\text{chain axis})=19.48 \text{ \AA}$ ,  $\alpha=\gamma=90^\circ$ , and  $\beta=125.4^\circ$ . In our simulations, both ends of the polymer chain were terminated by ethyl groups, as was the case with the work of Brown and coworkers [49]. The molecular formula of the simulated PEO is  $C_2H_5O-(C_2H_4O)_{26}-C_2H_5$ . The end-to-end length of the fully extended oligomer is around  $70 \text{ \AA}$ .

The structure reported from x-ray diffraction studies [29] was chosen as the initial configuration for the MD trajectory. The simulation box consisted of 4 unit cells each along the  $\vec{a}$  and the  $\vec{c}$  axes and 2 unit cells along the  $\vec{b}$  axis. In all, the system contained 32 PEO chains amounting to a total of 6304 atoms.

All atoms, including hydrogens were explicitly considered. Three dimensional periodic boundary conditions consistent with the symmetry of the unit cell were applied.

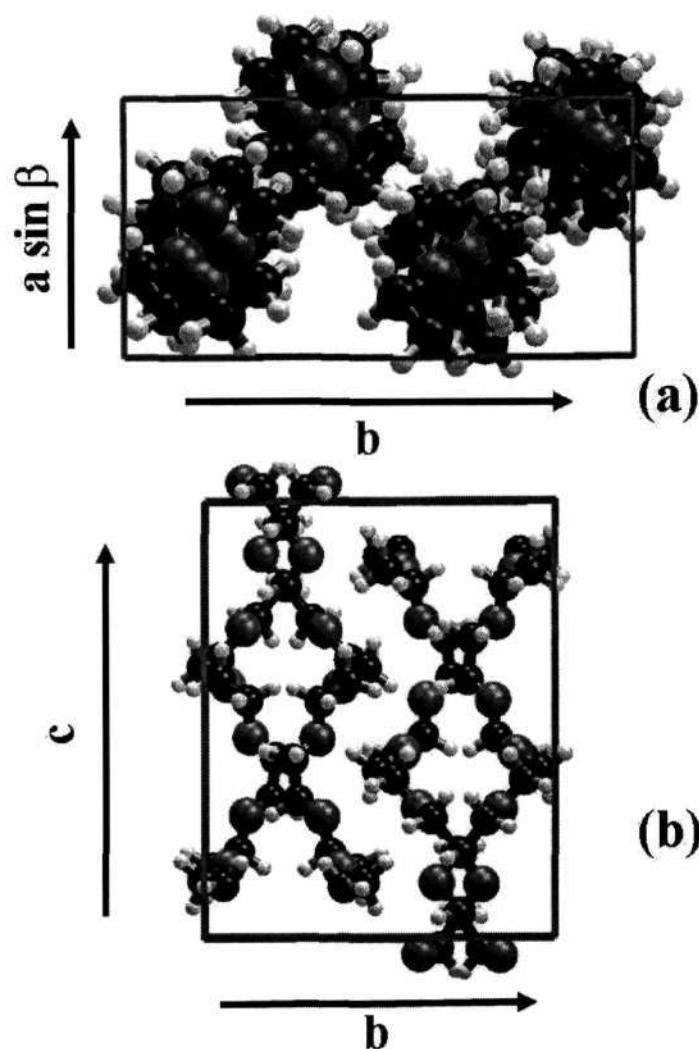


Figure 2.1: A representation of the crystalline PEO unit cells (a) along and (b) perpendicular to the chain axis. Here, black sphere represents carbon while grey and white spheres stand for oxygen and hydrogen, respectively.

A series of MD runs were performed using the PINY-MD program [64] in the temperature interval starting from 300K to 930K in steps of 5K. The simulations were carried out under isothermal-isobaric conditions in a fully flexible cell using the Parrinello-Rahman method [65, 66]. Temperature control was achieved using Nosé-Hoover chain thermostats [67]. Long range interactions were treated using the Ewald method [68, 69] with  $\zeta$  value of  $0.289\text{\AA}^{-1}$ , and around 4900 reciprocal space points were employed in the lattice sum. The number of reciprocal space points was tuned with increasing temperatures to guarantee the convergence of the Coulomb energy. The potential of interaction



used in our simulations is given as,

$$\begin{aligned}
 U(\{\mathbf{r}\}) = & \frac{1}{2} \sum_{ij}^{\text{bonded}} K_r^{ij} (\mathbf{r}_{ij} - \mathbf{r}_{ij}^0)^2 + \frac{1}{2} \sum_{ijk}^{\text{bonded}} K_\theta^{ijk} (\theta_{ijk} - \theta_{ijk}^0)^2 \\
 & + \sum_{ijkl}^{\text{bonded}} \sum_{n=0}^6 a_n \cos^n \phi_{ijkl} + \frac{1}{4\pi\epsilon_0} \sum_i^N \sum_{j>i}^N \frac{q_i q_j}{r_{ij}} \\
 & + \sum_i^N \sum_{j>i}^N \left[ A_{ij} e^{-B_{ij} r_{ij}} - \frac{C_{ij}}{r_{ij}^6} \right] \tag{2.1}
 \end{aligned}$$

where  $i, j, k$ , and  $l$  denote atom indices,  $q_i$  and  $q_j$  are the partial charges of  $i^{\text{th}}$  and  $j^{\text{th}}$  atom respectively,  $\epsilon_0$  is the permittivity of free space,  $K_r^{ij}$  and  $K_\theta^{ijk}$  are the stretching and bending force constants respectively,  $\phi_{ijkl}$  is the dihedral angle, and  $r_{ij}$  is the interatomic distance between atoms  $i$  and  $j$ . The last two terms in Eq.2.1 are applicable to interaction sites separated by more than three bonds in a molecule and to every pair of sites belonging to different molecules.

The potential parameters employed here are essentially from the work of Neyertz *et al* [49, 54] (hereinafter referred to as the NBT model). As remarked earlier, we use fully flexible backbone and methylene groups with interaction parameters taken from the CHARMM dataset [59] and from the work of Tobias and coworkers [60], in lieu of the rigid methylenes and fixed C-O and C-C distances of the NBT model. The parameters corresponding to both bonded and non-bonded interactions are provided in Table 2.1. These parameters have recently been used to characterize the phase behavior of crystalline  $n$ -alkanes [70, 71]. Real space interactions were cut off spherically at a distance of 12Å. It should be noted that the original work of Brown and coworkers [49] employed a real space interaction cutoff of 6.56Å, as their system size was small. Long range corrections to the total energy and the pressure of the system arising from the dispersive interactions were included. The equations of motion were integrated using the RESPA scheme [72], employing an outer time step of 4 fs. The bond stretch and bending interactions were integrated every 0.5 fs, while torsional degrees of freedom were integrated

Stretch	$r^0$ [Å]		$k_r$ [K Å <sup>-2</sup> ]				
C-C	1.53		237017.0				
C-O	1.43		171094.8				
C-H	1.09		332127.0				
Bend	$\theta^0$		$k_\theta$ [K rad <sup>-2</sup> ]				
C-O-C	112°		110255.50				
O-C-C	110°		76942.34				
O-C-H	109.5°		30193.20				
H-C-C	110°		45199.50				
H-C-H	106°		38033.50				
Torsions	$a_0$ [K]	$a_1$ [K]	$a_2$ [K]	$a_3$ [K]	$a_4$ [K]	$a_5$ [K]	$a_6$ [K]
C-C-O-C	622.99	-674.31	753.82	1854.37	-81.52	549.01	428.74
C-O-O-H	622.99	-674.31	753.82	1854.37	-81.52	549.01	428.74
H-C-C-H	265.70	-1826.19	2144.72	3901.46	-1667.17	142.91	1480.98
O-C-C-O	265.70	-1826.19	2144.72	3901.46	-1667.17	142.91	1480.98
H-C-C-O	265.70	-1826.19	2144.72	3901.46	-1667.17	142.91	1480.98
O-EC-EC-O	853.964	-2561.893	0.0	3415.857	0.0	0.0	0.0
H-EC-EC-H	853.964	-2561.893	0.0	3415.857	0.0	0.0	0.0
H-EC-EC-O	853.964	-2561.893	0.0	3415.857	0.0	0.0	0.0
Non-bonded	A [K]		B [Å <sup>-1</sup> ]	C [KÅ <sup>6</sup> ]			
C...C	15909350.62		3.3058	325985.916			
C...O	21604039.75		3.6298	177536.016			
C...H	7571800.37		3.6832	91334.430			
O...O	29337172.46		4.0241	96668.562			
O...H	10282092.97		4.0900	49718.136			
H...H	3603659.064		4.1580	25563.576			
Atomic charges [e]							
$q_C$		0.103					
$q_O$		-0.348					
$q_H$		0.0355					
$q_{\text{methyl H}}$		-0.0343333333333					

Table 2.1: Parameters of the interaction potential [49, 54, 59, 60]. Here  $C$ ,  $O$ ,  $EC$ , and  $H$  denote carbon, oxygen, ethyl carbon, and hydrogen, respectively.

with 1 fs resolution. The non-bonded interactions, divided as short-range (less than 6Å) and long-range (above 6Å) were integrated at 2 fs and 4 fs time step respectively. Time constants of 1 ps and 2 ps were used for the thermostat and barostat attached to the system respectively. At each temperature, the system was found to reach the set pressure within 30 ps. At each temperature, the system was equilibrated for 300 ps, and the final configuration of this run was used as the initial state for the MD run at the next higher temperature. To obtain the conformational, structural and energetic data, a MD run of duration 100 ps was performed at each temperature during which the coordinates of the particles were dumped every 1 ps. Additional runs of 2 ns duration were performed at 13 selected temperatures to evaluate mean-square displacements and rotational time correlation functions (TCF). These quantities were calculated with a 1 ps time resolution. Equipartition of the kinetic energy to the degrees of freedom was verified by comparing the momentum distribution of hydrogen atoms with the expected Maxwell distribution. In Figure 2.2, we show distributions of the components of the velocities of hydrogen atoms at three different temperatures. These distributions are compared with the expected Maxwell's velocity distribution for the corresponding temperatures. Note that hydrogen velocities follow the expected distribution at all temperatures of our study. This observation unambiguously demonstrates that the kinetic energy of the system is equipartitioned well to the degrees of freedom of the hydrogens.

## 2.3 Results and Discussion

In the discussion that follows, we do not show the data for temperatures between 300K and 600K, as all the properties exhibit only a monotonic dependence on temperature in this range. We have also examined the crystal structure by visualizing the atomic configurations and found no significant change in the structure in this temperature range.

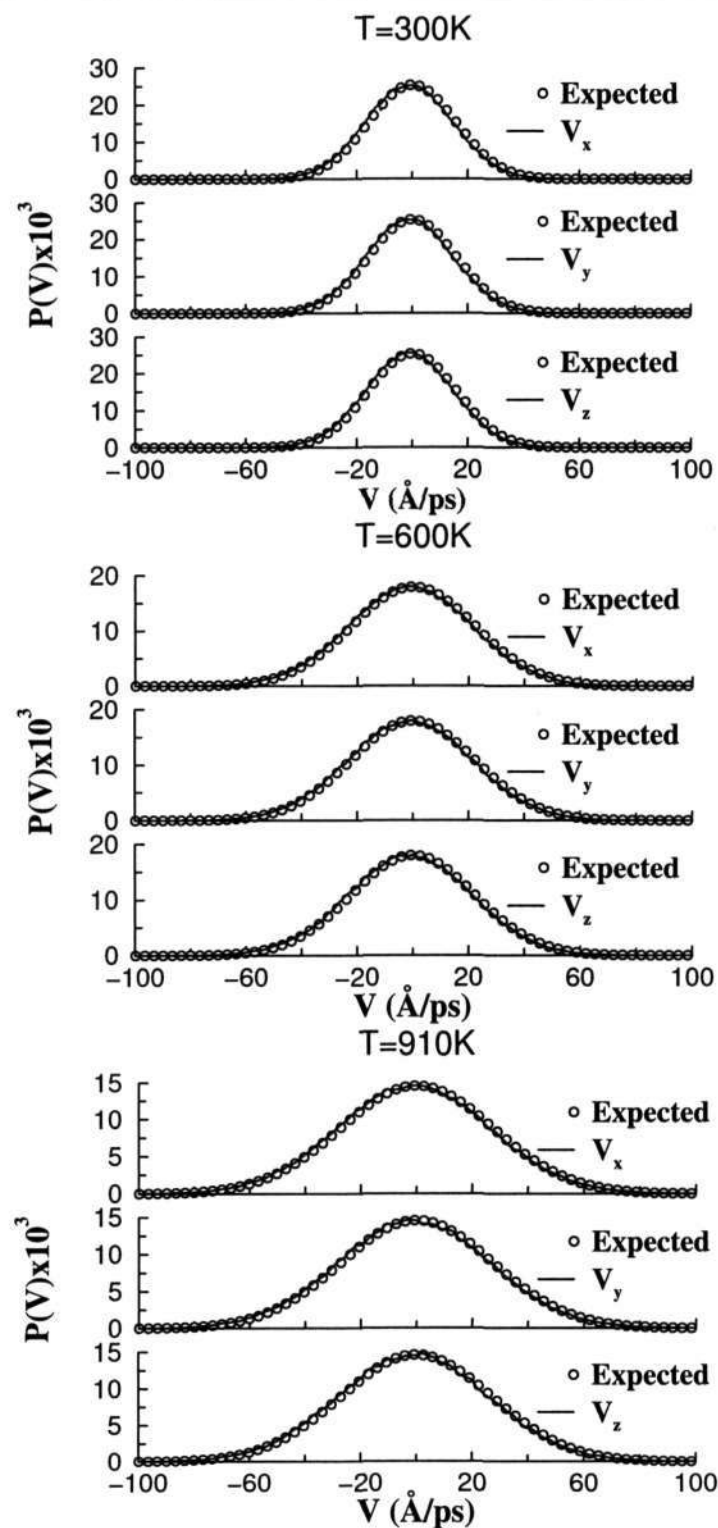


Figure 2.2: The distributions of the components of the velocities of hydrogen atoms at 300 K (top), 600 K (middle) and 910 K (bottom) are compared with the expected Maxwell's velocity distribution for the same temperatures. We have used a bin width of 2.1877 Å/ps for generating these distributions.

Parameter	Simulation	Experiment [29]
a (Å)	8.43	8.05
b (Å)	13.92	13.04
c (Å)	18.57	19.48
$\alpha$ (deg)	91.5	90.0
$\beta$ (deg)	127.9	125.4
$\gamma$ (deg)	90.1	90.0

Table 2.2: Unit cell parameters obtained from the simulation at 300K are compared against experimental values [29].

### 2.3.1 Structure

#### Stability :

We have generated a long molecular dynamics trajectory of 2.2 ns duration under isothermal-isobaric conditions at 300K and at 1 atm pressure. In Table 2.2, we compare the average lattice parameters obtained from this simulation at 300K against the experimental values. The parameters were averaged over the last 1.2 ns of this trajectory. The simulation results compare well with experiment except for marginal differences that could arise due to the finite chains employed here. The point to note is that the crystal structure predicted by the simulations for the finite chain model is nearly invariant from experimental data for the polymer.

#### Lattice Parameters and Energies :

We have monitored the evolution of the crystalline lattice parameters as a function of temperature to observe signs of any structural transition. In Figure 2.3, we present the cell lengths,  $a$ ,  $b$ , and  $c$  and the angles,  $\alpha$ ,  $\beta$ ,  $\gamma$ . A gradual reduction in the  $c$ -parameter is observed due to the formation of C-O *gauche* defects (see later). The signature of pre-melting is not quite obvious from the variation of cell lengths, while it is quite pronounced in the behavior of cell angles (Figure 2.3b). The angle  $\beta$  shows a marginal decrease with increasing temperature up to 700K. It decreases by about  $3^\circ$  at the premelting tempera-

ture of 720K and remains at that value until the onset of melting at 850K. The complete melting of the crystal is associated with very large drops in  $\beta$  to values near  $90^\circ$ . The large fluctuations and scatter of the cell parameters near the transition temperatures are

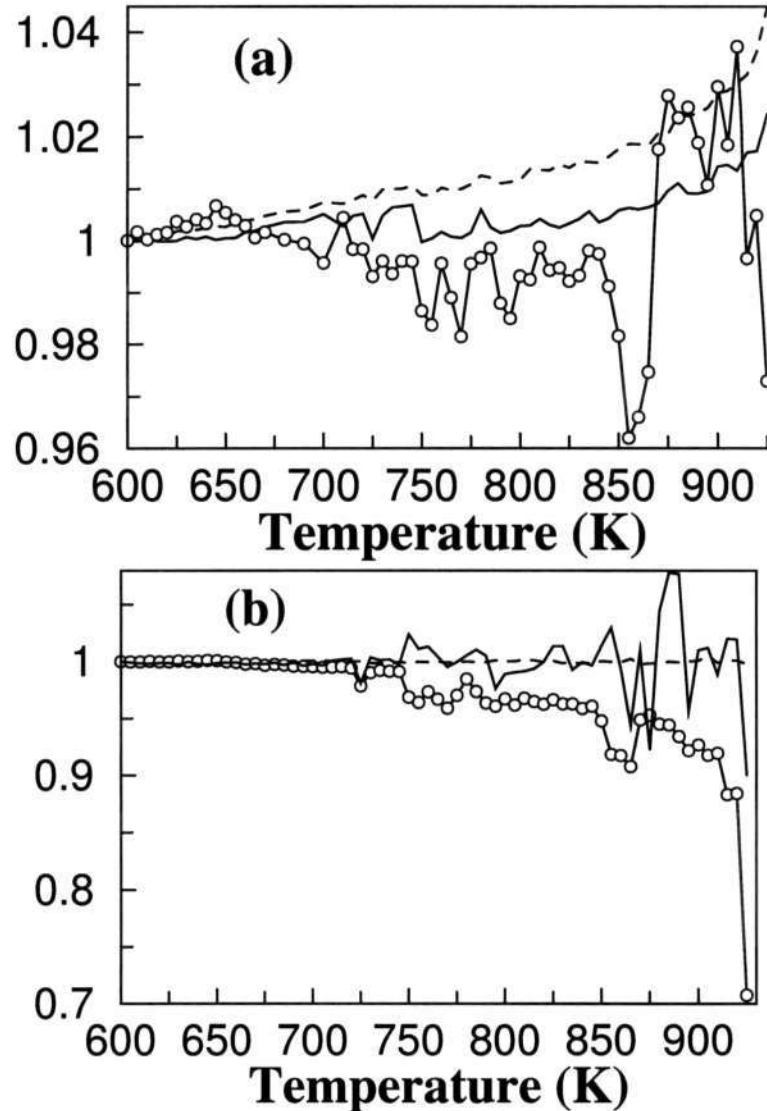


Figure 2.3: (a) Relative edge lengths of the simulation box along the crystallographic axes:  $a$  (solid line),  $b$  (dashed line), and  $c$  (solid line with open circles) (b)  $\alpha$  (solid line),  $\beta$  (solid line with open circles), and  $\gamma$  (dashed line) as a function of temperature. The values are normalized with respect to their average magnitude at 600K, given as follows:  $34.52\text{\AA}$  ( $a$ ),  $28.48$  ( $b$ ),  $70.64$  ( $c$ ),  $90.14^\circ$  ( $\alpha$ ),  $125.19^\circ$  ( $\beta$ ), and  $90.00^\circ$  ( $\gamma$ ). The simulation box was made of 4 crystallographic unit cells each along the  $\vec{a}$  and the  $\vec{c}$  axes and 2 unit cells along the  $\vec{b}$  axis.

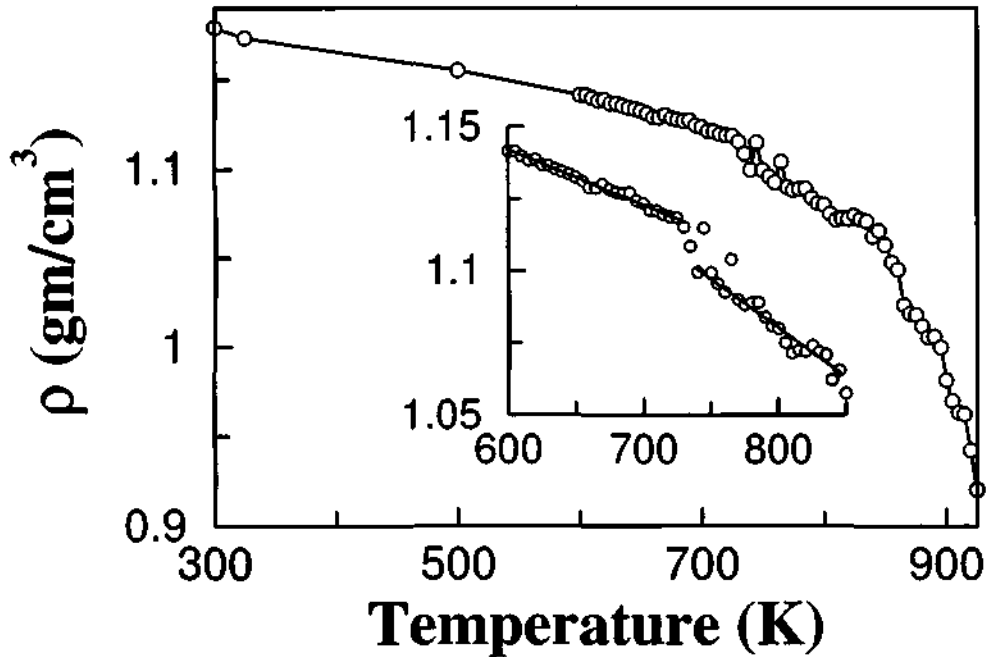


Figure 2.4: Density,  $\rho$  of the simulated system as a function of temperature. The inset shows the same across the premelting transition, in expanded scale. The lines are best fits to the data, and serve as guide to the eye.

likely due to the large heating rates employed here in comparison to experiments.

The changes in the individual cell parameters are reflected in the behavior of the density of the system, which is shown in Figure 2.4. A change of  $0.04 \text{ g/cm}^3$  in the density is observed during the premelting transition at  $720 \text{ K}$ , (see inset) while it is further decreased by at least  $0.17 \text{ g/cm}^3$  at melting. The experimental density of molten PEO at  $450 \text{ K}$  is  $1.007 \text{ g/cc}$  [73]. The density of the simulated melt at  $925 \text{ K}$  appears to be much below this value, probably due to the fact that the crystal was in a superheated state. In order to compare the liquid state density of flexible PEG simulated here with that of NBT model, we have performed additional isothermal-isobaric MD simulation that uses isotropic cell fluctuations [66]. Brown and co-workers have carried out simulations of molten PEO at  $400 \text{ K}$  as a function of polymer chain length. We have selected one of the system sizes from their study so as to make one-to-one comparison of our results with their results. Thus, we have carried out a simulation in a cubic box that contained 13

PEO chains each of which consisted of 32 backbone atoms. A long molecular dynamics trajectory of 2 ns duration at 400K and at 1 atm pressure was generated. The average density calculated from this trajectory is 1026.2 kg/m<sup>3</sup> which is only 0.6% less than what Brown and co-workers have reported while the interpolated experimental density at 400K and at 1 atm pressure is 1046 kg/m<sup>3</sup> [73]. It should also be noted that the data on lattice parameters in the molten state, i.e., for temperatures above 925K may not be proper, as the simulation cell can pancake in the melt. This is to be expected in simulations of the liquid state that employ the Parrinello-Rahman method. In our simulations at 930K, the angle  $\beta$  decreased to a small value signifying the attainment of a liquid state.

The changes in the lattice constants are associated with both conformational transitions as well as with intermolecular packing. We have studied these contributions through quantities such as the intramolecular potential energy, the intermolecular energy, helical and interchain correlations, and population of *gauche* defects. We first present data on the energetics. Figure 2.5 shows the intermolecular potential energy (Figure 2.5a) and compares it against the intramolecular potential energy (Figure 2.5b). The latter is a sum of the bond stretch, bend and torsional energies while the former is the grand sum of dispersive and ionic interactions of pairs of oligomers within the interaction cut-off. The non-bonded potential energy for pairs of atoms present in the same molecule and are separated by more than three bonds and those present in different molecules is a sum of Coulomb and 6-exponential terms. The intermolecular energy was calculated by subtracting the total intramolecular non-bonded potential energy (with the Coulomb energy obtained fully in real space without any cutoff) from the total non-bonded potential energy (with the Coulomb energy obtained using Ewald sum). We find that the intermolecular energy exhibits two discontinuities in slope, one at around 720-740K, and another at 850K, while the intramolecular energy shows a monotonic behavior up to 850K followed by a small discontinuity with increasing temperature. This suggests a relationship between the premelting transition and intermolecular interactions or ordering. The changes



in the intermolecular energy and a relatively smooth intramolecular energy across the premelting transition is in accord with temperature dependent x-ray measurements [74] and the polarized IR spectra of PEO [30]. These experiments demonstrated changes in the intermolecular arrangement at high temperatures, relative to the low temperature

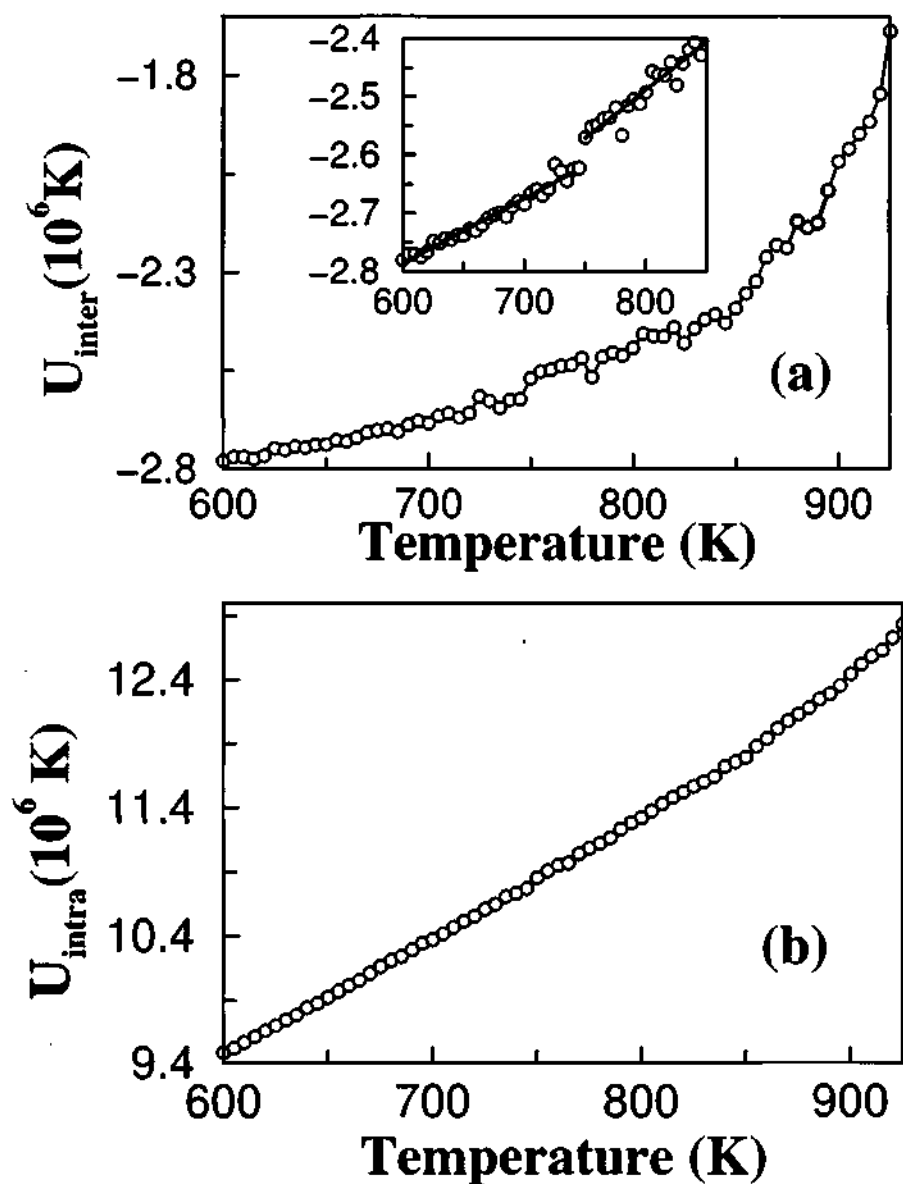


Figure 2.5: Plot of the (a) intermolecular energy and (b) intramolecular energy of the simulated system versus temperature. Inset in (a) shows the same across the premelting transition, in expanded scale. Solid lines are best fits to the two regions of data and serve to guide the eye.

structure.

We turn now to a comprehensive analysis of the conformational and structural changes associated with these transitions.

### Conformation and Intramolecular Structure :

In crystalline PEO, the C-O bond is in the *trans* state, while the C-C bond is in the *gauche* state. The consequent *ttg* sequence along the PEO chain is the basis of its helicity. Figure 2.6 shows the distribution of the torsional angle around the C-O bond at selected temperatures. At temperatures below 600K, the distribution does not show any significant changes other than what is expected due to thermal broadening, whereas *gauche* defects are initiated at the onset of the premelting transition. We define C-O bonds with torsional angles between  $20^\circ$  and  $120^\circ$  or those between  $240^\circ$  and  $340^\circ$  as being in *gauche* state. A plot of the concentration of *gauche* defects with temperature, shown in Figure 2.7, reveals the onset of a large number of such defects at the premelting transition (around 720 K), over and above that expected from a mere increase of defect population with increasing temperature. A second, large discontinuity is observed at the onset of the melting transition at 850K. The small but non-zero value of the *gauche* concentration at temperatures below 600K is due to a minor number of torsions in the end groups that are not in the *trans* conformation (see later). Although the above analysis has shown the formation of conformational defects across the premelting transition, it does not reveal the distribution of defects along different segments of the polymer. In order to gain insight into this aspect, we have evaluated the C-O torsional distribution by considering only the C-O torsions that belong to the monomers present at either chain ends. Thus each chain is defined to contain two C-O end torsions. Figure 2.8 shows the results obtained from such calculations, where the percentage of C-O *gauche* defects present in the end groups are compared with that in other monomeric segments. The data are normalized to the total number of C-O torsions present at the ends or otherwise, in the system.

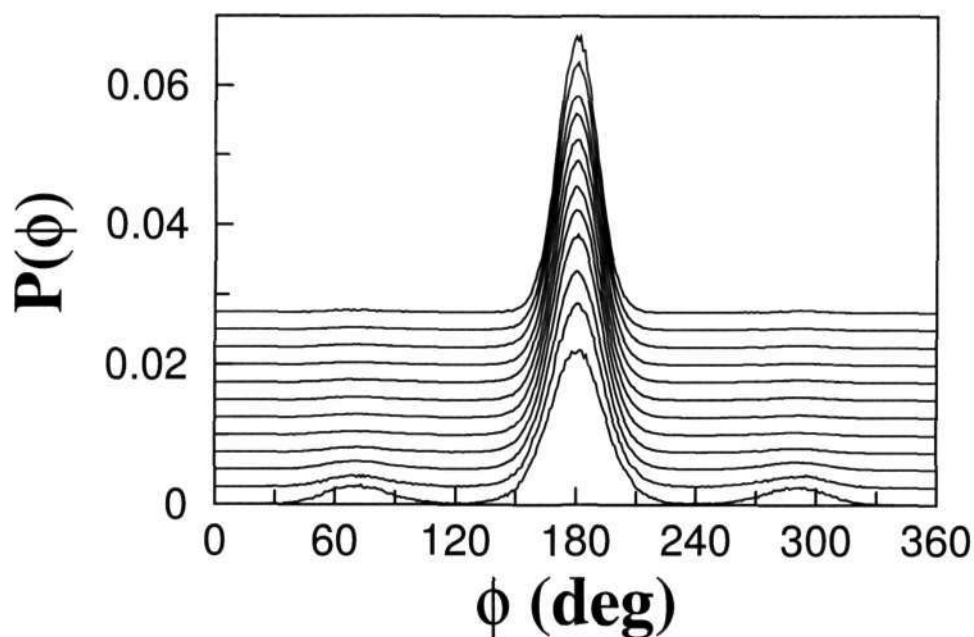


Figure 2.6: Distribution of the torsional angle,  $\phi$  around the C-O bond of PEO at different temperatures across the transitions. The distributions are shifted up for clarity. Temperatures (From top to bottom): 600K, 650K, 710K, 720K, 740K, 760K, 800K, 825K, 850K, 875K, 900K, and 925K.

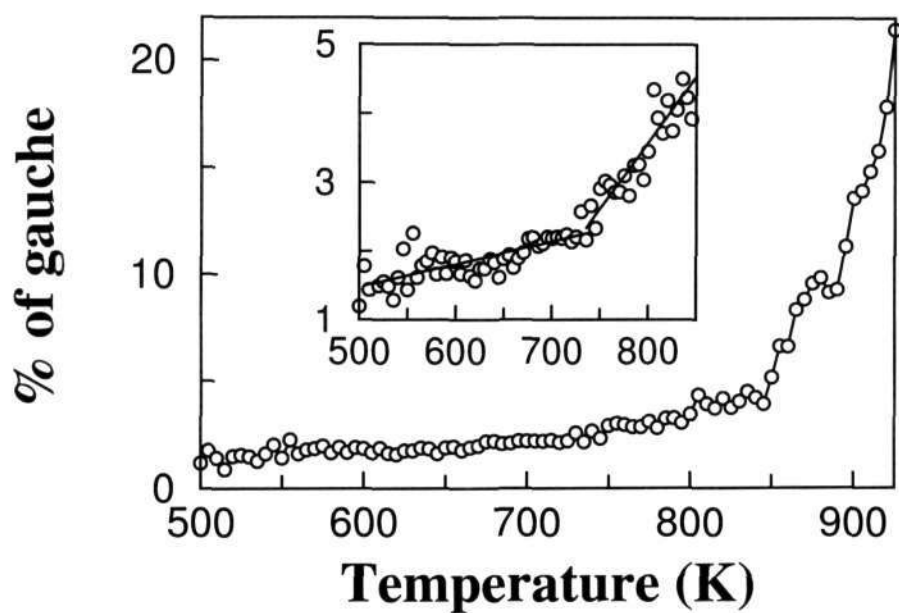


Figure 2.7: The variation in the percentage of *gauche* population in the C-O torsion is shown as a function of temperature. The inset shows the same across the premelting transition. Solid lines are linear fits to two different blocks of data.

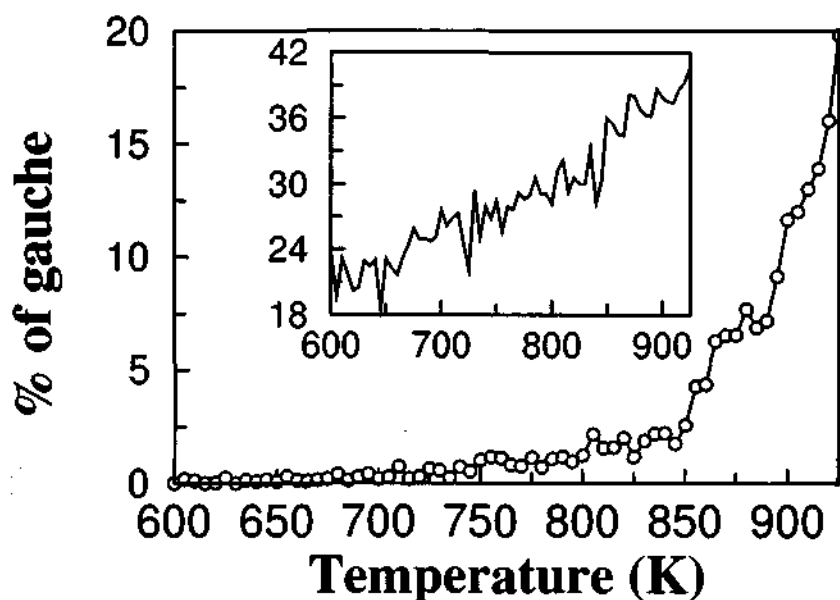


Figure 2.8: The variation in the percentage of *gauche* population in the C-O torsion for bonds present in the mid-segment of the PEO oligomer is shown as a function of temperature. Inset shows the same for C-O bonds present at the ends of the oligomer.

These data are shown for temperatures between 600K and 900K. As remarked earlier, a small number of molecules contain end defects even at 600K. The quantum of such end defects increases gradually with temperature, whereas *gauche* defects in the central part of the chains are initiated only after the premelting transition. Note also the rapid rise of such mid-segment defects. These observations demonstrate the higher propensity for the formation of conformational defects at the chain ends, and the association of the premelting temperature with the onset of mid-segment *gauche* defects. Unlike the changes observed in the C-O torsional distribution, we observe no changes in the distribution of the C-C torsional angle across premelting.

Apart from the torsional distributions, one can study the conformational properties of these systems through correlation functions that reveal the helical nature of the chains. We define the helical correlation function (HCF) as [61],

$$HCF(n) = \frac{1}{NN_b} \sum_{i=1}^N \sum_{m=1}^{N_b} (-1)^n \frac{\vec{d}_{i,m} \cdot \vec{d}_{i,m+n}}{|\vec{d}_{i,m}| |\vec{d}_{i,m+n}|} \quad (2.2)$$

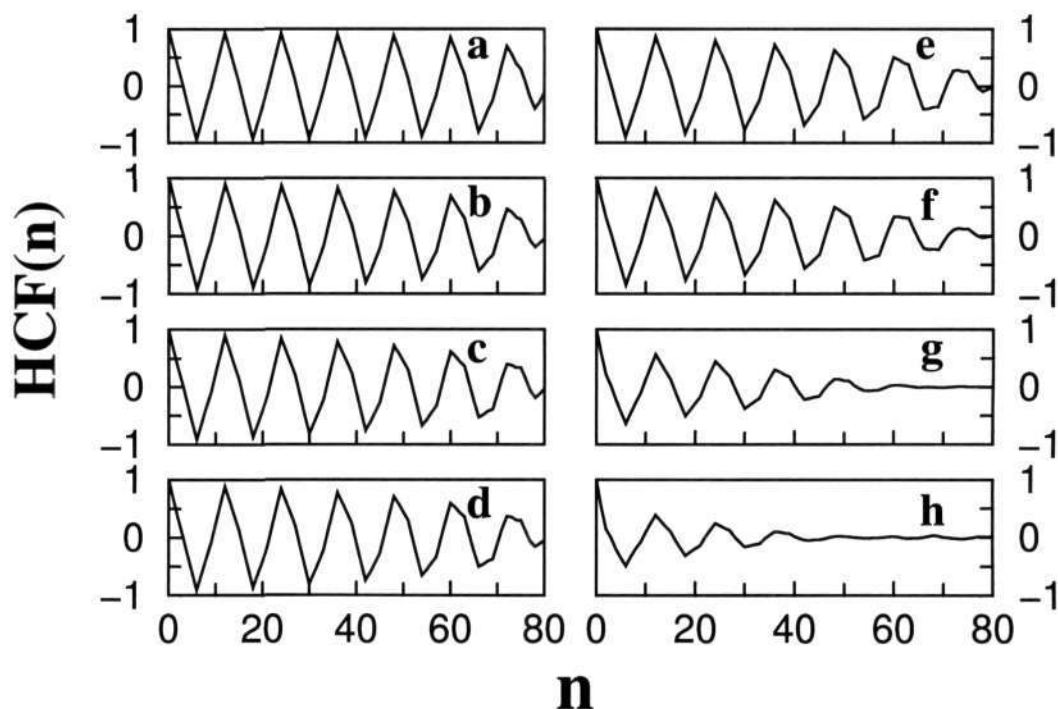


Figure 2.9: Helical correlation function,  $\text{HCF}(n)$  is shown at various temperatures across the transitions. Temperatures (from a to h): 650K, 710K, 740K, 760K, 800K, 850K, 900K, and 925K.

where  $N$  is the total number of molecules, and  $N_b$  is the number of backbone bisector vectors in every molecule. The backbone bisector vector is one half of the sum of pair of successive bond vectors.  $\vec{d}_{i,m}$  denotes the  $m$ -th backbone bisector of  $i$ -th molecule.  $\text{HCF}(n)$  is averaged over time and represents the correlation between the orientations of a given bisector and another that is  $n$  bonds apart within a molecule. Figure 2.9 shows  $\text{HCF}(n)$  at various temperatures. The total number of atoms in the backbone is 83, and hence the value of  $n$  ranges from zero to 80. Up to 700K, the correlation function exhibits well defined oscillations, the period of which corresponds to the pitch of the helix. The amplitude of these oscillations does not decay with  $n$  until 720K, while it decreases marginally with increasing  $n$  at temperatures above it. Thus the premelting transition is also associated with the onset of the long range decay of helical correlations. These observations suggest the preservation of short range intra-molecular correlations and a lack of long range correlation in the system at temperatures ranging from 700K to 850K.

We can thus conclude that the premelting transition is associated with helical unwinding of PEO chains. At temperatures beyond 900K,  $HCF(n)$  shows a weak dependence on  $n$ , signifying the residual conformational correlations in the molten state. We further study the molecular structure of the PEO chains through a combination of pair correlation functions,  $g(r)$ . We show the intramolecular  $g_{CC}(r)$  at selected temperatures in Figure 2.10a. The first two peaks arise trivially from C-C bonds and C-O-C triplets respectively, and are not of interest here. A small hump that is present at  $3.05\text{\AA}$  at 600K develops into a formal peak at higher temperatures. This arises from *gauche* states of the C-O bond. The large peak at  $3.75\text{\AA}$  whose position is independent of temperature originates from quartets of atoms of the type CCOC that are present in the *trans* conformation.

The intramolecular OO  $g(r)$  shown in Figure 2.10b exhibits a peak at  $2.85\text{\AA}$  arising from oxygen neighbors around a CC bond (OCCO). Unlike the large changes found in the third peak (at  $3.05\text{\AA}$ ) in  $g_{CC}(r)$  that arose from COCC quartets, this peak does not show any significant change than what is normally expected with an increase of temperature. This agrees with the near invariance of the CC torsional angle with temperature. Above 850K, this  $g(r)$  exhibits a non-zero intensity at distances near  $4\text{\AA}$ , possibly from two oxygen atoms along a PEO chain between which a C-O torsion exists in the *gauche* state. The  $g_{CO}(r)$  shown in Figure 2.10c shows a third peak at  $4.15\text{\AA}$  at temperatures below 720K that arise out of COCCO bonded quintuplets. The coordination number under this feature is 1.0, as expected. A marginal decrease in the intensity and a broadening at lower distances is observed in this peak, at temperatures between 650K and 925K. Consequently, an increase in the coordination number to 1.25 is observed. These changes are due to a large increase in the population of CO *gauche* defects. A similar trend can be observed for the peak at  $5.0\text{\AA}$  that comes from the carbon and oxygen atoms that are separated by bonded COCC quartets.

The changes in the conformation of the chains with increasing temperature are reflected in their radii of gyration as well.

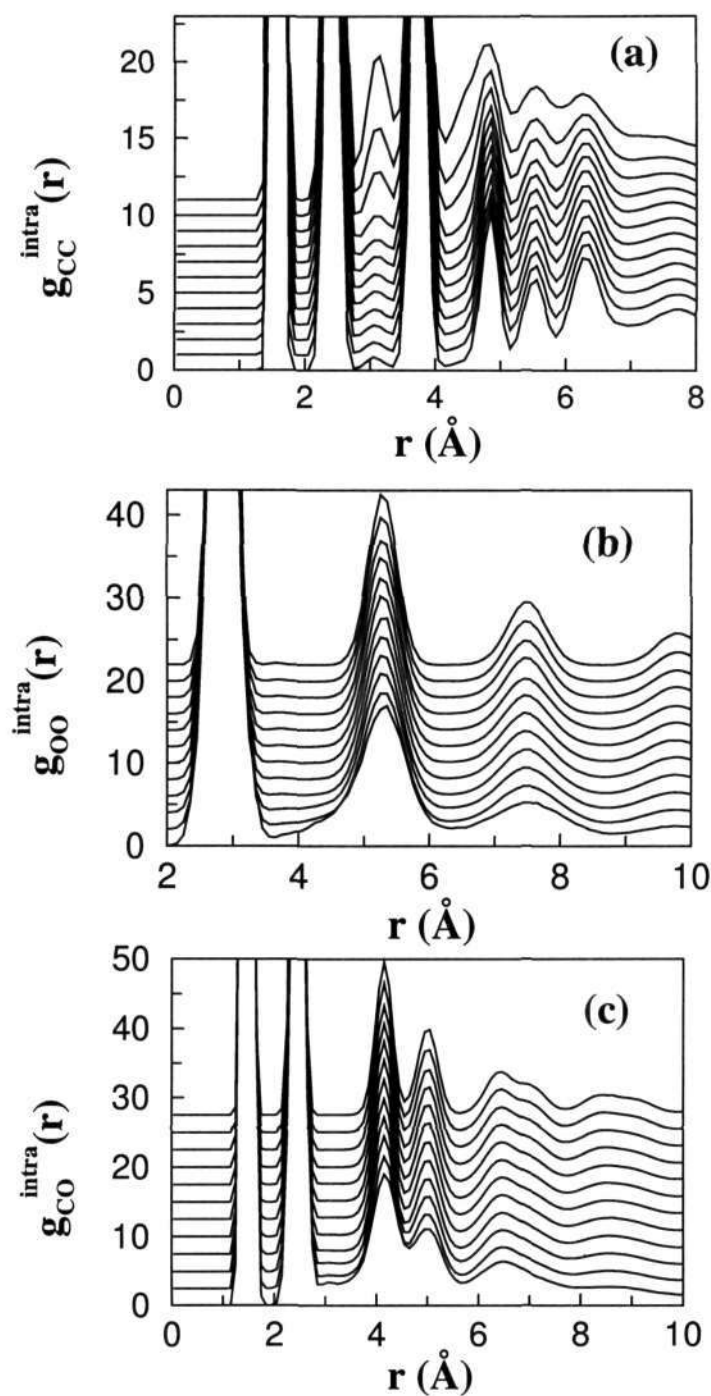


Figure 2.10: Intramolecular radial distribution functions (a)  $g_{CC}^{intra}$  (b)  $g_{OO}^{intra}$  and (c)  $g_{CO}^{intra}$  are shown at different temperatures. The functions are shifted for clarity. Temperatures (in (a) From bottom to top, and in (b) & (c) From top to bottom): 600K, 650K, 710K, 720K, 740K, 760K, 800K, 825K, 850K, 875K, 900K, and 925K.

We define this quantity as,

$$R_g^2 = \frac{1}{NN_m} \sum_{j=1}^{N_m} \sum_{i=1}^N (\vec{r}_{com}^j - \vec{r}_i^j)^2 \quad (2.3)$$

where  $N$  is the total number of atoms in a chain,  $\vec{r}_i^j$  are coordinates of atoms in the  $j$ -<sup>th</sup> molecule,  $\vec{r}_{com}^j$  is the center of mass of the  $j$ -<sup>th</sup> chain and  $N_m$  is the total number of molecules present in the simulation cell. We show in Figure 2.11, the evolution of  $R_g^2$  with temperature. The large transition at 850K signifies the melting of the crystal. The premelting transition at 720K does not change the value of  $R_g^2$  significantly, as very few *gauche* defects are present at temperatures between 720K and 850K. The large fluctuations in  $R_g^2$  across the premelting transition could be due to the helical unwinding as observed in HCF( $n$ ). The overall decrease of  $R_g^2$  is a consequence of increasing number of defects in the chain which fold the chains onto themselves.

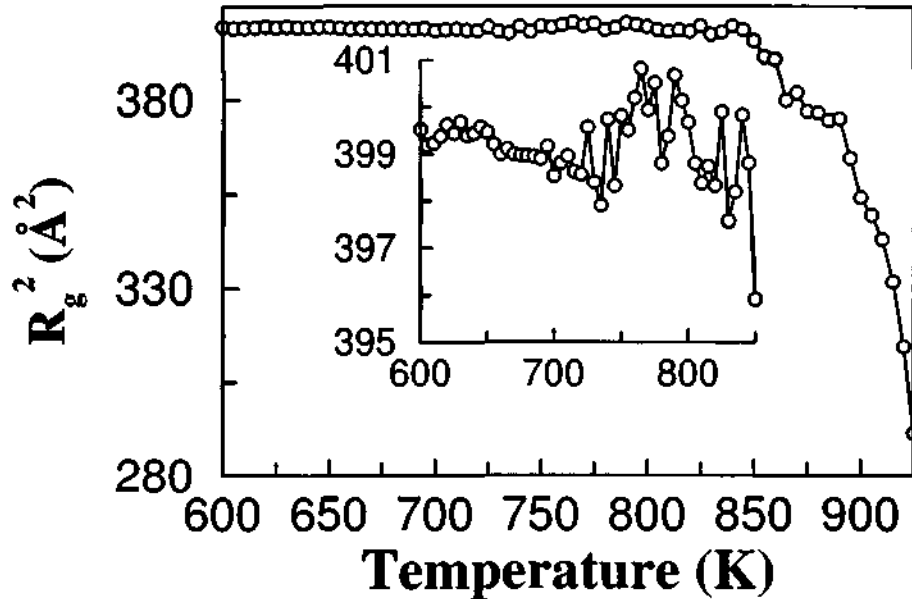


Figure 2.11: Temperature dependence of the squared radius of gyration of PEO oligomers. The inset shows the same across the premelting transition.



### Intermolecular Structure :

The intermolecular  $g_{CC}(r)$ , shown in Figure 2.12a exhibits a first peak at  $4.95\text{\AA}$ . It is quite broad, even at low temperatures, with its minimum extending up to  $5.95\text{\AA}$ . The coordination number calculated by integrating the intermolecular  $g_{CC}(r)$  up to  $5.95\text{\AA}$  is 23.0 at 600K.  $g_{CC}(r)$  also exhibits a hump between  $5.95\text{-}6.85\text{\AA}$  with a maximum at  $6.35\text{\AA}$ . The coordination evaluated within this range is 9.7 at 600K. We now discuss the temperature dependence of the intermolecular  $g_{CC}(r)$ . Upon increasing the temperature between 600-740K (premelting regime), the first peak position gradually shifts towards lower distances, from a value of  $4.95\text{\AA}$  at 600K to  $4.75\text{\AA}$  at 740K. The peak position does not show any further shift with increasing temperature. The minimum of this peak shifts marginally towards higher distances, from  $5.95\text{\AA}$  at 600K to  $6.05\text{\AA}$  at 720K, with a small increase of 0.5 in the coordination number. In addition, the hump present at lower temperatures vanishes at 740K. The anomalous temperature dependence of the first peak position, the corresponding increase in the coordination number, and the disappearance of the sub-peak at  $6.35\text{\AA}$  suggest a subtle structural changes across the premelting temperature. An investigation into the origin of the hump at  $6.35\text{\AA}$  (at 600K) reveals that it is due to two contributions:

- (i) chains that do have at least one carbon atom within the first coordination shell (i.e., within  $5.95\text{\AA}$  at 600K) of a carbon atom in the central molecule.
- (ii) chains that do not have any carbon atom within the first coordination shell of a carbon atom in the central molecule.

We find that the former class of neighboring molecules are restructured in such a way that the carbon atoms in them which contributed to the hump enter into the proper first coordination shell soon after premelting. In other words, the neighbors which contributed to the hump get subsumed into the first peak. The temperature dependence of the hump feature can thus be rationalized. Further increase in temperature above 800K results in the loss of long-range correlations thus leading to an isotropic liquid state. The

intermolecular O-O pair correlation function shown in Figure 2.12b also exhibits a hump between 6.45-7.55Å at low temperatures. This peak again vanishes across the premelting transition similar to that observed in the intermolecular C-C pair correlation function, likely due to the same reason as given above.

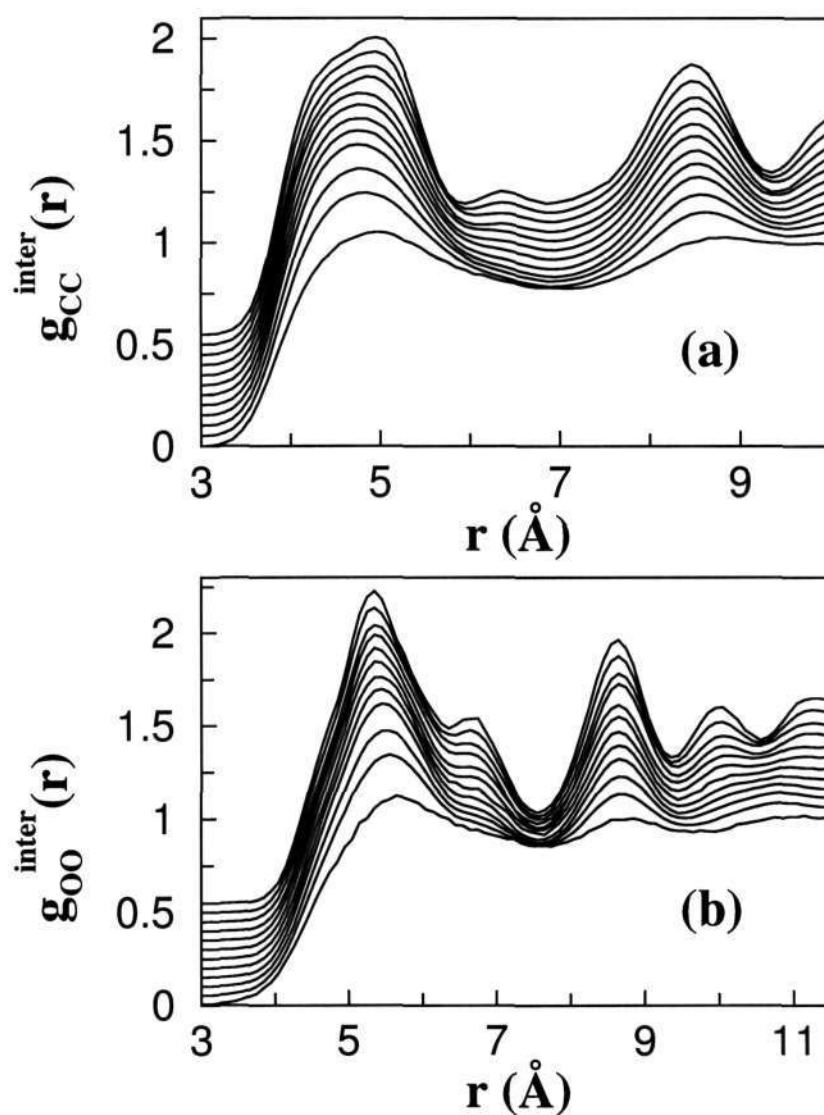


Figure 2.12: Intermolecular radial distribution functions (a)  $g_{CC}^{inter}$  (b)  $g_{OO}^{inter}$  at different temperatures. The functions are shifted for clarity. Temperatures (From top to bottom): 600K, 650K, 710K, 720K, 740K, 760K, 800K, 825K, 850K, 875K, 900K, and 925K.

In order to further characterize the intermolecular order, we calculate the two dimensional pair correlation function. This is defined as,

$$g_{CC}(\ell) = \left\langle \frac{n_{CC}}{2\pi\ell d\ell \left(\frac{N_s}{A}\right)} \right\rangle \quad (2.4)$$

$g_{CC}(\ell)$  represents the normalized correlation of the positions of carbon atoms belonging to two different molecules and which are present within a slab of width  $w$ , the slab being oriented perpendicular to the instantaneous  $\vec{c}$ -axis.  $n_{CC}$  denotes the number of carbon atoms present within circular shells of radii  $\ell$  and  $\ell + d\ell$  in the slab.  $N_s$  corresponds to the total number of carbon-carbon pairs present in the slab, and  $A$  denotes the area of the slab. The angular bracket represents a configurational average. The interatomic vector is denoted by  $\vec{r}$  and  $\ell$ , the two-dimensional distance between the two carbon atoms is defined as,

$$\ell = |\vec{r} - (\vec{r} \cdot \hat{c}) \hat{c}| \quad (2.5)$$

and  $\hat{c}$  denotes the unit vector along the instantaneous  $\vec{c}$ -axis of the lattice. A slab thickness  $w$ , of  $0.4\text{\AA}$  was used in our calculations to include all the nearest neighbor molecules into account. around the premelting transition. At 600K (Figure 2.13a), a first peak at  $5.25\text{\AA}$  is observed which is rather broad and contains two distinct sub-features. The integrated coordination number at the minimum of this peak (i.e., at  $7.25\text{\AA}$ ) is found to be 4.7. At temperatures just above the premelting transition, the side lobes of the main peak essentially disappear and the coordination number within the first shell is found to be reduced to 4.1. Thus, we conclude that the premelting transition is not only reflected in conformational changes, but also in the way molecules are arranged with respect to each other. Specifically the arrangement of methylene groups exhibits a significant change across this transition. Note also the hump present at  $8.15\text{\AA}$  at 600K. The running coordination up to the minimum of this hump (i.e., up to  $8.9\text{\AA}$  at 600K) is around 6. This implies that on average, six molecules surround a given chain. This hump loses

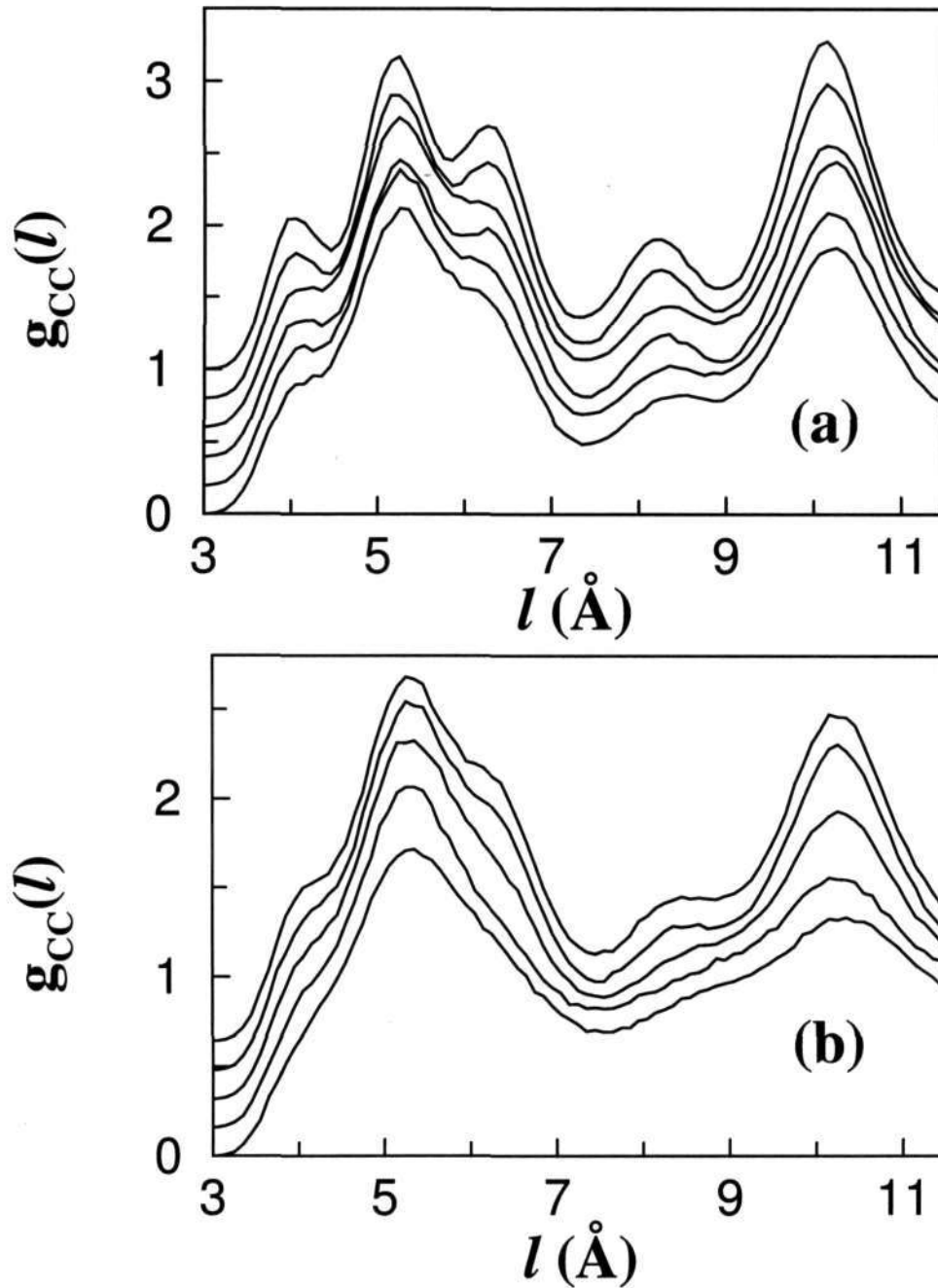


Figure 2.13: Two dimensional radial distribution function,  $g_{CC}(l)$  is shown across (a) the premelting transition and (b) melting. Temperatures (From top to bottom): (a) 600K, 650K, 710K, 720K, 740K, and 760K (b) 800K, 825K, 850K, 875K, and 900K.

significant intensity across the premelting transition, similar to the disappearance of the hump present in the  $g_{CC}(r)$  function at 600K. At temperatures above 800K (Figure 2.13b),

we find the total loss of such correlations in  $g_{CC}(\ell)$ . We present  $g_{CC}(\ell)$  in Figures 2.13 for different temperatures

### Interchain Orientational Correlations :

We are interested in finding out if the premelting transition at 720K is associated with subtle changes in intermolecular order. In order to do this, we group molecules based on their handedness. At low temperatures, molecules of the same helical type separated even by large distances exhibit a high degree of correlation in the orientation of backbone conformations. We characterize the local conformations of molecules by calculating the bisector of successive triplets of backbone atoms. We then try to identify if the bisectors in the same plane (plane perpendicular to  $\vec{c}$ -axis) which belong to different molecules are correlated orientationally or not. Such long-range intermolecular correlations are determined using an interchain orientational order parameter (ICOOP) defined as,

$$ICOOP = \frac{\int_0^1 P(\cos\eta) d\cos\eta - 0.5}{0.5} \quad (2.6)$$

where  $\eta$  is the angle between the projection of the backbone bisectors on to a plane perpendicular to the  $\vec{c}$ -axis of the crystal. Since we are interested in the long-range correlations, we have considered only those neighbors that are present at a distance of 8-11Å away from a given central molecule and that possess the same handedness as the central one. The calculation proceeds as follows. At a given temperature, we first determine the distribution of  $\cos\eta$ ,  $P(\cos\eta)$ . For a perfect crystal, one expects  $P(\cos\eta)$  to have a sharp peak at  $\cos\eta=1$  while for an orientationally disordered state it should be an uniform distribution. Later we use Eq. 2.6 to calculate the order parameter. In Figure 2.14a, we show the behavior of  $P(\cos\eta)$  at a few selected temperatures. As anticipated, the 600K data shows a sharp peak at  $\cos\eta=1$ , while the uniform distribution at 925K signals the attainment of the disordered liquid state. The ICOOP is defined such that it is unity for the crystalline state and is zero for an orientationally disordered state. We examine

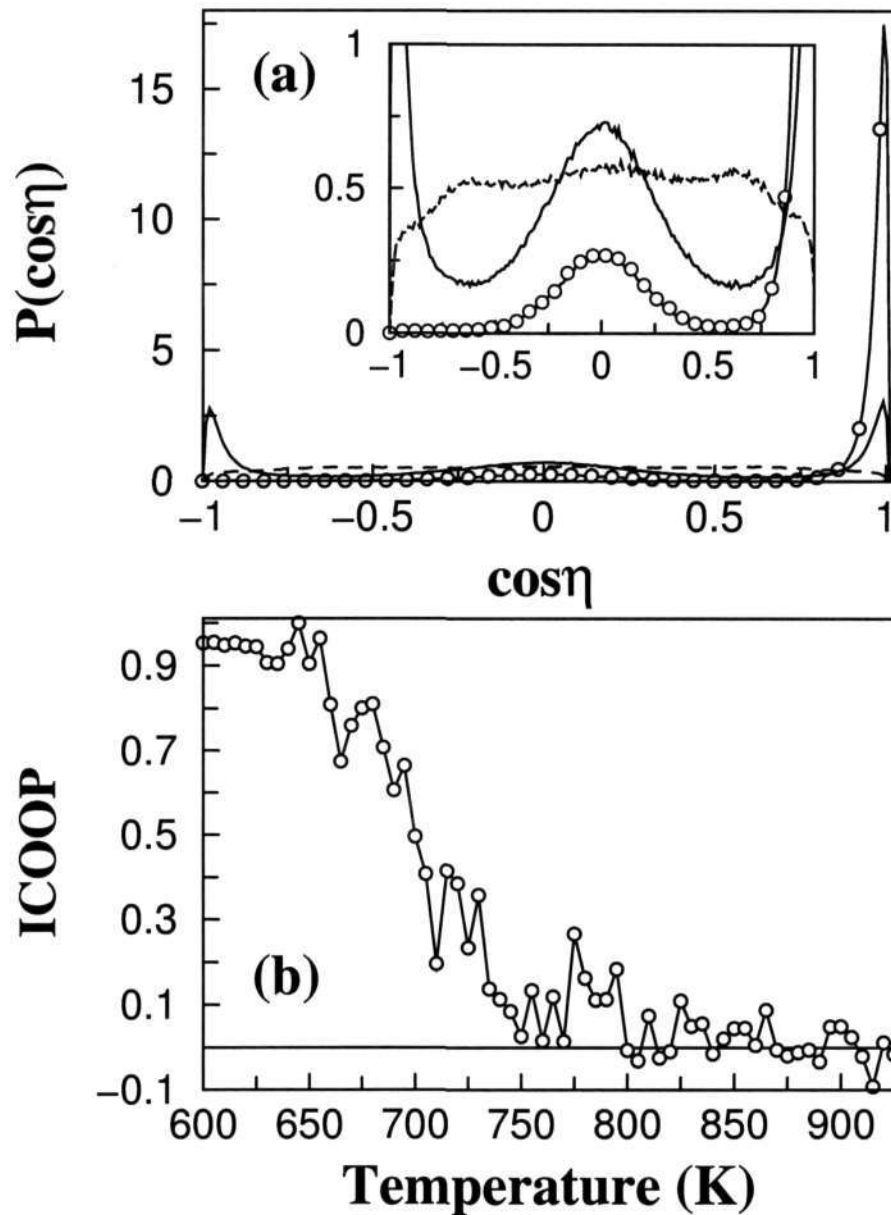


Figure 2.14: (a) The distribution of the angle,  $\eta$ , between the projection of the backbone bisectors on to a plane perpendicular to the  $\bar{c}$ -axis of the crystal at 600K (solid line with circles), 760K (solid line), and 925K (dashed line). Inset shows the same in expanded scale. (b) The variation of ICOOP with temperature (see text for definition).

the thermal evolution of ICOOP in Figure 2.14b. With increasing temperature, ICOOP decreases rapidly near 720K and oscillates around zero up to 925K. It is evident that interchain orientational correlations are lost across the premelting transition.

### Molecular Orientation :

To examine if the system has reached an isotropic melt state, one needs to calculate the relative orientation of the molecules with the  $\vec{c}$ -axis of the lattice. We have calculated the angle  $\theta$ , between the end-to-end vector of a PEO chain and the  $\vec{c}$ -axis. The end-to-end vectors are oriented parallel to the  $\vec{c}$ -axis at 600K. In Figure 2.15, we show the temperature dependence of  $\langle \cos\theta \rangle_{\frac{1}{2}}$  calculated using the following expression,

$$\langle \cos\theta \rangle_{\frac{1}{2}} = \frac{\int_0^1 \cos\theta f(\cos\theta) d\cos\theta}{\int_0^1 f(\cos\theta) d\cos\theta} \quad (2.7)$$

where  $f(\cos\theta)$  is the distribution of  $\cos\theta$  evaluated from the MD trajectory. A value of 0.5 for  $\langle \cos\theta \rangle_{\frac{1}{2}}$  signifies an isotropic melt state. We find that  $\langle \cos\theta \rangle_{\frac{1}{2}}$  remains constant at its upper bound up to 850K, and then decreases rapidly towards a value of around 0.9 near the melting temperature.

The invariance of  $\langle \cos\theta \rangle_{\frac{1}{2}}$  across the first transition implies that the PEO chains retain

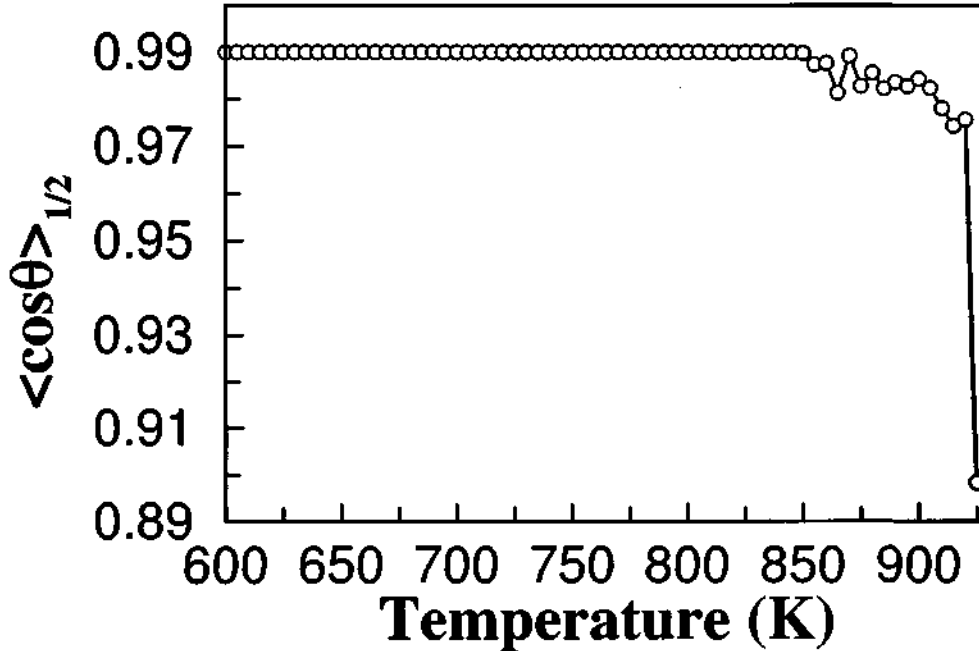


Figure 2.15: The variation of  $\langle \cos\theta \rangle_{\frac{1}{2}}$  with temperature, where  $\theta$  is the angle between the end-to-end vector of a PEO chain and the  $\vec{c}$ -axis of the crystal.

their orientations during the first stage (premelting) of the melting process. The rapid decrease of  $\langle \cos\theta \rangle_{\frac{1}{2}}$  at 925K signifies the melting transition. Since the averaging of this data has been carried out only for 100 ps, the value at 925K is not 0.5. A run of longer duration yields this value, as expected.

To summarize, we observe signatures of a premelting transition at 720K in terms of crystal density and intermolecular energy. Across this transition, the molecules continue to be oriented along the  $\vec{c}$ -axis. However, orientational correlations between methylene groups present in oligomers separated by 10Å are lost at premelting, although the chains continue to retain their helicity. Thus the premelting transition in PEO points to a subtle rearrangement between molecules.

### 2.3.2 Dynamics

The transitions in the structure of the PEO crystal give rise to pronounced changes in its dynamics. We have characterized these in terms of three functions. (i) the mean squared displacement of the chains in the direction of the  $\vec{c}$ -axis and that in the transverse plane (ii) reorientational time correlation function of the vector that bisects the methylene groups, and (iii) the reorientational time correlation function of the bisector of successive triplets of atoms along the backbone of each chain.

#### Anisotropic Diffusion :

Let  $\vec{r}^i$  denote the center of mass vector of the  $i$ -th chain. We define its projection on the  $\vec{c}$ -axis as,  $\vec{r}_c^{\parallel}$ , and the residual vector as  $\vec{r}_c^{\perp}$ . The latter is defined as,

$$\vec{r}_c^{\perp} = \vec{r}^i - (\vec{r}^i \cdot \hat{c}) \hat{c} \quad (2.8)$$



The MSD are defined as,

$$\text{MSD}_c^{\parallel}(t) = \langle (\vec{r}_c^{\parallel}(t) - \vec{r}_c^{\parallel}(0))^2 \rangle$$

$$\text{MSD}_c^{\perp}(t) = \langle |\vec{r}_c^{\perp}(t) - \vec{r}_c^{\perp}(0)|^2 \rangle$$

where the angular brackets denote averaging over initial time origins 0, and over the chain index  $i$ . In what follows, we define the plane that is perpendicular to  $\vec{c}$ -axis as  $c_{\perp}$ -plane. The MSD data are shown in Figures 2.16a and 2.16b at various temperatures. In Figure 2.16a, we show  $\text{MSD}_c^{\parallel}$  and  $\text{MSD}_c^{\perp}$  for temperatures between 650K and 760K, i.e., across the premelting transition. At 650K and 710K, the displacements are small along the  $\vec{c}$ -axis as well as in-plane, as is expected in a crystal. At 720K, we observe a significant displacement of the chains along the  $\vec{c}$ -axis, and negligible motion in the transverse direction. This indicates the sliding diffusion of chains along their long axes, coincident with the changes in the conformation and structure of the system, discussed earlier. Note that the interchain energy showed a jump around 720K (Figure 2.5a) and the interchain order parameter, ICOOP too decreased at premelting (Figure 2.14b). It can be thus surmised that the loss in interchain interactions enables the chains to diffuse past each other. This anisotropic diffusion is present up to 850K. At 850K (Figure 2.16b), the diffusion in the  $c_{\perp}$ -plane too picks up, supporting the notion of the onset of complete melting at this temperature. The evolution of the displacements with temperature is monotonic across both the transitions. At higher temperatures, the effect of disorder caused by the *gauche* defects is compensated by the increased kinetic energy in the system (Figure 2.16b). Hence the polymer chains exhibit large displacements at 800K and 825K, culminating in the melting transition at 850K. The nominal diffusion coefficients obtained from the mean squared displacement data are shown in Table 2.3. The values were obtained from the slopes of the MSD curves for times between 200 and 300 ps. The slopes along the  $\vec{c}$ -axis and in the  $c_{\perp}$ -plane were divided by factors of 2 and 4 respectively

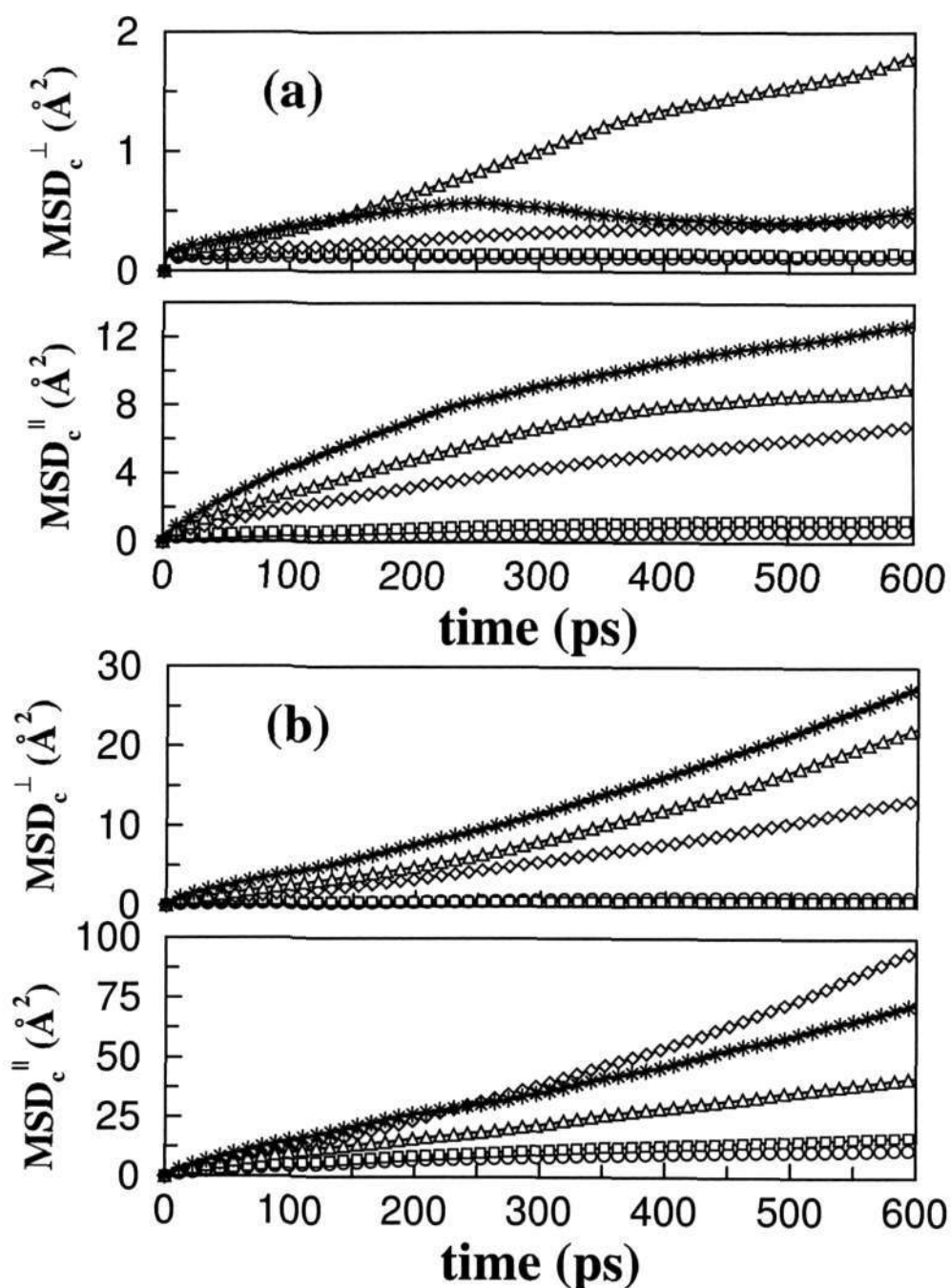


Figure 2.16: Mean squared displacement of PEO chains along the  $\vec{c}$ -axis ( $MSD_c^\parallel(t)$ ) and in the plane perpendicular to the  $\vec{c}$ -axis ( $MSD_c^\perp(t)$ ) are compared at temperatures across (a) the premelting transition and (b) melting. Temperatures: (a) 650K (circles), 710K (squares), 720K (diamonds), 740K (triangles), 760K (stars) (b) 800K (circles), 825K (squares), 850K (diamonds), 875K (triangles), 900K (stars). Note the one order of magnitude difference in the values of the displacements parallel to and perpendicular to the c-axis, in (a). Symbols are provided infrequently for clarity.

Temperature [K]	$D_c^{\parallel} [\times 10^{-11} \text{m}^2/\text{s}]$	$D_c^{\perp} [\times 10^{-11} \text{m}^2/\text{s}]$
650	0.4	Uncertain
710	1.0	Uncertain
720	5.3	0.2
740	9.0	0.8
760	9.6	Uncertain
800	5.6	0.5
825	11.7	Uncertain
850	74.1	5.4
875	28.9	8.0
900	43.2	9.5

Table 2.3: Nominal diffusion coefficients of the polymer center of mass along the  $\vec{c}$ -axis,  $D_c^{\parallel}$ , and perpendicular to  $\vec{c}$ -axis,  $D_c^{\perp}$ .

to obtain the diffusion coefficients in the corresponding directions (denoted as  $D_c^{\parallel}$  and  $D_c^{\perp}$ ). Note the increase in  $D_c^{\parallel}$  at 720K, while  $D_c^{\perp}$  continues to be insignificant up to 850K, the onset temperature of melting. Above 850K, both the values are healthy and approach isotropy.

### Methylene Reorientation :

As discussed in the Introduction, the  $^1\text{H}$  NMR spectrum in PEO and PEG is known to exhibit motional narrowing at a certain temperature in the crystalline state [32]. This reduction in linewidth can come about due to the sliding diffusion of chains discussed in the previous section, as well as from the intrinsic rotation of the methylene groups. We have studied the latter through the time correlation function of the vector that bisects the two C-H bonds in the  $\text{CH}_2$  group. Along the same lines as the discussion on MSD, we have considered the reorientation of components of this vector along the  $\vec{c}$ -axis and across it. The definitions are as follows.

$$M_c^{\parallel}(t) = \frac{\langle \vec{R}_{\text{CH}_2}^{\parallel}(t) \cdot \vec{R}_{\text{CH}_2}^{\parallel}(0) \rangle}{\langle \vec{R}_{\text{CH}_2}^{\parallel}(0) \cdot \vec{R}_{\text{CH}_2}^{\parallel}(0) \rangle} \quad (2.9)$$

$$M_c^{\perp}(t) = \frac{\langle \vec{R}_{\text{CH}_2}^{\perp}(t) \cdot \vec{R}_{\text{CH}_2}^{\perp}(0) \rangle}{\langle \vec{R}_{\text{CH}_2}^{\perp}(0) \cdot \vec{R}_{\text{CH}_2}^{\perp}(0) \rangle} \quad (2.10)$$

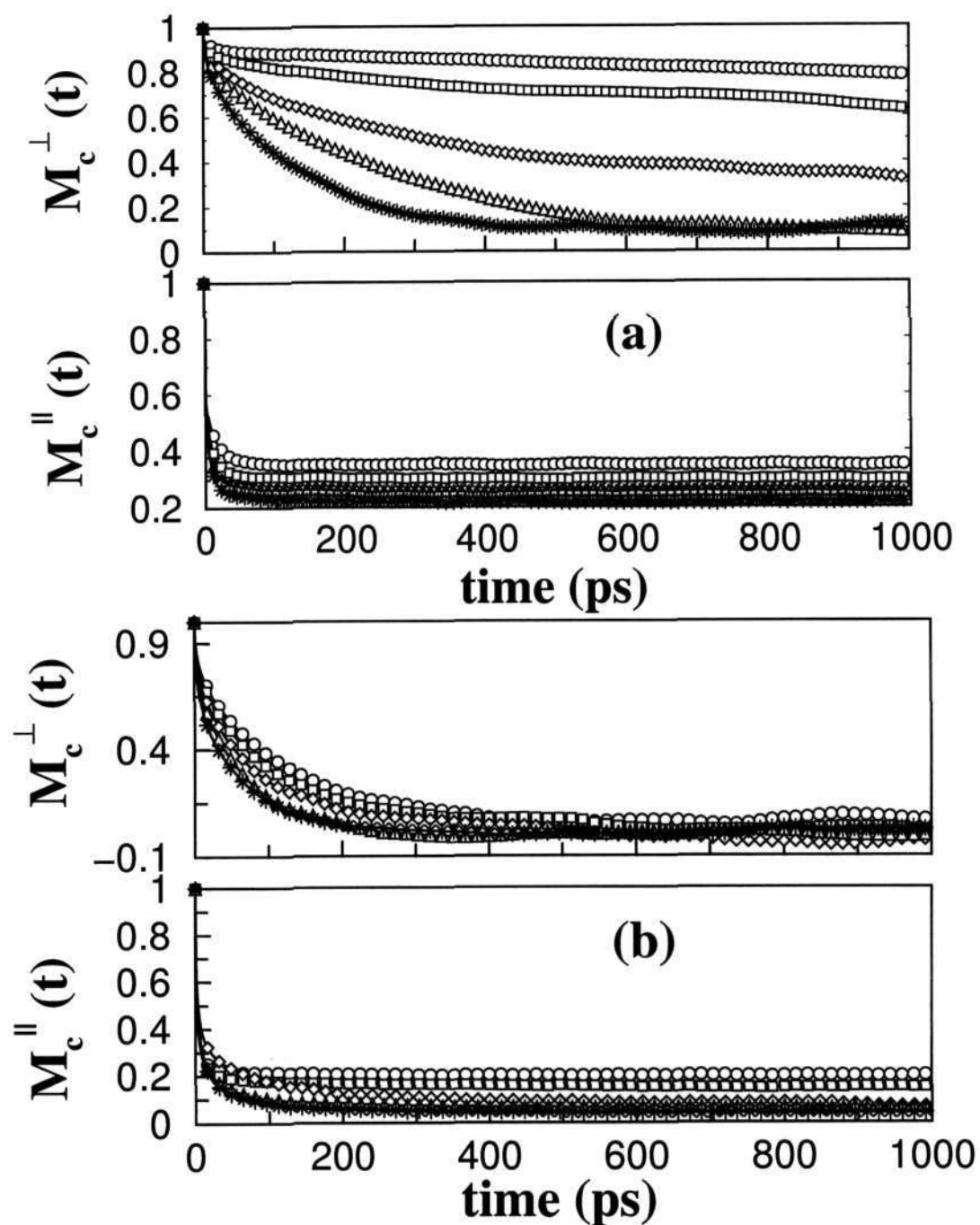


Figure 2.17: Behavior of the rotational time correlation function of the vector that bisects the C-H bonds in the  $\text{CH}_2$  group. The rotation along the  $\bar{c}$ -axis ( $M_c^{\parallel}(t)$ ) and in the plane perpendicular to  $\bar{c}$ -axis ( $M_c^{\perp}(t)$ ) are shown at temperatures across (a) the premelting transition and (b) melting. Temperatures: (a) 650K (circles), 710K (squares), 720K (diamonds), 740K (triangles), 760K (stars) (b) 800K (circles), 825K (squares), 850K (diamonds), 875K (triangles), 900K (stars). Symbols are provided infrequently for clarity.

where  $\vec{R}_{CH_2}^i(t)$  is the vector that bisects the two C-H bonds in a methylene group of index  $i$ , at time  $t$ . The vectors  $\vec{R}_{CH_2}^{i\parallel}(t)$  and  $\vec{R}_{CH_2}^{i\perp}(t)$  are the components of  $\vec{R}_{CH_2}^i(t)$  along and perpendicular to  $\vec{c}$ -axis respectively. The angular brackets denote averaging over all methylene groups and time origins 0. In Figure 2.17a, we show these TCFs at temperatures through the premelting transition. At 650K, the TCF of the component parallel to the  $\vec{c}$ -axis exhibits a fast initial relaxation, with a subsequent non-zero plateau. This behavior persists at all temperatures across the premelting transition. For instance, the value of the plateau at 760K is 0.22. The fast initial relaxation of this function is due to the fact that the magnitude of the projection of the CH<sub>2</sub> bisector on the  $\vec{c}$ -axis is quite small, and any fluctuation in the position of the hydrogen can cause a decorrelation of the TCF. This shows the increased propensity of the methylene groups to rock in the direction of the  $\vec{c}$ -axis rather than in the  $c_{\perp}$ -plane. The constant values of the TCF for long times in this temperature range indicate the rotation of the methylene groups only within a narrow range of angles along the  $\vec{c}$ -axis and in the plane perpendicular to it. Below 720K, the constant value of the TCF for the component in the  $c_{\perp}$ -plane is larger than that along the  $\vec{c}$ -axis. The behavior of these TCFs at higher temperatures is shown in Figure 2.17b. At 760K and higher, the reorientation of the methylene groups is facile, and the anisotropy in rotation vanishes.

### Backbone Reorientation :

We have studied the reorientational motion of the polymer backbones, a process that has earlier been termed helical oscillations [32]. We define  $\vec{R}^i$  as the vector that bisects successive bond vectors along a chain. As earlier, we obtain its component along the instantaneous  $\vec{c}$ -axis of the system and denote it as  $\vec{R}_c^{i\parallel}$ , and the residual vector as  $\vec{R}_c^{i\perp}$ . We show in Figure 2.18, the TCF of these functions  $B(t)$ , (whose definitions are similar to those in Eq. 2.10 ) at selected temperatures. At temperatures below the premelting transition,  $B_c^{\perp}(t)$  does not decay with time, indicating the rigid nature of the chain in the

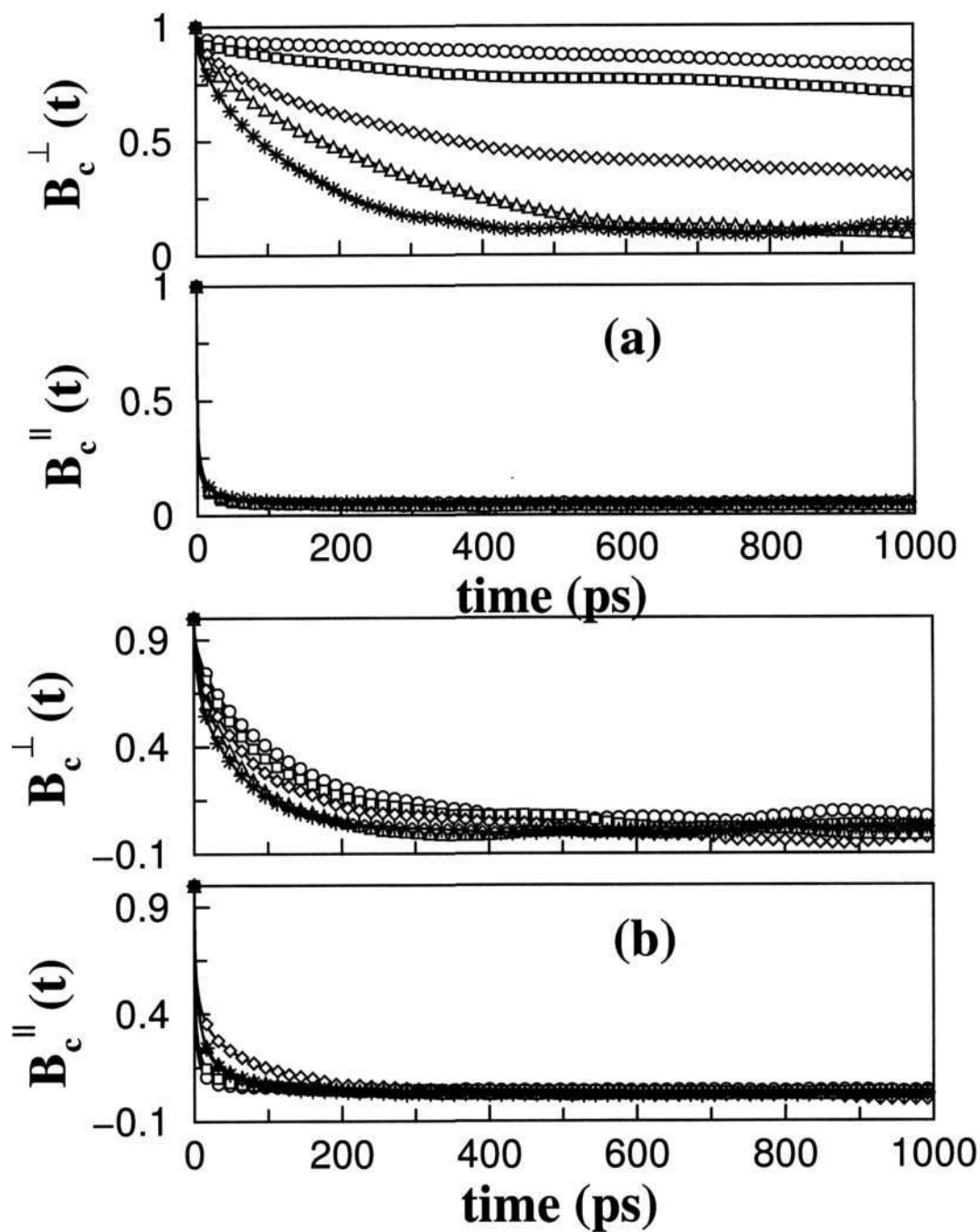


Figure 2.18: Rotational time correlation function of the vector that bisects two successive bonds along the backbone. The rotation along the  $\vec{c}$ -axis ( $B_c^{\parallel}(t)$ ) and in the plane perpendicular to it ( $B_c^{\perp}(t)$ ) are shown at temperatures across (a) the premelting transition and (b) melting. Temperatures: (a) 650K (circles), 710K (squares), 720K (diamonds), 740K (triangles), 760K (stars) (b) 800K (circles), 825K (squares), 850K (diamonds), 875K (triangles), 900K (stars). Symbols are provided infrequently for clarity.

transverse direction. However, at the same temperatures,  $B_c^{\parallel}(t)$  relaxes to a much smaller value of around 0.05. This decay is likely to be due to a buckling motion exhibited by the chains, that will change the sign of  $R_c^{\parallel}(t)$  periodically. Note also that the magnitude of the projection of the vector on the c-axis will also be quite small, and hence will be prone to frequent changes in sign, which can cause a decorrelation of its TCF. The constant value is also independent of temperature. Above 720K,  $B_c^{\perp}(t)$  exhibits signs of relaxation, however slow. This decay is due to helical oscillations of the polymer chain around its backbone axis. We cannot determine if this rotation involves the coherent motion of the entire chain, or if only certain segments of the chain participate. At 850K and beyond, the two time correlation functions are found to decay with roughly similar time scales, consistent with the isotropy in the orientation of the chains.

## 2.4 Conclusions

Large scale, atomistic molecular dynamics calculations on a model of poly(ethylene oxide) has shown the possibility of a premelting transition that leads to a state which is intermediate to the crystal and the melt. These calculations have been carried out at 127 temperatures, with a run length totaling around 75 ns, on 32 molecules of poly(ethylene oxide) of molecular weight 1220. The calculations employed an empirical potential model that has earlier been used in MD studies of crystalline PEO [49], of vibrational dynamics of PEO [75] and of ion transport in glassy polymer electrolytes [49,54] with the inclusion of flexible backbone and methylene groups [59,60].

We observe thermodynamic, structural, and dynamical signatures for two transitions as a function of temperature. Quantities such as the intermolecular energy, lattice constants, and the fraction of *gauche* defects exhibit discontinuities at the premelting transition of 720K, and also at the onset of melting of the simulated crystal, at 850K. At temperatures just above premelting, molecules are able to rotate about their long axes, and diffuse along the  $\bar{c}$ -axis of the crystal. This anisotropic diffusion of chains *within the*

*crystalline state* has earlier been observed and discussed as sliding diffusion in the polymer literature [76,77]. The mobility of the chains and the ability of the methylene groups to rotate, explain the motional narrowing of the  $^1\text{H}$  NMR linewidth with increasing temperature [32]. Thus our results are consistent with and provide a microscopic explanation for the calorimetric [33] and NMR data [32]. These observations are also consistent with our earlier MD simulations that employed infinite chain model of PEO [78]. Three issues related to the endless PEO model that motivated us to the study finite PEO chain are as follows: (i) The infinite chain model prevents transitions to helices with a pitch that is a non-integral divisor of the c-axis. (ii) It may also dissuade structural transitions of low activation energies that get initiated at chain ends and which could lead to complete melting in a single stage. (iii) During diffusion, the "endless" chains cannot cross each other's paths. They can only slide past each other, by construction. Also, in the simulations of finite PEO, we find torsional defects to be initiated at the chain ends, a feature that cannot be observed in the endless chain model.

The transition temperatures obtained from this study are higher than that observed from experiments. The increase could be due to the inevitable large heating rates employed here that lead to superheating of the sample. It may also point to the overstabilization of the crystalline phase by the potential model. A third and often forgotten contribution in molecular simulations is the absence of surfaces in the models, due to the use of periodic boundary conditions. The use of such boundary conditions in Lennard-Jones crystals have been shown to lead to a 20% increase in the melting point [79]. It is difficult to quantify the magnitude of these contributions, which could vary between different systems. Molecular crystals, as opposed to crystals of spherical particles interacting via Lennard-Jones potentials, pose practical difficulties in determining the relative weight of these effects. However, we would like to offer some observations on the NBT model. Brown and coworkers, whose force field we employed here (with flexible backbone and  $\text{CH}_2$  groups), pioneered the simulation studies on PEO [49]. The force field param-



eters in the NBT model were optimized to achieve mechanical equilibrium for a small crystalline system consisting of eight crystallographic unit cells, that necessitated an interaction cutoff of only 6.56Å for non-bonded interactions. The use of tail corrections to the total energy and pressure requires that the pair correlation function is unity beyond the cutoff. This condition may not be fully satisfied with such a low cutoff. It may thus be appropriate to refine the potential parameters of the NBT model employing a larger cutoff. On the issue of surfaces, earlier calculations on the phase behavior of long chain molecules too have employed periodic boundary conditions without surfaces [61, 70, 80]. Despite the lack of an explicit surface, the phase boundary of crystalline *n*-octane has been predicted to within 3K of experiments [70]. Yet, this aspect needs to be studied in detail for PEO.

Despite the long runs employed here along with a fine temperature resolution of 5K, the simulated system may be falling out of equilibrium. While this could lead to an increase in the temperature of the transition(s), we believe that such effects will not alter the existence of a premelting transition, *and its molecular mechanism*. The effect of a limited sampling duration employed in MD simulations on the nature of such structural transitions in molecular systems with large relaxation times [81] is unclear, and needs to be investigated further.

As discussed in the Introduction, existing experimental data on PEO and PEG has not been unambiguous on the existence of a premelting transition. A variety of factors, including polydispersity in molecular weight, chain folding, poly-/semi-crystallinity, and heating rate effects could contribute to the lack of clarity. Our simulations point to the existence of a premelting transition in monodisperse, single crystalline PEO. However, the reality of these simulations need to be evaluated against precise experiments on good quality crystals of low molecular weight poly(ethylene oxide). The similarity of this transition in PEO to that observed in simulations of PTFE [61] allows us to place some degree of confidence in our results. Note that the solid-solid transition in PTFE at ambient pres-

---

sure is well understood and accepted in experiments. It is also important to reproduce our results with simulations that employ a different set of interaction potentials [82]. This needs to be studied further. We believe that our simulations would also motivate further experiments to probe the phase behavior of PEO.



## Bibliography

- [1] A.C. Barnes, J.E. Enderby, J. Breen, and J.C. Leyte, *Chem. Phys. Lett.* **142**, 405 (1987).
- [2] H. Matura, and K. Fukuhara, *J. Mol. Struct.* **126**, 251 (1985).
- [3] K. Devanand, and J.C. Selser, *Macromolecules* **24**, 5493 (1991).
- [4] T.W.N. Bieze, A.C. Barnes, C.J. Huige, J.E. Enderby, and J.C. Leyte, *J. Phys. Chem.* **98**, 6568 (1994).
- [5] X. Yang, Z. Su, D. Wu, S.L. Hsu, and H.D. Stidham, *Macromolecules* **30**, 3796 (1997).
- [6] S. Verheyen, P. Augustijns, R. Kinget, and G. Van den Mooter, *Thermochim. Acta* **380**, 153 (2001).
- [7] P.M. Bayley and S.R. Martin, *Biochimica et Biophys. Acta* **1160**, 16 (1992).
- [8] C.R. Cox, E.H. Dunlop, and A.M. North, *Nature* **249**, 243 (1974).
- [9] G.E. Gadd, *Nature* **217**, 1040 (1968).
- [10] C. Branca, S. Magazu, G. Maisano, P. Migliardo, and V. Villari, *J. Phys. Condens. Matter* **10**, 10141 (1998).
- [11] C. Branca, A. Faraone, S. Magazu, G. Maisano, P. Migliardo, and V. Villari, *J. Mol. Struct.* **87**, 21 (2000).

- 
- [12] S.P. Gejji, J. Tegenfeldt, and J. Lindgren, *Chem. Phys. Lett.* **226**, 427 (1994).
- [13] B.K. Annis, O. Borodin, G.D. Smith, C.J. Benmore, A.K. Soper, and J.D. Londono, *J. Chem. Phys.* **115**, 10998 (2001).
- [14] J.A. Johnson, M.-L. Saboungi, D.L. Price, S. Ansell, T.P. Russell, J.W. Halley, and B. Nielsen, *J. Chem. Phys.* **109**, 7005 (1998).
- [15] M.-L. Saboungi, D.L. Price, G. Mao, R.F. Perea, O. Borodin, G.D. Smith, M. Armand, and W.S. Howells, *Solid State Ionics* **147**, 225 (2002).
- [16] G.D. Smith, R.L. Jaffe, D.Y. Yoon, *J. Phys. Chem.* **97**, 12752 (1993).
- [17] H. Matsuura, and T. Miyazawa, *J. Polymer Sci.* **7**, 1735 (1969).
- [18] P. G. Bruce, *Solid State Electrochemistry* (Cambridge University Press, Cambridge, 1995).
- [19] M.A. Ratner and D.F. Shriver, *Chem. Rev.* **88**, 109 (1988).
- [20] C. Berthier, W. Gorecki, M. Minier, M.B. Armand, J.M. Chabagno, and P. Rigaud, *Solid State Ionics* **11**, 91 (1983).
- [21] G. Mao, M.L. Saboungi, D.L. Price, M.B. Armand, and W.S. Howells, *Phys. Rev. Lett.* **84**, 5536 (2000).
- [22] Z. Gadjourova, Y.G. Andreev, D.P. Tunstall, and P.G. Bruce, *Nature* **412**, 520 (2001).
- [23] S. Neyertz, *Ph.D. thesis*, Uppsala University, Uppsala, 1995.
- [24] F. Müller-Plathe and W.F. van Gunsteren, *J. Chem. Phys.* **103**, 4745 (1995).
- [25] K. Laasonen and M.L. Klein, *J. Chem. Soc., Faraday Trans.* **91**, 2633 (1995).
- [26] O. Borodin and G.D. Smith, *Macromolecules* **31**, 8396 (1998); *Macromolecules* **33**, 2273 (2000)

- 
- [27] J.P. Donoso, T.J. Bonagamba, H.C. Panepucci, L.N. Oliveira, W. Gorecki, C. Berthier, and M. Armand, *J. Chem. Phys.* **98**, 10 026 (1993).
- [28] H. Tadokoro, Y. Chatani, M. Yoshihara, S. Tahara, and S. Murahashi, *Makromol. Chem.* **74**, 109 (1964).
- [29] Y. Takahashi and H. Tadokoro, *Macromolecules* **6**, 672 (1973).
- [30] T. Yoshihara, H. Tadokoro, and S. Murahashi, *J. Chem. Phys.* **41**, 2902 (1964).
- [31] V.P. Privalko, V.B. Sobolev, N.A. Rekheta, and V.N. Shihko, *J. Macromol. Sci.-Phys* **B37**, 765 (1998).
- [32] K. Hikichi and J. Furuichi, *J. Polym. Sci. A* **3**, 3003 (1965).
- [33] M.C. Lang, C. Noël, and A.P. Legrand, *J. Polym. Sci., Polym. Phys. Ed.* **15**, 1319 (1977).
- [34] C.P. Buckley, and A.J. Kovacs, in *Structure of Crystalline Polymers* (Ed. I.H. Hall, Elsevier-Applied Science, London, 1984, pp. 261).
- [35] A.J. Kovacs, C. Straupe, and A. Gonthier, *J. Polym. Sci. Polym. Symp.* **59**, 31 (1977).
- [36] A.J. Kovacs, and C. Straupe, *J. Crystal Growth* **48**, 210 (1980).
- [37] A.J. Kovacs, and A. Gonthier, *Kolloid-Z.u.Z. Polymere* **250**, 530 (1972).
- [38] A.J. Kovacs, A. Gonthier, and C. Straupe, *J. Polym. Sci. Polym. Symp.* **50**, 283 (1975).
- [39] S.Z.D. Cheng, and B. Wunderlich, *Macromolecules* **22**, 1866 (1989).
- [40] G. Strobl, *The Physics of Polymers* (Springer, New York, 1997).
- [41] C.P. Buckley, and A.J. Kovacs, *Colloid and Polym. Sci.* **254**, 695 (1976).

- 
- [42] C.P. Buckley and A.J. Kovacs, *Progr. Colloid and Polym. Sci.* **58**, 44 (1975).
- [43] K. Ishikiriya and B. Wunderlich, *J. Polym. Sci., Part B* **35**, 1887 (1997).
- [44] Y. Kambe, *Polymer* **21**, 352 (1980).
- [45] K. Viras, Z.G. Yan, C. Price, C. Booth, and A.J. Ryan, *Macromolecules* **28**, 104 (1995).
- [46] E. Alfthan, and A. de Ruvo, *Polymer* **16**, 692 (1975).
- [47] S.Z.D. Cheng, and B. Wunderlich, *J. Polym. Sci., Part B : Polym. Phys.* **24**, 577 (1986).
- [48] G.E. Yu, T. Sun, Z.G. Yan, C. Price, C. Booth, J. Cook, A.J. Ryan, K. Viras, *Polymer* **38**, 35 (1997).
- [49] S. Neyertz, D. Brown, and J.O. Thomas, *J. Chem. Phys.* **101**, 10064 (1994).
- [50] D. Brown and S. Neyertz, *Mol. Phys.* **84**, 577 (1995).
- [51] S. Neyertz and D. Brown, *J. Chem. Phys.* **102**, 9725 (1995).
- [52] S. Neyertz, D. Brown, D. Colombini, N.D. Alberola, and G. Merle, *Macromolecules* **33**, 1361 (2000).
- [53] S. Neyertz, D. Brown, and J.O. Thomas, *Electrochim. Acta* **40**, 2063 (1995).
- [54] S. Neyertz, D. Brown, and J.O. Thomas, *Comput. Polym. Sci.* **5**, 107 (1995).
- [55] F. Müller-Plathe and W.F. van Gunsteren, *Macromolecules* **27**, 6040 (1994).
- [56] O. Borodin, and G.D. Smith, *Macromolecules* **31**, 8396 (1998); *Macromolecules* **33**, 2273 (2000).

- [57] O. Borodin, F. Trouw, D. Bedrov, and G.D. Smith, *J. Phys. Chem. B* **106**, 5184 (2002); O. Borodin, D. Bedrov, and G.D. Smith, *J. Phys. Chem. B* **106**, 5194 (2002); G.D. Smith, D. Bedrov, and O. Borodin, *Phys. Rev. Lett.* **85**, 5583 (2000).
- [58] G.D. Smith, O. Borodin, M. Pekny, B. Annis, D. Londono, and R.L. Jaffe, *Spectrochim. Acta A* **53**, 1273 (1997).
- [59] A.D. Mackerell Jr. *et al*, *J. Phys. Chem. B* **102**, 3586 (1998).
- [60] D.J. Tobias, K. Tu, and M.L. Klein, *J. Chim. Phys. Phys.-Chim. Biol.* **94**, 1482 (1997).
- [61] M. Sprik, U. Röthlisberger, and M.L. Klein, *Mol. Phys.* **97**, 355 (1999); *J. Phys. Chem. B* **101**, 2745 (1997).
- [62] G.F. Velardez, S. Alavi, and D.L. Thompson, *J. Chem. Phys.* **119**, 6698 (2003).
- [63] C. Das and D. Frenkel, *J. Chem. Phys.* **118**, 9433 (2003).
- [64] M.E. Tuckerman, D.A. Yarne, S.O. Samuelson, A.L. Hughes, and G.J. Martyna, *Comp. Phys. Comm.* **128**, 333 (2000).
- [65] M. Parrinello, and A. Rahman, *Phys. Rev. Lett.* **45**, 1196 (1980).
- [66] G.J. Martyna, M.E. Tuckerman, D.J. Tobias, and M.L. Klein, *Mol. Phys.* **87**, 1117 (1996).
- [67] G.J. Martyna, M.L. Klein, and M. Tuckerman, *J. Chem. Phys.* **97**, 2635 (1992).
- [68] J.-P. Hansen, in *Molecular Dynamics Simulations of Statistical Mechanics Systems*, Ed. G. Ciccotti, and W.G. Hoover, (North-Holland, Amsterdam, 1986).
- [69] M.P. Allen and D.J. Tildesley, *Computer Simulation of liquids* (Oxford: Clarendon, 1987).



- 
- [70] J.M. Polson, and D. Frenkel, *J. Chem. Phys.* **111**, 1501 (1999).
- [71] M. Krishnan and S. Balasubramanian, *J. Phys. Chem. B* **109**, 1936 (2005).
- [72] M.E. Tuckerman, B.J. Berne, and G. Martyna, *J. Chem. Phys.* **97**, 1990 (1992).
- [73] G.D. Smith, D.Y. Yoon, R.L. Jaffe, R.H. Colby, R. Krishnamoorti, and L.J. Fetters, *Macromolecules* **29**, 3462 (1996).
- [74] Y. Saruyama, *Polymer* **24**, 135 (1983).
- [75] M. Krishnan, and S. Balasubramanian, *Phys. Rev. B* **68**, 064304 (2003).
- [76] H.G. Olf and A. Peterlin, *J. Appl. Phys.* **35**, 3108 (1964).
- [77] A. Keller, G. Goldbeckwood, M. Hikosaka, *Farad. Discuss.* **95**, 109 (1993).
- [78] M. Krishnan and S. Balasubramanian, *Chem. Phys. Lett.* **385**, 351 (2004).
- [79] Z.H. Jin, P. Gumbsch, K. Lu, and E. Ma, *Phys. Rev. Lett.* **87**, 055703 (2001).
- [80] J.P. Ryckaert and M.L. Klein, *J. Chem. Phys.* **85**, 1613 (1986).
- [81] A. Johansson and J. Tegenfeldt, *Macromolecules* **25**, 4712 (1992).
- [82] O. Borodin and G.D. Smith, *J. Phys. Chem. B* **107**, 6801 (2003).

## Chapter 3

# Vibrational Dynamics of Solid Poly(Ethylene Oxide)

### 3.1 Introduction

Solid polymer electrolytes (SPE), composed of inorganic salts solvated in solid, high molecular weight polymer matrices, have been the focus of intense theoretical and experimental research because of their applications as solid state batteries [1, 2]. In spite of their wide technological applications, the precise mechanism of conduction in these materials is still unclear and remains a pursuit of interest. In non-polymeric crystalline and glassy electrolytes, the ionic species hop from one site to another within a rigid host frame. However, the conduction mechanism in solid polymer electrolytes is believed to be different [3–5]. NMR studies of line shape and relaxation rates in poly(ethylene oxide)-lithium salt complexes have demonstrated a relationship between the motion of the  $\text{Li}^+$  ions and the segmental motion of the PEO chains [6]. This notion gains support from other experimental studies such as Field-Gradient NMR spin echo technique [7], and Quasi-elastic Neutron Scattering (QENS) [8]. SPE, in general, contain both amorphous and crystalline regions, with conduction being facile in the amorphous regions. This is probably due to

differences in the chain dynamics [9]. The work of Armand and coworkers has shown that ion mobility in solid electrolytes is of a continuous, diffusive type, in the amorphous regions [10]. NMR, differential scanning calorimetry and electrical conductivity studies have demonstrated that both cations and anions are mobile in the amorphous phase [11]. Recently, Bruce and coworkers have shown that a SPE with a ratio of ether oxygen to lithium of 6:1, exhibits higher conductivity in its crystalline phase as compared to its amorphous phase and that the ion transport is dominated by the cations [12]. In such complexes, cross-linking between a pair of polymer chains results in a channel like structure. The ion moves in this channel, aided by the segmental motion of the polymer chain pair.

A large number of simulations have been carried out on PEO and PEO-salt complexes, both in their crystalline and amorphous phases over the last decade. Molecular dynamics studies by de Leeuw et al, using an united atom model (UAM) for PEO chains in their molten state, have examined the motion of methylene groups which they term as segmental motion [13]. Neyertz et al have performed extensive molecular dynamics simulations of bulk crystalline PEO [14, 15], PEO melts [16], crystalline NaI-PEO [17] and amorphous NaI-PEO [18] systems. The simulations of Muller-Plathe and coworkers on PEO-LiI complexes [19] have demonstrated that the ether oxygens belonging to consecutive monomers of a PEO chain coordinate to the same  $Li^+$  ion and that this segmental coordination is argued to be the driving force for salt dissolution. Laasonen and Klein have performed MD simulations of both crystalline and amorphous PEO-NaI complexes [20]. Their study showed that ion pairing is most probable in the crystalline rather than in the amorphous phase. Halley and coworkers have studied the structure of amorphous PEO using the Parrinello-Rahman method recently [21]. MD simulations have also been employed by Smith and coworkers to elucidate the structure and dynamics of poly(propylene oxide) melts [22], PEO-salt complexes [23] and aqueous PEO solutions [24], using a potential model derived from *ab initio* calculations [25].

In the previous chapter, we have elucidated the thermal behaviour and conformational transition in crystalline PEO. In the present chapter, we characterize the vibrational modes of the polymer backbone in the pristine polymer, with an emphasis on the low frequency modes. This could enhance our understanding on the exact relationship between the dynamics of the polymer and that of the cation in the PEO-salt complexes [26,27]. In the present investigation, we have employed both molecular dynamics simulation and normal mode analysis to understand the vibrational modes of crystalline PEO. Normal mode analyses to characterize vibrational spectra have been employed successfully to describe the dynamics of glassy systems [28], and are likely to be employed in the study of jammed granular materials [29]. These calculations have also helped our understanding of vibrational modes of polyethylene [30], of proteins in solution [31], and in determining the flexibility of proteins, and in the thermodynamics of hydration water in protein solutions [32,47]. Unlike polyethylene, PEO adopts a distorted helical conformation in its crystalline state, with the distortion arising from strong intermolecular interactions. It is thus important that such normal mode calculations be performed for the crystalline state, rather than for an isolated oligomer. In this chapter, we have presented the results of our investigation on the vibrational dynamics of PEO in its crystalline state.

## 3.2 Simulation Details

The unit cell of crystalline PEO is monoclinic with the PEO chains in a  $(7/2)$  distorted helical conformation with TTG sequence [33]. The experimental crystal structure of PEO was used as a starting configuration for the MD runs reported here. The two ends of a polymer chain were assumed to be bonded across the simulation cell boundary [14,20] to eliminate end effects. MD simulations were performed primarily for a system that we describe as  $\langle 422 \rangle$ , which contained 4 unit cells along the  $\vec{a}$ -axis, 2 unit cells along the  $\vec{b}$ -axis and 2 unit cells along the  $\vec{c}$ -axis, containing a total of 3136 atoms. To study system size effects and effects of inter-chain interactions, we have performed additional

simulations of only one unit cell, and also of one isolated finite length polymer chain. Thus the simulations for the  $\langle 422 \rangle$  cells and that for the one unit cell contained chains that had no ends, while that for the isolated molecule, contained a chain with two ends. An all atom model (AAM), with explicit consideration of hydrogen atoms was used, to properly account for the steric interactions expected to be dominant in the crystalline state. The simulations were carried out in the canonical ensemble at 5K for the NMA and in the constant pressure ensemble at 300K and 1 atmosphere to test the stability of the simulated crystal. Temperature control was achieved by the use of Nose-Hoover chain thermostats [34], using the PINY-MD program [35]. Long range interactions were treated using the Ewald method with an  $\alpha$  value of  $0.3 \text{ \AA}^{-1}$ , and 2399 reciprocal space points were included in the Ewald sum [36]. The methylene groups were treated as rigid entities, enabling us to employ a time step of 1 fs. To obtain the vibrational density of states, we performed these calculations at a temperature of 5K, where the atoms could be expected to be near their equilibrium positions. The equilibration period for the single molecule, the unit cell, and the  $\langle 422 \rangle$  system were 65 ps, 100 ps, and 750 ps, respectively. These were followed by an analysis run of duration 30 ps during which the coordinates and velocities of each particle were stored at regular intervals. Velocities were dumped every time step to obtain the power spectrum of their time correlation functions and the coordinates were dumped every 10 fs.

The potential of interaction used in our simulations is given as,

$$\begin{aligned}
 U(\{\mathbf{r}\}) = & \frac{1}{2} \sum_{ij}^{\text{bonded}} K_r^{ij} (\mathbf{r}_{ij} - \mathbf{r}_{ij}^0)^2 + \frac{1}{2} \sum_{ijk}^{\text{bonded}} K_\theta^{ijk} (\theta_{ijk} - \theta_{ijk}^0)^2 \\
 & + \sum_{ijkl}^{\text{bonded}} \sum_{n=0}^6 a_n \cos^n \phi_{ijkl} + \frac{1}{4\pi\epsilon_0} \sum_i^N \sum_{j>i}^N \frac{q_i q_j}{r_{ij}} \\
 & + \sum_i^N \sum_{j>i}^N \left[ A_{ij} e^{-B_{ij} r_{ij}} - \frac{C_{ij}}{r_{ij}^6} \right] \tag{3.1}
 \end{aligned}$$

where  $i, j, k$ , and  $l$  denote atom indices,  $q_i$  and  $q_j$  are the partial charges of  $i^{\text{th}}$  and  $j^{\text{th}}$

Stretch	$r_0$ [Å]		$k_r$ [K Å <sup>-2</sup> ]				
C-C	1.53		237017.0				
C-O	1.43		171094.8				
C-H	1.09		Constrained				
H-H	1.78		Constrained				
Bend	$\theta_0$		$k_\theta$ [K rad <sup>-2</sup> ]				
C-O-C	112°		110255.50				
O-C-C	110°		76942.34				
O-C-H	109.5°		30193.20				
H-C-C	110°		45199.50				
Torsions	$a_0$ [K]	$a_1$ [K]	$a_2$ [K]	$a_3$ [K]	$a_4$ [K]	$a_5$ [K]	$a_6$ [K]
C-C-O-C	-50.322	150.966	0.0	-201.288	0.0	0.0	0.0
C-O-C-H	-50.322	150.966	0.0	-201.288	0.0	0.0	0.0
H-C-C-H	83.03	-249.090	0.0	332.120	0.0	0.0	0.0
O-C-C-O	265.70	-1826.19	2144.72	3901.46	-1667.17	142.91	1480.98
H-C-C-O	98.128	-294.384	0.0	392.512	0.0	0.0	0.0
Non-bonded	A [K]		B [Å <sup>-1</sup> ]	C [KÅ <sup>6</sup> ]			
C...C	15909350.62		3.3058	325985.916			
C...O	21604039.75		3.6298	177536.016			
C...H	7571800.37		3.6832	91334.430			
O...O	29337172.46		4.0241	96668.562			
O...H	10282092.97		4.0900	49718.136			
H...H	3603659.064		4.1580	25563.576			
Atomic charges [e]							
	$q_C$		0.103				
	$q_O$		-0.348				
	$q_H$		0.0355				

Table 3.1: Parameters of the interaction potential [14, 37].

atom respectively,  $\epsilon_0$  is the permittivity of free space,  $K_r^{ij}$  and  $K_\theta^{ijk}$  are the stretching and bending force constants respectively,  $\phi_{ijkl}$  is the dihedral angle, and  $r_{ij}$  is the interatomic distance between atoms  $i$  and  $j$ . The last two terms in Eq.3.1 are applicable to interaction sites separated by more than three bonds in a molecule and to every pair of sites belonging to different molecules.

The simulations were performed with a force field obtained from the work of Ney-

ertz [14] with the torsional parameters of the CHARMM model [37]. The potential parameters are given in Table 3.1. The non-bonded interactions were truncated at 12Å for the <422> crystal, at 3.25Å for one unit cell, and at 12Å for the single molecule runs. The lower cutoff value for the unit cell run is necessitated by the fact that the interaction cutoff should be less than half of the minimum distance between any two opposite faces of the simulation cell.

### 3.2.1 Normal Mode Analysis (NMA)

Normal mode analysis is an useful theoretical tool for studying the dynamics of a complex many body system near its stable equilibrium. The basic aim of NMA is to represent the complex vibrations exhibited by a system around its equilibrium as a linear combination of  $3N$  independent normal modes, where  $N$  is the number of atoms present in the system. Let  $q_1, q_2, \dots, q_{3N}$  denote the Cartesian components of atomic coordinates. The potential energy of the system can be expanded in terms of atomic displacements from an equilibrium configuration as follows:

$$U(q_1, q_2, \dots, q_{3N}) = U(q_{01}, q_{02}, \dots, q_{03N}) + \sum_i \left( \frac{\partial U}{\partial q_i} \right)_0 \eta_i + \frac{1}{2} \sum_i \sum_j \left( \frac{\partial^2 U}{\partial q_i \partial q_j} \right)_0 \eta_i \eta_j + \dots \quad (3.2)$$

where the subscript 0 represents the equilibrium configuration and  $\eta_i$  are the deviations of the coordinates from equilibrium, represented as,

$$q_i = q_{0i} + \eta_i \quad (3.3)$$

It can be shown that the  $\eta_i$ 's obey the following equation [38] to within a harmonic approximation of Eq. 3.2 and assuming that the term linear in  $\eta_i$  in Eq. 3.2 vanishes:

$$\ddot{\eta}_i + \sum_{j=1}^{3N} H_{ij} \eta_j = 0 \quad (3.4)$$

where  $H_{ij}$  are elements of the Hessian matrix and are defined as,

$$H_{ij} = \frac{1}{\sqrt{m_i m_j}} \left( \frac{\partial^2 U}{\partial q_i \partial q_j} \right)_0 \quad (3.5)$$

We can rewrite the elements of the Hessian matrix in terms of atomic indices as follows:

$$H_{ln}^{\alpha\beta} = \frac{1}{\sqrt{m_l m_n}} \left( \frac{\partial^2 U}{\partial \beta_n \partial \alpha_l} \right) \quad (3.6)$$

where  $l, n$  represent particle indices and  $\alpha, \beta$  represent the spatial coordinates  $x, y, z$ .  $m_l$  is the mass of particle  $l$ . A simple scheme to obtain some of these Hessian elements for a macromolecular potential of crystals efficiently is provided in the Appendix. *All Hessian elements obtained from such analytical expressions were checked against numerical second derivatives [39] within our normal mode analysis code, and were found to match.* The eigenvalues and eigenvectors of the Hessian matrix were examined to understand the vibrational dynamics of PEO. The frequency,  $\nu_s$ , of a particular mode of vibration,  $s$ , is related to its eigen value,  $\lambda_s$ , by

$$\lambda_s = (2\pi\nu_s)^2 \quad (3.7)$$

With these set of interactions, the initial pressure of the (422) system was found to be around 4000 atmospheres. Hence, we performed a MD run in the NPT ensemble for 200 ps under ambient conditions. The change in volume was found to be 1.3% from that of the experimental crystal. Time correlation functions of atomic velocities were calculated, and were Fourier transformed to obtain the power spectra. These were compared with the spectrum obtained from the NMA. The spectra were convoluted with a Gaussian function of width  $4\text{cm}^{-1}$  so as to provide a width to the spectral features. The helical axis of a PEO chain possesses a 7-fold rotational symmetry. In addition, 7  $C_2$  axes lie perpendicular to it, making the molecular symmetry of PEO to be  $D_7$  [33]. We have characterized the symmetry of the normal modes by studying the transformation of atomic displacements, on application of the symmetry operations for this group. Specifically, the operation by



the  $C_2$  axes enables a distinction between the three irreducible representations,  $A_1$ ,  $A_2$ , and  $E$ .

We have also characterized the spatial extent of the modes of vibration using a quantity called the local character, defined as [31,40]

$$Localcharacter(j) = \sum_{i=1}^{3N} u_{ij}^4 \quad (3.8)$$

where  $u_{ij}$  is the  $i^{th}$  component of the  $j^{th}$  eigenvector. The local character value can range from 0 to 1 and it determines the extent of localization of a particular mode.

To obtain quantitative information on the length of the segment involved in the low frequency modes, we have defined a quantity called the Continuous Segment Size (CSS). We calculate the displacement of the  $k^{th}$  atom due to a  $i^{th}$  mode using the expression

$$\langle \delta r_{ik}^2 \rangle = k_B T \frac{|\vec{u}_i^k|^2}{m_k \omega_i^2} \quad (3.9)$$

where  $m_k$  is mass of  $k^{th}$  atom,  $\vec{u}_i^k$  is the vector formed by the components of the  $i^{th}$  eigen vector contributed by the  $k^{th}$  atom,  $T$  is temperature, and  $\omega_i$  is the frequency of the  $i^{th}$  normal mode. We then check if the displacement is greater than a specified cutoff. If  $n$  successive backbone atoms of a chain each have displacements greater than the displacement cutoff, they are defined to constitute a segment with  $CSS = n$ . Similarly, CSS was calculated for all possible modes with different vibrational frequencies from which the average segment size for a given frequency was calculated.

### 3.3 Results and Discussion

For crystalline systems, a close match between the experimentally determined cell parameters and that obtained from simulations is a crucial first step in the veracity of the parameters used. We show in Figure 3.1, the time evolution of the cell parameters at

300K and 1 atmospheres, generated by a MD run in the constant pressure ensemble using the Parrinello-Rahman method [41]. The  $b$  and the  $\beta$  parameters of the unit cell exhibit

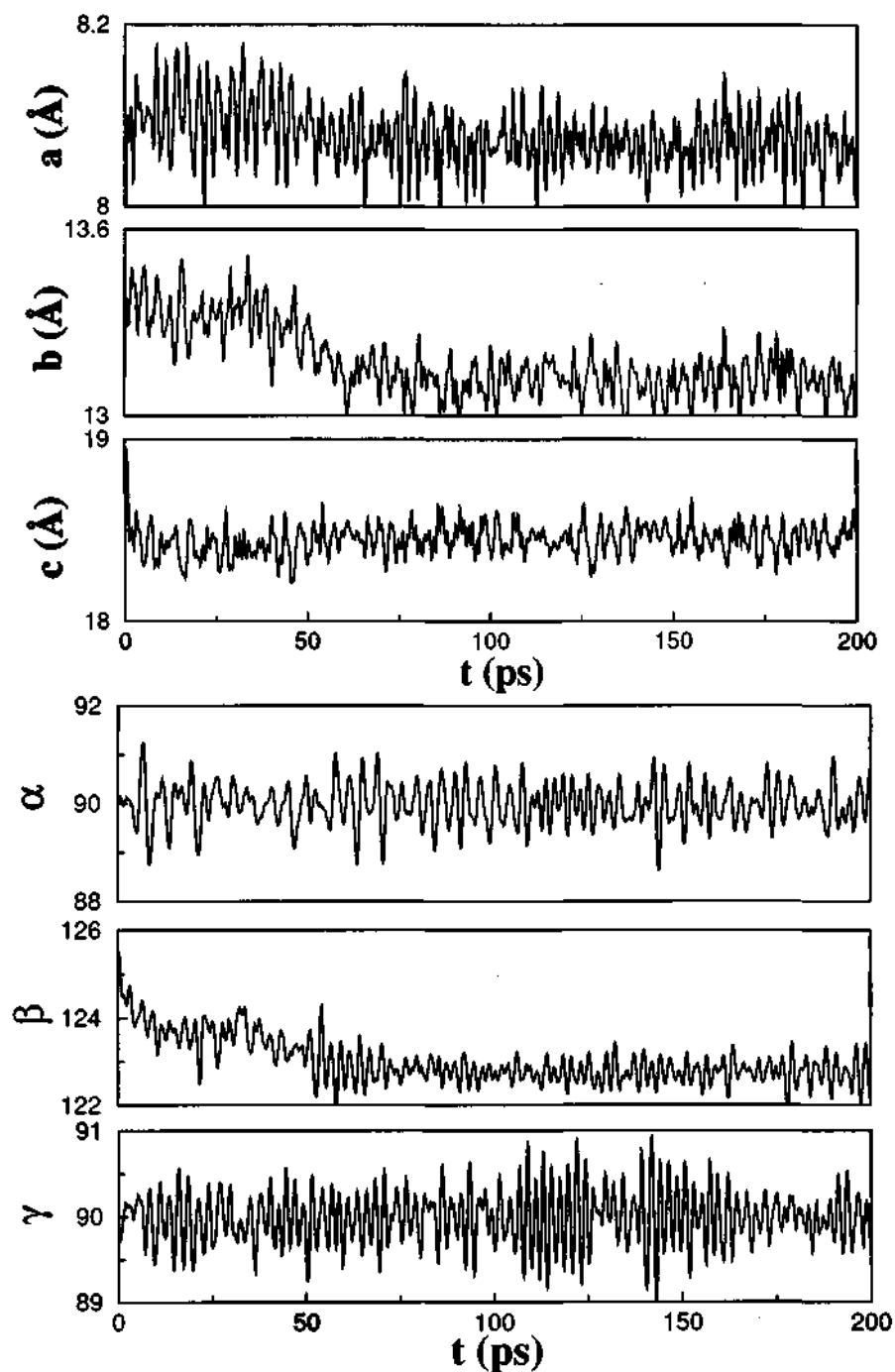


Figure 3.1: Plot of instantaneous cell parameters of PEO crystal obtained from simulations : (a) cell lengths, (b) cell angles. The zero time configuration corresponds to the experimental crystal structure.

a relaxation from the zero time experimental value, due possibly to relatively minor deficiencies in the interaction model used to represent this system. The constancy of the cell parameters for over 100 ps, shows that the simulated crystal is in a stable state, and that the potential parameters are indeed able to reproduce the high demands of the crystal symmetry. Table 3.2 compares the cell parameters obtained from our simulations to the experimental data.

An interesting feature associated with polymer dynamics is the variation of the various vibrational modes of a chain encountered during its transformation from the isolated state to the crystalline state. The vibrational spectra of a single molecule, one unit cell and that of the  $\langle 422 \rangle$  crystal are compared in Figure 3.2. When the chains assemble to form a crystal, each chain might prefer a new conformational state relative to its structure in the isolated state. A comparison of the vibrational spectra between that of one isolated molecule of finite length and of the  $\langle 422 \rangle$  system provides information on the effect of intermolecular interactions. As expected, the vibrational states of the isolated molecule showed marked differences from the crystalline state, particularly in the low frequency regions, where large amplitude, collective motions are predominant (see later).

However, there are no significant changes in the high frequency regions of the spectrum. The spectrum for the one unit cell compares well with that of the  $\langle 422 \rangle$  crystal. However,

Lattice parameter	Simulation	Experiment
a [ $\text{\AA}$ ]	8.08	8.05
b [ $\text{\AA}$ ]	13.17	13.04
c [ $\text{\AA}$ ]	18.45	19.48
$\alpha$ [ $^\circ$ ]	89.98	90.0
$\beta$ [ $^\circ$ ]	123.01	125.40
$\gamma$ [ $^\circ$ ]	89.99	90.0

Table 3.2: Lattice parameters obtained from simulation compared to experiment [33].

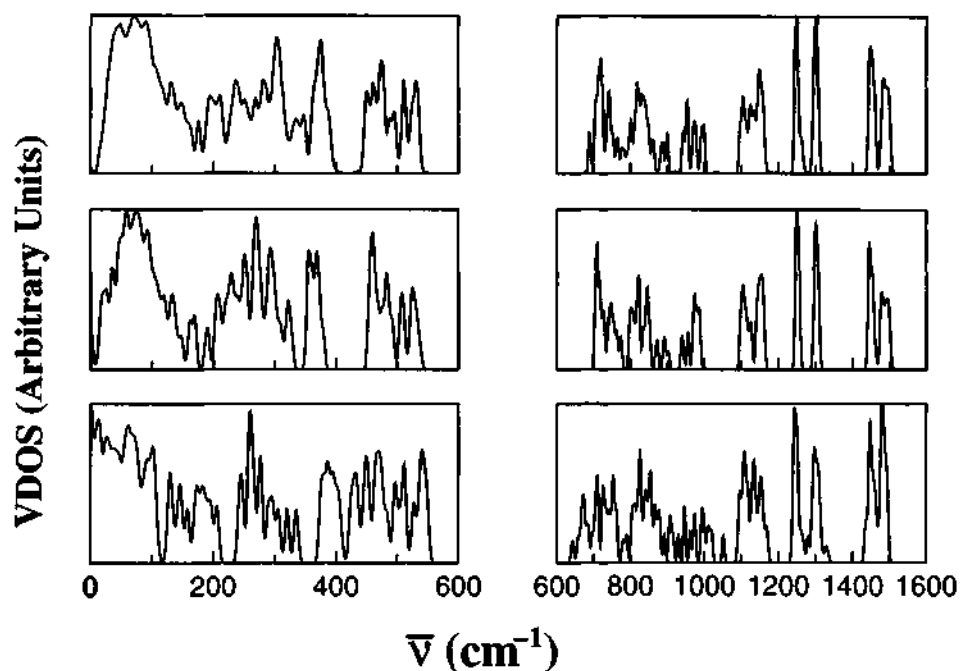


Figure 3.2: (a) The vibrational density of states of a single molecule (bottom), for one unit cell (middle) and for the  $\langle 422 \rangle$  crystal (top) of PEO, each obtained from normal mode analysis. The two sections of each spectrum are normalized independently to enable better comparison among the three system sizes. These spectra are convoluted with a Gaussian function of width  $4\text{cm}^{-1}$ .

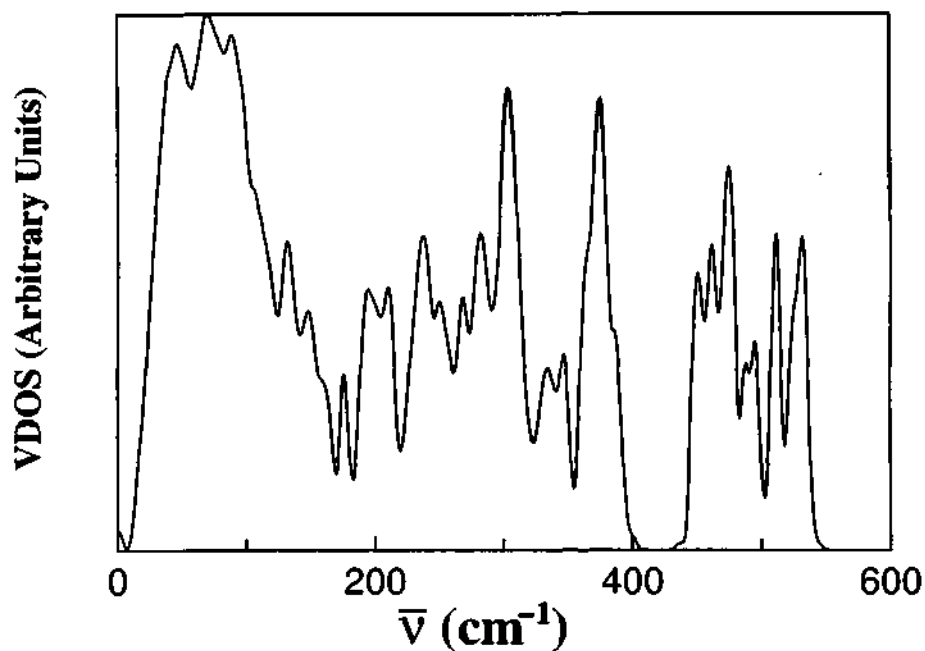


Figure 3.3: The vibrational density of states of the  $\langle 422 \rangle$  crystal, obtained by NMA shown in expanded scale.

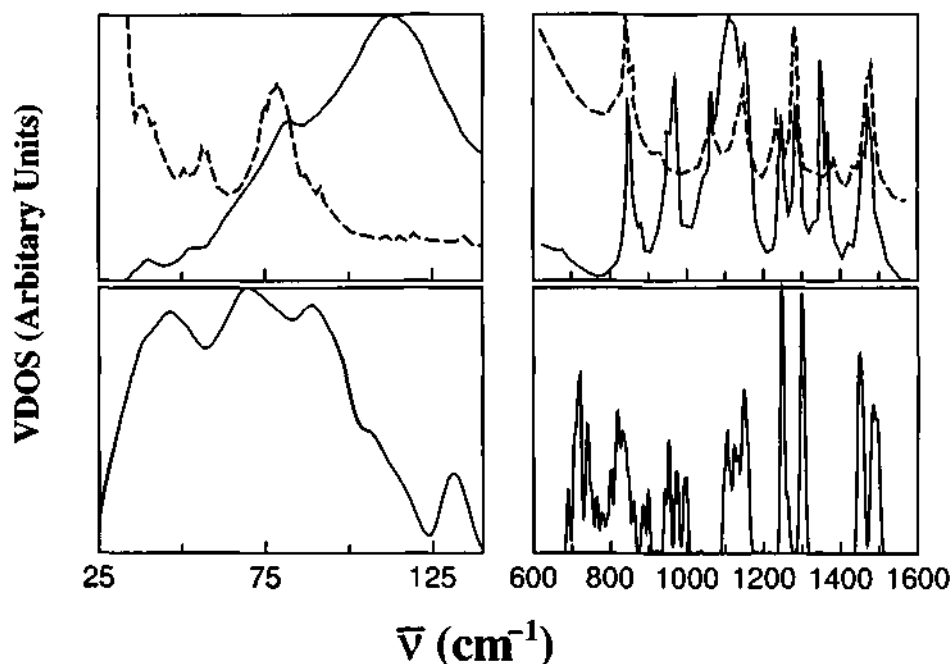


Figure 3.4: Vibrational density of states obtained from the NMA method (bottom panels) are compared with experimental Raman (Dashed lines) and Infrared (Continuous lines) absorption intensities. Experimental data presented in the top left and top right panels were obtained from Ref. [42] and Ref. [45] respectively. Note that the simulated spectrum is the raw density of states and does not contain any other terms that are needed to calculate the experimental absorption spectra. Thus only the peak positions are comparable, and not their intensities.

the features in the VDOS of the  $\langle 422 \rangle$  crystal is much better resolved, particularly at low frequencies. For instance, the features at around  $40 \text{ cm}^{-1}$  and  $75 \text{ cm}^{-1}$  are clearly evident in the larger system than in the spectrum for the unit cell, pointing to effects of long range interactions. The spectrum for the  $\langle 422 \rangle$  system is shown in an expanded scale in Figure 3.3. The split in the feature below  $100 \text{ cm}^{-1}$  is evident and compares well with experimental infrared (IR) spectra [42] that shows features at  $37 \text{ cm}^{-1}$ ,  $52 \text{ cm}^{-1}$ ,  $81 \text{ cm}^{-1}$  and  $107 \text{ cm}^{-1}$ . We do observe a prominent shoulder at  $108 \text{ cm}^{-1}$  which has been attributed to modes involving C-O internal rotation earlier [42]. A comparison of the simulated vibrational density of states with the experimental IR and Raman spectra, exhibited in Figure 3.4, shows that the potential model captures well nearly all the vibrational modes [42–44]. Note that the simulated spectrum is the raw density of states and does

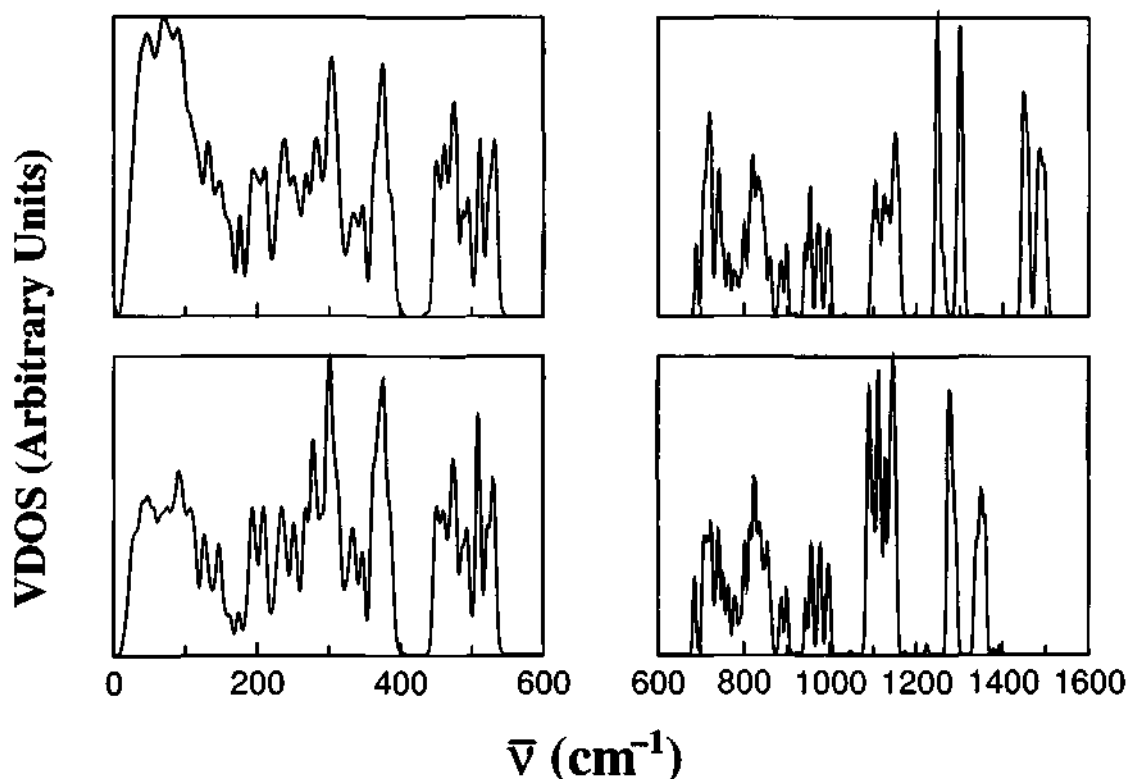


Figure 3.5: The vibrational density of states of  $\langle 422 \rangle$  PEO crystal obtained from normal mode analysis (top panels) is compared with that obtained as the power spectrum of the velocity autocorrelation function of all atoms (bottom panels). The two sections of each spectrum are normalized independently to enable better comparison among the two methods. The spectra are convoluted with a Gaussian function of width  $4\text{cm}^{-1}$ .

not contain any other terms that are needed to calculate the experimental spectra. Thus only the peak positions need to be compared, and not their intensities. Almost all the features found in the IR and Raman spectra seem to be present in the simulated VDOS. Another noteworthy feature of the spectrum is the absence of modes with imaginary frequencies which would have corresponded to either the presence of atoms away from equilibrium locations or to a mismatch between the empirical potential function and the crystal structure.

We have also calculated the vibrational spectrum through the Fourier transformation of the velocity auto correlation function of the atoms. This is compared with the VDOS obtained by the NMA in Figure 3.5. The agreement between the spectra is excellent

except for features above  $1200\text{ cm}^{-1}$ . Also, the peak at around  $1470\text{ cm}^{-1}$  is missing in the spectrum obtained through the velocity autocorrelation function (VACF). Visualization of the atomic displacements associated with this mode revealed HCH bending in methylene groups. Since all the  $\text{CH}_2$  groups were constrained to be rigid during the MD runs for the VACF analysis, the absence of a peak in the VDOS obtained from VACF, in this region can be rationalized. The comparison of the VDOS obtained from the two methods is good, despite the fact that the NMA method is only a harmonic approximation to the potential. Close examination of the two shows a marginal (approximately  $4\text{-}5\text{ cm}^{-1}$ ) shift to higher frequencies in the spectrum obtained by the NMA method relative to that from the VACF. We visualized the eigenvectors corresponding to different vibrational modes to assign the nature of atomic displacements that are responsible for the spectral features. In general, our assignments are consistent with earlier calculations [45, 46]. In Figure 3.6a and Figure 3.6b, we display a few of the modes. The zero frequency mode characterizes rigid body translation. The features at around  $40\text{ cm}^{-1}$ , have earlier been attributed to chain deformations [42]. Based on visualization of atomic displacements shown in Figure 3.6a, we assign these modes specifically to the twisting of the polymer backbone. The mode at  $88\text{ cm}^{-1}$  arises from torsional motion around the C-O bond. The  $A_1$  mode at  $216\text{ cm}^{-1}$  can be assigned to torsions around the C-C bond, while the  $510\text{ cm}^{-1}$  feature involves bending of CCO triplets. COC bending is observed at  $952\text{ cm}^{-1}$  while the wagging motion of the methylene groups is found to be present at  $1244\text{ cm}^{-1}$ , in good agreement with IR and Raman measurements [45]. The symmetry of the modes are also shown in Figures 3.6 agree well with experimental assignments [42, 45, 46].

For characterizing the normal modes further, we have calculated the local character for each mode [31, 40] which is shown in Figure 3.7. In the range, 0 to  $160\text{ cm}^{-1}$ , the local character value is very small, implying the participation of a large number of atoms. However, the local character does not provide any information on the proximity of the atoms that exhibit significant displacement in a mode. Thus this quantity has to be

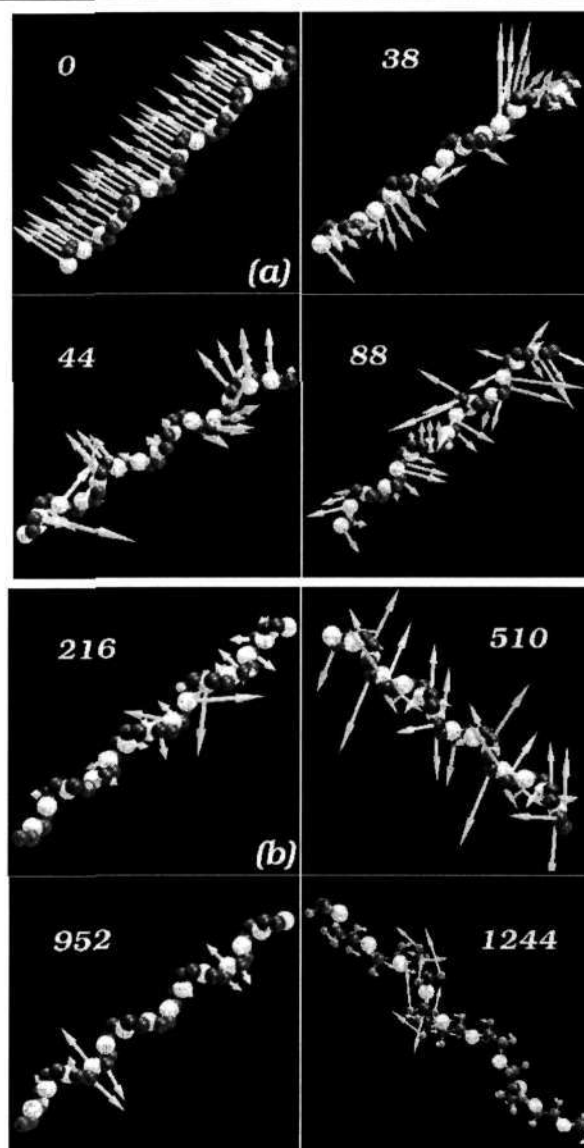


Figure 3.6: (a),(b) : Atomic displacements of representative normal modes of the PEO crystal. For each mode, one of the chains which exhibit significant atomic displacement is shown, for clarity. Black spheres denote carbon atoms and white spheres denote oxygens. Hydrogen atoms are not shown for clarity in all the modes, except the one with frequency  $1244\text{ cm}^{-1}$ . Arrows denote the directions of atomic displacements and their lengths are scaled up for the purpose of visualization. The mode at  $0\text{ cm}^{-1}$  is the rigid body translation of the chain, and that at  $1244\text{ cm}^{-1}$  arises from wagging of  $\text{CH}_2$  groups. Frequencies in  $\text{cm}^{-1}$  are as provided in the figures. The representation of these modes in the  $D_7$  group, are as follows, with frequencies in  $\text{cm}^{-1}$  given in parenthesis:  $A_2$  (38),  $A_2$  (44),  $E$  (88),  $A_1$  (216),  $E$  (510),  $E$  (952), and  $E$  (1244).



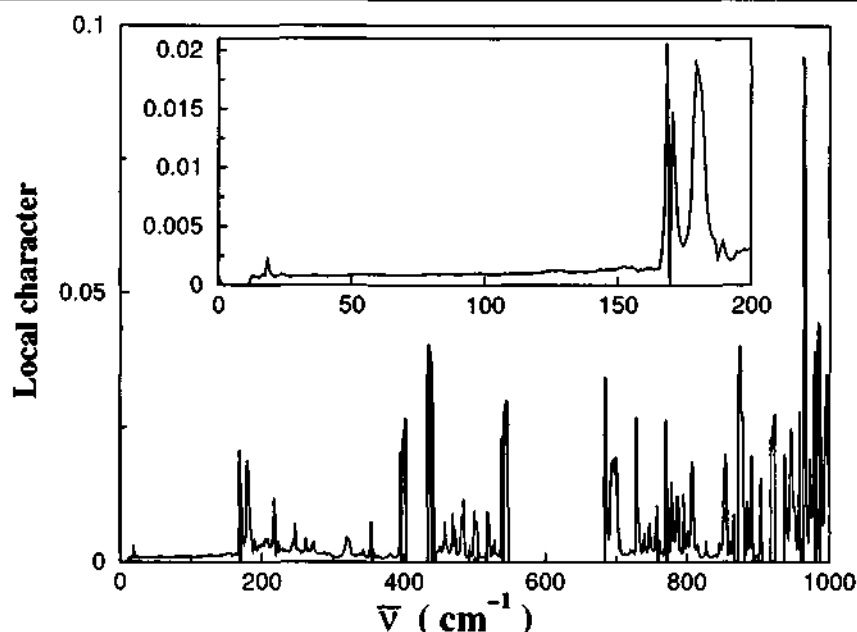


Figure 3.7: Local character indicator for the normal modes of PEO crystal. The inset shows the frequency range where collective motion is most probable with very small local character indicator values.

augmented by a further analysis of the concomitancy or proximity of atoms excited in a mode.

We have developed such an index that takes into account the connectivity of the atoms involved in a mode. We determine the number of successive atoms,  $n$ , that participate in a mode of a given frequency, by calculating the distribution of segment sizes,  $f(n)$ , for that vibrational mode. As a representative example, the distribution of the CSS for one such vibrational mode of frequency  $44 \text{ cm}^{-1}$  is shown in Figure 3.8 for four selected displacement cutoffs. It is our contention that a large number of atoms in proximity to each other participate in these modes. This is evident from the non-zero value of  $f(n)$  for  $n$  values in the range of 5 to 10, for some of the cutoff values.

The average segment size was calculated by evaluating the following summation,

$$\langle CSS \rangle = \frac{\sum_{n=5}^{42} n f(n)}{\sum_{n=5}^{42} f(n)} \quad (3.10)$$

In our study, we define a segment as a chain of connected atoms whose displacements

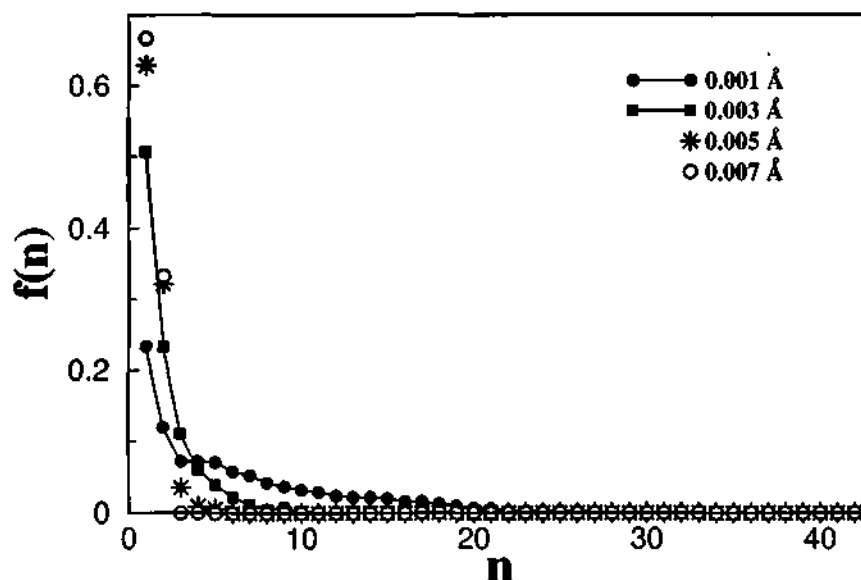


Figure 3.8: The segment size distribution,  $f(n)$ , corresponding to the mode at  $44 \text{ cm}^{-1}$  of the PEO crystal. The distribution is shown for four different displacement cutoffs. Such distributions are used to calculate the average continuous segment size ( $\langle \text{CSS} \rangle$ ) which is defined in Eq. 3.10.

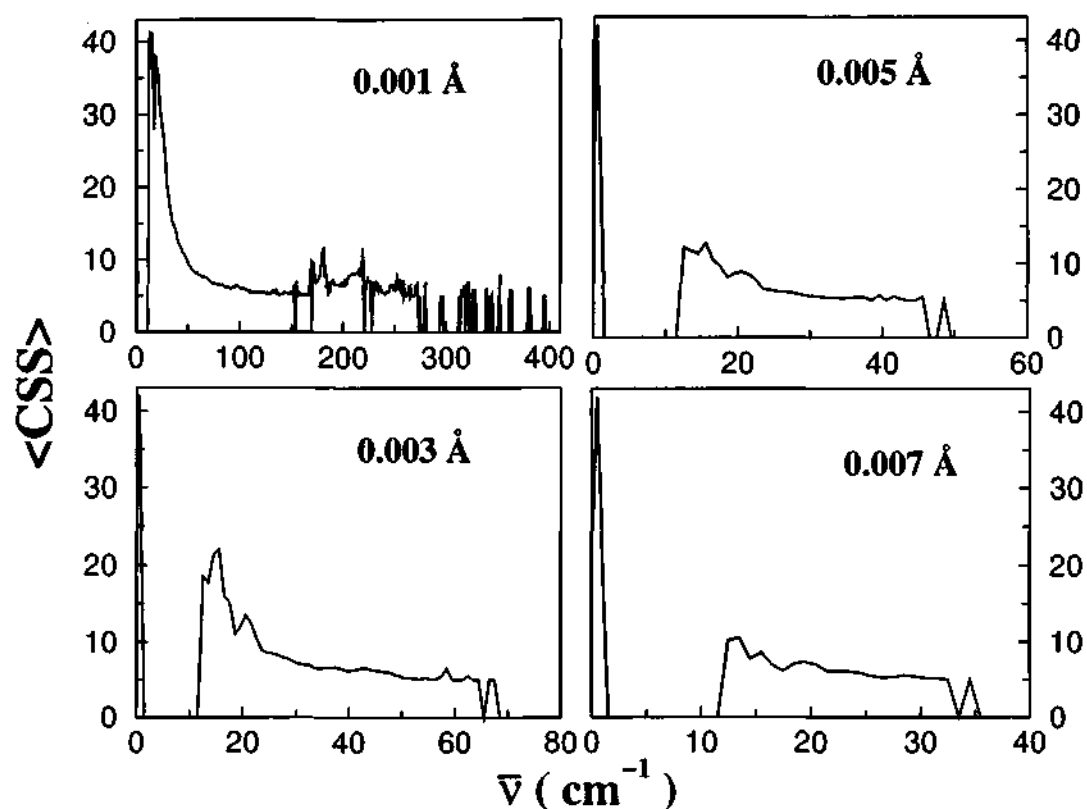


Figure 3.9: Variation of the average continuous segment size ( $\langle \text{CSS} \rangle$ ) with respect to the vibrational frequencies for different displacement cutoffs.

are larger than a specified cutoff, with  $n \geq 5$ . Values with  $n < 5$ , which correspond to intramolecular excitations that arise out of bonded interactions like the stretch, bend and torsion, have been omitted in  $\langle CSS \rangle$  calculations, as their origin is trivially known. It should also be noted that the exact values of the average segment size will depend on the chosen displacement cutoff. Hence, we have performed these calculations for a variety of cutoffs and these are exhibited in Figure 3.9 as a function of the frequency of the modes. Notice that the segment size for the zero frequency modes, *i.e.*, translations, is 42, which is the number of backbone atoms in a given chain. It is also evident from the figure that the average segment size decays with increase in frequency.

Figure 3.9 also shows the variation of  $\langle CSS \rangle$  as a function of frequency, for four different displacement cutoffs. The displacement cutoff which spans the frequency range relevant to collective motion, where the local character value is almost zero is the one of significance. It can be seen that in the frequency range of  $10 \text{ cm}^{-1}$  and  $100 \text{ cm}^{-1}$ , which is the range of collective motion, around 8 to 12 successive atoms of the backbone are involved in the excitations.

### 3.4 Conclusions

We have studied the vibrational dynamics of crystalline poly(ethylene oxide) using molecular dynamics and normal mode analysis. A code to perform NMA for bulk systems interacting via generic macromolecular potential has been developed. The vibrational density of states obtained from NMA matches well with that obtained from the Fourier transformation of velocity autocorrelation function and also with experimental IR and Raman data [42–44]. The VDOS of an isolated PEO chain of finite length showed marked differences from that of the crystal in the low frequency region where collective modes are predominant. We have also explored system size effects by comparing the VDOS obtained from a simulation containing 16 unit cells and that of one unit cell. The spectrum obtained from the former is much better resolved, particularly at low frequencies, where

three clear features, at  $44 \text{ cm}^{-1}$ ,  $70 \text{ cm}^{-1}$ , and  $88 \text{ cm}^{-1}$  are observed. The results of our calculations agree well with assignments of mode symmetry by earlier workers, that used standard methods for a single chain of PEO, or for an unit cell [42, 45, 46]. Such calculations have the added advantage, over the MD route presented here, of being able to obtain dispersion of the vibrational modes. However, the method described here can be used to characterize these vibrations in the amorphous and liquid phases of PEO.

The normal modes obtained from the present analysis were characterized by the local character indicator and by a new quantity that determines the number of concomitant atoms excited by a mode, called the CSS. In the range 0 to  $160 \text{ cm}^{-1}$ , the value of the local character indicator was very small, indicating the participation of a large number of atoms in the vibrational modes in this range. A distribution of segment sizes was calculated for each mode from which the average continuous segment size was calculated as a function of the vibrational frequency. The frequency dependence of  $\langle \text{CSS} \rangle$  clearly shows collective modes to be present for frequencies less than  $100 \text{ cm}^{-1}$ , in which around 8 to 12 successive atoms of the backbone participate. This quantitative analysis is also corroborated by visualization of the atomic displacements for the low frequency modes.

### 3.5 Appendix 1

The form of the potential used in our simulations is generic to macromolecular interactions, and can be found in Ref. [14]. Here, we provide only the torsional and Coulomb terms.

$$U_{\text{coulomb}} = \frac{q_i q_j}{r_{ij}} \quad (3.11)$$

and

$$U_{\text{torsion}} = f(\cos\phi) = \sum_{i=0}^6 a_i \cos^i \phi \quad (3.12)$$

We provide here a procedure to obtain the Hessian elements, which is easy to program. We limit these details to contributions from the torsional interactions, the reciprocal space

part and the real space part of the Ewald sum. Contributions from other terms in the potential energy are much simpler to derive and are not given here.

### 3.5.1 Hessian from the torsional interaction

The torsional angle  $\phi$  between the planes formed by the bond vectors  $\vec{r}_{12}$ ,  $\vec{r}_{23}$ , and  $\vec{r}_{34}$  is,

$$\cos\phi = \hat{A} \cdot \hat{B} = A_\gamma B_\gamma \quad (3.13)$$

where the Einstein summation convention has been used and

$$\hat{A} = \frac{\vec{r}_{12} \times \vec{r}_{23}}{|\vec{r}_{12} \times \vec{r}_{23}|}, \quad \text{and} \quad \hat{B} = \frac{\vec{r}_{23} \times \vec{r}_{34}}{|\vec{r}_{23} \times \vec{r}_{34}|} \quad (3.14)$$

The second derivative of  $U_{torsion}$  with respect to a spatial coordinate  $\alpha_n$ , where  $\alpha$  can be either x, y, or z and  $n=1, 2, \dots, N$ , can be written as,

$$\frac{\partial^2 U_{torsion}}{\partial \beta_m \partial \alpha_n} = \left( \frac{\partial f}{\partial \cos\phi} \right) \left( \frac{\partial^2 \cos\phi}{\partial \beta_m \partial \alpha_n} \right) + \left( \frac{\partial \cos\phi}{\partial \alpha_n} \right) \left( \frac{\partial \cos\phi}{\partial \beta_m} \right) \left( \frac{\partial^2 f}{\partial \cos\phi^2} \right) \quad (3.15)$$

The derivatives of  $\cos\phi$  can be calculated as follows.

$$\frac{\partial^2 \cos\phi}{\partial \beta_m \partial \alpha_n} = A_\gamma \frac{\partial^2 B_\gamma}{\partial \beta_m \partial \alpha_n} + \frac{\partial B_\gamma}{\partial \alpha_n} \frac{\partial A_\gamma}{\partial \beta_m} + B_\gamma \frac{\partial^2 A_\gamma}{\partial \beta_m \partial \alpha_n} + \frac{\partial A_\gamma}{\partial \alpha_n} \frac{\partial B_\gamma}{\partial \beta_m} \quad (3.16)$$

We can write  $A_\gamma$  as

$$A_\gamma = \frac{N_\gamma^A}{D_A} \quad (3.17)$$

with

$$N_\gamma^A = \epsilon_{\gamma\nu\xi} (\vec{r}_{12})_\nu (\vec{r}_{23})_\xi \quad (3.18)$$

and

$$D_A = \left[ \sum_l (N_l^A)^2 \right]^{\frac{1}{2}} \quad (3.19)$$

where  $\gamma, \nu$ , and  $\xi$  stand for any of the three indices  $x, y, z$  and  $\epsilon_{\gamma\nu\xi}$  is the antisymmetric Levi-Civita tensor of rank 3. A similar expression can be written for  $B_\gamma$ .

The first derivative of  $A_\gamma$  are,

$$\frac{\partial A_\gamma}{\partial \alpha_n} = \frac{1}{D_A} \frac{\partial N_\gamma^A}{\partial \alpha_n} - \frac{N_\gamma^A}{D_A^3} \sum_l N_l \frac{\partial N_l^A}{\partial \alpha_n} \quad (3.20)$$

where,

$$\frac{\partial N_\gamma^A}{\partial \alpha_n} = \sum_{\nu=x,y,z} \epsilon_{\gamma\nu\alpha} [(\vec{r}_{12})_\nu (\delta_{n3} - \delta_{n2}) - (\vec{r}_{23})_\nu (\delta_{n2} - \delta_{n1})] \quad (3.21)$$

The second derivative of  $A_\gamma$  is calculated as follows.

$$\frac{\partial}{\partial \beta_m} \frac{\partial A_\gamma}{\partial \alpha_n} = \frac{\partial \left[ \frac{1}{D_A} \frac{\partial N_\gamma^A}{\partial \alpha_n} \right]}{\partial \beta_m} - \frac{\partial \left[ \frac{N_\gamma^A}{D_A^3} \sum_l N_l \frac{\partial N_l^A}{\partial \alpha_n} \right]}{\partial \beta_m} \quad (3.22)$$

with

$$\frac{\partial \left[ \frac{1}{D_A} \frac{\partial N_\gamma^A}{\partial \alpha_n} \right]}{\partial \beta_m} = \frac{1}{D_A} \frac{\partial}{\partial \beta_m} \frac{\partial N_\gamma^A}{\partial \alpha_n} - \frac{1}{D_A^2} \frac{\partial N_\gamma^A}{\partial \alpha_n} \frac{\partial D_A}{\partial \beta_m} \quad (3.23)$$

$$\begin{aligned} \frac{\partial \left[ \frac{N_\gamma^A}{D_A^3} \sum_l N_l \frac{\partial N_l^A}{\partial \alpha_n} \right]}{\partial \beta_m} &= \frac{N_\gamma^A}{D_A^3} \left[ \sum_l \left[ N_l \frac{\partial^2 N_l}{\partial \beta_m \partial \alpha_n} + \left( \frac{\partial N_l}{\partial \alpha_n} \right) \left( \frac{\partial N_l}{\partial \beta_m} \right) \right] \right] \\ &+ \left( \sum_l N_l \frac{\partial N_l}{\partial \alpha_n} \right) \left( \frac{1}{D_A^3} \frac{\partial N_\gamma}{\partial \beta_m} - \frac{3}{D_A^4} N_\gamma \frac{\partial D_A}{\partial \beta_m} \right) \end{aligned} \quad (3.24)$$

where,

$$\frac{\partial}{\partial \beta_m} \frac{\partial N_\gamma^A}{\partial \alpha_n} = \epsilon_{\gamma\beta\alpha} [(\delta_{m2} - \delta_{m1}) (\delta_{n3} - \delta_{n2}) - (\delta_{m3} - \delta_{m2}) (\delta_{n2} - \delta_{n1})] \quad (3.25)$$

Using equations (3.16), (3.20), and (3.22) we can calculate  $\frac{\partial^2 \cos \phi}{\partial \beta_m \partial \alpha_n}$  which can be substituted in equation (3.15) to get the torsional contribution to the Hessian.

### 3.5.2 Hessian from the Coulomb interaction

The reciprocal space energy in the Ewald sum method is,

$$U_{reci} = \frac{1}{V\epsilon_0} \sum_{\vec{k} \neq 0} \frac{e^{-\frac{k^2}{4\zeta^2}}}{k^2} (a_k^2 + b_k^2) \quad (3.26)$$

where,

$$a_k = \sum_{j=1}^N q_j \cos(\vec{k} \cdot \vec{r}_j), \quad \text{and} \quad b_k = \sum_{j=1}^N q_j \sin(\vec{k} \cdot \vec{r}_j) \quad (3.27)$$

Here,  $V$  denotes the volume of the simulation cell,  $\zeta$  determines the width of the Gaussian charge distribution centered on the point charges in the Ewald sum method,  $\vec{k}$  denote the reciprocal lattice vectors, and  $\epsilon_0$ , the permittivity of free space.

It can be shown that

$$\begin{aligned} \frac{\partial^2 U_{reci}}{\partial \beta_m \partial \alpha_n} &= \frac{1}{V\epsilon_0} \sum_{\vec{k} \neq 0} \frac{e^{-\frac{k^2}{4\zeta^2}}}{k^2} \left\{ 2q_n k_\alpha \left[ -k_\beta \delta_{mn} \left( a_k \cos(\vec{k} \cdot \vec{r}_n) + b_k \sin(\vec{k} \cdot \vec{r}_n) \right) \right. \right. \\ &\quad \left. \left. + q_m k_\beta \cos(\vec{k} \cdot (\vec{r}_n - \vec{r}_m)) \right] \right\} \end{aligned} \quad (3.28)$$

The expression for the real space energy in the Ewald summation is,

$$U_{real} = \frac{1}{4\pi\epsilon_0} \sum_{i=1}^N \sum_{j>i}^N q_i q_j \rho \quad (3.29)$$

where,

$$\rho = \frac{\text{erfc}(\zeta r_{ij})}{r_{ij}} \quad (3.30)$$

The second derivatives of  $U_{real}$  are

$$\frac{\partial}{\partial \beta_m} \left( \frac{\partial U_{real}}{\partial \alpha_n} \right) = \frac{1}{4\pi\epsilon_0} \sum_{i=1}^N \sum_{j>i}^N q_i q_j \frac{\partial}{\partial \beta_m} \left( \frac{\partial \rho}{\partial \alpha_n} \right) \quad (3.31)$$

with

$$\frac{\partial}{\partial \beta_m} \left( \frac{\partial \rho}{\partial \alpha_n} \right) = \left( \frac{\partial \rho}{\partial r_{ij}} \right) \frac{\partial}{\partial \beta_m} \left( \frac{\partial r_{ij}}{\partial \alpha_n} \right) + \left( \frac{\partial r_{ij}}{\partial \alpha_n} \right) \frac{\partial}{\partial \beta_m} \left( \frac{\partial \rho}{\partial r_{ij}} \right) \quad (3.32)$$

$$\frac{\partial}{\partial \beta_m} \left( \frac{\partial r_{ij}}{\partial \alpha_n} \right) = \frac{(\delta_{jn} - \delta_{in})(\delta_{jm} - \delta_{im})}{r_{ij}} \left[ \delta_{\alpha\beta} - \frac{(\alpha_j - \alpha_i)(\beta_j - \beta_i)}{r_{ij}^2} \right] \quad (3.33)$$

It can be shown that

$$\frac{\partial \rho}{\partial r_{ij}} = -(s_1 + s_2) \quad (3.34)$$

and

$$\frac{\partial^2 \rho}{\partial r_{ij}^2} = 2\zeta^2 s_1 r_{ij} + \frac{2(s_1 + s_2)}{r_{ij}} \quad (3.35)$$

with,

$$s_1 = \frac{2\zeta}{\sqrt{\pi}} \frac{e^{-\zeta^2 r_{ij}^2}}{r_{ij}} \quad \text{and} \quad s_2 = \frac{\text{erfc}(\zeta r_{ij})}{r_{ij}^2} \quad (3.36)$$

These can be used in Eq. 3.31 to obtain the Hessian elements.



# Bibliography

- [1] J.W. Halley, and Y. Duan, *J. Power Sources* **89**, 139 (2000).
- [2] M. Wakihara, *Mat. Sci. Engg.* **R33**, 109 (2001).
- [3] P.G. Bruce, *Solid State Electrochemistry*, Cambridge University Press, Cambridge, 1995.
- [4] P.G. Bruce, and C.A. Vincent, *J. Chem. Soc. Faraday Trans.* **89**, 3187 (1993).
- [5] X.G. Sun, W. Xu, S.S. Zhang, and C.A. Angell, *J. Phys. Cond. Matt.* **13**, 8235 (2001).
- [6] J.P. Donoso, T.J. Bonagamba, H.C. Panepucci, L.N. Oliveira, W. Gorecki, C. Berthier and M. Armand, *J. Chem. Phys.* **98**, 10026 (1993).
- [7] I.M. Ward, N. Boden, J. Cruickshank, and S.A. Leng, *Electrochim. Acta.* **40**, 2071 (1995).
- [8] G. Mao, R.F. Perea, W.S. Howells, D.L. Price, and M.-L. Saboungi, *Nature* (London) **405**, 163 (2000); M.-L. Saboungi, D.L. Price, G. Mao, R.F. Perea, O. Borodin, and G.D. Smith, M. Armand, and W.S. Howells, *Solid State Ionics* **147**, 225 (2002);
- [9] C.A. Angell, *Solid State Ionics* **9-10**, 3 (1983).
- [10] C. Berthier, W. Gorecki, M. Minier, M.B. Armand, J.M. Chanbagno, and P. Rigaud, *Solid State Ionics* **11**, 91 (1983).

- 
- [11] W. Gorecki, P. Donoso, C. Berthier, M. Mali, J. Roos, D. Brinkmann, M.B. Armand, *Solid State Ionics* **28-30**, 1018 (1988).
- [12] Z. Gadjourova, Y.G. Andreev, D.P. Tunstall, and P.G. Bruce, *Nature* **412**, 520 (2001)
- [13] B. Mos, P. Verkerk, A. van Zon, and S.W. de Leeuw, *Physica B* **276**, 351 (2000); S.W. de Leeuw, A. Van Zon, and G.J. Bel, *Electrochim. Acta* **46**, 1419 (2001); J.J. de Jonge, A. van Zon, and S.W. de Leeuw, *Solid State Ionics* **147**, 349 (2002).
- [14] S. Neyertz, D. Brown, and J.O. Thomas, *J. Chem. Phys.* **101**, 10064 (1994).
- [15] S. Neyertz, *Ph.D. thesis*, Uppsala University, Uppsala, 1995.
- [16] S. Neyertz, and D. Brown, *J. Chem. Phys.* **102**, 9725 (1995).
- [17] S. Neyertz, D. Brown, and J.O. Thomas, *Electrochim. Acta* **40**, 2063 (1995).
- [18] S. Neyertz, D. Brown, and J.O. Thomas, *Comput. Polym. Sci.* **5**, 107 (1995).
- [19] F. Muller-Plathe, and W.F. van Gunsteren, *J. Chem. Phys.* **103**, 4745 (1995).
- [20] K. Laasonen, and M.L. Klein, *J. Chem. Soc. Faraday Trans.* **91**, 2633 (1995).
- [21] J.W. Halley, Y. Duan, B. Nielsen, P.C. Redfern, and L.A. Curtiss, *J. Chem. Phys.* **115**, 3957 (2001); B. Lin, P.T. Boinske, and J.W. Halley, *J. Chem. Phys.* **105**, 1668 (1996).
- [22] P. Ahlström, G. Wahnström, P. Carlsson, O. Borodin, and G.D. Smith, *J. Chem. Phys.* **112**, 10669 (2000).
- [23] O. Borodin, and G.D. Smith, *Macromolecules* **31**, 8396 (1998); *Macromolecules* **33**, 2273 (2000);
- [24] O. Borodin, F. Trouw, D. Bedrov, and G.D. Smith, *J. Phys. Chem. B* **106**, 5184 (2002); O. Borodin, D. Bedrov, and G.D. Smith, *J. Phys. Chem. B* **106**, 5194 (2002); G.D. Smith, D. Bedrov, and O. Borodin, *Phys. Rev. Lett.* **85**, 5583 (2000).

- [25] G.D. Smith, O. Borodin, M. Pekny, B. Annis, D. Londono, and R.L. Jaffe, *Spectrochim. Acta A* **53**, 1273 (1997).
- [26] G. Carini, G. D'Angelo, G. Tripodo, A. Bartolotta, and G. Di Marco *Phys. Rev. B* **54**, 15056-15063 (1996).
- [27] P. Mustarelli, C. Capiglia, E. Quartarone, C. Tomasi, P. Ferloni, and L. Linati, *Phys. Rev. B* **60**, 7228 (1999).
- [28] S.I. Simdyankin, M. Dzugutov, S.N. Taraskin, and S.R. Elliott, *Phys. Rev. B* **63**, 184301 (2001); S.N. Taraskin, and S.R. Elliott, *Phys. Rev. B* **61**, 12017 (2000); S.N. Taraskin, and S.R. Elliott, *Phys. Rev. B* **59**, 8572 (1999).
- [29] C.S. O'Hern, S.A. Langer, A.J. Liu, and S.R. Nagel, *Phys. Rev. Lett.* **86**, 111 (2001).
- [30] K. Fukui, B.G. Sumpter, D.W. Noid, C. Yang, and R.E. Tuzun, *J. Phys. Chem. B* **104**, 526 (2000); D.W. Noid, K. Fukui, B.G. Sumpter, C. Yang, and R.E. Tuzun, *Chem. Phys. Lett.* **316**, 285 (2000).
- [31] H.W.T. van Vlijmen and M. Karplus, *J. Phys. Chem. B* **103**, 3009 (1999).
- [32] N.P. Barton, C.S. Verma, L.S.D. Caves, *J. Phys. Chem. B* **107**, 2170 (2003); *J. Phys. Chem. B* **106**, 11036 (2002).
- [33] Y. Takahashi and H. Tadokoro, *Macromolecules* **6**, 672 (1973).
- [34] G.J. Martyna, M.L. Klein, and M. Tuckerman, *J. Chem. Phys.* **97**, 2635 (1992).
- [35] M.E. Tuckerman, D.A. Yarne, S.O. Samuelson, A.L. Hughes, and G. Martyna, *Comput. Phys. Commun.* **128**, 333 (2000).
- [36] J.-P. Hansen, in *Molecular Dynamics Simulations of Statistical Mechanics Systems*, Ed. G. Ciccotti, and W.G. Hoover, (North-Holland, Amsterdam, 1986).
- [37] A.D. MacKerell Jr. *et al*, *J. Phys. Chem. B* **102**, 3586 (1998).

- 
- [38] H. Goldstein, *Classical Mechanics* (Addison-Wesley/Narosa, India, 1985).
- [39] M. Abramowitz, and I.A. Stegun, *Handbook of Mathematical Functions*, (Dover, New York, 1970).
- [40] S.N. Taraskin, and S.R. Elliott, *Phys. Rev. B* **56**, 8605 (1997).
- [41] M. Parrinello, and A. Rahman, *Phys. Rev. Lett.* **45**, 1196 (1980).
- [42] J.F. Rabolt, K.W. Johnson, and R.N. Zitter, *J. Chem. Phys.* **61**, 504, (1974).
- [43] V.M. Da Costa, T.G. Fiske, and L.B. Coleman, *J. Chem. Phys.* **101**, 2746, (1994).
- [44] C. Branca, A. Faraone, S. Magazu, G. Maisano, P. Migliardo, and V. Villari, *J. Mol. Liquids* **87**, 21 (2000).
- [45] T. Yoshihara, H. Tadokoro, S. Murahashi, *J. Chem. Phys.* **41**, 2902 (1964).
- [46] K. Song, and S. Krimm, *J. Polym. Sci. Polym. Phys. Ed.* **28**, 35, (1990).
- [47] D.A. Case, *Curr. Opin. Struct. Biol.* **4**, 285 (1994).

## Chapter 4

# *n*-Heptane Under Pressure: Structure and Dynamics from Molecular Simulations

### 4.1 Introduction

A common element of several complex molecular systems is the alkyl group [1]. It forms a crucial component of a wide variety of systems ranging from membranes, micelles, self assembled monolayers [2], and even organic molten salts [3]. Thus a study of the phase diagram of linear and branched alkanes continues to be interesting, and relevant to the understanding of complex phenomena. Alkanes are also important in their own right; the long chain ones are active components of lubricants, and short chain alkanes such as *n*-heptane are employed as solvents. Mixtures of liquid *n*-heptane with isooctane are also used as standards to characterize the anti-knocking properties of engine fuel [4]. Crystalline linear alkanes also exhibit interesting rotator phases that have been studied well through neutron scattering experiments [5] and computer simulations [6]. The structure and dynamics of crystalline *n*-alkanes has been the subject of renewed interest lately [7–9].

In a recent study of the vibrational spectra of *n*-heptane under high pressure, Chronister and coworkers reported the occurrence of a possible solid-solid phase transition near 30 kbar [10]. The experiments, performed at room temperature, also investigated the liquid-solid transition that takes place at around 12-15 kbar. The presence of a large number of *gauche* defects in the liquid state produces large broadening of the infrared peaks, in contrast to sharp bands in the crystal. However, the nature of the solid-solid transition was not clear from this study. Near 30 kbar, in the solid state, they observed (i) a split in the asymmetric CH<sub>3</sub> and CH<sub>2</sub> bending modes in the 1400-1500 cm<sup>-1</sup> region, and (ii) a change in the slope of the linewidth as a function of pressure for the C-C stretching modes and the antisymmetric CH<sub>3</sub> mode. Specifically, the underlying structural changes (if any) that cause these splitting of the peaks and changes in their linewidths are yet to be studied. In view of this, we have undertaken a comprehensive investigation of *n*-heptane under pressure, using computer simulation methods. We report molecular dynamics (MD) calculations of *n*-heptane performed at a temperature 300K, and at pressures ranging from 1 kbar to 70 kbar. Our goals are (i) to find out whether these transitions can be observed in computer models and (ii) to study the structural and dynamical behavior of the system as a function of pressure.

## 4.2 Simulation Details

*n*-heptane crystallizes in a triclinic cell (Space Group: P $\bar{1}$ ) with the following lattice parameters [11]:  $a=4.15\text{\AA}$ ,  $b=19.97\text{\AA}$ ,  $c=4.69\text{\AA}$ ,  $\alpha=91.3^\circ$ ,  $\beta=74.3^\circ$ , and  $\gamma=85.1^\circ$ . The crystal density is 0.890 gm/cm<sup>3</sup>. The unit cell consists of two molecules that adopt the *all-trans* conformation. The chain axis of each molecule makes an angle of 2° with the *ab* plane and 71° with the *a*-axis. This experimental crystal structure was generated and used as the initial configuration for our molecular dynamics calculations. The simulation box consisted of a total of 128 such unit cells: 8 unit cells each along  $\vec{a}$  and  $\vec{c}$  axes and 2 along the  $\vec{b}$ -axis. We have used an all-atom representation for the description of *n*-heptane [13].

This model has previously been used to characterize the phase behavior of *n*-octane in bulk [14] and the organization of *n*-hexane on graphite [15]. Although such a model increases the computational cost, it is inevitable in studies of molecular crystals, particularly at high pressures, where steric effects are expected to play a significant role [12]. Thus, the simulated crystal consisted of 256 molecules with a total of 5888 atoms. The interaction potential contained bond stretch, bending, torsional and non-bonded interactions of the Williams type. Its form and the parameters are the same as reported in Ref. [13]. In order to closely mimic the high pressure experiments [10], we have carried out the simulations in the constant temperature and constant pressure (NPT) ensemble. Pressure control was achieved through the Parrinello-Rahman algorithm [16, 17] that allows the simulation cell to vary both its shape and size. A Nosé-Hoover chain thermostat [18] attached to the system controlled the temperature. Both the thermostat and the barostat time constants were set at 1 ps. The molecular model was considered to be fully flexible and interaction potentials for the bond stretches, bends and torsional angles were applied. The equations of motion were integrated using the reversible reference system propagator algorithm (RESPA) [19] with an outer time step of 4 fs. The innermost time step that handled the C-H vibrations was 0.5 fs. Long range interactions were thus integrated with the full time step of 4 fs, while short range forces were integrated with a time step of 2 fs. The torsional interactions were integrated at a time step of 1 fs, and bond bending and stretching interactions were handled at a time resolution of 0.5 fs. The potential of interaction was cut off at 12Å, and long range corrections to energy, and pressure were calculated using standard methods [20]. The calculations were carried out using the molecular dynamics package, PINY\_MD on a parallel computer [21].

The initial configuration for the MD runs was based on the experimental structure at 100K. In order to check the veracity of the empirical interaction potentials used in this study, we first performed molecular dynamics simulations in the canonical ensemble at a temperature of 100 K and a pressure of 1 bar. The system was equilibrated for

450 ps, followed by a production run of 400 ps during which the lattice parameters of the simulated crystal were monitored as a function of time. We found the system to be stable with average lattice parameters as follows:  $a=4.15\text{\AA}$ ,  $b=20.01\text{\AA}$ ,  $c=4.51\text{\AA}$ ,  $\alpha=91.2^\circ$ ,  $\beta=76.25^\circ$ , and  $\gamma=86.56^\circ$ , in good agreement with x-ray diffraction data. The maximum difference in the cell parameters between simulations and experiment is 4%, and the density is predicted to within 2%. The equilibrated system obtained from the above run was used as a starting configuration for the constant pressure simulations. Note that the spectroscopy studies of Chronister et al. on *n*-heptane were performed at 300K, where *n*-heptane is in the liquid phase at atmospheric pressure. Upon a gradual increase in pressure, they report two transitions: the liquid-solid transition at around 14 kbar and a solid-solid transition near 30 kbar. The simulation pathway follows a different protocol than that of the experiment; one cannot start the simulation from a liquid state at 1 bar pressure (at 300K) and increase the pressure, as the process of crystallization is time consuming, beyond the limits of atomistic computer simulations. On the other hand, a direct heating of the crystal that was equilibrated at 100K and 1 bar, to 300K would melt it or at least induce considerable disorder, and an ordered lattice that is expected at higher pressures will be impossible to attain. In order to overcome this limitation in the computational procedure, we have employed a procedure that is different from the experiment. We stabilized the solid phase at 300K and 10 kbar by tracing a path in the phase diagram of *n*-heptane, that starts with the crystal at 100K and 1 bar. A stepwise heating followed by gradual application of pressure was then carried out as shown in Figure 4.1. Specifically, we heated the crystal in steps of 50K starting from 100K up to 300K. At each temperature, the system was equilibrated for 400 ps, followed by an increase in pressure of 5 kbar with a corresponding equilibration run of duration, 300 ps. We followed this procedure up to 300K and 10 kbar, where we found the solid phase to be stable. Maintaining the temperature at 300K, we could study both the the reported solid-solid transition by increasing the pressure, or the liquid-solid transition by decreasing the



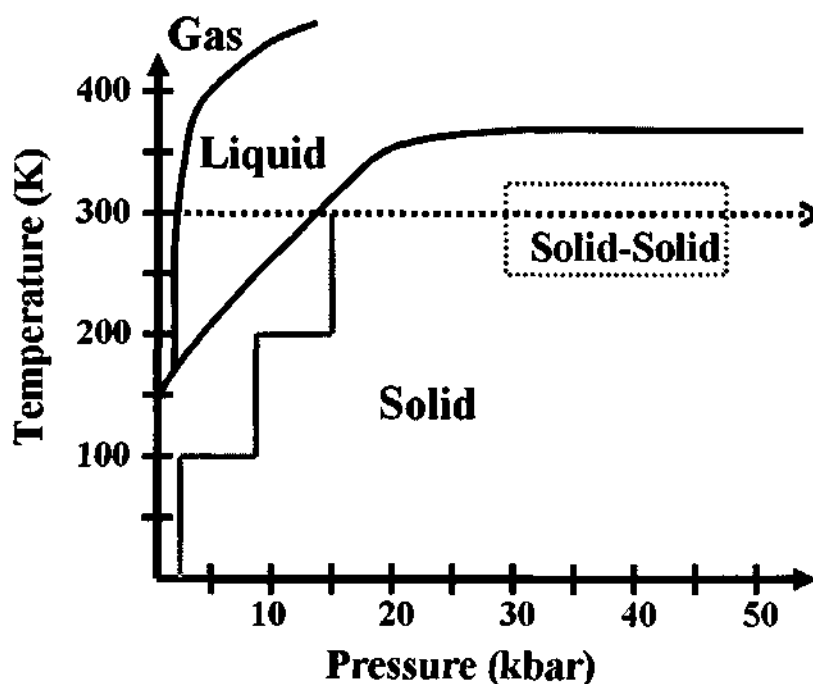


Figure 4.1: Schematic phase diagram of n-heptane. The dashed line represents the experimental path while the solid grey line denotes the simulation path.

applied pressure. At 300K, the system was studied at pressures ranging from 10 kbar to 70 kbar in steps of 2.5 kbar. At each pressure, MD runs were performed for 100 ps. Additional runs of 2 ns duration were carried out at selected 9 pressures for analyses.

The vibrational density of states (VDOS) was calculated by two methods. A normal mode analysis by analyzing the eigenvalue spectrum of the Hessian matrix yielded the VDOS within the harmonic approximation. The exact, classical VDOS was also computed as the power spectrum of the velocity autocorrelation function of the atoms. For the latter, 20 ps long trajectories in which atomic velocities were stored every time step, were generated at each pressure. The power spectrum was obtained as an average from five such independent trajectories that were each separated by 20 ps. The spectra were convoluted with a Gaussian function of spread  $4 \text{ cm}^{-1}$  so as to mimic a lineshape.

## 4.3 Results and Discussion

In the following discussion, results at high pressures are compared to those obtained from the crystal at 10 kbar and 300K.

### 4.3.1 Crystal structure, Volume, and Energetics

*n*-heptane crystallizes in a triclinic unit cell with  $Z=2$  [11]. Figure 4.2 shows the molecular arrangement in the crystal. The molecules are arranged in layers. Within each layer, a given molecule is surrounded by 6 neighbors. Application of pressure in the crystalline phase leads to interesting and subtle changes in the environment of the terminal methyl groups. We have examined the variation of cell lengths as a function of pressure. These were averaged over configurations obtained from the molecular trajectory of duration 400 ps. Their monotonic decrease (Figure 4.3a) with increasing pressure suggests the absence of a first order phase transition in the solid phase. The relative changes in the cell lengths with respect to the values at 10 kbar (Figure 4.3a) reveals a greater effect on the *a* and *c*-axes compared to the *b*-axis. Note that the molecular axis is nearly oriented

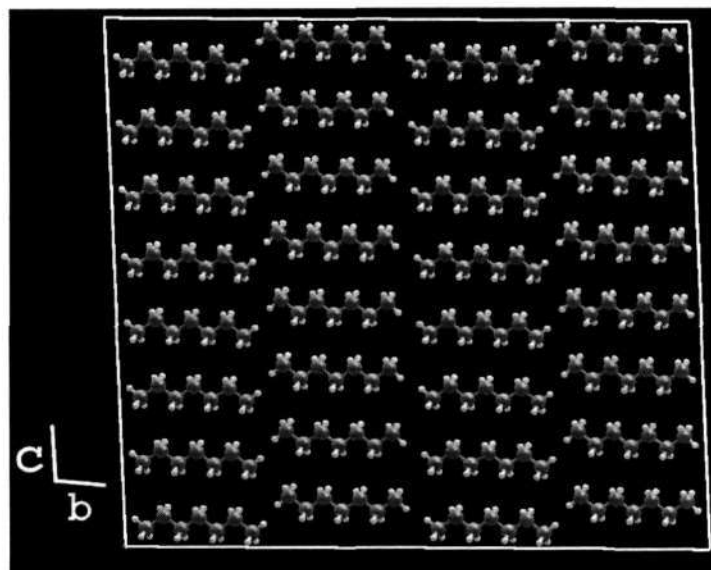


Figure 4.2: The crystal structure of *n*-heptane as used in our simulations is shown as a view through the  $\vec{a}$  axis. The grey spheres represent carbon atoms and the white spheres denote hydrogen atoms.

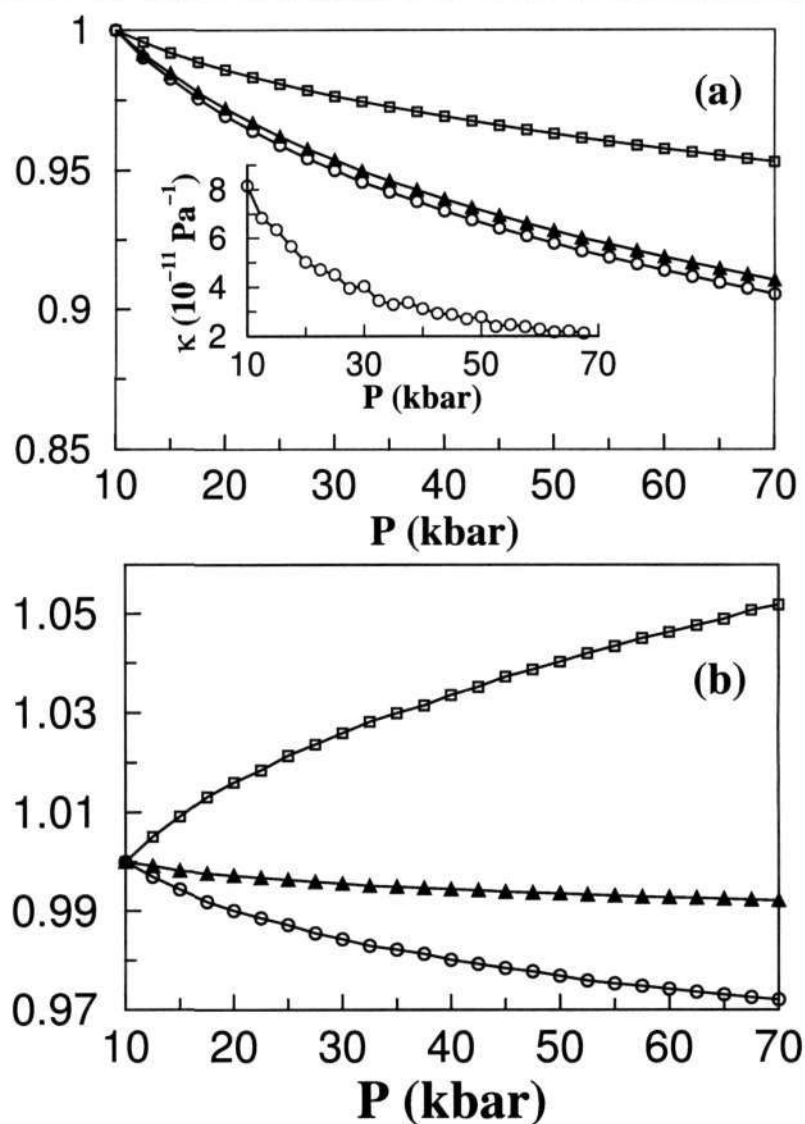


Figure 4.3: Pressure dependence of (a) cell lengths:  $a$  (circles),  $b$  (squares) and  $c$  (triangles) and (b) cell angles:  $\alpha$  (triangles),  $\beta$  (squares) and  $\gamma$  (circles). The values are normalized with respect to their magnitude at 10 kbar. The inset to (a) shows the isothermal compressibility as a function of pressure.

along the  $b$ -axis of the crystal. Thus, the difference in pressure dependence indicates that the molecular packing along the  $b$ -axis is different from that along the  $a$  and  $c$ -axes. The smaller relative change in the  $b$ -parameter with increasing pressure suggests that the crystal is densely packed along  $b$ -axis as compared to the other two directions. As a consequence of this distinction, near neighbor methyl-methyl distances are shorter along the  $b$ -axis than along  $a$  and  $c$ -axes (see discussion on Figure 4.5 later). By examining

P (kbar)	$\rho$ (gm/cm <sup>3</sup> )
10	0.98
20	1.05
30	1.10
40	1.14
50	1.17
60	1.20
70	1.23

Table 4.1: Density  $\rho$ , of *n*-heptane at selected pressures P, from simulation.

the variation of the unit cell volume with pressure, we have calculated the isothermal compressibility which is defined as [22],

$$\kappa = -\frac{1}{V} \left( \frac{dV}{dP} \right)_T \quad (4.1)$$

where V is volume, P is pressure and T denotes temperature. The pressure dependence of isothermal compressibility ( $\kappa$ ) is shown in the inset to Figure 4.3a which too exhibits only a monotonic decay, with no discontinuities. Similarly, an examination of the variation of the cell angles with pressure reveals a larger relative change in the parameter  $\beta$  (see Figure 4.3b) than that in the other two angles, indicating a larger change in intermolecular structure. The variation of the density of *n*-heptane crystal with pressure calculated from this study is given in Table 4.1 for a few selected pressures. The density increases monotonically with pressure. The internal energy of the system increases with pressure without any discontinuities.

### 4.3.2 Structure around terminal group

#### Pair correlation functions :

The changes in the intermolecular structure exhibit a pattern that is consistent with our observations on the cell parameters above. In Figure 4.4, we show the intermolecular pair correlation functions,  $g(r)$ , of CH<sub>3</sub>-CH<sub>3</sub> pairs. *For simplicity, henceforth the carbon atom of the methyl group will be denoted as C3, that of the methylene group as C2, and the*

hydrogens of the methyl groups as  $H3$ . With increase in pressure, two distinct features in the C3-C3  $g(r)$  are discernible. The first peak develops a shoulder at around  $3.3\text{\AA}$ , and the broad hump present near  $5.2\text{\AA}$  at 10 kbar grows into a formal peak. The coordination number, integrated up to the minimum of the first peak ( $5.9\text{\AA}$  at 10 kbar and  $5.45\text{\AA}$  at 70 kbar) is around 10.3, while the corresponding value at the start of the hump ( $4.9\text{\AA}$  at 10 kbar and  $4.55\text{\AA}$  at 70 kbar) is 8. The main peak present at around  $4\text{\AA}$  at 10 kbar shifts to lesser distances with increasing pressure, as expected.

In order to have a better understanding of the near neighbor structure of a methyl carbon, we have subdivided the C3-C3  $g(r)$  into intra- and interlayer contributions.  $g_{intra-layer}(r)$  is the pair correlation function of a central C3 with other methyl carbons which are in the same layer as itself while  $g_{inter-layer}(r)$  is the pair correlation function of C3 with methyl carbons that belong to adjacent layers. We show the behavior of these functions at 10 kbar and 70 kbar in Figure 4.5.

At low pressure (10 kbar), the  $g_{intra-layer}(r)$  function shows a broad peak at  $4.25\text{\AA}$  followed by a shoulder at  $5.15\text{\AA}$ . We observe that four neighbors contribute to the peak at  $4.25\text{\AA}$  while the next two neighbors give rise to the shoulder at  $5.15\text{\AA}$ . At high pressure

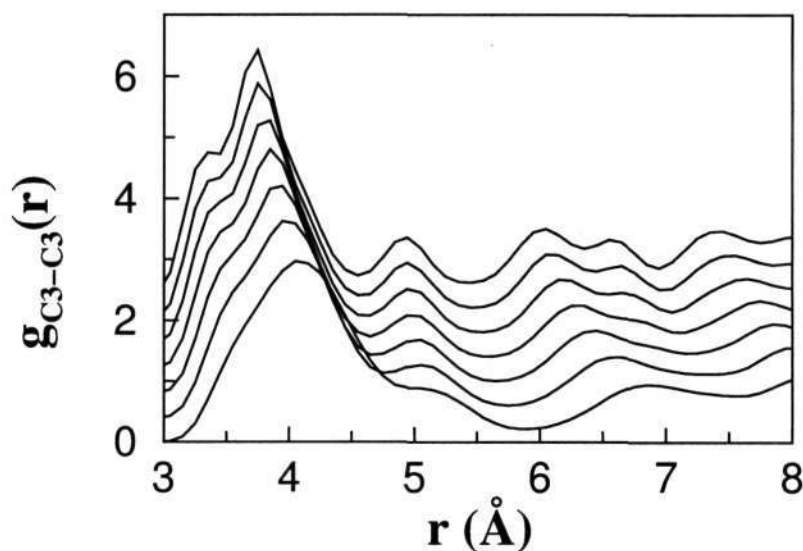


Figure 4.4: The radial distribution function  $g_{c3c3}(r)$ , is shown at various pressures. The functions are shifted for clarity. Pressures (From bottom to top): Starting from 10 kbar up to 70 kbar in steps of 10 kbar.

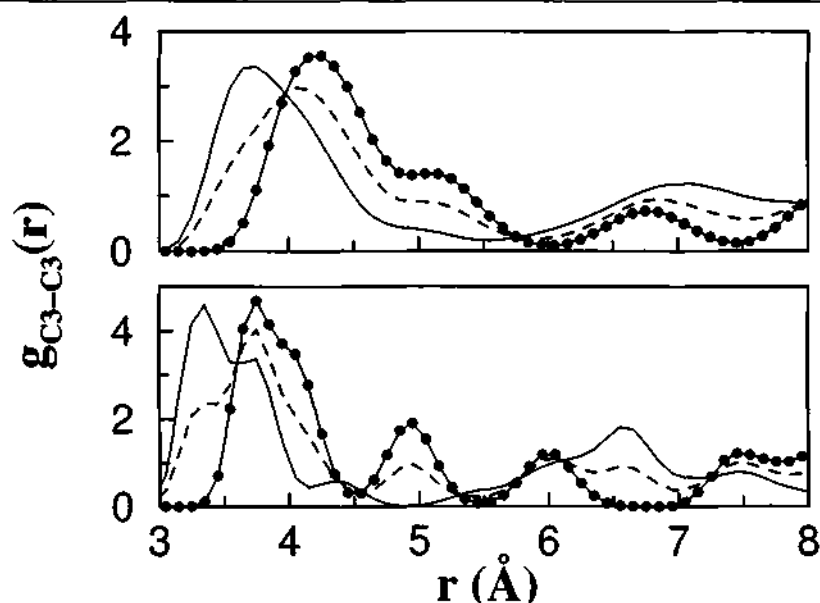


Figure 4.5: C3-C3 radial distribution functions, to show the contribution from intra- and inter-layer neighbors. Solid line:  $g_{inter-layer}(r)$ , Solid line with filled circles:  $g_{intra-layer}(r)$  Dashed line: Full  $g(r)$ ; Top Panel: At 10 kbar, Bottom Panel: At 70 kbar.

(70 kbar), these peak positions shift to lower  $r$  values and the shoulder observed at 10 kbar emerges as a formal peak at 4.95 Å indicating that the second coordination shell acquires a well defined structure at high pressures. The coordination number up to the second shell does not change at high pressures. At 10 kbar, the  $g_{inter-layer}(r)$  function shown in Figure 4.5 exhibits a broad peak at 3.75 Å while its tail stretches up to 5.5 Å. The coordination number calculated up to 5.5 Å is 4. At 70 kbar, we observe the  $g_{inter-layer}(r)$  to show sub-peaks within the range of the first coordination shell (up to 4.9 Å) preserving the coordination number to be 4. The formation of such sub-peaks, keeping the coordination number intact, can be attributed to the structural rearrangement of the inter-layer methyl carbons that lie within the first coordination shell of the central C3 atom. The contribution of the second peak ( $r > 4.9$  Å) of the  $g_{inter-layer}(r)$  to the coordination number of the second peak of the total C3-C3  $g(r)$  (Figure 4.4) is 0.3. The above analysis leads to a clear picture of the environment around a methyl carbon atom at these two pressures and can be summarized as follows. The first sub-shell around the central C3 consists of eight methyl carbons: four are present in the same layer as the central C3 while the

other four are present in the adjacent layers. The second sub-shell, on average consists 2.3 neighbors of which more than 70% contribution comes from molecules in the same layer (intra-layer) and the rest comes from adjacent layers. The arrangement of these neighbors at 10 kbar and 70 kbar are shown in Figure 4.6 as a probability density map. It shows the locations of C3 atoms in the first and second coordination shells, using different color

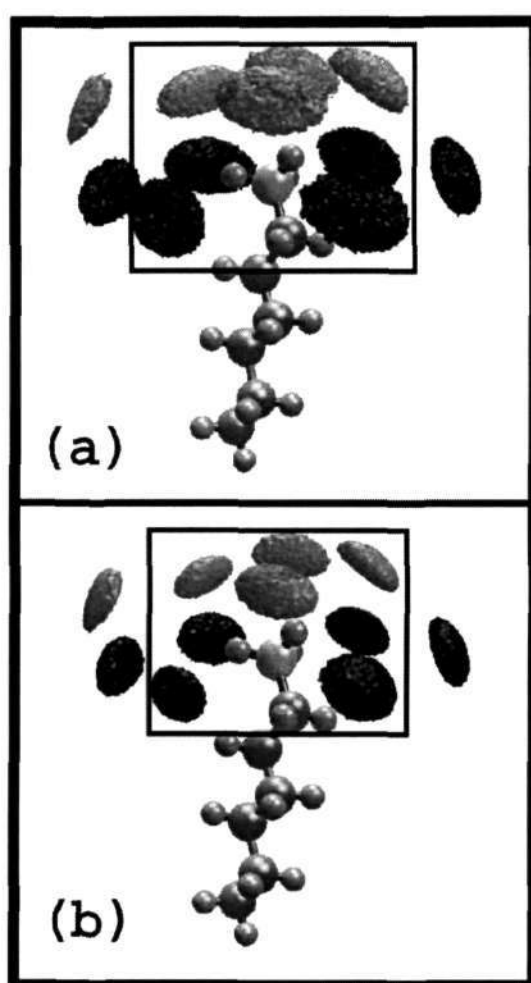


Figure 4.6: The atomic probability density map of a methyl carbon around a given methyl group is shown up to its second coordination shell at (a) 10 kbar (b) 70 kbar. The black lobes denote the probability density of finding neighboring methyl carbons that belong to same layer as the central methyl (grey sphere of the molecule shown), while the grey lobes denote that of adjacent layer methyl carbons. The rectangular box is the boundary around the closest eight neighbors. The probability density values greater than  $0.00008 \text{ methyl carbons}/\text{\AA}^3$  are only shown.

schemes. Note the clear emergence of the eleventh neighbor at 70 kbar at the top left corner. This density is only weakly present at 10 kbar. The pressure dependence of the radial distribution functions suggest that the coordination shell around a C3 unit to be intact in quantity, although subtle differences in the location of the neighbors arise with increasing pressure. In addition, we find that the increase in pressure brings the molecules in the adjacent layer closer to a central methyl group. In Figures 4.7a, 4.7b, and 4.7c, we show the intermolecular pair correlation functions,  $g(r)$ , of C3-C2, C3-H3, and H3-H3 pairs respectively. In contrast to the results on C3-C3  $g(r)$ , the behavior of the C3-C2  $g(r)$  does not show any significant change with pressure. Note the emergence of the hump around  $3.5\text{\AA}$  in the C3-H3 radial distribution function shown in Figure 4.7b. The function at 70 kbar exhibits minima at  $3.35\text{\AA}$ ,  $4.05\text{\AA}$  and at  $5.3\text{\AA}$ . The running coordination numbers at these positions are 8.2, 15.7 and 31.0 respectively. The total coordination number of 31 hydrogens, when considered along with the 10 C3 atoms in the first coordination shell (as discussed in Figure 4.4) makes it tempting to conclude that each neighboring C3 provides the same number of hydrogens (i.e., three) to a central C3 group. However, this is not borne out by even a cursory visualization of a few molecules with their neighbors. The values of the C3-H3  $g(r)$  at these minima are too large. The only explanation consistent with this large magnitude is that each of the neighboring C3 groups contribute unequal number of hydrogen atoms to the features present under the first peak of the C3-H3  $g(r)$ . The H3-H3  $g(r)$  is shown in Figure 4.7c. Here too we see that the first peak is split at high pressures. It is rather difficult to interpret the origin of these peaks as (i) a large number of hydrogens are present, and (ii) the methyl groups rotate. The latter is the reason for the rather large value of  $g(r)$  at the minima.

### Three body correlation functions :

We delve into the environment around C3 by studying the angle distributions. In Figure 4.8a, we show the C3-C3-C3 angle distributions at various pressures. The triplets are



chosen such that the atoms at the two ends of the triangle are within the first coordination shell of the central C3 atom. The distribution exhibits a large peak at an angle of  $180^\circ$ , which arises out of neighbor pairs that are diagonally opposite to each other with respect to the central C3 atom. These pairs are performed in the same layer as the central

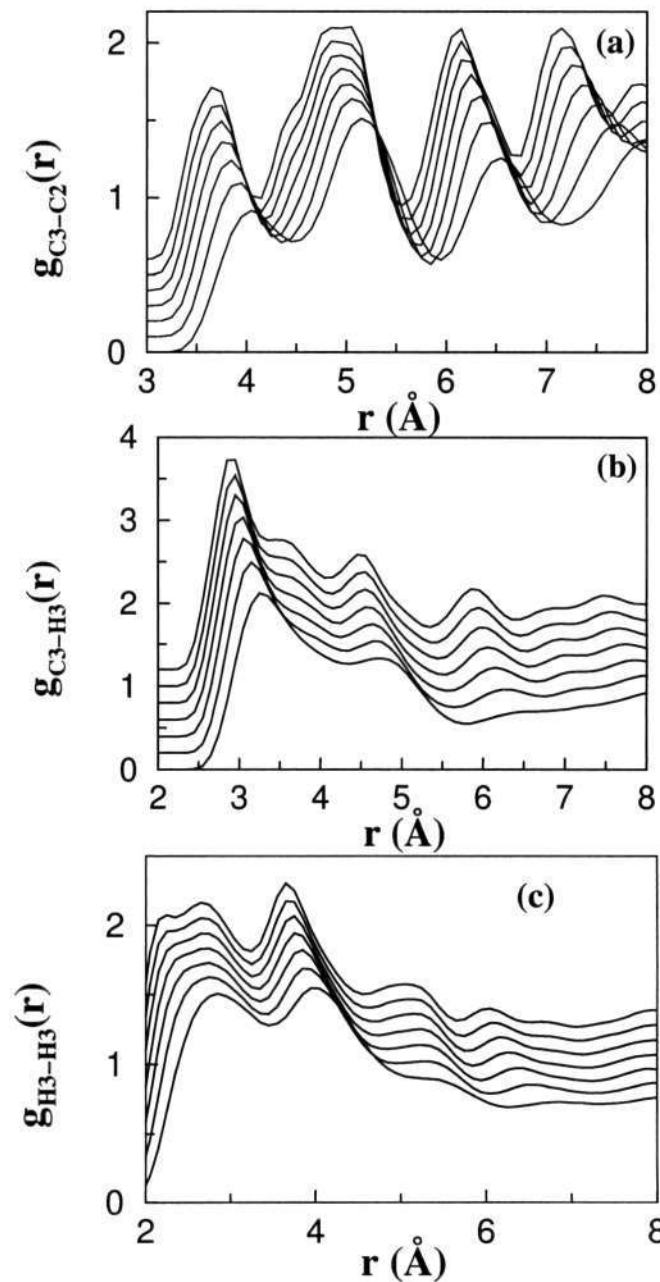


Figure 4.7: Radial distribution function (a)  $g_{c3c2}(r)$ , (b)  $g_{c3h3}(r)$  and (c)  $g_{h3h3}(r)$  shown at various pressures. The functions are shifted for clarity. Pressures (From bottom to top): Starting from 10 kbar up to 70 kbar in steps of 10 kbar.

atom. Systematic variations are observed at specific angles with increasing pressure. In order to identify the source of each of these peaks, we have divided the neighbors into

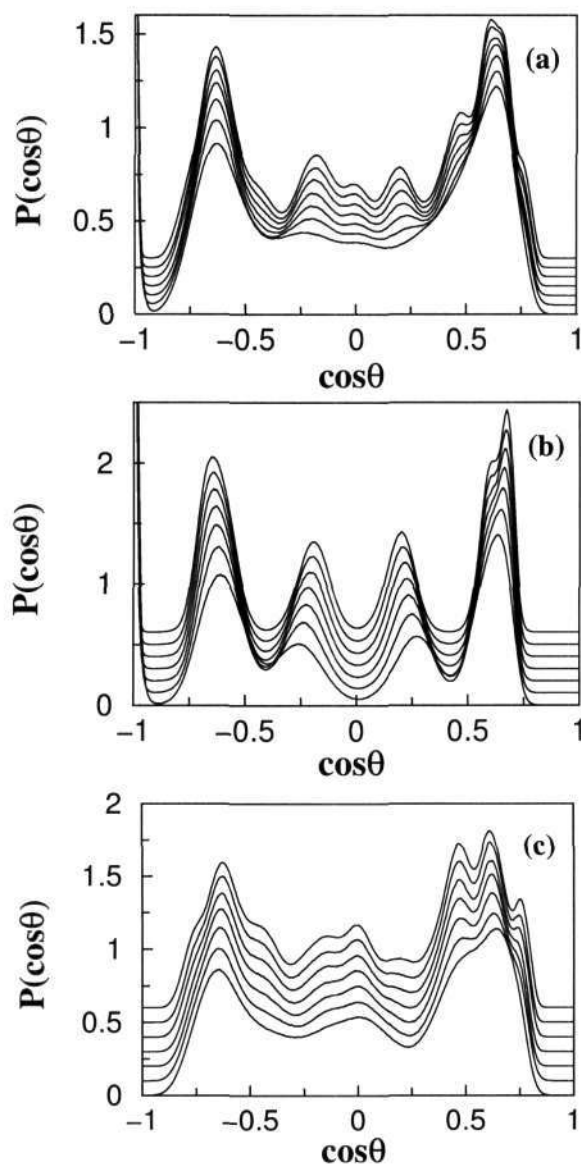


Figure 4.8: (a) The distribution of the cosine of the angle,  $\theta$ , between the vectors that connect the central methyl carbon with any of the neighboring methyl carbons that lie within the second sub-shell of the central methyl group. The functions are shifted for clarity. Pressures (From bottom to top): Starting from 10 kbar up to 70 kbar in steps of 10 kbar. (b) Same as Figure 4.8a, with contributions from intra-layer neighbors only. (c) Same as Figure 4.8a, with contributions from inter-layer neighbors only.

two categories – those belonging to the same layer as the central C3 atom are called *intralayer* and those that are present in the adjacent layer as *interlayer*. The C3-C3-C3 angle distribution was again calculated at 70 kbar for triplets that are in the same layer, and for those in which at least one C3 neighbor belonged to the adjacent layer. These distributions are shown in Figure 4.8b and 4.8c. We notice that the peaks at  $\cos\theta$  values of -0.22 and +0.22 that are present in the full distribution (Figure 4.8a) are present in the intralayer function, but are absent in that for the interlayer. Thus, these features arise from neighbors that are present in the same layer as the central carbon atom. The angles corresponding to these values are around  $102^\circ$  and  $80^\circ$  respectively. These values are consistent with the probability density map of near neighbors discussed in Figure 4.6, and suggest a rhombus like arrangement (upon projection onto a plane perpendicular to the chain axis) of intralayer neighbors, around the central C3 atom. A similar analysis of the functions in Figures 4.8b and 4.8c shows that the peaks at  $\cos\theta$  values of 0, 0.5 and 0.75 come purely from interlayer contributions. We also find that both intralayer and interlayer neighbors contribute to the large peaks at 0.3 and -0.68. The peaks at 0.6 and 0.7 are due to the molecules in the intralayer that are coordinated as the ninth and tenth neighbors to the central C3 group. It is also pertinent to study the location of near neighbor C3 atoms with respect to the C2-C3 bond (i.e., the methylene-methyl bond). In Figure 4.9, we show the angle distribution of C2-C3-C3 triplets at various pressures. All the features that exist at 10 kbar increase in intensity with increasing pressure. However, a new peak emerges at a  $\cos\theta$  value of -0.9 that can be ascribed to interlayer contributions, through a similar analysis as above. Note also the strong peak at a value of -1, that can arise again, only out of interlayer C3 neighbors.

Do these increasing structural correlations observed in the C3-C3 pair correlation function (for instance), arise merely due to an increase in the density of the system? In order to answer this question, we have calculated the pair correlation function of one configuration of atoms that was obtained from the MD simulation at 10 kbar, but whose

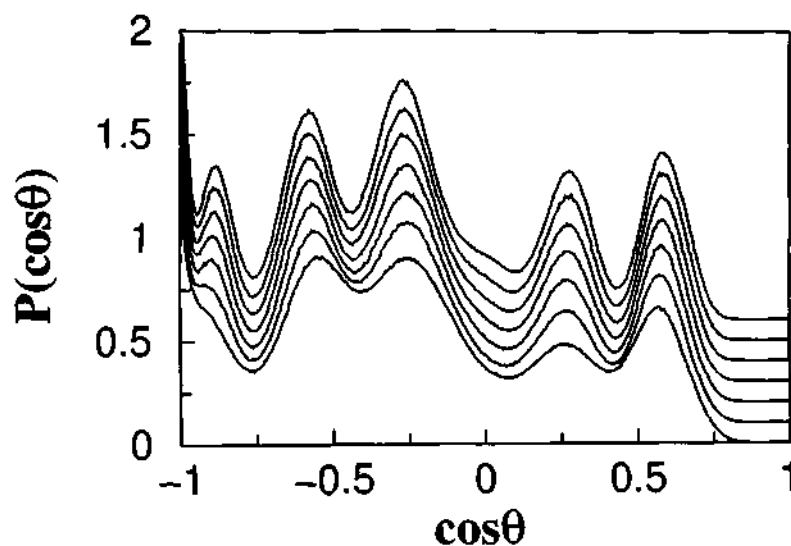


Figure 4.9: The distribution of the cosine of the angle,  $\theta$ , between the terminal C2-C3 vector of the central molecule and the vector that connect the central methyl carbon with any of neighboring methyl carbons that lie within the second sub-shell of the central methyl group. Pressures (From bottom to top): Starting from 10 kbar up to 70 kbar in steps of 10 kbar.

atomic coordinates are scaled with the density of the simulated system at 70 kbar. The calculation proceeded as follows. Scaled atomic coordinates at 10 kbar were obtained as the product of the inverse of the simulation box matrix of 10 kbar and the real world coordinates. These scaled coordinates were brought back into real units, by unscaling them with the box matrix of 70 kbar. This procedure yields atomic coordinates that correspond to the low pressure configuration and the high pressure density. A variant of this method has earlier been used by Bagchi *et al* to analyze the structure of liquid water at high pressure [23]. The “pseudo” or reconstructed  $g(r)$  so obtained is compared against the true function at 70 kbar in Figure 4.10. The agreement between the true  $g(r)$  at 70 kbar and that obtained from this procedure is striking. The shift in the first peak and the emergence of a large hump at  $5\text{\AA}$  is captured quite well by this procedure. However the small shoulder at  $3.35\text{\AA}$  that is present at 70 kbar is absent in this reconstructed  $g(r)$ . However tempting it might be, one should not belittle the effort in obtaining the true pair correlation functions at high pressures such as 70 kbar by actually carrying out the simulations. We draw the attention of the reader to Figure 4.3 (relative cell parameters

versus pressure). It is impossible to predict the exact behavior of the unit cell size and shape with increase in pressure, and thus such reconstructed  $g(r)$ s cannot be obtained in the absence of a simulation. The fact that the  $g(r)$  at 70 kbar can be obtained from the atomic configuration at 10 kbar shows that, at least in our simulations, no solid-solid transition is observed within this pressure range. This is in agreement with the behavior of first order quantities (see Figures 4.3) with pressure.

### 4.3.3 Conformation

The distribution of CCCC torsional angles at various pressures is shown in Figure 4.11. The presence of *gauche* population at 1 kbar and 5 kbar signifies the liquid state, while the chains adopt an all-*trans* conformation in the crystal. The pressure induced changes in the population of *gauche* conformers of *n*-alkanes across the solid-liquid transition has earlier been studied using Raman scattering experiments [24, 25].

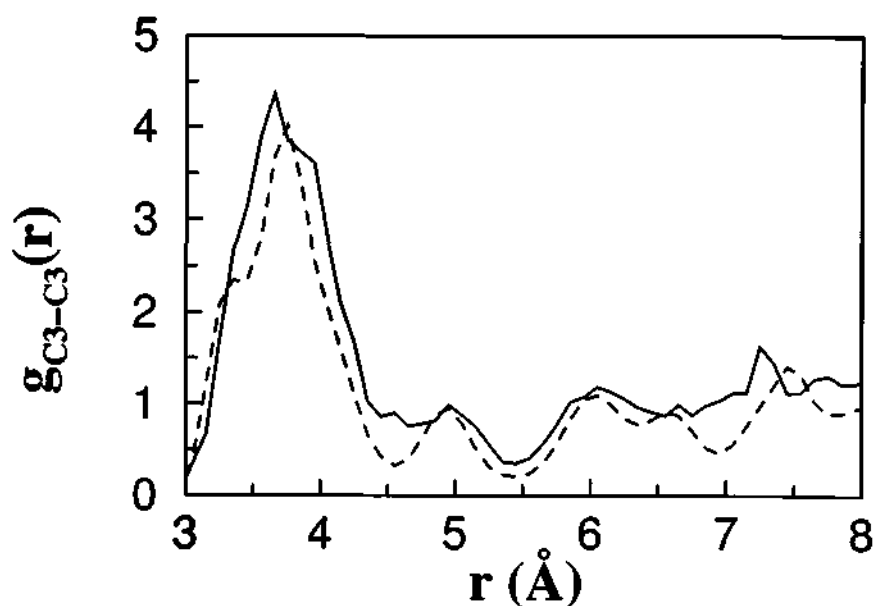


Figure 4.10: A reconstructed radial distribution function,  $g_{c3c3}(r)$  (solid line) (see text for definition) is compared with that obtained from the actual MD trajectory at 70 kbar (dashed line)

### 4.3.4 Dynamics

#### Vibrational Density of States :

The methods to obtain the classical vibrational density of states are two fold: (i) The atomic displacements relative to the equilibrium positions are approximated to be harmonic, and a matrix of the second derivative of the total potential energy of the system with respect to these displacements, i.e., a Hessian is constructed. The eigenvalue spectrum of this matrix is the vibrational density of states within the harmonic approximation, and the corresponding eigenvectors are related to atomic displacements excited in a mode of that frequency. (ii) The VDOS can also be calculated as the power spectrum (cosine transform) of the velocity autocorrelation function (VACF) of the atoms in the system. Unlike the Hessian method which does not need any dynamical trajectory to be generated, this method needs a MD trajectory. However it includes anharmonic contributions as well. We have carried out both these calculations for *n*-heptane under pressure. The VDOS at 10 kbar obtained from these methods are compared against the

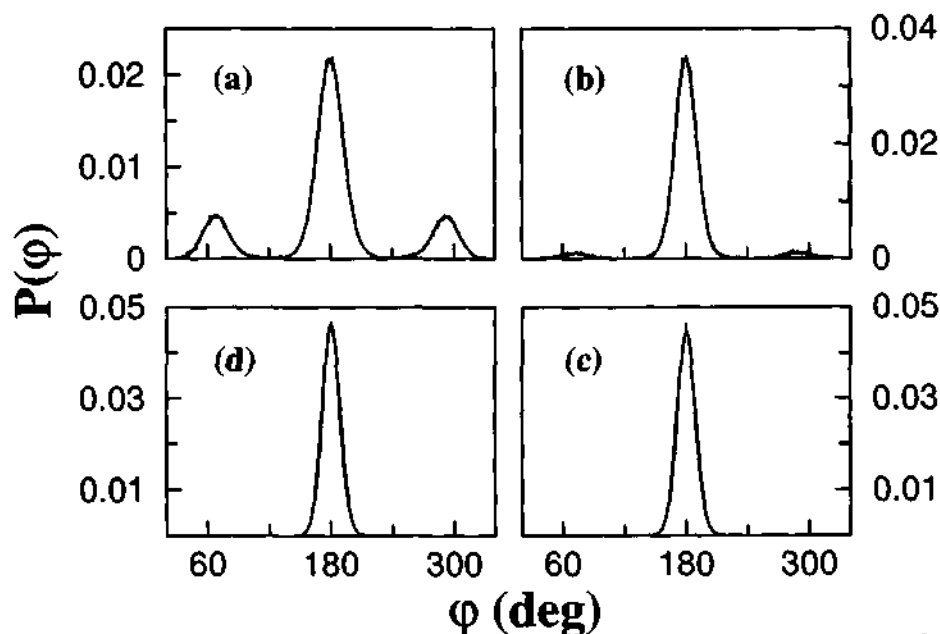


Figure 4.11: The distribution of the torsional angle,  $\phi$ , around the C-C bond of the alkane backbone is shown at different pressures across the solid-liquid transition. (a) 1 kbar, (b) 5 kbar, (c) 7.5 kbar, (d) 10 kbar.

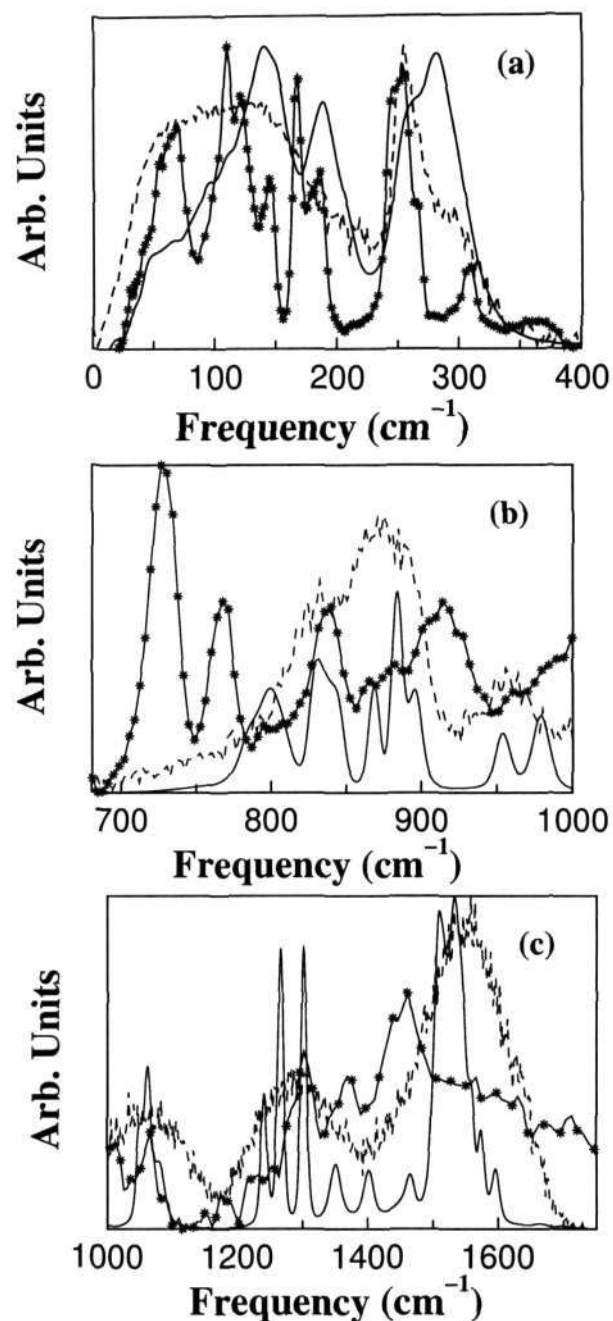


Figure 4.12: The vibrational density of states obtained from normal mode analysis (dashed line), and from the velocity auto correlation function (solid line) are compared with neutron scattering data (solid line with stars) [37]. Note that the experimental data is the dynamic structure factor of *n*-heptane at atmospheric pressure and 100 K, while the theoretical results are obtained from MD configurations at 10 kbar and 300 K. (a) 0-400 cm<sup>-1</sup>, (b) 680-1000 cm<sup>-1</sup>, (c) 1000-1750 cm<sup>-1</sup>.

dynamic structure factor obtained from a quasielastic neutron scattering experiment, in Figures 4.12a, 4.12b, and 4.12c. Note that the experiment was performed for the crystal at a temperature of 100K and a pressure of 1 bar, while the spectra from simulations are at 300K and 10 kbar. The agreement between the two computational methods and with experiment is good. The power spectrum of the VACF has better resolved peaks than the NMA spectrum at low frequencies (less than  $200\text{ cm}^{-1}$ ) indicating the significant role of anharmonic effects in these modes.

The features near  $3000\text{ cm}^{-1}$  correspond to the C-H stretching modes (not shown). Various peaks in the C-C stretching region ( $1030\text{-}1140\text{ cm}^{-1}$ ), the H-C-H bending region ( $1300\text{-}1500\text{ cm}^{-1}$ ) are reproduced well in the simulations, as they are built within the model for intramolecular interactions. Of interest to us are the spectral features that correspond to methyl rocking ( $850\text{-}910\text{ cm}^{-1}$ ) [26], the longitudinal acoustic mode (LAM-3) at  $435\text{ cm}^{-1}$ , the methyl torsion mode ( $250\text{ to }280\text{ cm}^{-1}$ ) and modes in the far infrared region ( $<200\text{ cm}^{-1}$ ). The modes are assigned based on visualization of atomic displacements obtained through the normal mode analysis. The low frequency assignments are compared to the work of Braden *et al* [27, 28] while high frequency modes are compared with the work of Snyder *et al* [29]. Marginal differences are noticed between the peak positions obtained from the normal mode analysis and that obtained from the VACF. The peaks are much better resolved in the latter, particularly at low frequencies.

#### **Pressure dependence of VDOS :**

The VDOS calculated from the VACF at various pressures ranging from 10 kbar to 70 kbar are shown in Figure 4.13 and the results are compared with experimental infrared absorption spectrum in Figure 4.14 [10]. In general, most vibrational bands shift to higher frequencies with increase in pressure, consistent with infrared spectroscopic measurements [10]. The bands also broaden, possibly due to phonon-phonon interactions and also due to reduced phonon lifetimes. Significantly, at high pressures some vibrational



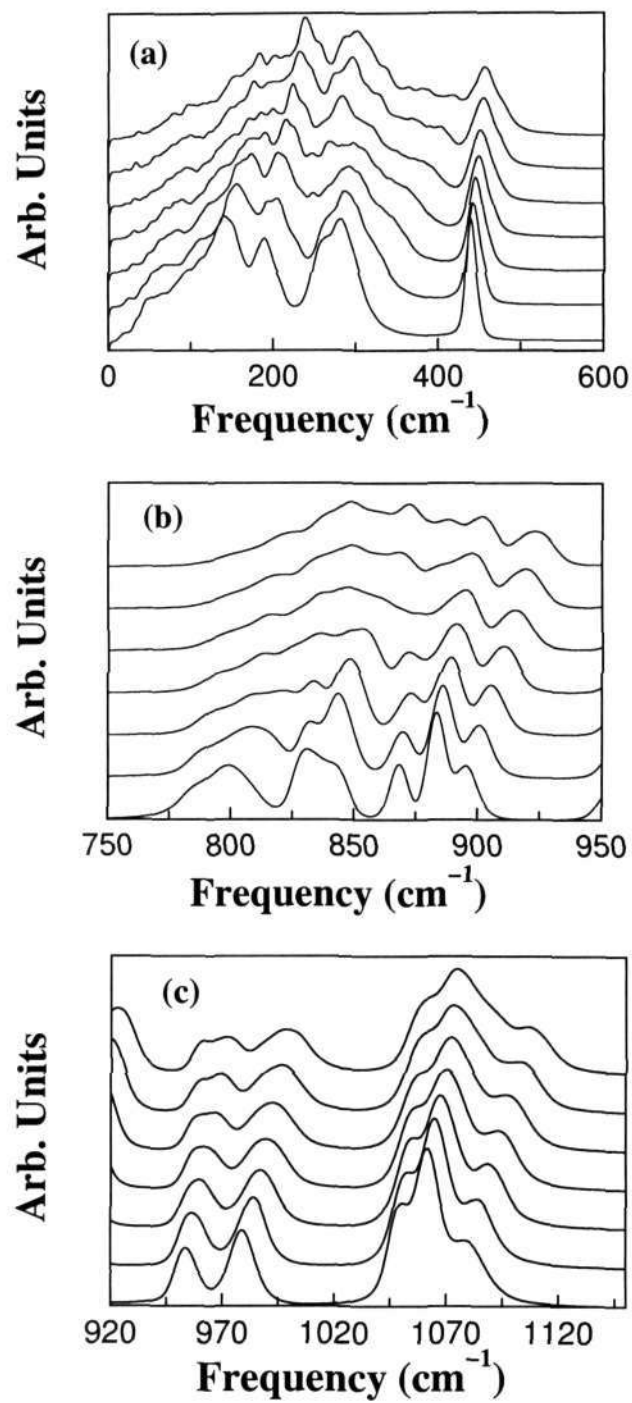


Figure 4.13: The vibrational density of states obtained by Fourier transformation of the velocity auto correlation function is shown at different pressures, in three ranges of frequencies. The functions are shifted for clarity. Pressures (From bottom to top): starting from 10 kbar up to 70 kbar in steps of 10 kbar. (a) 0-600 cm<sup>-1</sup>, (b) 750-950 cm<sup>-1</sup>, (c) 920-1150 cm<sup>-1</sup>.

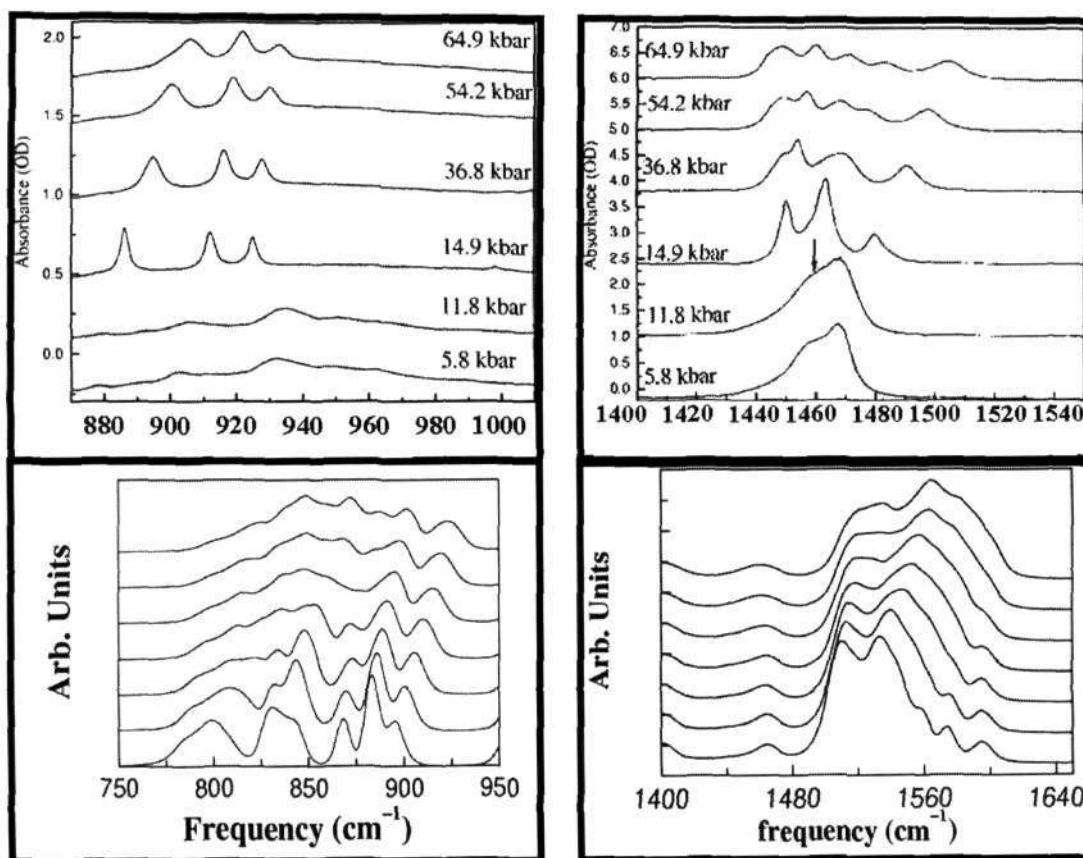


Figure 4.14: The vibrational density of states obtained by Fourier transformation of the velocity auto correlation function (bottom panels) are compared with experimental infrared absorption intensity [10] (top panels). Pressures (In bottom panels - From bottom to top) : starting from 10 kbar up to 70 kbar in steps of 10 kbar.

features are found to disappear from the spectrum, or are most likely subsumed under neighboring peaks. The peak at  $146\text{ cm}^{-1}$  corresponds to transverse acoustic mode (TAM) vibrations and is found to decrease in intensity at high pressures. TAM vibrations involve atomic displacements in directions perpendicular to the molecular long axis. Hence they will be affected by changes in the intermolecular structure within a crystalline layer. The TAM feature at  $260\text{ cm}^{-1}$  that corresponds to methyl rotation (or end group torsion) is considerably weakened with increase in pressure. We show (see later) that although the rotation of the methyl group slows down at 70 kbar, it is not completely arrested. The finite intensity of the spectrum at this frequency confirms this fact. Similarly the peak at around  $870\text{ cm}^{-1}$  nearly vanishes at high pressures. This peak corresponds to methyl rocking motions. These observations are consistent with the details on the structure discussed

earlier. The symmetric methyl bending modes at  $1350\text{ cm}^{-1}$  [31,32] also show interesting changes with pressure. The intensity of the peak diminishes rapidly with increasing pressure and it becomes a plateau at 70 kbar. The C-C stretching region ( $1030\text{-}1140\text{ cm}^{-1}$ ) consists of three peaks (at  $1048$ ,  $1061$ , and  $1080\text{ cm}^{-1}$ ) at low pressure which is consistent with experiments [10,29]. These modes exhibit a blue shift, while the peak at  $1048\text{ cm}^{-1}$  vanishes at high pressures. Three peaks corresponding to methyl rocking are present in the range of  $850\text{-}910\text{ cm}^{-1}$ . They too show a shift to higher frequencies with increasing pressure. While two peaks ( $884$  and  $895\text{ cm}^{-1}$ ) shift systematically with increasing pressure, the peak at  $868\text{ cm}^{-1}$  vanishes at high pressures. The pressure dependence of the methyl rocking mode that we have observed is consistent with the results inferred for *n*-pentane [30]. Thus, the distribution of the vibrational frequencies generated from the normal mode analysis captures all the essential features of the experimental spectra. The additional advantage that one gains from the NMA are the atomic displacements associated with a given vibrational mode. The atomic displacements are related to the eigen vectors obtained from the NMA. We have investigated the nature of atomic motions at selected frequencies and present these results in Figures 4.15a and 4.15b. The procedure that we follow to analyze the atomic displacements is as follows: We select a frequency at which the VDOS exhibits a peak and pick up a few molecules that undergo large amplitude displacements in modes excited at such frequencies. The modes were assigned based on the visualization of atomic displacements. The vibrational mode at  $54\text{ cm}^{-1}$  shown in Figure 4.15a, is a longitudinal mode in which the atomic displacements are along the chain axis of the molecule. The nature of the atomic displacements shown for the mode at  $140\text{ cm}^{-1}$  suggests that it is a transverse mode with atomic vibrations perpendicular to the long axis of the molecule. The eigen vectors shown for the mode at  $237\text{ cm}^{-1}$  (Figure 4.15b) can be conveniently assigned to methyl rotation while that at  $817\text{ cm}^{-1}$  can be associated with the methyl rocking mode. The umbrella motion of the methyl group is evident from the modes at  $1351$  and  $1353\text{ cm}^{-1}$  which is consistent with

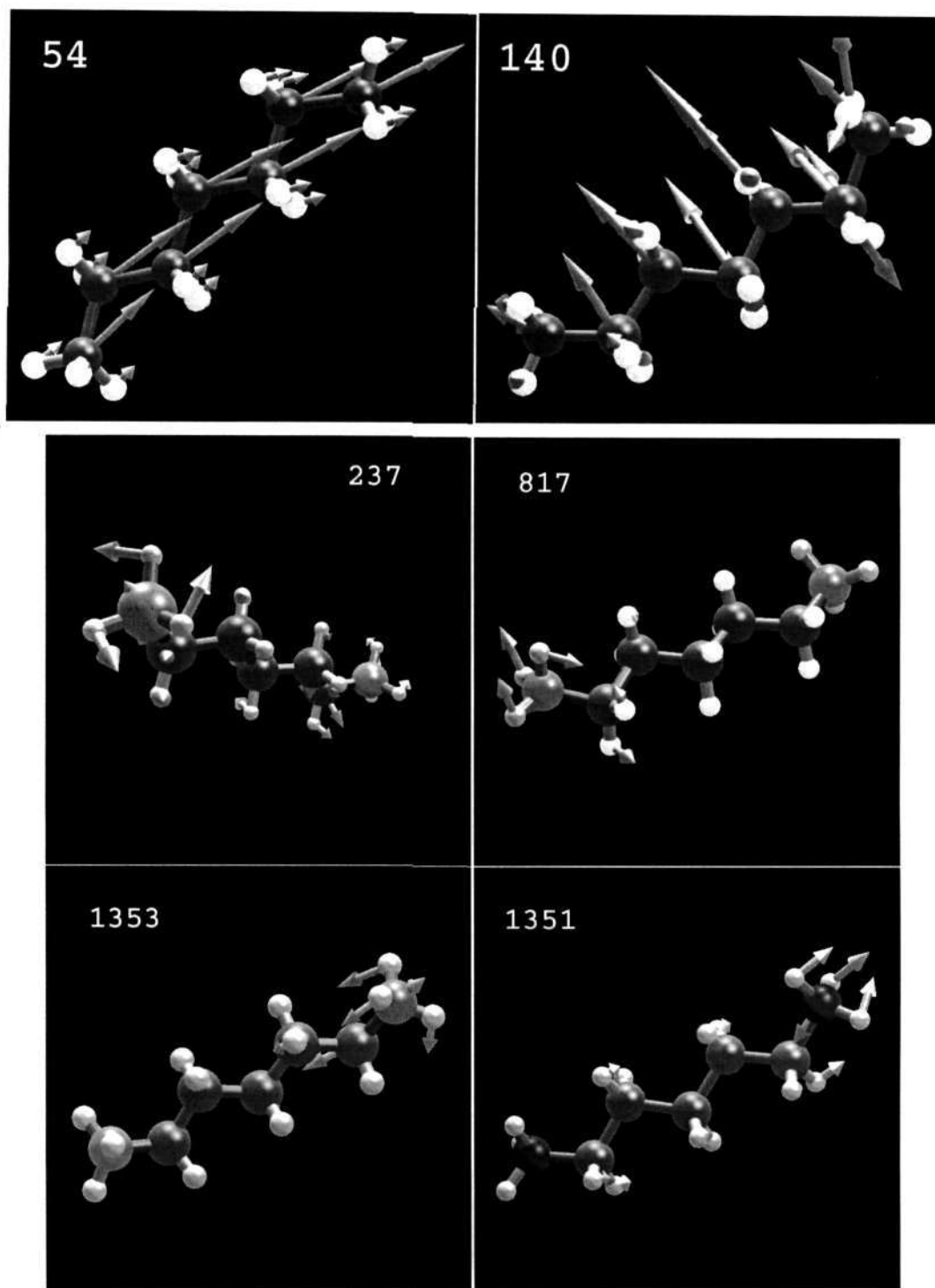


Figure 4.15: The atomic displacement vectors of a molecule exhibiting large amplitude motion are shown at different frequencies: (a)  $54\text{ cm}^{-1}$  (Longitudinal vibrations);  $140\text{ cm}^{-1}$ , (b)  $237\text{ cm}^{-1}$  (methyl rotation);  $817\text{ cm}^{-1}$  (methyl rocking);  $1351\text{ cm}^{-1}$  and  $1353\text{ cm}^{-1}$  (umbrella motion of methyl group [31,32]).

the experiments of Jona et al. [31] and Snyder [32].

#### Mode properties :

A large amount of information on the modes can be obtained by calculating quantities such as the participation ratio and the phase quotient. The participation ratio ( $PR_j$ ) of the  $j^{th}$  eigen mode is defined as [33]

$$PR_j = \frac{\left(\sum_{i=1}^N |\vec{u}_{ij}|^2\right)^2}{N \sum_{i=1}^N |\vec{u}_{ij}|^4} \quad (4.2)$$

and the phase quotient ( $PQ_j$ ) is defined as,

$$PQ_j = \frac{1}{N_b} \sum_i \sum_k \frac{\vec{u}_{ij} \cdot \vec{u}_{kj}}{|\vec{u}_{ij}| |\vec{u}_{kj}|} \quad (4.3)$$

where  $\vec{u}_{ij}$  is the displacement vector of atom  $i$  in the vibrational mode  $j$ ,  $N$  is the total number of atoms, and  $N_b$  is the total number of bonds present in the system. The double summation in Eq.4.3 denotes all bonded pair of atoms  $i$  and  $k$ .

The participation ratios at 10 kbar and 70 kbar are plotted in Figure 4.16a against the frequency of the modes. Large values of PR implies that a significant fraction of the system participate in that particular mode. A value of unity is obtained when all the  $N$  atoms of the system get displaced by the mode. As expected, this value is obtained for the rigid body translational mode at zero frequency. At 10 kbar, the PR value is large at frequencies less than  $100 \text{ cm}^{-1}$ . Larger values are also observed for the methyl rotation at  $250 \text{ cm}^{-1}$ . The pressure dependence of PR is interesting. At 70 kbar, the frequency range of large PR values gets extended up to about  $300 \text{ cm}^{-1}$ . Moreover, the values too are marginally larger (about 0.27) compared to the values at 10 kar of about 0.25. The PR of the methyl rocking mode at around  $880 \text{ cm}^{-1}$  and the vibrational modes around  $960 \text{ cm}^{-1}$ ,  $1080 \text{ cm}^{-1}$ , and  $1575 \text{ cm}^{-1}$  undergo significant changes upon increasing pressure. Although the participation ratio of these modes increase with pressure, the

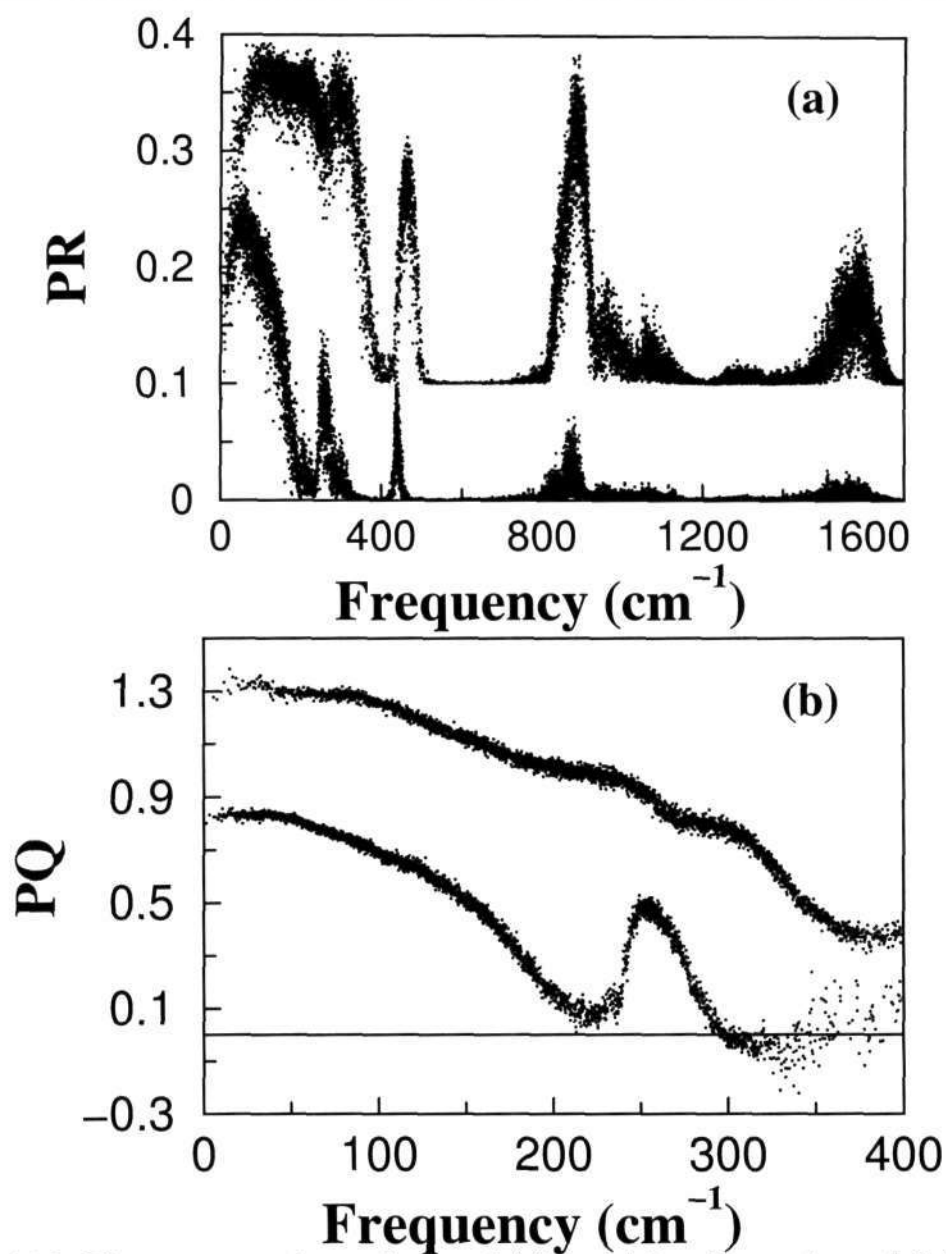


Figure 4.16: The pressure dependence of (a) participation ratio and (b) phase quotient of vibrational modes are shown against the frequency of the mode at 10 kbar (bottom) and 70 kbar (top). The high pressure data is shifted up from that at 10 kbar for the sake of clarity.

prominent changes at  $880 \text{ cm}^{-1}$  can be attributed to the fact that the environment of the end methyl groups are affected significantly by increasing pressure.

The increased PR values are a consequence of increased order in the system. Modes tend to localize due to disorder. In a perfect crystal, all modes will be extended. We

have already discussed the increase in structural ordering using pair correlation functions. This result on PR ties in well with the data on the evolution of structure with pressure.

The vibrational modes can be further classified into optic-like and acoustic-like based on the phase relationship between the vibrations of the bonded pair of atoms. The phase quotient (PQ) defined in Eq. 4.3 is a measure of such a phase relationship and it is the average cosine of the angle between the displacement vectors of a bonded pair of atoms. PQ can take values between -1 to +1 corresponding to out-of-phase and in-phase vibrations of neighboring (bonded) atoms respectively. Thus, PQ values are close to +1 for acoustic-like modes and are around -1 for optic-like modes.

The data on the phase quotient (PQ) too is quite instructive. This is shown in Figure 4.16b against frequency at 10 kbar and 70 kbar. A positive value of PQ indicates that the mode has an acoustic character, and a negative value implies optic character. All modes of vibration below about  $300\text{ cm}^{-1}$  are acoustic in nature, while modes in the frequency range  $1000$  to  $1200\text{ cm}^{-1}$  are optic modes. These observations agree well with earlier assignments of LAM and TAM modes at low frequency [27,28].

#### Methyl Rotation :

The methyl rotation mode at around  $250\text{ cm}^{-1}$  is particularly interesting and is found to occur at the same frequency in all linear alkanes [27]. To illustrate the nature of this rotation, we show in Figure 4.17, the time dependence of the angle subtended by a CH vector of a methyl group of a molecule at time  $t$  with the same vector at time zero. These are plotted at 10 kbar and 70 kbar for two arbitrary molecules. Note the rather sharp nature of the transitions from one orientation of the CH vector to another, that are separated by  $120^\circ$ . These processes are *single molecule events* of methyl rotation. Not so surprisingly, one observes much fewer transitions at 70 kbar relative to the data at 10 kbar. We now examine this mode further by studying the time correlation function (TCF) of the CH vector of the methyl group.

One can obtain an estimate of the time scales of the rotation of the methyl groups by calculating a normalized time correlation function (TCF) defined as,

$$B(t) = \frac{\langle \vec{R}(0) \cdot \vec{R}(t) \rangle}{\langle \vec{R}(0) \cdot \vec{R}(0) \rangle} \quad (4.4)$$

where  $\vec{R}(t)$  is the HCH bisector vector at time  $t$ . In what follows,  $B_{c2}(t)$  denotes the TCF of the HCH bisector vector of methylene groups and  $B_{c3}(t)$  represents that of the HCH bisector belonging to  $\text{CH}_3$  groups.

Figures 4.18a and 4.18b show the behavior of both  $B_{c2}(t)$  and  $B_{c3}(t)$  at various pressures. Two important features are to be noted: (a) at all pressures,  $B_{c3}(t)$  decays to lower values while  $B_{c2}(t)$  does not decay at all. (b) the rate of decay of  $B_{c3}(t)$  decreases with

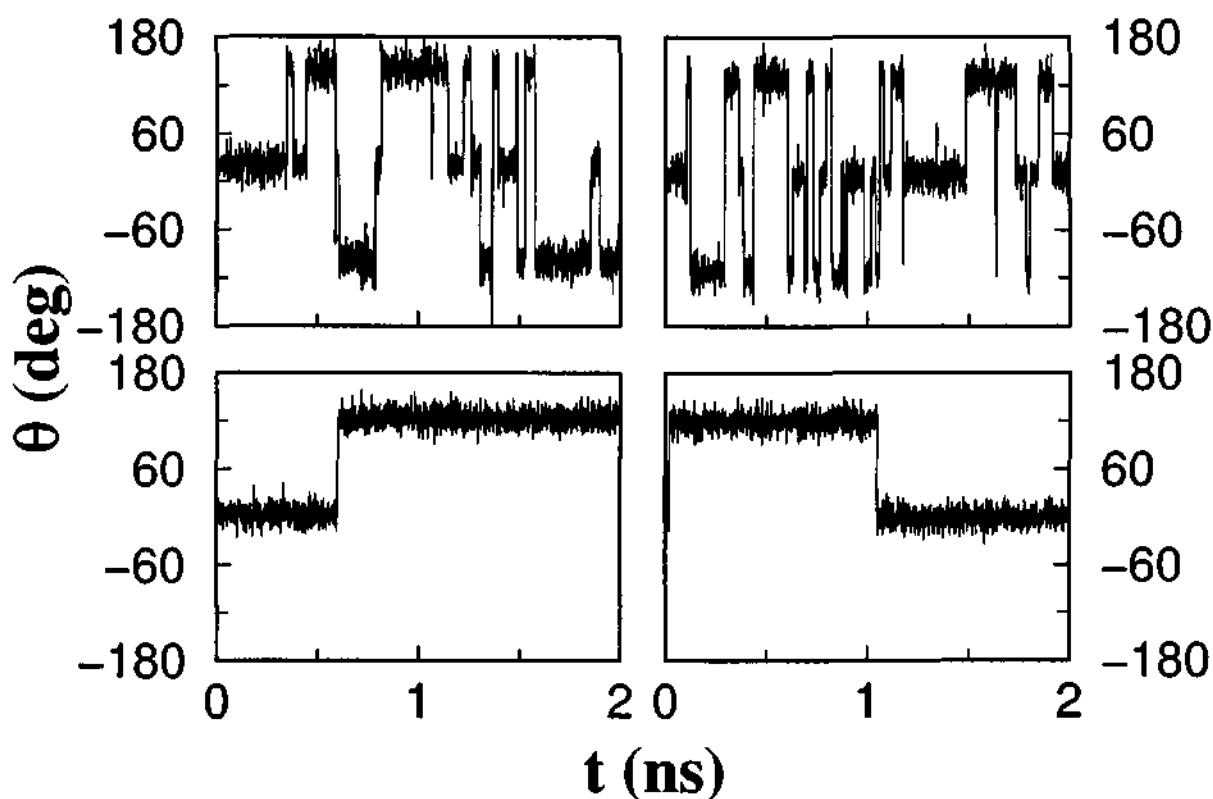


Figure 4.17: The time evolution of the angle,  $\theta$ , between a CH vector of a methyl group at time  $t$  and at time zero is shown for two molecules chosen arbitrarily. Left panels: Molecule 1, Right Panels: Molecule 2. Top: At 10 kbar, Bottom: At 70 kbar.



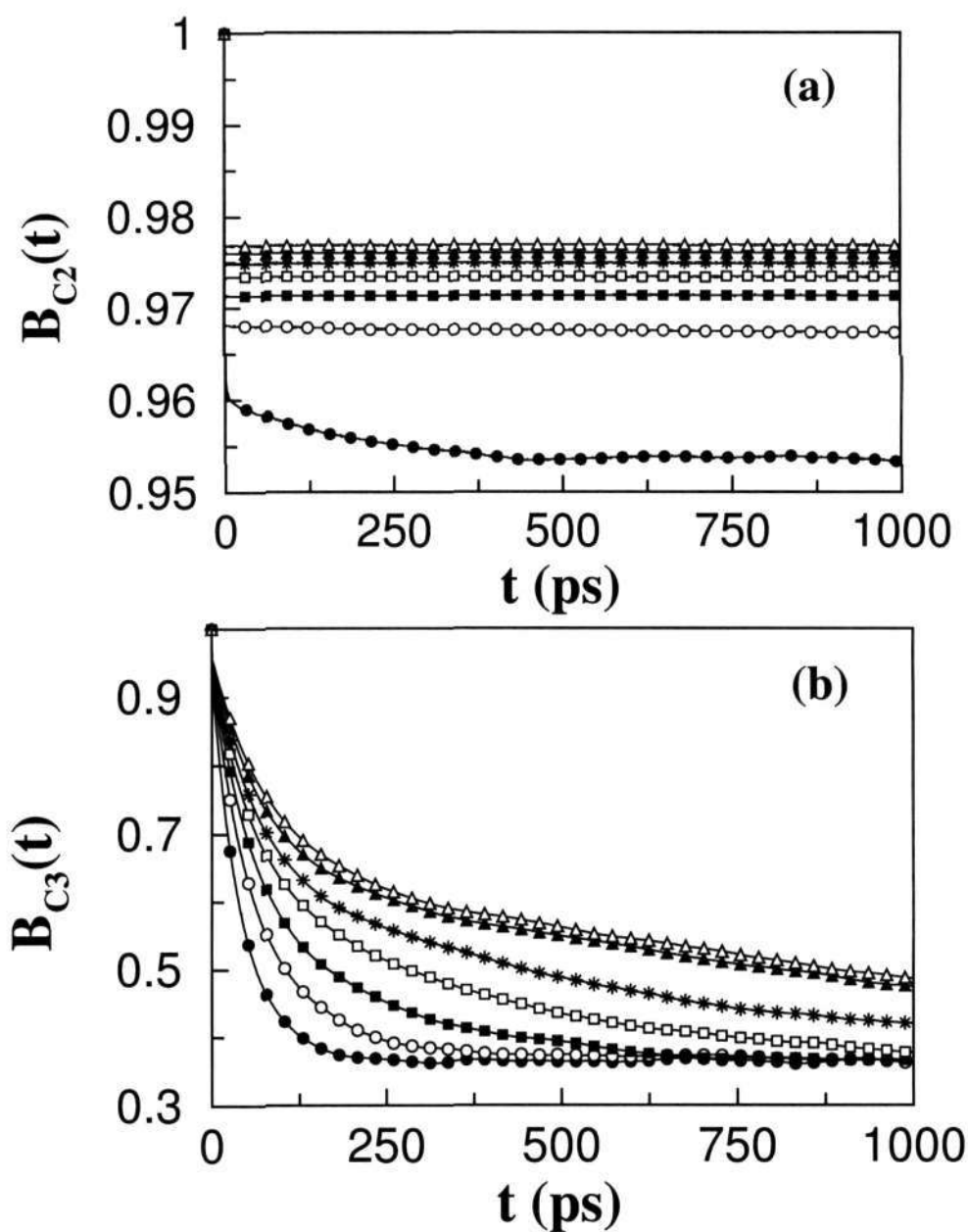


Figure 4.18: The rotational time correlation functions of a HCH bisector that belongs to (a) methylene group,  $B_{C_2}(t)$ , and (b) methyl group,  $B_{C_3}(t)$ , are shown at different pressures. Pressures (From bottom to top): Starting from 10 kbar up to 70 kbar in steps of 10 kbar. The initial decay of the function in (a) is faster than 1 ps. Symbols are shown infrequently for clarity.

increasing pressure while  $B_{C_2}(t)$  does not show much change with pressure. It is clear from these observations that the HCH bisector belonging to  $\text{CH}_3$  group is able to explore different orientations at low pressures than the HCH bisector of  $\text{CH}_2$  group. This points to

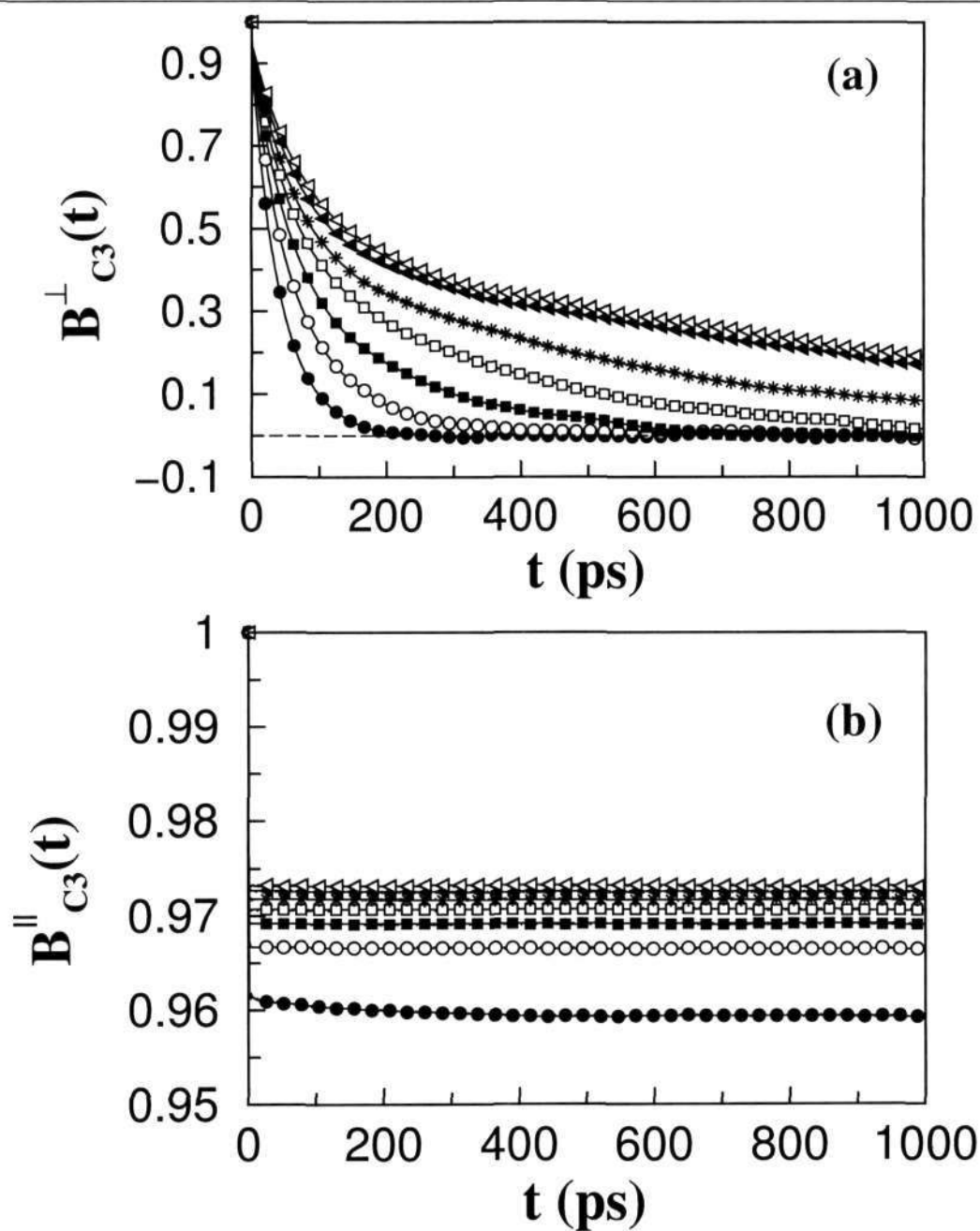


Figure 4.19: The rotational time correlation functions of a HCH bisector for atoms belonging to a methyl group (a) projected onto a plane perpendicular to the terminal C2-C3 bond of the *n*-heptane chain,  $B_{C3}^{\perp}(t)$  and (b) projected along (i.e., parallel to) the terminal C2-C3 bond,  $B_{C3}^{\parallel}(t)$ , are shown at different pressures. Pressures (From bottom to top): Starting from 10 kbar up to 70 kbar in steps of 10 kbar. The initial decay of the function in (b) is faster than 1 ps. Symbols are shown infrequently for clarity.

P (kbar)	$\tau_1$ (ps)	$w_1$ (%)	$\tau_2$ (ps)	$\langle \tau \rangle$ (ps)
10	44.4	90	0.6	40.2
20	96.0	63	24.7	69.7
30	180.0	54	34.6	112.6
40	297.7	55	36.9	179.7
50	567.7	47	51.9	294.9
60	1000.0	48	59.0	509.6
70	954.3	52	60.2	527.4

Table 4.2: Biexponential fit of the form,  $B_{C_3}^\perp(t) = w_1 e^{-\frac{t}{\tau_1}} + (1 - w_1) e^{-\frac{t}{\tau_2}}$  to the data presented in Figure 4.19.

the additional free volume available to the methyl end-groups while the packing around  $\text{CH}_2$  is rigid. In addition, the slowing down of the decay of  $B_{C_3}(t)$  at higher pressures suggests that the environment of a methyl group is altered at higher pressures than that of a methylene group. This can be attributed to the reduction of available volume for the  $\text{CH}_3$  groups with increasing pressure. Note that the HCH bisector of  $\text{CH}_3$  can explore only half of the sphere around methyl carbon and the remaining half is forbidden due to the presence of the chain backbone. This explains the non-zero saturation value of  $B_{C_3}(t)$  at long times. Although the above analysis provides an idea of the methyl group rotation, it does not resolve the issue of whether the rotation is a full rotation about the terminal C2-C3 bond or not. To address this, we have divided  $B_{C_3}(t)$  into two parts:  $B_{C_3}^\perp(t)$  evaluates the TCF of HCH bisector of the methyl group projected onto a plane perpendicular to the terminal C2-C3 bond while  $B_{C_3}^\parallel(t)$  determines the TCF of HCH bisector of  $\text{CH}_3$  along the terminal C2-C3 bond. In Figure 4.19a and 4.19b we show the behavior of  $B_{C_3}^\perp(t)$  and  $B_{C_3}^\parallel(t)$ . At low pressures,  $B_{C_3}^\perp(t)$  decays to zero within the timescales of the analysis, and at higher pressures the TCF slows down considerably. The decay to a value of zero indicates the full rotation of the methyl group about the C2-C3 axis. Expectedly, the TCF for the function parallel to the C2-C3 bond ( $B_{C_3}^\parallel(t)$ ) does not decay at all.

We have fitted  $B_{C_3}^\perp(t)$  to a multiexponential function and have obtained time constants for methyl rotation. The data could not be fitted to a single exponential, and hence a two-exponential function was used. The parameters of the fit, along with the average time

constants are provided in Table 4.2. At 10 kbar, the behavior is nearly single exponential with a time constant of around 40ps. This increases precipitously to nearly 1 ns at 70 kbar. Beyond 10 kbar, an additional contribution emerges in the decay of  $B_{c3}^{\perp}(t)$ , whose time constant is surprisingly small – of the order of tens of picoseconds. Currently, we are not clear about the origin of these two timescales. This needs to be probed further.

The increase in pressure decreases the free volume available for rotation for the methyl group and increases the energy barrier. As a first step to estimate the barrier for this hindered rotation, we have calculated the probability of the projection of a methyl CH vector onto the plane perpendicular to the terminal C2-C3 vector, to be oriented at an angle  $\theta$  with respect to its value at  $t=0$ . The quantity is defined as,

$$P(\theta) = \langle \delta(\theta - \theta_i(t)) \rangle \quad (4.5)$$

where  $\theta_i(t)$  represents the  $\theta$  of  $i^{th}$  CH vector at time  $t$ . The angular brackets imply that the probability distribution is evaluated over CH vectors of all the methyl groups in the system and over all time. The  $P(\theta)$  function shown in Figure 4.20a exhibits three peaks, one at  $0^\circ$  and others at  $\pm 120^\circ$ . These peaks signify the possible three states of the CH vector. The time variation of occupation of these states, for a single methyl group has been discussed in Figure 4.17. The time scales of transition between these states has been discussed in Figures 4.18 and 4.19. Here we study the energy barriers of the transition between these states. At 10 kbar, the intensity of these peaks are equal, implying that the CH vector is able to explore these states equally likely. Upon increasing the pressure we find the behavior of  $P(\theta)$  function to change significantly. At 70 kbar, the probability of finding the CH vector in  $\theta=0^\circ$  state is higher than the other states within the timescales of simulation. The states at  $\theta=\pm 120^\circ$  are equally likely for the CH vectors to visit. The taller peak at  $\theta=0^\circ$  can be attributed to restricted dynamics of the CH vectors at higher pressures. These observations are consistent with both the time dependence of  $\theta$  of tagged molecules shown in Figure 4.17 and with the TCF of HCH vector shown in Figure 4.19b.

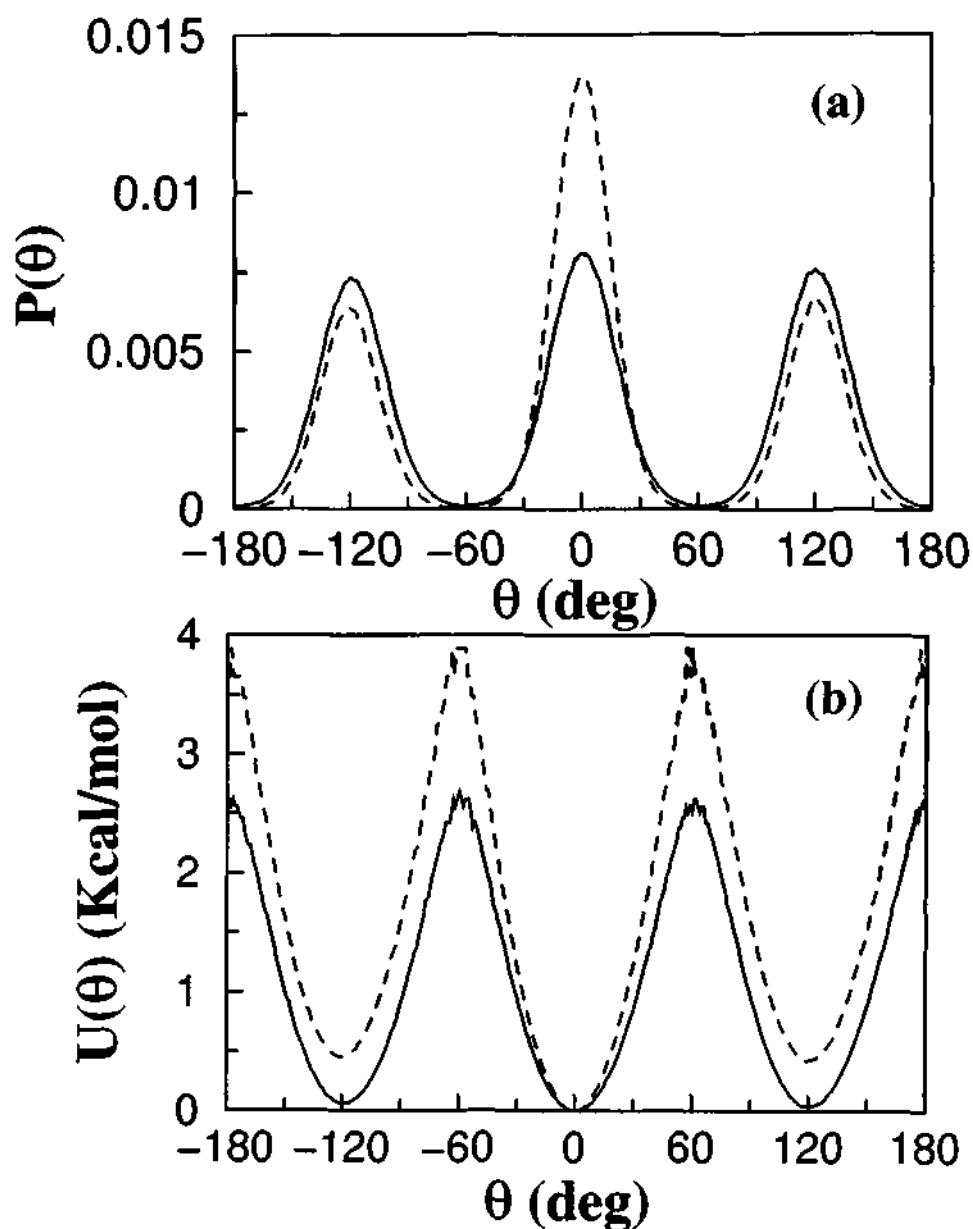


Figure 4.20: (a) The distribution of the angle,  $\theta$ , between a CH vector of a methyl group at time  $t$  and at time zero is shown at 10 kbar (solid line) and at 70 kbar (dashed line). (b) The potential of mean force (PMF) obtained from the above distribution is shown at 10 kbar (solid line) and at 70 kbar (dashed line).

Based on the knowledge of  $P(\theta)$  one can estimate the energy required for a CH vector to transit from the  $\theta=0^\circ$  state to either of the  $\theta=\pm 120^\circ$  states. This is done by inverting the probability distribution and obtaining the potential of mean force (PMF),  $U(\theta)$  which

is a measure of the energy barrier for the hindered methyl rotation as,

$$U(\theta) = -T\ln(P(\theta)) \quad (4.6)$$

The PMF is shown in Figure 4.20b at the two extreme pressure conditions. We have shifted the data in such a way that the energy at  $\theta=0^\circ$  state is 0 kcal/mol. The energy barrier to cross from the initial orientation to the final is obtained as the energy difference between the state at angle  $120^\circ$  and  $0^\circ$ . The barrier height is calculated to be 2.6 and 3.8 kcal/mole at 10 kbar and 70 kbar respectively, and their magnitudes compare well with experiments [34–36]. A caveat needs to be added here regarding this analysis. Evidently, at 70 kbar the probability function  $P(\theta)$  has not converged to the equilibrium value. At equilibrium, all three states are equally likely. The difference in the heights of the three peaks in Figure 4.20a at 70 kbar is a consequence of the transition time scale being larger than the time scale of observation. Thus, an inversion of this data to obtain the PMF at 70 kbar is erroneous. However, this educative exercise provides us with an estimate of the barrier height involved in methyl rotation, at least at 10 kbar.

The features observed from the above analyses can be validated by determining the atomic density distribution of hydrogens around the carbon atom of the methyl group. We have carried out such an analysis to show that the methyl group is able to rotate in the solid state, at low pressures. To achieve this goal, the molecular orientation needs to be fixed. We rotate the plane formed by the terminal C3-C2-C2 triplet in such a way that it lies parallel to the  $xz$ -plane with the  $z$ -axis coinciding with the C3-C2 bond vector. The density distribution of hydrogen atoms around a C3 atom in this frame was averaged over all molecules and configurations. The results obtained from this analysis are shown in Figure 4.21 for various pressures. At low pressures, we find that the hydrogen atoms are distributed uniformly to form a circular ring in a plane perpendicular to C3-C2 bond vector. This scenario changes as a function of increasing pressure, where one finds three lobes in the atomic density map. The presence of distinct regions at high pressures

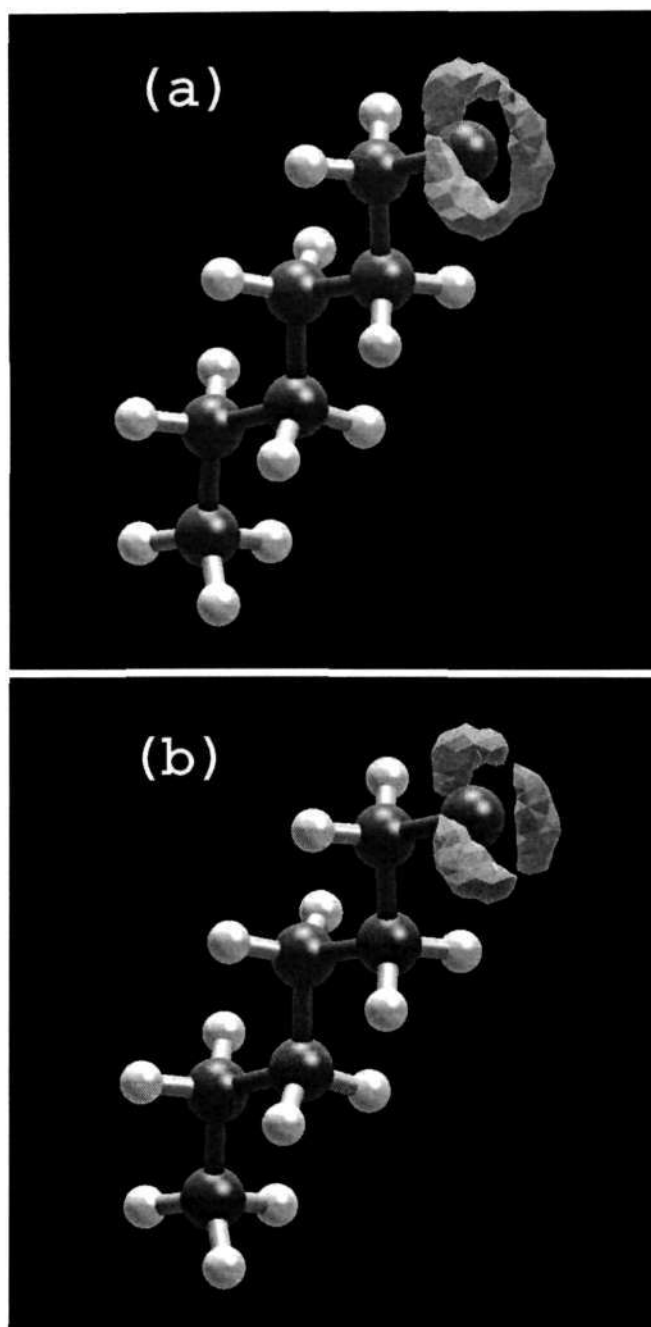


Figure 4.21: The atomic probability density map of methyl hydrogen around the carbon atom are shown (a) at 10 kbar and (b) at 70 kbar. The probability density values greater than  $0.0002$  hydrogen atoms/ $\text{\AA}^3$  are shown for clarity.

signifies the localization of hydrogen atoms in three specific locations around the C3-C2 bond vector.

## 4.4 Conclusions

We have presented extensive, atomistic molecular dynamics simulations of crystalline *n*-heptane under pressure conditions that include the liquid-crystal transition as well. The total length of all MD trajectories runs to around 23 ns. Such long trajectories have been employed to precisely map the structural and the gradual dynamical changes that are wrought by pressure.

We observe signatures of the liquid-solid transition in the structure of the system. Conformational changes, principally the formation of *gauche* defects have been studied in the liquid state at pressures below 10 kbar. Above 10 kbar, with increasing pressure, significant changes occur in the environment around the methyl group rather than around the methylene groups. Pair correlation and angle distribution functions reveal that at 10 kbar, the first coordination shell of CH<sub>3</sub> contains around 10 neighbors that are loosely packed. At 70 kbar, this neighbor shell resolves into specific subshells that contains 4 CH<sub>3</sub> neighbors from the layer across the central CH<sub>3</sub>, and 6 neighbors that belong to the same layer. Within the latter, two CH<sub>3</sub> groups are present farther than the rest four methyls. Angle distributions and probability density maps for CH<sub>3</sub> groups within the first coordination shell have shown their precise locations. These subtle changes in the crystalline phase, however, are not accompanied by any discontinuities in first order thermodynamic quantities, such as the volume, cell parameters or the internal energy of the system. Based on these calculations, we are thus led to believe that the increase in pressure does not lead to a first order solid-solid transition. A preliminary examination of the isothermal compressibility does not show any discontinuity with increase in pressure, thus diminishing the possibility of a second order transition too.

However various issues such as system size effects, timescales associated with the transition, and accuracy of the interaction potentials, particularly at high densities need to be considered before one can safely rule out any solid-solid transition. Despite the long runs adopted here, the system may have been evolving along a metastable path due to



large relaxation times at high densities. This could preclude the experimentally alluded transition at 30 kbar in the simulations and needs to be investigated further. Although the empirical nature of the interaction potential could shift the solid-solid transition towards higher pressures, the success of the present interaction model in characterizing the phase behavior of *n*-alkanes [14] guides us to believe that the highest pressure employed here is large enough for the transition to occur.

We have also studied the vibrational dynamics of this system. The vibrational density of states has been computed within the harmonic approximation through a normal mode analysis, as well as through the velocity autocorrelation function method. Results obtained from these two methods agree with each other, and with inelastic neutron scattering experiments [37] and spectroscopic data [10, 29, 32]. We find a blue shift in nearly all the vibrational bands as a function of pressure. In particular, the low frequency modes shift by as much as  $45\text{ cm}^{-1}$ . The width of the bands increase with pressure in agreement with infra-red experiments. Some of the bands, such as the TAM vibration at  $146\text{ cm}^{-1}$ , and the methyl rocking mode at  $800\text{ cm}^{-1}$ , nearly vanish at 70 kbar. The normal mode analysis enabled us to visualize the modes to aid in their assignments. The methyl rotation mode at  $260\text{ cm}^{-1}$  was also investigated through a time correlation function of the projection of the CH vector on the plane perpendicular to the C2-C3 axis. We found the methyl groups to rotate even at high pressures, although considerably slower than at 10 kbar.

The comprehensive characterization of this system in terms of thermodynamics, structure, vibrational analysis, and dynamics leads us to conclude the absence of any first order solid-solid transition in the model *n*-heptane under pressure, up to 70 kbar.

## Bibliography

- [1] D.M. Small, *The Physical Chemistry of Lipids* (Plenum, New York, 1988).
- [2] D. Chapman, M. Jones, and M.N. Jones, *Micelles, Monolayers and Biomembranes* (John Wiley, New York, 1994).
- [3] B.-R. Hyun, S.V. Dzyuba, R.A. Bartsch, and E.L. Quitevis, *J. Phys. Chem. B* **106**, 7579 (2002).
- [4] P. Dagaut, M. Reuillon, and M. Cathonnet, *Combust. Sci. Tech.* **95**, 233 (1994).
- [5] E.B. Sirota, H.E. King Jr., G.J. Hughes, and W.K. Wan, *Phys. Rev. Lett.* **68**, 492 (1991).
- [6] J.-P. Ryckaert, M.L. Klein, and I.R. McDonald, *Phys. Rev. Lett.* **58**, 698 (1987);  
J.-P. Ryckaert, M.L. Klein, and I.R. McDonald, *Mol. Phys.* **83**, 439 (1994).
- [7] H. Yamamoto, N. Nemoto, and K. Tashiro, *J. Phys. Chem. B* **108**, 5827 (2004).
- [8] F. Guillaume, J.-P. Ryckaert, V. Rodriguez, L.G. MacDowell, P. Girard, and A.J. Dianoux, *Phase Transitions* **76**, 823 (2003).
- [9] R. Boese, H.C. Weiss, and D. Bläser, *Angew. Chem. Int. Ed.* **38**, 988 (1999).
- [10] M. Yamaguchi, S.V. Serafin, T.H. Morton, and E.L. Chronister, *J. Phys. Chem. B* **107**, 2815 (2003).

- 
- [11] A.M. Merle, M. Lamotte, S. Risemberg, C. Hauw, J. Gaultier, and H. Ph. Grivet, *Chem. Phys.* **22**, 207 (1977).
- [12] B. Chen, M.G. Martin, and J.I. Siepmann, *J. Phys. Chem. B* **102**, 2578 (1998); B. Chen, and J.I. Siepmann, *J. Phys. Chem. B* **103**, 5370 (1999).
- [13] D.J. Tobias, K. Tu, and M.L. Klein, *J. Chim. Phys. Phys.-Chim. Biol.* **94**, 1482 (1997).
- [14] J.M. Polson, and D. Frenkel, *J. Chem. Phys.* **111**, 1501 (1999).
- [15] M. Krishnan, S. Balasubramanian, and S. Clarke, *J. Chem. Phys.* **118**, 5082 (2003).
- [16] M. Parrinello, and A. Rahman, *Phys. Rev. Lett.* **45**, 1196 (1980).
- [17] G.J. Martyna, M.E. Tuckerman, D.J. Tobias, and M.L. Klein, *Mol. Phys.* **87**, 1117 (1996).
- [18] G.J. Martyna, M.L. Klein, and M. Tuckerman, *J. Chem. Phys.* **97**, 2635 (1992).
- [19] M.E. Tuckerman, B.J. Berne, and G.J. Martyna, *J. Chem. Phys.* **97**, 1990 (1992).
- [20] M.P. Allen, and D.J. Tildesley, *Computer Simulation of liquids* (Oxford: Clarendon, 1987).
- [21] M.E. Tuckerman, D.A. Yarne, S.O. Samuelson, A.L. Hughs, and G.J. Martyna, *Comput. Phys. Commun.* **128**, 333 (2000).
- [22] E. Paci, *Biochimica et Biophysica Acta* **1595**, 185 (2002).
- [23] K. Bagchi, S. Balasubramanian, and M.L. Klein, *J. Chem. Phys.* **107**, 8561 (1997).
- [24] P.E. Schoen, R.G. Priest, J.P. Sheridan, and J.M. Schnur, *J. Chem. Phys.* **71**, 317 (1979).
- [25] R.G. Snyder, *J. Chem. Phys.* **76**, 3921 (1982).

- 
- [26] J.P. Gorce, S.J. Spells, X.B. Zeng, and G. Ungar, *J. Phys. Chem. B* **108**, 3130 (2004).
- [27] D.A. Braden, S.F. Parker, J. Tomkinson, and B.S. Hudson, *J. Chem. Phys.* **111**, 429 (1999).
- [28] J. Tomkinson, S.F. Parker, D.A. Braden, and B.S. Hudson, *Phys. Chem. Chem. Phys.* **4**, 716 (2002).
- [29] R.G. Snyder, and J.H. Schachtschneider, *Spectrochimica Acta* **19**, 85 (1963).
- [30] M. Kato, and Y. Taniguchi, *J. Chem. Phys.* **94**, 4440 (1991).
- [31] P. Jona, M. Gussoni, and G. Zerbi, *J. Mol. Struct., Theochem.* **119**, 329 (1985).
- [32] R.G. Snyder, *J. Mol. Spectroscopy.* **7**, 116 (1961).
- [33] S.N. Taraskin, and S.R. Elliott, *Phys. Rev. B* **56**, 8605 (1997).
- [34] N.D. Morelon, G.R. Kneller, M. Ferrand, A. Grand, and M. Bee, *J. Chem. Phys.* **109**, 2883 (1998).
- [35] D.C Chatfield, A. Augsten, C. D'cunha, and S.E. Wong, *J. Comp. Chem.* **24**, 1052 (2003).
- [36] T. Kundu, B. Pradhan, and B.P. Singh, *Proc. Indian Acad. Sci. (Chem. Sci.)* **114**, 623 (2002).
- [37] <http://www.isis.rl.ac.uk/insdatabase/ascii/Heptane.dat>



## Chapter 5

# Structure of Solid Monolayers and Multilayers of *n*-Hexane on Graphite

### 5.1 Introduction

#### 5.1.1 *n*-Alkanes on Graphite Surface

In the previous chapters, we explored the vibrational, thermal, and high pressure phases of some linear molecules in bulk crystalline form. It is also interesting to know how such molecules behave when they are in contact with solid surfaces. Such investigations are of interest in the context of adsorption and formation of molecular films. In the present and the next chapters, we have attempted to understand the phase behaviour of ultra-thin *n*-alkanes physisorbed on graphite basal plane. As discussed in Chapter 1, *n*-alkanes exhibit an interesting variety of phase behaviour in the bulk, with particular structural differences between alkanes that have an even number of carbon atoms and those that have an odd number [1]. The origin of such odd-even effects in three dimensional molecular materials has been attributed to differences in the strengths of the methyl-methyl interactions to the ones between methylene groups [2]. This interplay between the interaction strengths of different groups in *n*-alkanes is accentuated in the presence of a surface.

The interplay between molecular structure, intermolecular interactions and the effect of an external corrugated surface gives rise to a diversity in two dimensional structures that is quite different and possibly richer than in bulk three dimensional crystals. The study of the complex phase behaviour exhibited by these nearly two dimensional systems has applications to phenomena such as lubrication, wetting, and spreading [4–6]. Graphite is well suited to study the evolution of the structure of *n*-alkanes, as alkanes can adsorb in a commensurate manner, due to the fact that one of the lattice constants of graphite (2.46Å) is quite close to the 1-3 distance (the distance between methylene groups separated by one CH<sub>2</sub> group is about 2.54Å) in a linear alkane [3]. Thus all the methylene groups of *n*-alkanes can possibly adsorb at preferred sites on the graphite lattice. As a result, linear alkanes form crystalline adsorbate layers at the fluid/graphite interface. The packing and orientation of these adsorbed species decide the properties of the solid layers thus formed. However, the experimental characterization of these adlayers are difficult because they are buried at the interface between the solution and the graphite. The phase behaviour of solid monolayers of single and multi-component short chain *n*-alkanes have been extensively studied recently [7].

### 5.1.2 *n*-Hexane on Graphite

*n*-hexane crystallizes in a herringbone pattern on graphite. Hansen and Taub [8] and Herwig et al [9] have studied the mechanism of melting of *n*-butane and *n*-hexane monolayers on graphite using both neutron diffraction experiments and molecular dynamics (MD) simulations. They concluded that the melting of such short alkanes proceeds by the creation of vacancies and thus theories of melting that are strictly two dimensional are inapplicable to such systems. In an extensive study of the structure of *n*-hexane monolayers on graphite, Hansen et al [10] have shown that the low temperature phase is herringbone ordered, and that on increasing temperature it transforms into a rectangular centred structure that coexists with the liquid phase. Peters and Tildesley [11] have

studied the melting of hexane monolayer using MD simulations. They found that the anisotropic united atom model produces the same herringbone configuration at low temperatures as an isotropic model. They also found that the monolayer described by either model melts at approximately 175K, with subtle structural differences between the two cases. Peters [12] has also studied the melting and other phase behavior of a *n*-hexane bilayer on graphite, and have observed that the melting point of a bilayer is increased by about 20K with respect to that of the monolayer.

Low energy electron diffraction and neutron scattering [13,14] experiments of *n*-hexane adsorbed on graphite have shown a rather interesting dependence of the structure of the first adsorbed layer upon coverage. Quite close to monolayer coverages, the *b*-parameter of the lattice decreases significantly, by about 0.35Å, i.e., by 7%. The compression is associated also with a transition from a structure that is uniaxially incommensurate with the underlying graphite lattice to one that is fully commensurate. Such a transition in the structure of the first adsorbed layer has also been observed recently in neutron scattering studies of other even and odd alkanes adsorbed on graphite at submonolayer coverages and at multilayer coverages [14].

In order to understand this phenomenon and to provide microscopic details, we have performed atomistic molecular dynamics (MD) simulations of *n*-hexane on graphite at two coverages. The simulations described here differ from earlier works [8–12] significantly, in its purpose. Our intention is to reproduce the experimental observation of the lateral compression of the *n*-hexane lattice upon increase in coverage, in as independent a manner as possible. In pursuit of this aim, we have performed MD simulations of a large cluster of *n*-hexane molecules on graphite, using the all-atom interaction model.

We have also performed simulations of monolayers of *n*-hexane on graphite, that employed periodic boundary conditions (PBC). A comparison of the results obtained from simulations with and without the use of PBCs enable us to independently verify the assumptions underlying the MD simulations, and its relationship to experiments. In ad-



dition, this chapter deals with our results of simulations that were started with “reversed” initial configurations for the monolayer and for the multilayer, so that issues related to adequate sampling of configurational space can be resolved.

## 5.2 Simulation Details

We have studied *n*-hexane on graphite at two coverages; One, a full monolayer, and the other a system containing three layers of *n*-hexane, hereafter called the multilayer. These simulations have been performed at low temperatures and also at temperatures where the bulk alkane would be liquid. Simulations of adsorbed species on surfaces are usually performed with periodic boundary conditions. However, such simulations force a periodicity on the system and it is not possible to obtain an independent validation of experimentally determined unit cell parameters.

In these simulations, the surface is represented by an external corrugated potential, and one cannot use a Parrinello-Rahman type of a procedure [15]. This is because, on a surface, the simulation box length has to be an integral multiple of the periodicity of the external potential that represents the surface, which is inconsistent with the continuous change in box size that the constant stress ensemble demands. Thus, to obtain structural data that is independent of the initial selection of the dimensions of the simulation box, our simulations were performed *without* the use of periodic boundary conditions in any of the three spatial directions, i.e., the simulations were essentially carried out for a cluster of *n*-hexane molecules adsorbed on graphite. The molecules on the surface of such a cluster can, in principle, evaporate into the gas phase, depending on the vapour pressure of the system. Given the strongly attractive nature of the interaction of the molecules with the graphite substrate, the hexane molecules are unlikely to desorb from the surface. However, in the absence of periodic boundary conditions in the lateral directions, molecules at the periphery of the cluster can leave the cluster, but still be present on the surface. We do not include such molecules in our analyses of the structure factor and

other quantities. Cheng and Klein have employed such a methodology of not employing periodic boundary conditions in all three directions to study the melting of ethylene on graphite [16]. Earlier simulations [8–10] to study the phase behaviour of *n*-hexane and other small alkanes on graphite have consistently employed periodic boundary conditions, with the cell parameters either obtained from experiments, or from static calculations. We have consciously chosen not to impose a periodicity on the simulated samples, as our primary purpose is to reproduce the lattice compression as *independently* as possible from experiments.

For computational efficiency, one has to study a cluster that is large enough such that the ratio of molecules that are present on the surface to those in bulk is reasonably small. The monolayer system studied here consists of 350 molecules with linear dimensions of 126 Å, and 90 Å. The three-layer system consisted of 360 hexane molecules, with lateral dimensions of 71 Å, and 91 Å. The system sizes studied here are comparable to the domain sizes of adsorbed alkanes on graphite, which is around 100 Å to 200 Å [10]. Recent calorimetry results have indicated that only a few additional layers are required to obtain a reasonable approximation to the bulk properties of alkanes [17]. We use three layers instead of just a bilayer to make sure that we had a complete second layer during the course of the simulation. The possibility of molecules desorbing during the high temperature annealing exists, and this could lead to voids in the second layer of a bilayer simulation. This could expose the molecules of the first layer, and might influence the structural transition that we anticipate. We have used three layers to avoid this possibility, however rare desorption might be.

For a comparison to the simulations without the use of periodic boundary conditions, we have performed MD calculations of *n*-hexane on graphite at monolayer and two-layer coverages *with* the use of periodic boundary conditions. As explained succinctly in Refs. [10,18], in this case, the simulation box has to be an integer multiple of both the graphite unit cell as well as that of the adsorbate unit cell. We have used lattice parameters

obtained from experiments for these quantities. The monolayer simulations with periodic boundary conditions were performed in a box of linear dimensions  $105.78\text{\AA} \times 102.26\text{\AA}$ , which corresponds to 120 unit cells of the  $n$ -hexane lattice. The number of atoms in the simulation was 4800. The multilayer simulations were performed for two layers of  $n$ -hexane adsorbed on graphite, each containing 150 molecules in a box of linear dimensions  $73.80\text{\AA} \times 85.22\text{\AA}$ , with a system size of 6000 atoms. The systems were equilibrated for 800 ps at 70K, after which the structure factor of  $n$ -hexane was averaged over 250 ps.

The MD simulations were performed under constant temperature conditions using the Nosé-Hoover chains method [19], with a thermostat time constant of 1 ps. An all-atom potential [20] was used for the hexane molecules and the interaction of the alkane atoms with graphite was represented by the anisotropic Steele potential [21–23] which is given as,

$$U_{\text{graphite}}(x_j, y_j, z_j) = U_0(y_j) + \sum_{m=1}^{\infty} U_m(y_j) f_m(x_j, z_j) \quad (5.1)$$

where

$$U_m(y_j) = \frac{2\pi\epsilon\sigma^6}{a_s} \left[ \frac{\sigma^6 g_m^5}{960 y_j^5} \left( K_5 + \gamma_r \left\{ K_5 - \frac{g_m y_j}{10} K_6 \right\} \right) - \frac{g_m^2}{2 y_j^2} \left( K_2 + \gamma_a \left\{ K_2 - \frac{g_m y_j}{4} K_3 \right\} \right) \right] \quad (5.2)$$

$$U_0(y_j) = \frac{4\pi\epsilon\sigma^6}{a_s} \sum_{n=0}^{\infty} \left[ \frac{2\sigma^6}{5(y_j + nd)^{10}} - \frac{1}{(y_j + nd)^4} \right] \quad (5.3)$$

$$f_m(x_j, z_j) = 2e^{i\mathbf{g}_m \cdot \mathbf{r}_j} \cos \left[ \mathbf{g}_m \cdot \frac{\mathbf{a}_1 + \mathbf{a}_2}{3} \right] \quad (5.4)$$

Here,  $d=1.38 a$  is the separation between successive layers of carbon atoms in graphite,  $a_s = \sqrt{3}a^2/2$  is the area of a unit cell of the graphite surface lattice and  $\mathbf{g}_m$  is the appropriate reciprocal lattice vector of magnitude  $g_m$ .  $K_l = K_l(g_m y_j)$  is the modified Bessel function of the second kind,  $\sigma$  and  $\epsilon$  are the Lennard-Jones parameters associated with the

graphite-adsorbate interaction,  $\gamma_r$  and  $\gamma_a$  are the anisotropic dispersion coefficients. The vectors  $\mathbf{a}_1$  and  $\mathbf{a}_2$  are the primitive lattice vectors of the graphite surface and  $a = 2.46\text{\AA}$  is the lattice constant of the graphite basal plane and  $\mathbf{r}_j$  is the position vector of atom  $j$  with Cartesian components  $x_j$ ,  $y_j$ , and  $z_j$ . It has been reported that the first term (i.e.,  $m = 1$ ) in the sum over  $m$  is sufficient enough for the study of adsorption of atoms and molecules on graphite [24, 25]. The summation appearing in the expression of  $U_0(y_j)$  given in Eq. 5.3 was truncated at  $n=100$ . The  $\sigma$  and  $\epsilon$  of the surface interactions in the Steele potential were chosen to be  $3.3\text{\AA}$  and  $47.72\text{K}$  for carbon and  $2.98\text{\AA}$  and  $17.0\text{K}$  for hydrogen respectively. The all-atom potential has bond stretching, bending, and torsional terms apart from a non-bonded term of the 6-exponential form. The simulations had no distance constraints between atoms in a molecule, thus necessitating a timestep of integration of 0.5 fs, which was determined by the fastest degree of freedom, i.e., the C-H vibration. The potentials of interaction between sites on alkane molecules were truncated at a distance of  $12\text{\AA}$ , and were shifted so that the value of the potential at the cutoff distance was zero. Long range corrections to energy or pressure were not applied as our system is a cluster. The interaction potential with the graphite lattice was not truncated.

Earlier simulations [8-10] have used an united atom model to study the melting of butane and hexane monolayers on graphite, and also to study the structure of fluid films of butane and  $n$ -decane as a function of coverage [18]. Such united atom models have also been used to study ultrathin liquid films of  $n$ -hexadecane on graphite [26]. Here, we have employed an all-atom approach in order to more accurately represent the steric effects that would arise in the solid state. In particular, we have included the explicit interactions of the hydrogen atoms with the graphite which is expected to be a key in the adsorption behaviour of alkanes. Physisorbed layers are a delicate balance of adsorbate and substrate forces and several possible molecular structures and orientations can have comparable energies. Such atomistic details are expected to be significant if we are to reliably calculate the rather subtle structural changes that occur e.g. as a function of

coverage. The use of an all-atom model for the study of dense phases of alkanes has been advocated earlier [27, 28].

The initial configurations of the molecules were obtained from the experimental neutron scattering data [14]. In the initial configuration of the three-layer system, the second and third layers were reproductions of the first layer displaced by about 5Å from the preceding layer. Typically, the systems were equilibrated for around 400 ps at 70 K, and were later subjected to thermal cycling, during which they were annealed at a temperature of 195 K for over 300 ps and were recooled back to 70 K. We believe that this annealing procedure allowed the system to evolve to its thermodynamically stable state without bias from the initial configuration. Structural properties were averaged over a time period of 200 ps at the final temperature of 70 K. In addition, we have adopted a rigorous methodology of performing the simulations for the monolayer and for the multilayer, starting from “reversed” initial configurations, i.e., simulations were also performed with the monolayer and the multilayer set up initially with intermolecular distances of 4.92Å, and 5.25Å respectively. In these simulations with reversed initial configurations, we noticed the sample to get considerably disordered due to annealing at 195K, and particularly so for the multilayer runs starting from an expanded lattice configuration. In this case, we found that annealing at a slightly reduced temperature of 160K for about 100 ps retains the ordering of the molecules, as well as enables them to explore the configuration space effectively. The corresponding monolayer configuration was annealed at 195K for 150 ps. The systems were then slow cooled to 70K at which temperature they were equilibrated for over 300 ps, followed by runs for structural analyses of duration 200 ps. These runs with “reversed” initial configurations were performed to test the robustness of the potential of interaction and the simulation procedures adopted here.

*In the following, we present and discuss the results obtained from the MD runs that started from the initial configurations appropriate to the coverage, unless stated otherwise.* The structures of the monolayer and the multilayer systems were studied using configu-

rations averaged over time. Instantaneous MD configurations at an interval of 5 ps were stored for analyses, and these were averaged over 150 to 250 ps to obtain the time averaged configurations. Such an averaging procedure is valid and is necessary to analyze the structure of heated crystals. In such situations, analyses of individual snapshots might be misleading due to phase mismatch between the atoms or molecules that need not be exactly at their equilibrium locations due to vibrations. The time averaging procedure is clearly invalid for molecules that are mobile; in the present case, for molecules in the periphery of the solid cluster. However, in all our analyses, we include *only* those molecules that are present in the core region of the cluster.

We have also calculated the neutron scattering intensity for scattering from the first adsorbed layer for the two coverages. In experiments, the scattering would arise from ordered domains of *n*-hexane which are oriented in different directions. This would amount to powder diffraction from the sample. In the absence of a periodic box, molecules in our simulation get disordered at the periphery of the large cluster. Thus correlations from such molecules should not be included in the calculation of structure factor. In practice, we visually define a large region that is ordered and molecules present within this region are taken to contribute to the structure factor. This rectangular region of linear dimensions around  $50\text{\AA}$ , is described by the box lengths,  $L_x$  and  $L_z$ , with the surface normal along the  $y$  direction. Note that this box has to be chosen such that the atomic configuration is periodic with respect to it. The crystal structure factor  $F_{hk}(q)$ , for a given set of Miller index  $(h, k)$  is given by the lattice sum,

$$|F_{hk}|^2 = \left\{ \sum_i b_i \cos[2\pi(hs_{x,i} + ks_{z,i})] \right\}^2 + \left\{ \sum_i b_i \sin[2\pi(hs_{x,i} + ks_{z,i})] \right\}^2 \quad (5.5)$$

where  $s_{x,i}$  and  $s_{z,i}$  are the scaled  $x$  and  $z$  coordinates of atom  $i$ . The scaled coordinates are obtained as the real coordinates divided by the box lengths defined above. The neutron scattering lengths are denoted by  $b_i$ . In order to make a comparison to experiments in which the samples are deuterated, the scattering lengths are taken to be 6.6484 fm and

6.674 fm for carbon and deuterium atoms respectively. The magnitude of the scattering vector  $q$  is given by the expression,

$$q = 2\pi \left[ \frac{h^2}{L_x^2} + \frac{k^2}{L_z^2} \right]^{\frac{1}{2}} \quad (5.6)$$

and the scattering angle  $2\theta$  is obtained from the relation,

$$q = \frac{4\pi \sin\theta}{\lambda} \quad (5.7)$$

where  $\lambda$  is the wavelength of the neutrons used, which is 2.42Å. The neutron scattering intensity calculated from MD simulations is a stick pattern in the intensity versus  $2\theta$  plot. Convolution of this stick pattern with the instrumental resolution function (lineshape function) leads to a continuous, line broadened intensity profile which can be compared with the experimental profile. The neutron scattering intensities were calculated from the structure factor  $F_{h,k}(q)$ , using such a lineshape function as outlined in Warren [29] and in Kjems et al [30], with the same parameters as that in Ref. [30].

In the lattice sum method of calculating the structure factor discussed above, one has to select the periodic box with care. However, the structure factor could as well be calculated from interatomic distances. We have employed the Debye scattering formula [31] to obtain the intensity as,

$$I(q) = \sum_i \sum_j b_i b_j \frac{\sin(qr_{ij})}{qr_{ij}} \quad (5.8)$$

where  $i$  and  $j$  denote atom indices,  $r_{ij}$  the distance between them, and the expression is a sum over all such interatomic distances in the system. This expression can be used to obtain the structure factor of a system with no obvious periodicity, or of a crystalline configuration with some amount of disorder. It is also not necessary to define the wave vectors in terms of a periodic box; hence a configuration that includes all the ordered region of the first adsorbed layer can be studied using this relation. We have also calculated

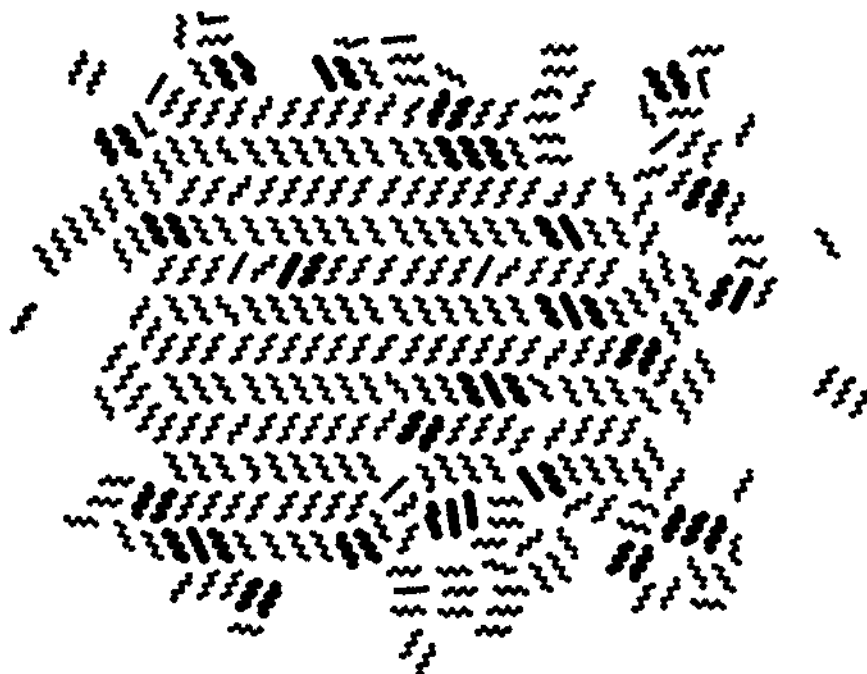


Figure 5.1: Top view of the time averaged configuration of the  $n$ -hexane monolayer on graphite. Molecules in black have at least one intermolecular distance between molecules in the same layer that is less than  $5.0\text{\AA}$ . Hydrogen atoms are not shown for clarity.

the neutron intensities using this procedure including a lineshape analysis as in Ref. [30].

### 5.3 Results and Discussion

The unitcell of  $n$ -hexane on graphite is experimentally found to be rectangular with lattice parameters  $5.30\text{\AA}$  and  $17.04\text{\AA}$  at sub-monolayer coverages and  $4.92\text{\AA}$  and  $16.9\text{\AA}$  at multilayer coverages [10, 14]. Comparing these unit cell parameters with those of the graphite substrate, we find that at both high and low coverage cases, the  $a$ -parameter of the unit cell is a multiple of the underlying graphite substrate,  $a_g$  ( $\sqrt{3}a_g=4.26\text{\AA}$ ). Only at multilayer coverages is the  $b$ -parameter of the unit cell commensurate with the underlying lattice. It is thus evident that there is a uniaxial compression of the lattice parameter,  $b$ , which decreases from a value of  $5.30\text{\AA}$  for submonolayer coverages to  $4.92\text{\AA}$  for multilayer coverages.





Figure 5.2: Top view of the time averaged configuration of the first adsorbed layer of *n*-hexane *multilayer* on graphite. Molecules in black have at least one intermolecular distance that is less than  $5.0\text{\AA}$ . Hydrogen atoms are not shown for clarity.

It is of interest to follow the evolution of this 'intermolecular' *b*-parameter with coverage. Since we have direct access to real space data in simulations, this change in intermolecular spacing can be easily identified and interpreted in real space. The top view of the time averaged configurations of hexane molecules on graphite are shown in Figure 5.1 and Figure 5.2. In Figure 5.1, we show the configuration of the monolayer at 70K. Molecules in black have at least one intermolecular distance that is less than  $5.0\text{\AA}$ , while the ones depicted in grey have intermolecular distances larger than this cutoff value. The average intermolecular distance in the monolayer along the *x*-axis is found to be  $5.31\text{\AA}$ . In Figure 5.2, we show the equivalent data for the three-layered system, where the top view of the first adsorbed layer is shown. The distance cutoff to distinguish between molecules depicted in black and grey is the same as in Figure 5.1. The difference between the two figures is evident; far fewer molecules in the monolayer have an intermolecular distance that is less than  $5.0\text{\AA}$ , unlike the case in the multilayer. The average intermolec-

ular distance in the multilayer is found to be  $4.93\text{\AA}$ , a value that signifies commensurate adsorption and which is in close agreement with the experimental data [13,14]. From Figures 5.1 and 5.2, one can also observe few molecules that do not belong to the cluster, but yet are physisorbed on the surface, which can be called “monomeric”. At 70K, we have found the core region of the first adsorbed layer to be essentially intact, without much loss of molecules to such a monomeric state. This shows that the system appears to be in a steady state within the time scales of the simulation. Additionally, we found no evidence of molecules desorbing from the substrate, even at 195K.

The reduced intermolecular distance for the multilayer coverage results in an increase in the density of the first adsorbed layer. The number of carbon atoms increases from a value of  $0.132\text{ \AA}^{-2}$  for monolayer coverage to  $0.144\text{ \AA}^{-2}$  for the multilayer coverage system, a significant increase of 9%. The compression of the lattice was observed even in a run where the initial configurations were chosen in the reverse manner, i.e., when the monolayer was set up with an initial intermolecular distance of  $4.92\text{\AA}$ , and the multilayer was set up with an initial intermolecular distance of  $5.25\text{\AA}$ . Averaged configurations for these two cases are shown in Figure 5.3, with the same coloring scheme as used in Figures 5.1 and 5.2. The monolayer configuration shown in Figure 5.3a, is largely devoid of molecules with intermolecular distances less than  $5.0\text{\AA}$ . The average intermolecular distance was found to be  $5.21\text{\AA}$ . This monolayer configuration has indeed expanded from its initial lattice constant of  $4.92\text{\AA}$  to the value reported above. The multilayer configuration shows the presence of one large region and few small regions containing molecules with intermolecular distances less than  $5.0\text{\AA}$  (molecules colored in black). Such regions are interspersed with small pockets of molecules with intermolecular distances larger than  $5.0\text{\AA}$ , but much less than the  $5.25\text{\AA}$  distance of the monolayer assembly. The average intermolecular distance in the region with molecules colored in black is found to be  $4.98\text{\AA}$ . This is a significant reduction when compared to the distance in the initial configuration that was  $5.25\text{\AA}$ . It is thus evident that the systems simulated here are robust enough to

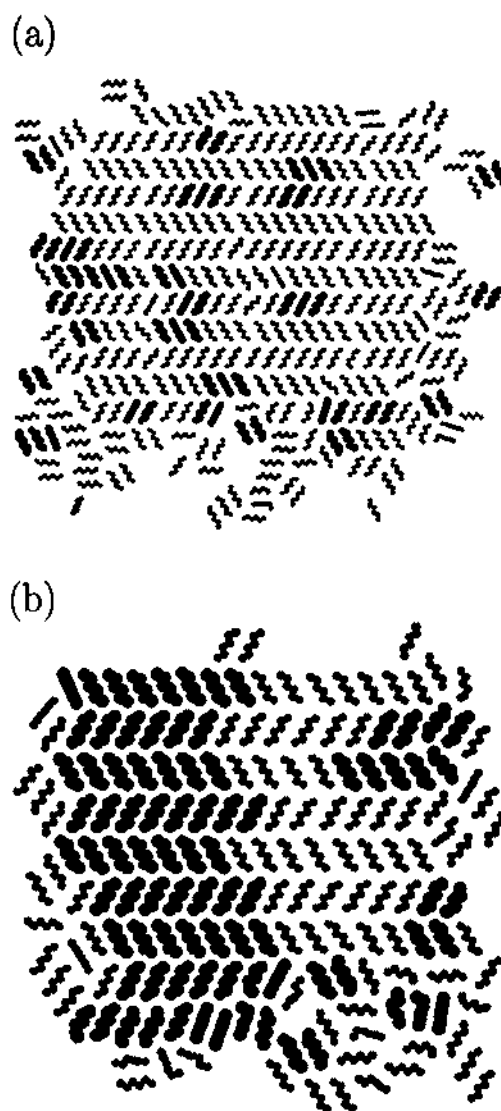


Figure 5.3: Top view of the time averaged configuration of the first adsorbed layer of *n*-hexane (a) monolayer and (b) multilayer on graphite. Here the initial configurations of the two runs were “reversed”, i.e., the monolayer run was started with a compressed lattice, and the multilayer run was started with an expanded lattice. Molecules in black have at least one intermolecular distance that is less than  $5.0\text{\AA}$ . Hydrogen atoms are not shown for clarity. The left hand side of the multilayer configuration contains molecules that have commensurately adsorbed to the graphite lattice as a large region.

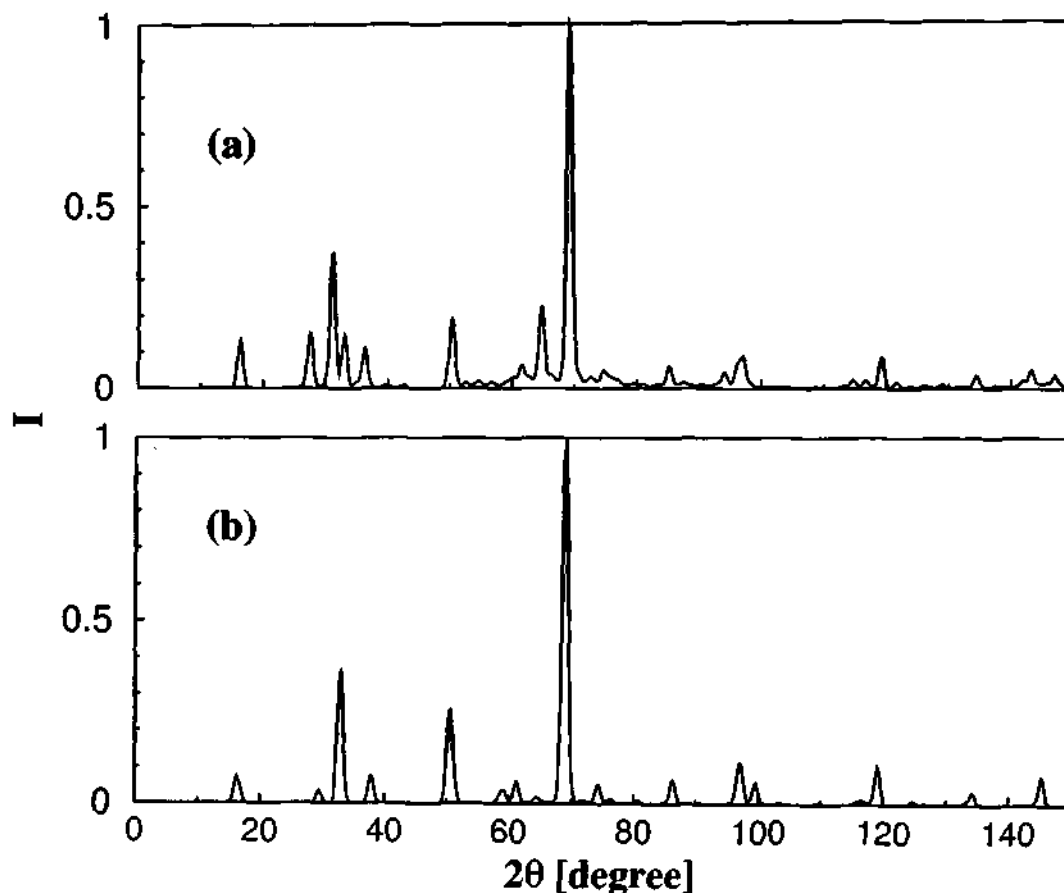


Figure 5.4: Neutron diffraction intensity as a function of scattering angle obtained from simulations using Eq. 5.5 at the two coverages. (a) is for the monolayer and (b) is for the multilayer coverage.

reproduce the lattice compression despite a drastic change in the initial conditions.

Thus, our simulations are able to reproduce the two key experimental observations:

- (i) the compression of the lattice while going from monolayer to multilayer coverages,
- (ii) the commensurate adsorption of *n*-hexane for multilayer coverages.

Groszek's model of adsorption of alkanes on graphite predicts the alkane molecules to be oriented with an angle of  $30^\circ$  with respect to the long axis of the alkane unit cell. We have calculated the distribution of this angle for the two systems studied here, and find it to be peaked at an angle of  $27^\circ$ , in close agreement with Groszek's model, and with diffraction experiments that obtain a value of  $25^\circ$  [13,14].

We next proceed to calculate the neutron scattering intensities. These were obtained

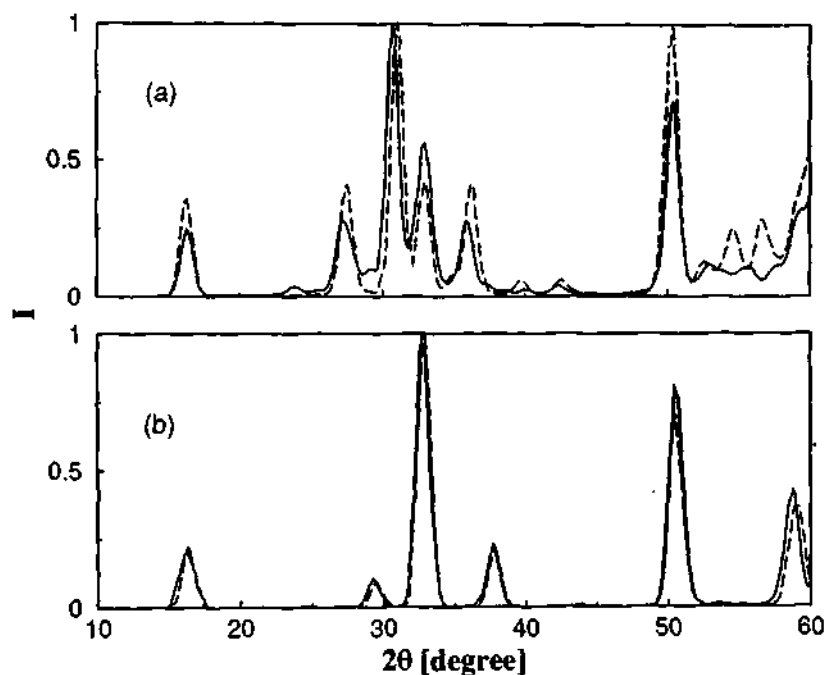


Figure 5.5: Neutron diffraction intensity as a function of scattering angle obtained from simulations using Eq. 5.5 for the (a) monolayer, and (b) multilayer systems starting from “reversed” initial configurations as shown in Figure 5.3. In each of the graphs, the continuous lines are for the “reversed” initial configurations, and the dashed lines are for normal initial configurations (the latter is same as in Figure 5.4).

from the structure factor using Eq. 5.5 and are shown in Figure 5.4 for both the coverages. The diffraction patterns obtained from simulations are in excellent agreement with experimental values for the peak positions and reasonable agreement for relative intensity. As expected, the peaks in the vicinity of  $30^\circ$  are shifted to higher angles for the multilayer coverage relative to the peak positions for the monolayer due to the compression of the lattice in the  $b$ -direction. The peak positions and intensities for the two coverages are compared to experiments in Tables 5.1 and 5.2, where the Miller indices  $(h, k)$  for the reflections obtained from simulations are also provided. Note that reflections  $(h, 0)$  with  $h$  odd, and  $(0, k)$  with  $k$  odd, are absent, consistent with the experimental identification of  $pgg$  as the space group. The neutron intensities obtained using a similar procedure for the runs with “reversed” initial configurations are shown in Figure 5.5. The similarity of the results between the two initial configurations, both for the multilayer and for

the monolayer is striking. In calculating the structure factor for the multilayer with the “reversed” initial configuration, we included only the large region found on the left hand side of Figure 5.3b that has molecules colored in black. These simulations have indeed been able to reproduce the lattice compression for the multilayer.

For completeness, we compare the results obtained from simulations without periodic boundary conditions with the ones that used them, in Figure 5.6. For the latter, the same procedure as in Eq. 5.5 was used, with the difference that the wave vectors were defined using the simulation box, and not with respect to a periodic lattice defined visually as for the former. The intensities shown in the figure are normalized with respect to the peak at around  $33^\circ$  for the case of multilayers, and with respect to the peak at around  $31^\circ$  for the monolayers. The agreement between the two data is quite good, both for the monolayer as well as for the multilayer, signifying that the absence of periodic boundary conditions in our simulations does in no way affect the results.

The neutron intensities obtained using the Debye formula, Eq. 5.8 is shown in Figure 5.7 for the two coverages. The diffraction patterns obtained from simulations are in excellent agreement with experimental values for the peak positions and in reasonable agreement for the relative intensities. As expected, the peaks in the vicinity of  $1.4\text{\AA}^{-1}$  are shifted to higher wavevectors for the multilayer coverage relative to the peak positions for

Experiment		Simulation		
$2\theta$	Intensity	$2\theta$	Intensity	(h,k)
16.30	0.26	16.30	0.35	(0,2)
27.77	0.50	27.50	0.40	(1,1)
31.37	1.00	31.04	1.00	(1,2)
33.03	0.16	32.95	0.39	(0,4)
36.40	0.18	36.24	0.29	(1,3)
50.59		50.35	0.51	(0,6)
65.31	1.33	64.70	0.59	(2,4)

Table 5.1: Peak positions and intensity ratios of calculated neutron scattering data for the *n*-hexane monolayer compared with experiment [14]. The intensities are normalized with respect to the feature near  $31^\circ$ .

Experiment		Simulation		
$2\theta$	Intensity	$2\theta$	Intensity	(h,k)
16.37	0.23	16.32	0.20	(0,2)
29.60	0.40	29.49	0.09	(1,1)
32.98	1.00	32.98	1.00	(0,4)
37.82	0.33	37.82	0.21	(1,3)
50.75	0.63	50.40	0.69	(0,6)
62.65	0.75	61.19	0.06	(2,2)

Table 5.2: Peak positions and intensity ratios of calculated neutron scattering data for the first adsorbed layer of a *n*-hexane multilayer system compared with experiment [14]. The intensities are normalized with respect to the feature near 33°.

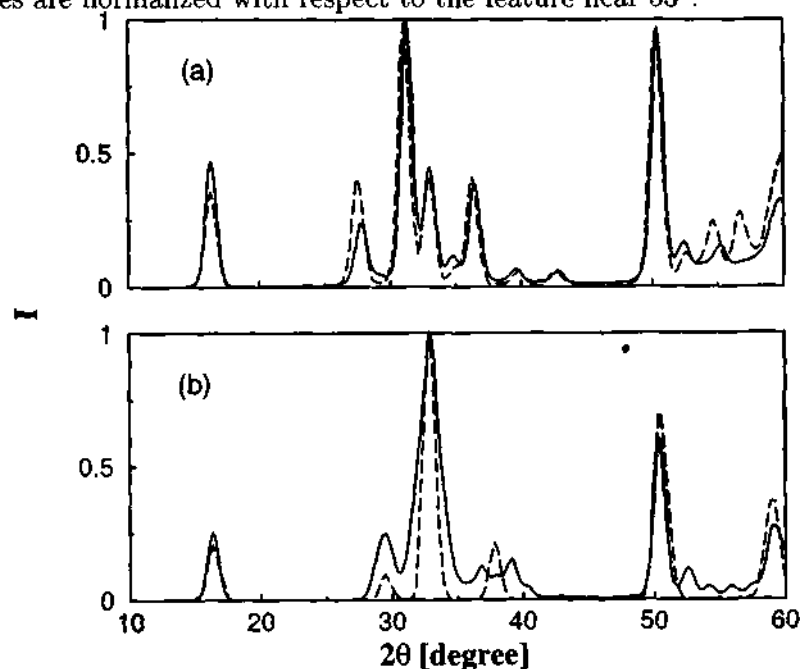


Figure 5.6: Neutron diffraction intensity as a function of scattering angle obtained from simulations using Eq. 5.5 for the (a) monolayer, and (b) multilayer systems for the runs with periodic boundary conditions. In each of the graphs, the continuous lines are for the runs with periodic cells, and the dashed lines are for runs with no assumed periodic boundary conditions (the latter is same as in Figure 5.4).

the monolayer due to the compression of the lattice in the *b*-direction and is in line with the observations in Figure 5.4. Miller indices corresponding to the observed features are also shown in the figure. Note again that reflections  $(h, 0)$  with  $h$  odd, and  $(0, k)$  with  $k$  odd, are absent, consistent with the experimental identification of *pgg* as the space group.

At the low temperature of 70K, a negligible population of gauche defects in the alkyl

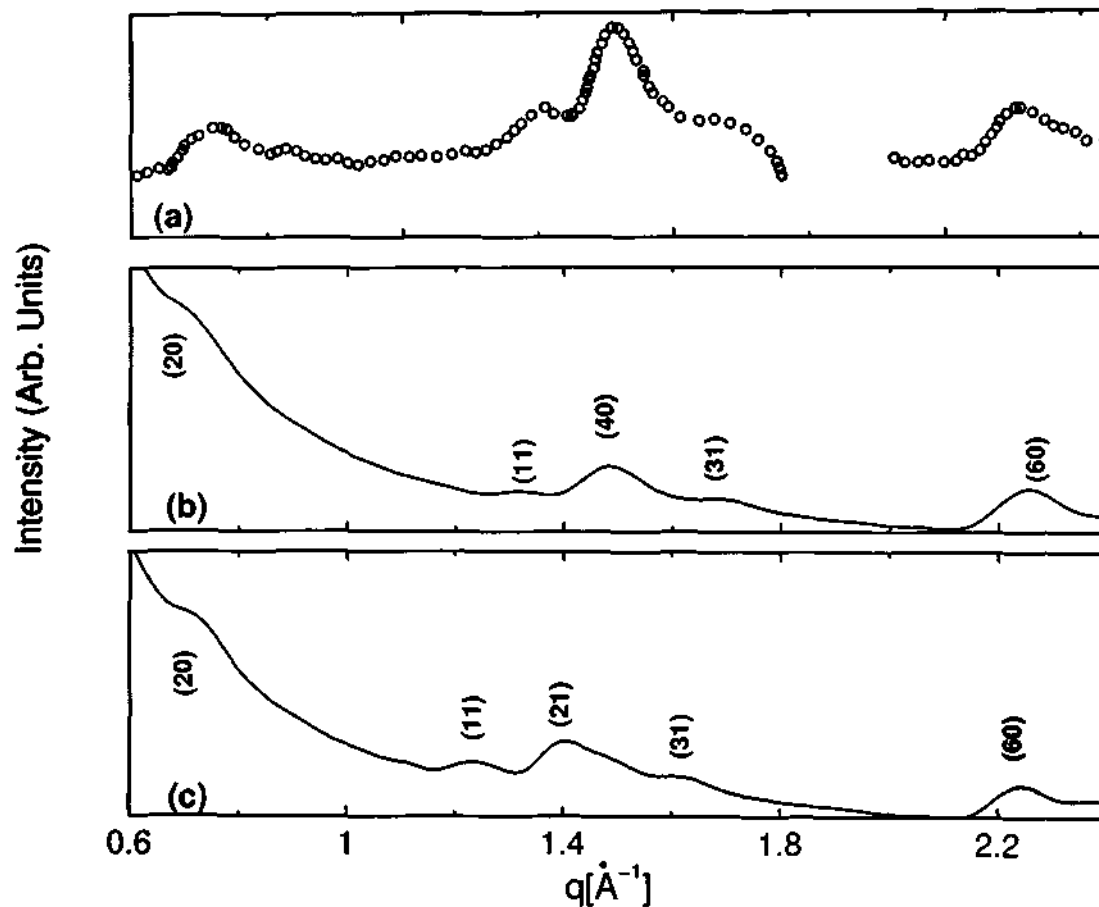


Figure 5.7: Neutron diffraction intensity as a function of wave vector. (a) Experimental data of Taub [34] for one complete monolayer at 165K, Simulation data using the Debye scattering formula, Eq 5.8 for (b) multilayer, and (c) monolayer coverages. Miller indices corresponding to the reflections are shown in brackets.

chains is to be expected. Our results indicate that indeed, in the ordered regions of the first adsorbed layer, all molecules are in the *all-trans* conformation. Although gauche defects are not particularly likely, molecular rotations about the long axis are possible. It has been well established by several workers that the preferred configuration of alkane molecules is to have their backbone zig-zag plane parallel to the surface [10, 32, 33]. We have studied this molecular orientation with respect to the surface. In Figure 5.8, we plot the distribution of the angle made by the normal of the backbone zig-zag planes of the molecules with the surface normal.

At the monolayer coverage, one can observe that a few molecules have their backbone



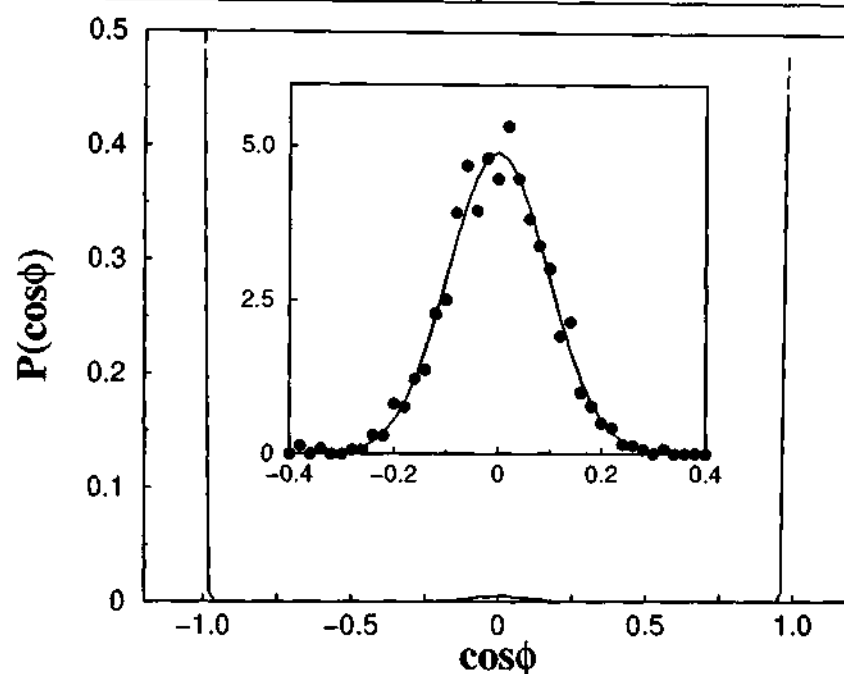


Figure 5.8: The distribution of the angle,  $\phi$ , between the normal of the zig-zag backbone planes of the hexane molecules with the substrate normal. Solid line is for the monolayer and the dashed line is for the first adsorbed layer of the multilayer. The two curves are nearly identical except at  $\cos\phi$  values around zero. Solid circles in the inset shows the data for  $\cos\phi$  values around zero in expanded scale (factor of one thousand) for the monolayer, while the corresponding function for multilayers is identically zero. The solid line in the inset is a Gaussian fit to the data and is shown as a guide to the eye.

plane rotated by  $90^\circ$ , while such excitations are not found in the first adsorbed layer for multilayer coverage. Integration of the data for the monolayer coverage between  $\cos\theta$  values of  $-0.4$  to  $+0.4$ , shows that around 6% of the molecules are oriented with their backbone planes perpendicular to the surface. This molecular rotation along the long axis possibly decreases the efficiency of packing resulting in an expanded lattice for the monolayer coverage. These molecular rotations are also discernible from the configurations shown in Figure 5.1, where most, but not all, molecules are found to be with their backbone planes parallel to the surface. This is unlike the case of the multilayer coverage (Figure 5.2), where all the molecules in the core region of the cluster are with their backbone planes parallel to the surface. We interpret these changes in molecular orientation to result in the increased compression in the lattice on increasing the coverage. Molecules

with backbone planes perpendicular to the surface do not have all their carbon atoms in favorable adsorption sites on the graphite lattice, and are thus not in the ground state.

## 5.4 Conclusions

We have employed isothermal molecular dynamics simulations to characterize the phase behaviour of ultra-thin films of *n*-hexane physisorbed on the basal plane of graphite. The aim of this work was to provide microscopic insights into the coverage depended structural changes exhibited by these molecular films. In these simulations, the atomic details of the graphite were not considered explicitly but their presence were incorporated through the anisotropic Steele potential [21–23] that almost accurately represents the surface corrugation and symmetry of the graphite. A flexible all-atom model was used for *n*-hexane molecules. The calculations were performed for two different film coverages : One, a full monolayer, and the other a system containing three layers of *n*-hexane. Two sets of simulations were performed : one in which periodic boundary conditions were not used in any of the three spatial directions while the other impose periodicity along the lateral directions of the film. We have made two key observations; (i) the uniaxial compression of the lattice, and (ii) the commensurancy of the first adsorbed layer, upon increase in coverage. We have also been able to calculate the neutron diffraction intensities for direct comparison with experiment. Excellent agreement in peak positions, and reasonable agreement in the intensity ratios, with experiments have been obtained. An examination of the angle that the molecular backbone makes with the surface reveals that at monolayer coverage, some molecules tend to rotate such that their zig-zag axis is perpendicular to the surface, while at multilayer coverages, all molecules have their backbone plane parallel to the surface. The latter results in the lattice compression. These observations were further confirmed through additional MD simulations which started from a compressed monolayer and an expanded multilayer.



# Bibliography

- [1] D.M. Small, *The Physical Chemistry of Lipids: From Alkanes to Phospholipids* (New York, Plenum, 1986).
- [2] A.I. Kitaigorodskii, *Molecular crystals and molecules* (New York, Academic, 1973).
- [3] A.J. Groszek, *Proc. Royal Soc. London Ser. A* **314**, 473 (1970).
- [4] B. Bhushan, J.N. Israelachvili, and U. Landman, *Nature (London)* **374**, 607 (1995);  
J. Gao, W.D. Luedtke, and U. Landman, *J. Chem. Phys.* **106**, 4309 (1997).
- [5] J.P. Rabe, and S. Buchholz, *Science* **253**, 424 (1991).
- [6] U.G. Volkmann, M. Pino, L.A. Altamirano, H. Taub, and F.Y. Hansen, *J. Chem. Phys.* **116**, 2107 (2002).
- [7] M.A. Castro, S.M. Clarke, A. Inaba, and R.K. Thomas, *J. Phys. Chem. B* **101**, 8878 (1997) ; M.A. Castro, S.M. Clarke, A. Inaba, T. Arnold, and R.K. Thomas, *J. Phys. Chem. B* **102**, 10528 (1998); M.A. Castro, S.M. Clarke, A. Inaba, T. Arnold, and R.K. Thomas, *Phys. Chem. Chem. Phys.* **1**, 5203 (1999).
- [8] F.Y. Hansen, and H. Taub, *Phys. Rev. Lett.* **69**, 652 (1992).
- [9] K.W. Herwig, Z. Wu, P. Dai, H. Taub, and F.Y. Hansen, *J. Chem. Phys.* **107**, 5186 (1997).
- [10] F.Y. Hansen, J.C. Newton, and H. Taub, *J. Chem. Phys.* **98**, 4128 (1993).

- 
- [11] G.H. Peters, and D.J. Tildesley, *Langmuir* **12**, 1557 (1996).
- [12] G.H. Peters, *Surf. Sci.* **347**, 169 (1996).
- [13] J. Krim, J. Suzanne, H. Shechter, R. Wang, and H. Taub, *Surf. Sci.* **162**, 446 (1985).
- [14] T. Arnold, R.K. Thomas, M.A. Castro, S.M. Clarke, L. Messe, and A. Inaba, *Phys. Chem. Chem. Phys.* **4**, 345 (2002).
- [15] M. Parrinello, and A. Rahman, *Phys. Rev. Lett.* **45**, 1196 (1980).
- [16] A. Cheng, and M.L. Klein, *Langmuir* **8**, 2798 (1992).
- [17] S.M. Clarke, A. Inaba, R.K. Thomas and J. Fish, *J. Phys. Soc. Jpn.* **70A**, 297 (2001).
- [18] S. Leggetter, and D.J. Tildesley, *Mol. Phys.* **68**, 519 (1989).
- [19] G.J. Martyna, M.L. Klein, and M. Tuckerman, *J. Chem. Phys.* **97**, 2635 (1992).
- [20] D.J. Tobias, K. Tu, and M.L. Klein, *J. Chim. Phys. PCB* **94**, 1482 (1997).
- [21] W.A. Steele, *Surf. Sci.* **36**, 317 (1973).
- [22] G. Vidali and M.W. Cole, *Phys. Rev. B* **29**, 6736 (1984).
- [23] Y.P. Joshi and D.J. Tildesley, *Mol. Phys.* **55**, 999 (1985).
- [24] W. A. Steele, A. V. Vemov, and D. J. Tildesley, *Carbon* **25**,7 (1987).
- [25] R. Hentschke, B.L. Schtirmann, and J.P. Rabe, *J. Chem. Phys.* **96**, 6213 (1992).
- [26] C.J. Mundy, S. Balasubramanian, K. Bagchi, J.I. Siepmann, and M.L. Klein, *Farad. Discuss.* **104**, 17 (1996).
- [27] J.P. Ryckaert, I.R. McDonald, and M.L. Klein, *Mol. Phys.* **67**, 957 (1989).
- [28] J.M. Polson, and D. Frenkel, *J. Chem. Phys.* **111**, 1501 (1999).

- 
- [29] B.E. Warren, *Phys. Rev.* **59**, 693 (1941).
- [30] J.K. Kjems, L. Passell, H. Taub, J.G. Dash, and A.D. Novaco, *Phys. Rev. B* **13**, 1446 (1976).
- [31] S.R. Elliott, *The Physics and Chemistry of Solids* (New York, Wiley, p 114, 1998).
- [32] K.W. Herwig, J.C. Newton, and H. Taub, *Phys. Rev. B* **50**, 15287 (1994).
- [33] S. Balasubramanian, M.L. Klein, and J.I. Siepmann, *J. Chem. Phys.* **103**, 3184 (1995).
- [34] H. Taub, in *The time domain in surface and structural dynamics* (Vol. 228, NATO ASI Ser. C, ed. G.J. Long, and F. Grandjean) (Kluwer, Dordrecht, p. 486, 1988).



## Chapter 6

# Phase Behaviour of Ultrathin Crystalline *n*-Heptane Films on Graphite: An Atomistic Simulation Study

### 6.1 Introduction

Adsorption studies of *n*-alkanes on the basal plane of graphite has gained considerable attention recently and interesting phenomena such as competitive adsorption [1], incommensurate to commensurate transitions [2–4], chain length dependent structural diversity, and mixing [5–7] have been explored. Functionalized alkanes, specifically studies of adsorbed linear chain alcohols have also been carried out [8]. Understanding the organization and phase behavior of such chain molecules is important to explore such diverse properties. Experimental techniques such as calorimetry [9–11], STM [12,13], LEED [2], neutron diffraction [14], incoherent elastic neutron scattering (IQNS) [14,15], NMR [16,17] and computer simulation methods [18–24] have played a vital role in understanding the struc-



tural and thermodynamics properties of these adlayers. The presence of solid layers at the interface has been confirmed by the IQNS studies, while the structural elucidation is accomplished through combined neutron and x-ray diffraction experiments. The temperature dependence of the elastically scattered intensity has been used to estimate the melting point of these adlayers. These have generally been found to be higher than the bulk melting temperature.

We give a brief overview of earlier studies on the thermal behavior of molecular films of *n*-alkanes physisorbed on graphite. Although such studies have a long history, a proper molecular level understanding of the structure and orientation of adsorbed molecules was first proposed by Groszek [9]. Based purely on calorimetric studies, he envisaged a model for alkanes physisorbed on graphite in which the hydrocarbon backbones lie parallel to the substrate while the hydrogens on the adhering side of the molecule are present at the centers of the carbon hexagons in the graphite basal plane.

Askadskaya *et al* have investigated the order-disorder transitions in *n*-alkanes (with chain length greater than 23) adsorbed on graphite using variable temperature STM [13]. At low temperatures, they have observed ordered lamellae consisting of molecules lying flat on the surface. Upon heating, near an order-disorder transition, the molecules were found to undergo anisotropic motions within the layer which leads to a dynamic roughening of the lamellae on the order of one methylene unit. Interestingly, the intermolecular distance within a lamella and the all-*trans* conformation of the molecules were found to be intact during this process of roughening.

While the modeling of adsorption of alkanes in zeolitic cages has attracted a wide attention [25,26], computer simulation studies of alkanes on graphite has been much fewer. Taub and coworkers have used a combination of neutron diffraction and molecular dynamics simulations to understand the melting of solid monolayers of both short length [22,24] and intermediate length [27] alkanes adsorbed on graphite. They have observed different melting behavior for the butane and hexane monolayers. Both exist in a herringbone

structure at low temperatures. The formation of rectangular centered crystalline patches coexisting with the fluid phase was observed for hexane monolayer across its melting transition, while an abrupt change in the orientational and translational order was observed for butane. In addition, they have demonstrated the essential role of conformational defects for the melting of hexane overlayer which is insignificant for butane monolayer. For higher alkanes, they have observed a simultaneous melting of intramolecular and lattice order thus making the molecules to adopt a more globular shape. An interesting observation that emerged from their study is that the "footprint reduction" mechanism, whereby the adsorbed molecules move perpendicular to the substrate thus creating vacancies in the crystalline lattice, plays a dominant role in the melting of long-chain alkane monolayer.

Combined neutron and x-ray diffraction studies along with calorimetry on adsorbed layers of *n*-heptane have yielded a wealth of information on their phase behaviour [4, 28]. At submonolayer coverage, an uniaxially commensurate structure is observed (i.e., commensurancy along the direction of the alkane backbone). At high coverages, the lattice undergoes a compression in the direction between near neighbour molecules, which leads to a fully commensurate structure. The uniaxially commensurated *n*-heptane film is found to melt at a lower temperature (151 K) than the fully commensurate structure (206 K). Note that bulk *n*-heptane melts at 183 K. Thus, in a narrow window of temperature between bulk melting and monolayer melting, Clarke and coworkers have been able to carry out remarkable scattering experiments to obtain the lattice structure of the buried layer [29]. The structure of the monolayer is obtained by subtracting the contributions from the liquid layers present above, and that from graphite.

Despite substantial efforts undertaken to explain the structure, dynamics, and melting of these quasi two-dimensional systems, a comprehensive understanding of these systems demands studies on several alkanes, through complimentary techniques. In this chapter, we report results on the temperature dependence of energy and structure of three different *n*-heptane films on graphite, using atomistic molecular dynamics simulations. Our study

thus complements the experimental work of Clarke and coworkers on *n*-heptane. As remarked earlier, our aim here is to study the melting behaviour of *n*-heptane films at two different in-plane densities and coverages. We have investigated three systems that include the two experimental structures corresponding to the submonolayer (UCM) and fully commensurate bilayer (FCB) systems. We have also examined the thermal behaviour of a model bilayer (UCB) with a uniaxially commensurate lattice, in order to find out whether the observed increase in the melting temperature is a consequence of the presence of the second layer or if it is due to an increased intralayer density in the first adsorbed layer. We also study the nucleation of “defect” molecular states – molecules that are rotated about their long axis such that their zigzag backbones are oriented normal to the surface. The temperature dependence of structural correlations between such molecules and its relationship to the melting of the film is also investigated.

## 6.2 Details of Simulation

Neutron and X-ray diffraction studies carried out by Clarke and coworkers have shown that *n*-heptane adsorbed on graphite forms an ordered structure with a centred rectangular unit cell [4,28]. The unit cell contains two molecules which are arranged with their backbone zig-zag planes parallel to the substrate. The initial configuration for the simulation of UCM and FCB consisted of *n*-heptane molecules lying flat on the substrate and forming a centred rectangular structure with corresponding lattice parameters taken from experimental data. The long-axis of the heptane molecules are oriented parallel to the unit cell vector,  $b_g$  of graphite. Atomic coordinates in the model UCB system was generated from the FCB structure by expanding the lattice along the b-axis. The starting configuration of the bilayer films consisted of two layers with the molecular backbones of the first layer are at a distance  $4.4\text{\AA}$  away from the substrate. An interlayer separation of  $4\text{\AA}$  was used between heptane molecules across layers. The initial configuration for the bilayer systems had the same molecular arrangement in the top layer as that in the

bottom layer. Each layer was rectangular in shape with linear dimensions,  $65.4\text{\AA}$  by  $80.58\text{\AA}$  for the uniaxially commensurate structures and  $66.0\text{\AA}$  by  $72.42\text{\AA}$  for the fully commensurate film. The UCB, FCB, and UCM systems contained 204, 204, and 102 molecules respectively.

The simulation box lengths were chosen such that they were nearly integral multiples of the periodicities of the graphite lattice. The basal plane consisted of 27 and 19 unit cells of graphite along x and z axes for uniaxially commensurate systems while the fully commensurate structure consisted of 27 and 17 graphite unit cells. Substrate-adsorbate interactions were included in the form of the Steele's potential [32–34] which was defined in the previous chapter. The Steele potential has earlier been used in a number of studies on the phase behaviour of atomic and molecular films adsorbed on graphite [18, 20, 21, 30, 31, 34–37].

An all atom model was used for *n*-heptane [38]. Such an interaction model has previously been used successfully to model the coverage dependent structural transition in *n*-hexane films on graphite [30, 31] as discussed in Chapter 5, and the behaviour of bulk crystalline *n*-heptane under pressure [39] reviewed in Chapter 4. The model is fully flexible, and contains intramolecular interaction terms that treat bond stretches, bends, and torsional excitations, as well as non-bonded interactions that are of the 6-exponential form. The simulations were carried out under constant temperature (NVT) conditions, achieved by attaching a Nosé-Hoover chain of thermostats to the system [40]. Periodic boundary conditions were applied along the two lateral directions and the system was open in the direction of the surface normal. The equations of motion were integrated with a time step of 0.5 fs to take into account the high frequency C-H stretching modes. We monitored the conserved quantity corresponding to the Nosé-Hoover chain dynamics method as a function of time, and the standard deviation in that quantity was found to be less than one part in  $10^4$ .

We have carried out the simulations over a wide temperature range between 150K and

325K for the bilayer systems and between 90K and 295K for the monolayer film with a resolution of 5K. The latter was started at a lower temperature than the bilayer films, to allow for the possibility of it melting at a lower temperature. At each temperature, the system was equilibrated for 100 ps followed by a production run of 100 ps during which the atomic coordinates were stored at every 1 ps. The configurations thus stored were used later to analyse the energetics and the structure of these adlayers. The equilibrated configuration obtained at a given temperature was used as the starting structure for the next higher temperature MD run.

## 6.3 Results and Discussion

### 6.3.1 Energetics

The delicate balance between the competing interactions such as surface-adsorbate and the adsorbate-adsorbate relative to thermal energy leads to densely packed ordered layers of linear alkanes on graphite. Thus, the onset of temperature induced structural disorder in such adlayers are dependent on the relative strengths of these competing interactions. Keeping this in mind, we monitor the intermolecular as well as the molecule-substrate interactions as a function of temperature. The intermolecular energy of a layer is defined as a sum of interaction energies of the molecules present in the layer with all other molecules in the system that are separated by not more than the interaction cutoff. In view of the different number of molecules present in the first adsorbed layer in the three different systems, and to account for changes in their number as a function of temperature, the total intermolecular energy is divided by the number of molecules present in the first layer to enable a proper comparison.

In Figure 6.1, we show the temperature dependence of intermolecular energy per molecule of the bottom layer for the three systems. The discontinuous change in the intermolecular energy per molecule for UCM around 250 K (Figure 6.1a) signifies the on-

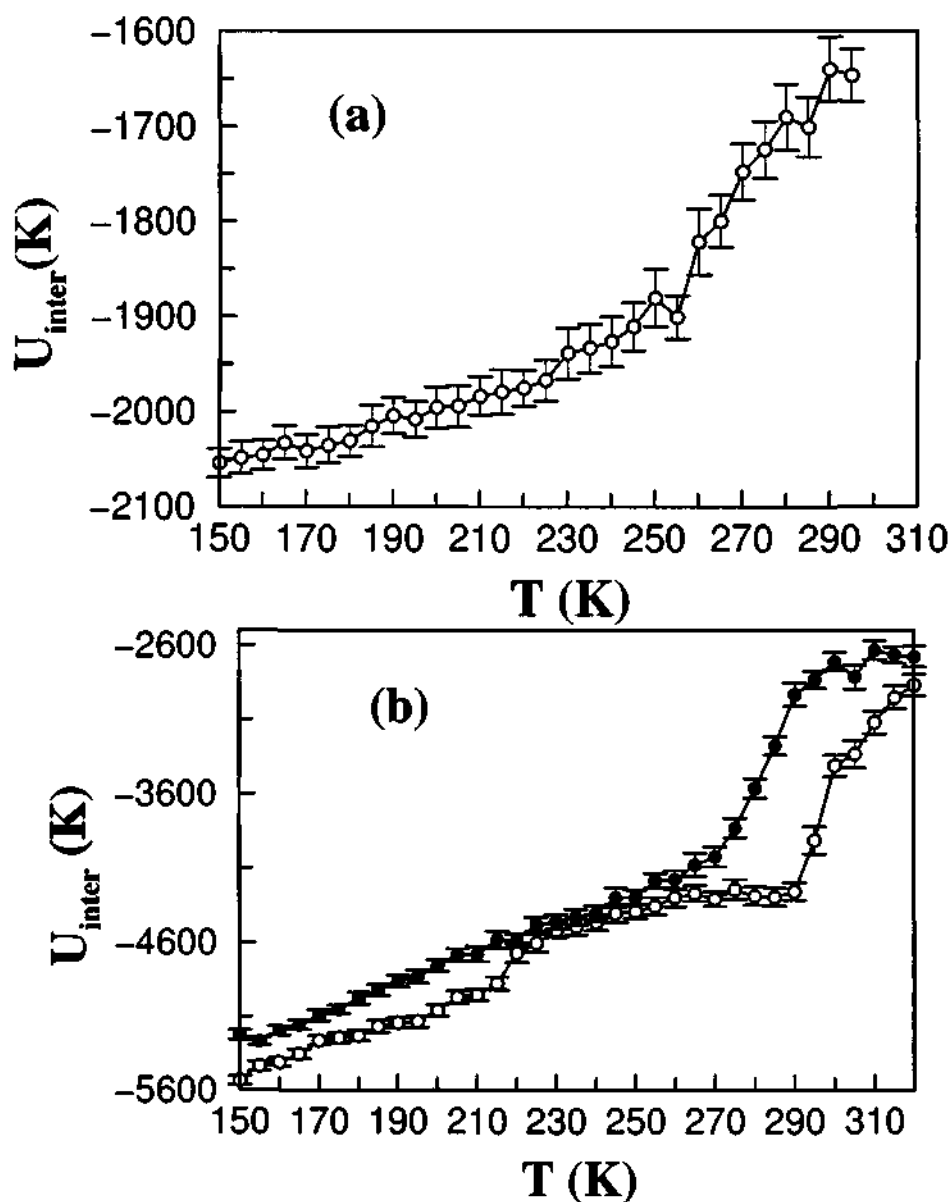


Figure 6.1: The intermolecular energy per molecule of the bottom layer is shown as function of temperature (a) UCM (b) FCB (solid line with open circles) and UCB (solid line with filled circles)

set of melting of this layer. Now, we compare its behavior with that of the bilayer systems (Figure 6.1b). At 150K, the molecules in the bottom layer of the FCB system are found to be energetically more stable than that of the UCB system. The stabilisation energy for a molecule in the first adsorbed layer of FCB over that in UCB is around 0.64 kcal/mol. Upon increasing the temperature, the intermolecular energy of the FCB shows two dis-

continuities, a minor one at 220 K and a major one at 290 K, while that corresponding to UCB shows only one discontinuity at 270 K. The large discontinuity (at 290 K for FCB and at 270 K for UCB) can be attributed to the melting of these layers. The slope change exhibited by the FCB around 220 K suggests the occurrence of structural changes at this temperature. Visualization of the atomic configuration of the first adsorbed layer of FCB indicates subtle structural changes.

In Figure 6.2, we show the instantaneous configuration of the fully commensurate bottom layer at two different temperatures: one below and one above 220 K. At 200 K, we find this layer to be perfectly ordered with molecules lying flat on the graphite substrate. For temperatures above 220 K, a fraction of molecules have rotated such that their CCC planes are perpendicular to the graphite substrate. Thus, 220 K is the onset temperature of molecular rotation that results in the weakening of intermolecular attraction seen in Figure 6.1. Interestingly, recent calorimetry studies on odd alkanes films adsorbed on graphite have also suggested a possibility for an additional phase change below the melting transition [41].

Figure 6.3 shows the substrate potential per molecule for the bottom layers corresponding to different systems. The discontinuities at 250 K for UCM, at 290 K for FCB and at 270 K for UCB can be ascribed to the melting of these layers. The relative stability of the FCB structure compared to the UCB system can be seen in the substrate interaction energy as well. At 150K, each molecule in the bottom layer of FCB experiences a stronger attraction from the graphite substrate than that in UCB system, the difference in energy being 0.576 kcal/mol.

### 6.3.2 Density profile

We have analysed the density distributions of both the atomic and the centers of mass of heptane molecules along the direction normal to the graphite basal plane, as a function of temperature. In our calculations, the substrate normal was oriented along the  $y$ -axis

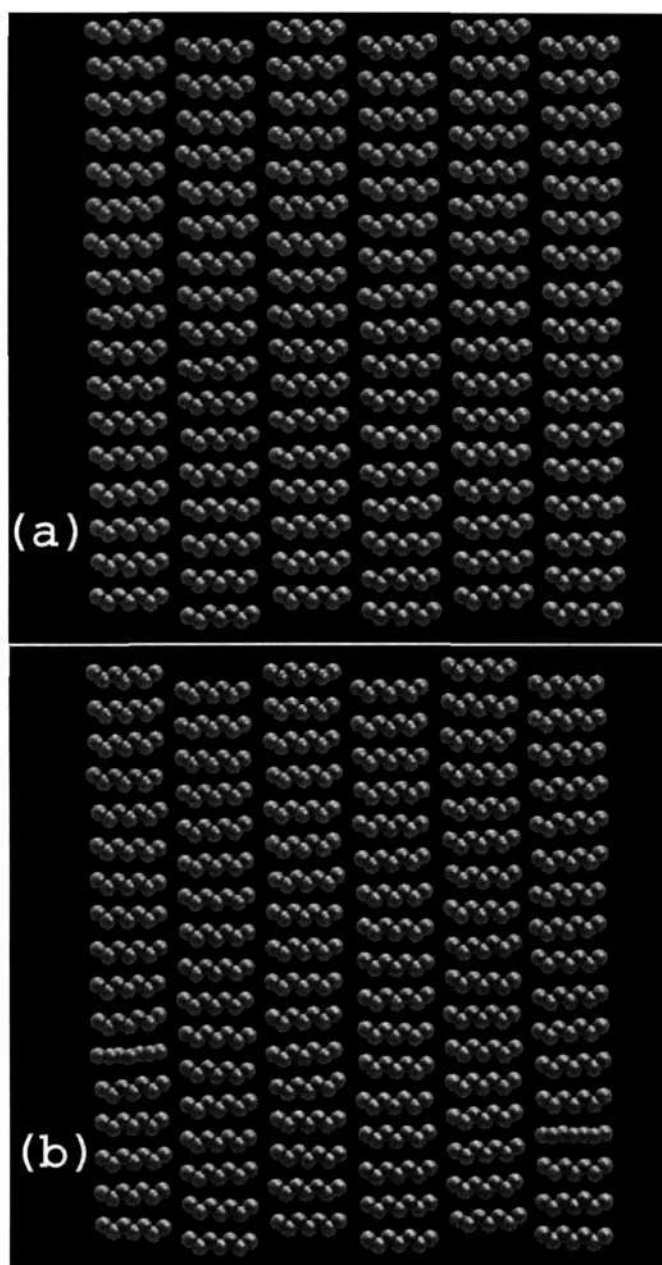


Figure 6.2: A snapshot of the atomic configurations exhibited by the bottom layer of FCB is shown at two different temperatures: (a) 200 K and (b) 230 K. The view is along the direction normal to the substrate. The hydrogens are not shown for clarity. Note the molecules that are rotated along their long axis at the leftmost and the rightmost column.

of the Cartesian coordinate system while the  $xz$ -plane was parallel to the adlayers.

We first present the distribution of the density of centers of mass of heptane molecules with respect to the substrate in Figure 6.4. The data for UCM shown in Figure 6.4a



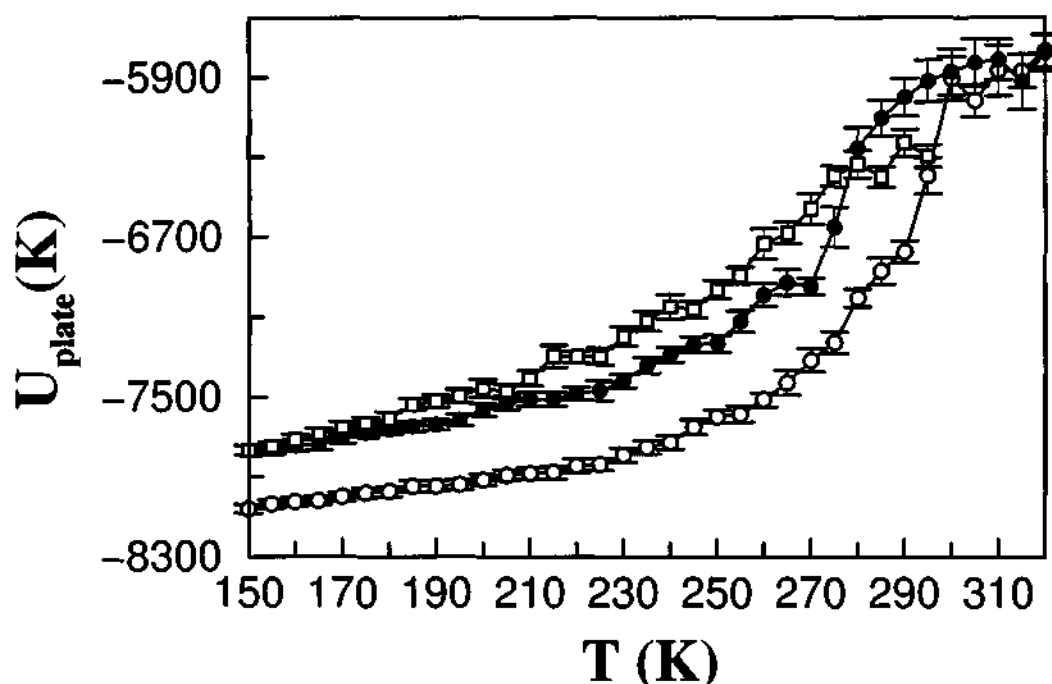


Figure 6.3: The substrate interaction energy per molecule of the bottom layer is shown as function of temperature for UCM (solid line with open squares), FCB (solid line with open circles), and UCB (solid line with filled circles)

exhibits a sharp peak at  $3.55\text{\AA}$  indicating the presence of an ordered solid monolayer at low temperatures. The peak intensity decreases with increasing temperature. However, the peak position is found to be intact up to 250 K. Thereafter, it shifts to higher distances due to increased molecular mobility away from the substrate coincident with the melting of this monolayer. At 150K, both the FCB (Figure 6.4b) and the UCB (Figure 6.4c) exhibit sharp peaks at around  $3.55\text{\AA}$  and a relatively broader peak at  $7.5\text{\AA}$  (not shown). The broadness in the second peak indicates that the second layer is considerably disordered even at the lowest temperature employed here. The peaks corresponding to the FCB are taller than that of UCB due to its increased in-plane density. With increasing temperature, the intensity of the second peak decreases followed by a shift in peak position to higher distances away from the graphite. Further, the intensity of the first layer which was almost constant up to 220 K (190 K for UCB), starts to decrease for temperatures above 220 K (190 K for UCB). While the intensity of the first peak decreases rapidly with temperature in the range between 220 K and 290 K (190 K and 270 K for UCB), its position however

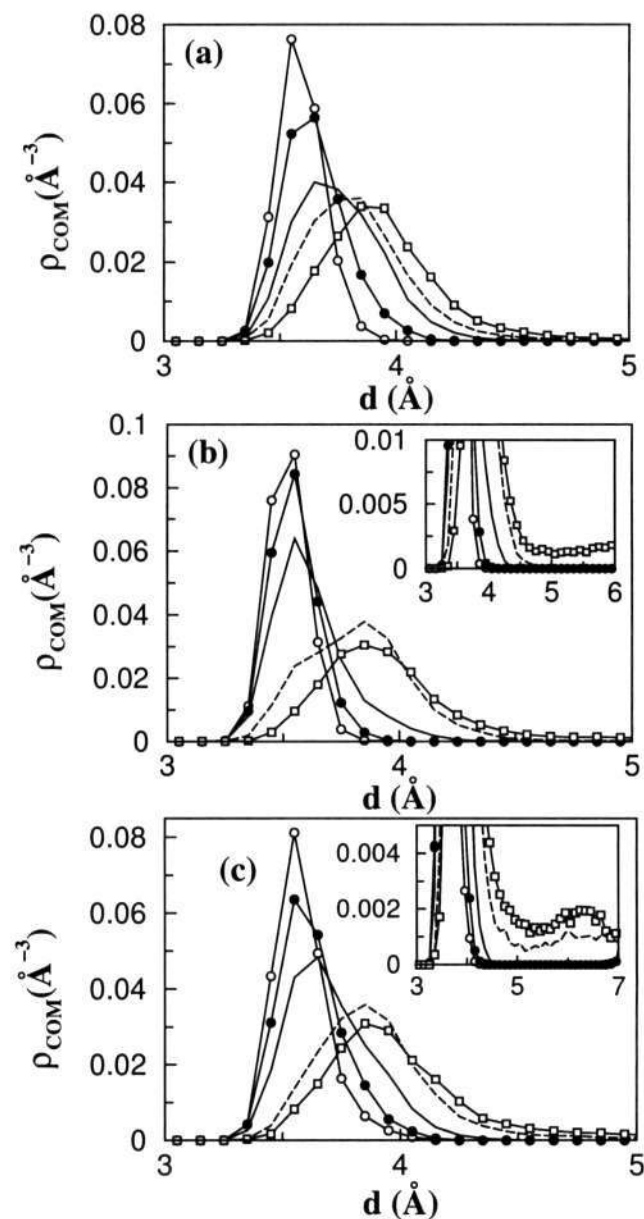


Figure 6.4: The density profile of the centers of mass of *n*-heptane molecules,  $\rho_{COM}(d)$ , is shown at various temperatures for different systems along the direction normal to the substrate. Here,  $d$  is the perpendicular distance of the centers of mass of *n*-heptane molecule from the substrate. Inset in (b) and (c) shows the same in expanded scale. (a) UCM at selected temperatures : 150 K (solid line with open circles), 200 K (solid line with filled circles), 240 K (solid line), 260 K (dashed line), and 295 K (solid line with open squares) (b) FCB at selected temperatures : 150 K (solid line with open circles), 200 K (solid line with filled circles), 250 K (solid line), 290 K (dashed line), and 310 K (solid line with open squares) and (c) UCB at selected temperatures : 150 K (solid line with open circles), 200 K (solid line with filled circles), 250 K (solid line), 280 K (dashed line), and 320 K (solid line with open squares).

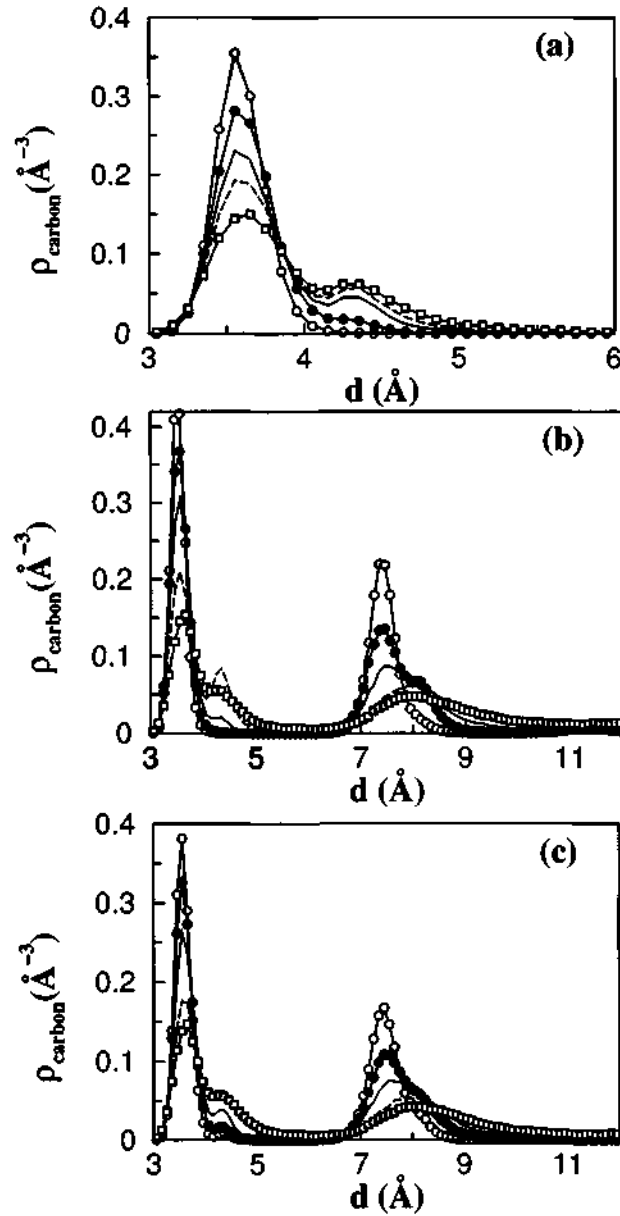


Figure 6.5: The density profile of carbon atoms,  $\rho_{\text{carbon}}(d)$ , is shown at various temperatures for different systems along the direction normal to the substrate. Here,  $d$  is the perpendicular distance of the carbon atom from the substrate. (a) UCM at different temperatures : 150 K (solid line with open circles), 200 K (solid line with filled circles), 240 K (solid line), 260 K (dashed line), and 295 K (solid line with open squares) (b) FCB at different temperatures : 150 K (solid line with open circles), 200 K (solid line with filled circles), 250 K (solid line), 290 K (dashed line), and 310 K (solid line with open squares) and (c) UCB at different temperatures : 150 K (solid line with open circles), 200 K (solid line with filled circles), 250 K (solid line), 280 K (dashed line), and 320 K (solid line with open squares).

is constant. For temperatures above 290 K (270 K for UCB), we observe a significant shift in this peak position to higher distances. Note that the broadening of the density distribution is due to molecular disordering (see later) while the shift in peak position could be due to both conformational defects as well as due to desorption.

Thus, we conclude that the bottom layer of FCB melts at 290 K (270 K for UCB). We show in Figure 6.5, the density profile for the carbon atoms with respect to the graphite. The temperature dependence of these distributions is quite similar to that of the molecular centers of mass except for a small feature at  $4.35\text{\AA}$ . We find this feature to be present in all the systems that we have investigated, below their respective melting points. For FCB (Figure 6.5b), this peak appears at 220 K and its intensity continues to increase with temperature. In contrast, for the UCB (Figure 6.5c), we observe this peak even at 150 K but its intensity does not change up to 190 K and continues to increase with temperature thereafter. The increase in intensity of this peak, above 220 K for FCB (190 K for UCB and 155 K for UCM (Figure 6.5a)) suggests that some of the CCC planes of a few molecules present in the bottom layer may have rotated such that they lie perpendicular to the substrate (see later).

### 6.3.3 Orientation of molecular zig-zag plane

In order to understand the molecular disordering processes that are responsible for the melting of these layers, we monitor the orientation of their backbone zig-zag planes with the basal plane of graphite. We calculate the distribution of the angle between the normal to the substrate plane and the normal to the plane formed by three consecutive carbon atoms of a heptane molecule.

In Figure 6.6, we show this distribution for the bottom layers of different systems at few temperatures. Up to 155 K, the distribution corresponding to UCM (Figure 6.6a) shows sharp peaks near  $\cos\eta=\pm 1$  indicating that all the molecules in the monolayer have their CCC planes parallel to the graphite substrate. For temperatures above 155 K,

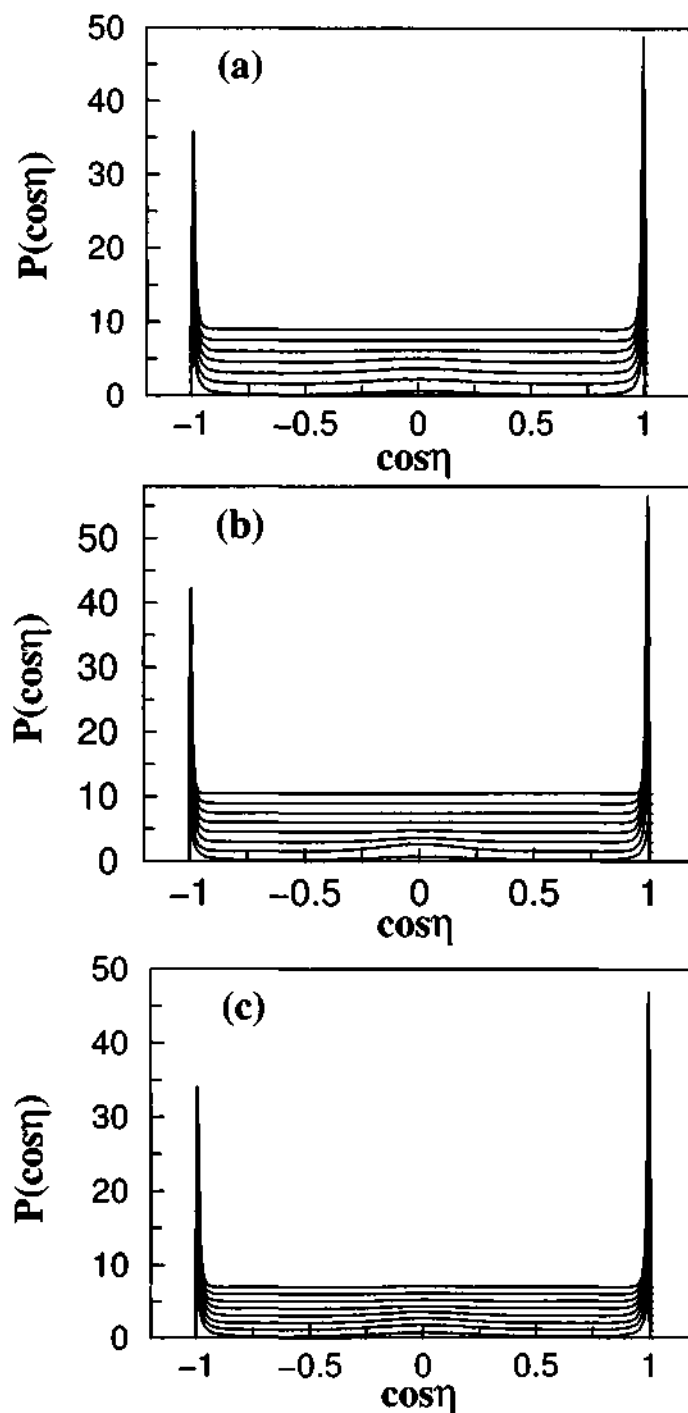


Figure 6.6: The distribution of cosine of the angle,  $\eta$ , between the graphite substrate and the plane formed by three consecutive carbon atoms of a heptane molecule present in the bottom layer is shown. (a) UCM at temperatures (from top to bottom) : 150 K, 160 K, 200 K, 240 K, 260 K, 280 K, and 290 K. (b) FCB at temperatures (from top to bottom) : 150 K, 200 K, 220 K, 230 K, 250 K, 270 K, 290 K, and 320 K. (c) UCB (from top to bottom) : 150 K, 175 K, 200 K, 230 K, 250 K, 260 K, 280 K, and 300 K.

an additional peak at  $\cos\eta=0$  appears, due to molecules which are rotated such that their CCC planes perpendicular to the graphite substrate. Thus, 155 K denotes the onset temperature for the molecules in the UCM to rotate about their long axis. We now discuss the results pertaining to the bilayer systems. At 150K, the distribution corresponding to the bottom layer of FCB (Figure 6.6b) is sharply peaked at  $\cos\eta=\pm 1$ , while that of UCB (Figure 6.6c) shows an additional peak at  $\cos\eta=0$ . The feature at  $\cos\eta=0$  indicates that few of the backbone CCC planes of the molecules in the bottom layer of UCB have oriented perpendicular to the substrate in view of its lower density. A similar feature appears for the bottom layer of FCB only for temperatures greater than 220 K. The intensity of this feature rapidly increases with temperature up to the melting point of 290 K (270 K for UCB). This disordering process has previously been called "footprint reduction" mechanism for these quasi-two dimensional systems [22, 24]. Above 290 K (270 K for UCB),  $P(\cos\eta)$  exhibits an almost uniform distribution for the bottom layer indicating that the system has reached an isotropic melt state.

A comparison of this data with experiment is in order now. Neutron scattering data on high coverage of *n*-heptane indicated that the molecules were rotated such that their zig-zag plane lies at an angle of  $45\pm 20^\circ$  with the substrate [4]. The position of the major peak in the distributions for the corresponding simulated system, FCB shown in Figure 6.6b is present at a value of 0.995 which translates into an angle of only  $6^\circ$ . This apparent difference with the experimental data is misleading and needs further elaboration. The distribution of  $\cos\eta$ ,  $P(\cos\eta)$ , discussed above has been obtained by averaging over all backbone CCC planes and over all molecules as a function of time. A striking feature of the distribution is the presence of two distinct states for the molecular zig-zag planes – either they are parallel to the substrate or perpendicular to it. We pose the following question: How facile are axial rotations of molecules so as to change the molecular backbone orientation from one state to another? At 270K, i.e., around 20K below the melting transition of FCB, we indeed observe quite a number of such molecular axial rotations. In

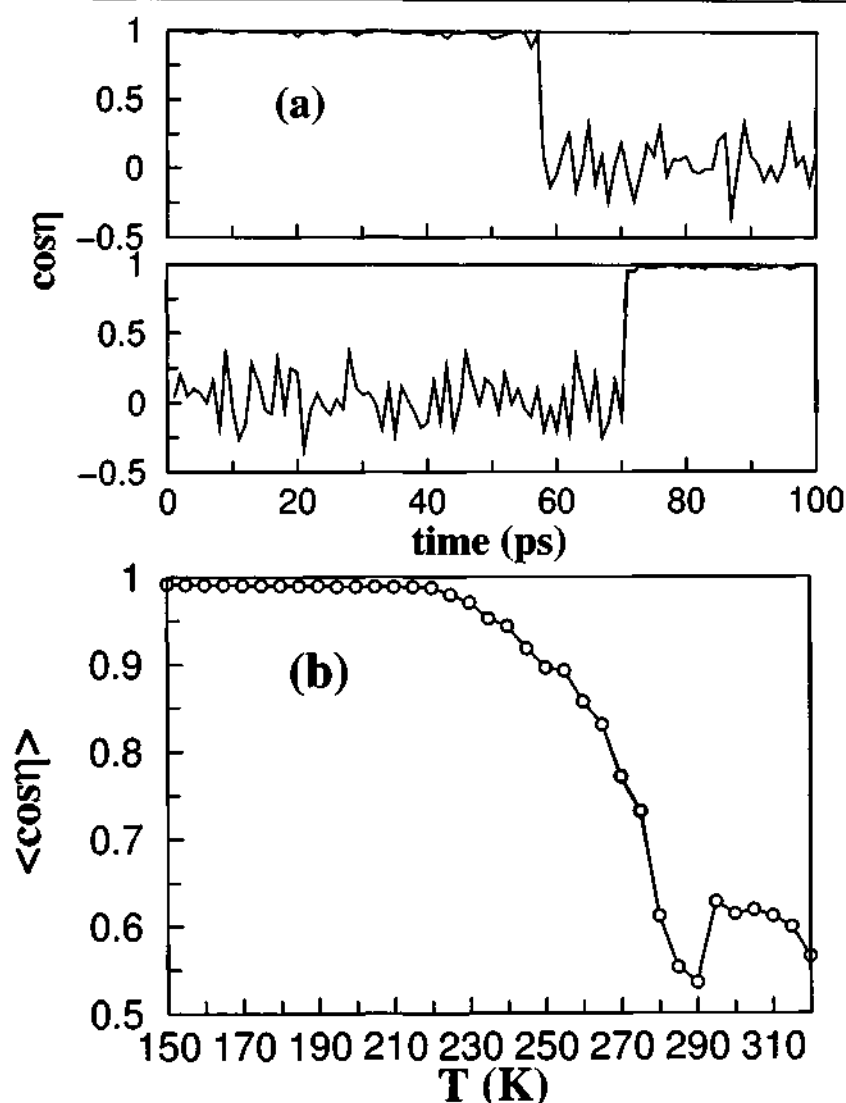


Figure 6.7: (a) The time evolution of  $\cos \eta$  of two arbitrarily selected molecules present in the bottom layer of FCB at 270 K.  $\eta$  is the angle made by the central zig-zag plane with the plane of the graphite. Behaviour of the other four planes in these molecules follow the same trend as the central CCC plane. (b) Temperature dependence of  $\langle \cos \eta \rangle$ , defined as in Eq. 6.2 for the molecules present in the bottom layer of FCB.

Figure 6.7a, we present the time evolution of  $\cos \eta$  corresponding to the central CCC plane of two arbitrarily selected molecules present in the bottom layer of FCB at 270 K. Since the behaviour of other four planes in these molecules follow the same trend as the central CCC plane, we do not provide their time evolution data here. The zig-zag plane of one of the molecules is flat on the substrate up to 57 ps and later it undergoes an axial rotation

such that all the CCC planes concertededly reorient perpendicular to the substrate. The second highlighted molecule has its zig-zag plane perpendicular to the substrate to start with, and after 70 ps it goes parallel. These single molecule events of axial rotation were observed for 12 molecules (out of a total of 102 molecules in this layer) at this temperature within our observation window of 100ps.

In view of the interesting dynamics exhibited by the molecules at temperatures close to, but below the monolayer melting, a comparison to experiment is possible only by calculating the mean (first moment) of  $\cos\eta$  from these distributions. We first define a folded distribution,  $P_f(\cos\eta)$  as

$$P_f(\cos\eta) = P(\cos\eta) + P(-\cos\eta) \quad (6.1)$$

The mean value of  $\cos\eta$  is thus,

$$\langle \cos\eta \rangle = \frac{\int_0^1 \cos\eta P_f(\cos\eta) d\cos\eta}{\int_0^1 P_f(\cos\eta) d\cos\eta} \quad (6.2)$$

In Figure 6.7b, we show  $\langle \cos\eta \rangle$  as a function of temperature for the molecules in the bottom layer of FCB. The value of  $\langle \cos\eta \rangle$  remains almost constant at unity for temperatures up to 220 K and starts decreasing thereafter. At 290 K,  $\langle \cos\eta \rangle$  stays close to 0.5 which is the value expected for a disordered liquid state. Bulk *n*-heptane melts at 182.4K, while the monolayer coexisting with its liquid is reported to melt at 206K [29, 41]. Neutron scattering studies on the system of monolayer coexisting with the liquid was performed at 190K [4], while that for the submonolayer was performed at 50K. The experiments concluded that the molecules in the former showed an axial rotation of 45°, while those in the latter had their zig-zag planes parallel to the substrate (i.e., an angle of 0°). We believe that the difference could arise not only due to the compressed lattice in the FCB (as rightly concluded in experiments) but also due to thermal excitations. Thus, in order for a proper comparison between experiments and the current simulations (in which the



systems exhibit superheating effects), one needs to arrive at a observation temperature in simulations that is equivalent to 190K (at which experiments were carried out for FCB). By scaling the temperatures of melting of the system of monolayer coexisting with the liquid between experiment and simulation (206K versus 290K), we arrive at this equivalent temperature for simulations to be 267K. The value of  $\langle \cos \eta \rangle$  for the FCB system at 270K is 0.77 which yields an axial angle,  $\eta$  of around  $40^\circ$ , in close agreement with the experimental finding. As mentioned earlier, experiments were performed at a very low temperature of 50K for the UCM system using neutrons and at 10K with x-rays. Hence no thermal excitations of rotations of molecular long axis is possible and a comparison to simulation is direct and perfect.

#### 6.3.4 Torsional distribution

In the previous subsection, we discussed the rotation of molecular backbone planes in these ultrathin films. Do these rotations involve a torsional excitation, or do they involve the full rotation of the molecule about its long axis? In order to resolve this issue, we have calculated the distribution of torsional angles of the molecules present in the bottom layer. We show in Figure 6.8 the distribution of the torsional angle around the C-C bonds of the heptane molecules. For the systems that we have investigated, at low temperatures, all the C-C torsions corresponding to the molecules in the bottom layer are in all-trans conformation which produces a sharp peak around  $180^\circ$  in the distributions. For FCB (Figure 6.8b), we do not find much change in this distribution even for temperatures up to 270 K. At temperatures higher than 270 K this function exhibits additional peaks in the distribution around  $60^\circ$  and  $300^\circ$  corresponding to the *gauche*(+) and *gauche*(-) conformational defect states respectively. Thus, the onset of conformational defects for the molecules in the bottom layer of FCB occurs at 270 K. Similarly, the distribution for UCM (Figure 6.8a) exhibit a few *gauche* defects for temperatures greater than 165 K. The relative difference between the the onset of molecular rotation and the conformational de-

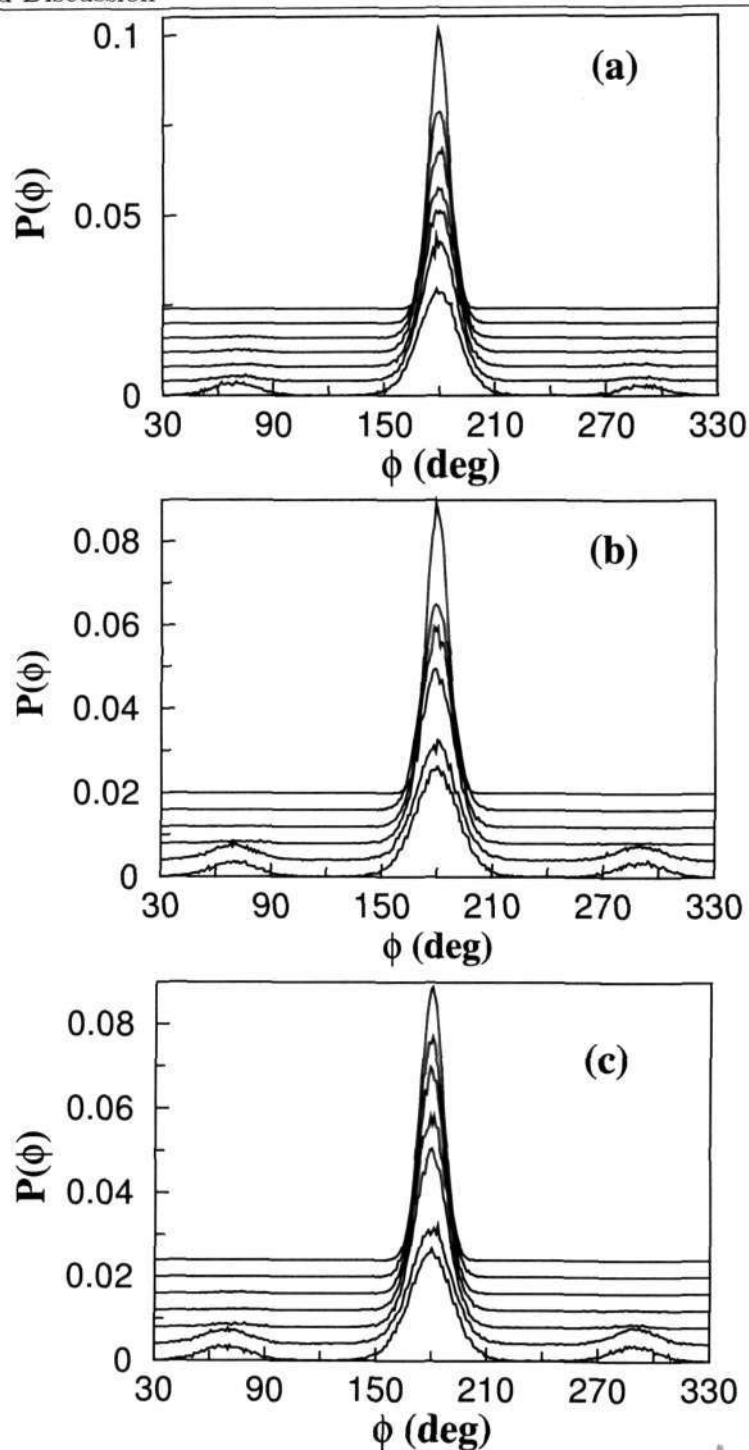


Figure 6.8: The C-C torsional distribution of molecules present in the bottom layer is shown at temperatures for various systems. (a) UCM at temperatures (from top to bottom) : 100 K, 160 K, 190 K, 220 K, 240 K, 260 K, and 290 K. (b) FCB at temperatures (from top to bottom) : 150 K, 250 K, 270 K, 290 K, 300 K, and 320 K. (c) UCB (from top to bottom) : 150 K, 190 K, 210 K, 250 K, 270 K, 300 K, and 320 K.

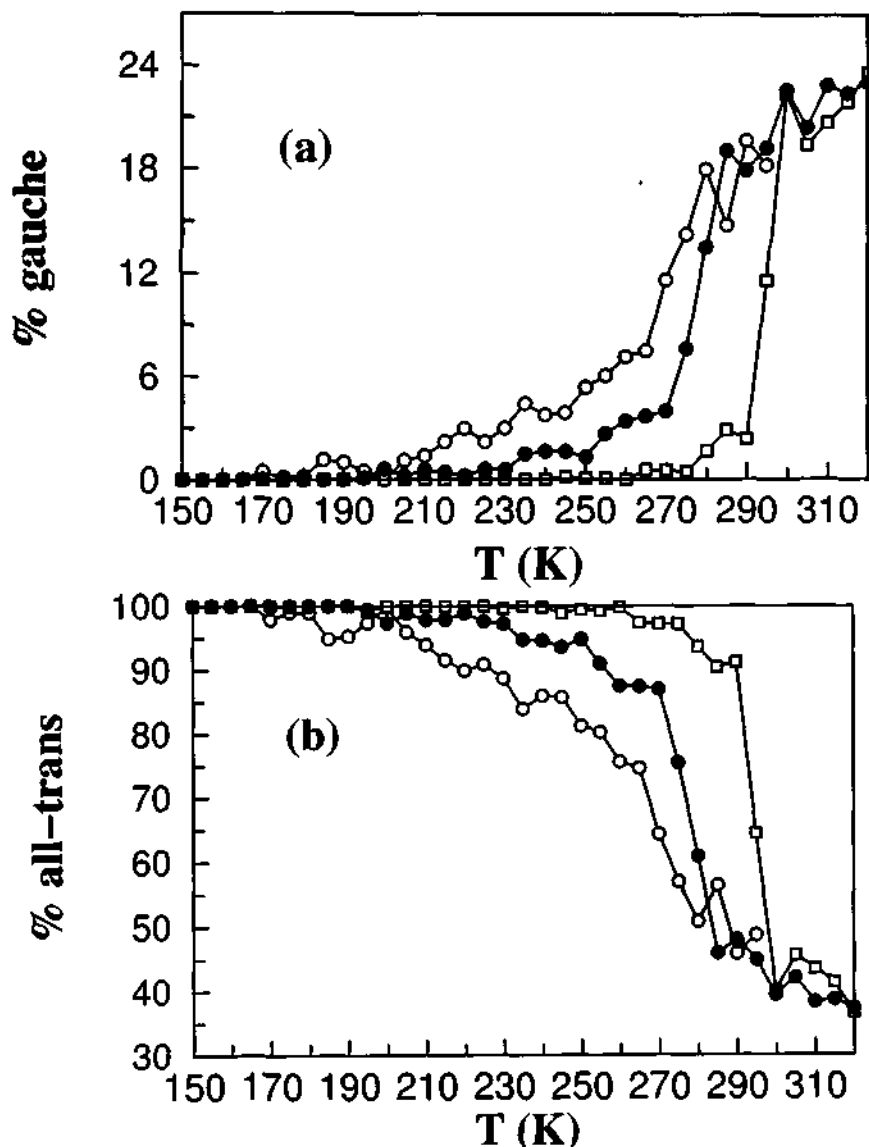


Figure 6.9: Temperature dependence of (a) the percentage of *gauche* defects and (b) the percentage of all-trans molecules in the bottom layer are shown for UCM (solid line with open circles), FCB (solid line with open squares), and UCB (solid line with filled circles)

fect is 50 K for FCB while it is 10 K for the UCM. In Figure 6.9a, we present the evolution of the percentage of *gauche* states in the bottom layer as a function of temperature. The concentration of *gauche* states for the bottom layer of FCB is almost zero up to 270 K and increases continuously thereafter. It changes abruptly at around 290 K (270 K for UCB) corresponding to the melting of this layer. We have calculated the distribution of *gauche* defects along the backbone of molecules present in the first adsorbed layer of FCB

and the results are shown in Figure 6.10. It is evident from this figure that the propensity of gauche defect formation is higher at the chain ends, as expected. The percentage of such end *gauche* defects increases considerably upon melting. However for temperatures below melting, such defects are rather few, with less than 1% of end torsions being in the *gauche* state. We calculate the percentage of molecules that possess all their torsional angles in the trans conformation. These results are shown in Figure 6.9b. Almost all the molecules in the bottom layer remain in their all-trans conformation up to 260 K in FCB (190 K for UCB and 165 K for UCM) and thereafter the formation of conformational defects gradually decreases the all-trans population. The discontinuous jump at 290K for FCB (270 K for UCB and 250 K for UCM) signifies the melting of this layer.

### 6.3.5 Defect Density

It is evident from the above analysis that molecular rotation about their long-axis is operative below the melting point. In what follows, we define a molecule as “defective” if

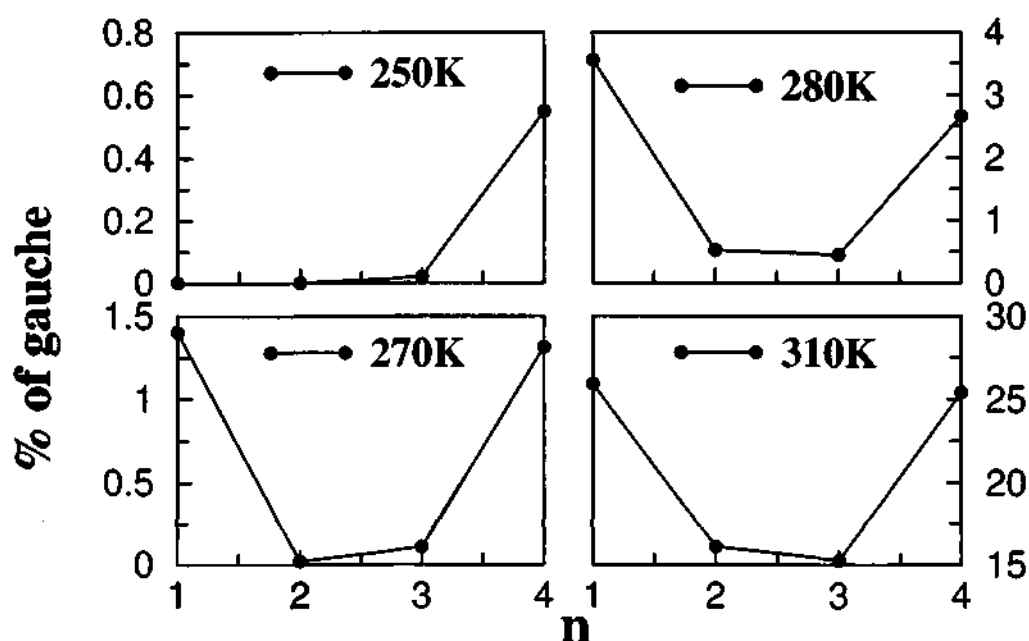


Figure 6.10: Distribution of gauche defects along the backbone of *n*-heptane molecules in the bottom layer of the fully commensurate bilayer (FCB) system at various temperatures. Here *n* is the C-C torsional index along the backbone.

at least one of its CCC plane is perpendicular to the substrate. We have determined the

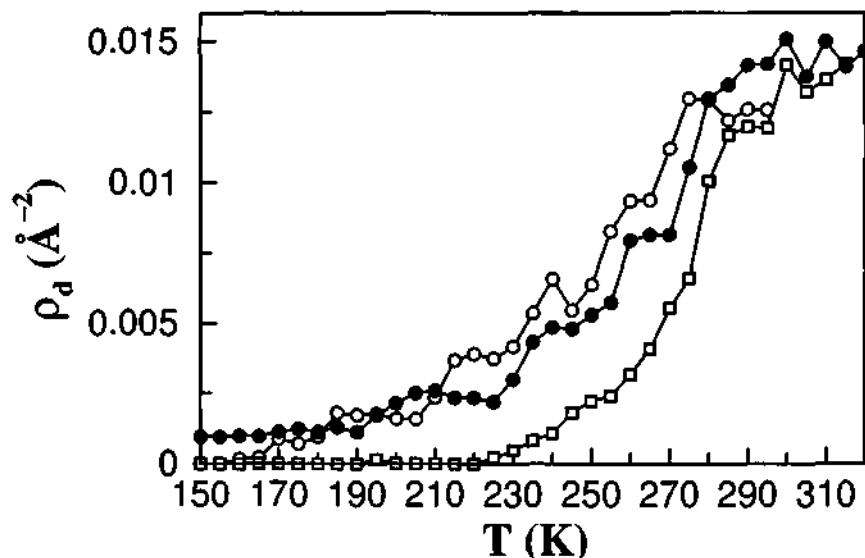


Figure 6.11: Temperature dependence of the defect density,  $\rho_d$ , of the bottom layer is shown for UCM (solid line with open circles), FCB (solid line with open squares), and UCB (solid line with filled circles)

density of such molecules in the bottom layer as a function of temperature and present the results in Figure 6.11. For UCM, we find a non-zero defect density only for temperatures greater than 155 K. Thus, 155 K denotes the onset of molecular rotation which is consistent with that observed in carbon density profile and the zigzag plane angle distribution. For UCB, the defect density of the the bottom layer remains constant up to 190 K and starts increasing for temperatures above it. The significant increase in the defect density between 190 K and 270 K shows that molecular rotations are operative below the melting point thus leading more number of CCC planes to lie perpendicular to the substrate. For the bottom layer of FCB system, we find non-zero defect population only after 220 K while that of UCB showed a few rotated molecules even at the lowest temperature of 150K. This can be rationalized purely from their difference in densities. The significant change in the defect density of the bottom layer of FCB around 290 K can be attributed to its melting.

### 6.3.6 Defect-Defect correlation

How are the molecules which are rotated so that their zigzag planes lie perpendicular to the substrate, correlated in space? Note that these “defected” molecules are energetically less stable compared to molecules with backbone CCC planes parallel to the substrate. Such molecules are prone to get desorbed from the substrate, thus creating a vacancy in the 2D crystalline lattice. We believe that understanding the spatial correlations exhibited by such molecules can aid in improving our knowledge about the spatial distribution of the vacancy sites in these two dimensional systems. We calculate the two dimensional radial distribution function for the center of mass of the defected molecules in the first layer and monitor its evolution as a function of temperature. In Figure 6.12, we present the temperature dependence of this function for molecules in the bottom layer of all the systems. Since the onset of defect formation for UCM (Figure 6.12a) occurs at 155 K, we show the defect-defect correlation function at few selected temperatures greater than 155 K. At 180 K, the defect molecules are well separated and an increase in defect population can be seen at higher temperatures. This significant change in this distribution at much higher temperature is due to melting of this layer that gives rise to the increased mobility of defected molecules. We now discuss the temperature dependence of the defect-defect correlation function calculated for the bilayer systems. For FCB at low temperatures (Figure 6.12b), the distribution shows two sharp peaks – one at 15.4Å (11Å for UCB) and another at 18.7Å (22Å for UCB) indicating that the number of defects are very few in the crystalline state and that they are widely separated from each other. The nature of the distribution changes significantly with increasing temperature between 230 K and 290 K where we find the emergence of additional peaks at larger distances. The behavior of the defect-defect correlation function for the bottom layer changes significantly at 290 K due to melting of this layer. Similar behaviour can be seen in such correlation functions corresponding to both the UCM and UCB (Figure 6.12a and 6.12c). Supporting evidence for the process of melting in these ultrathin films has

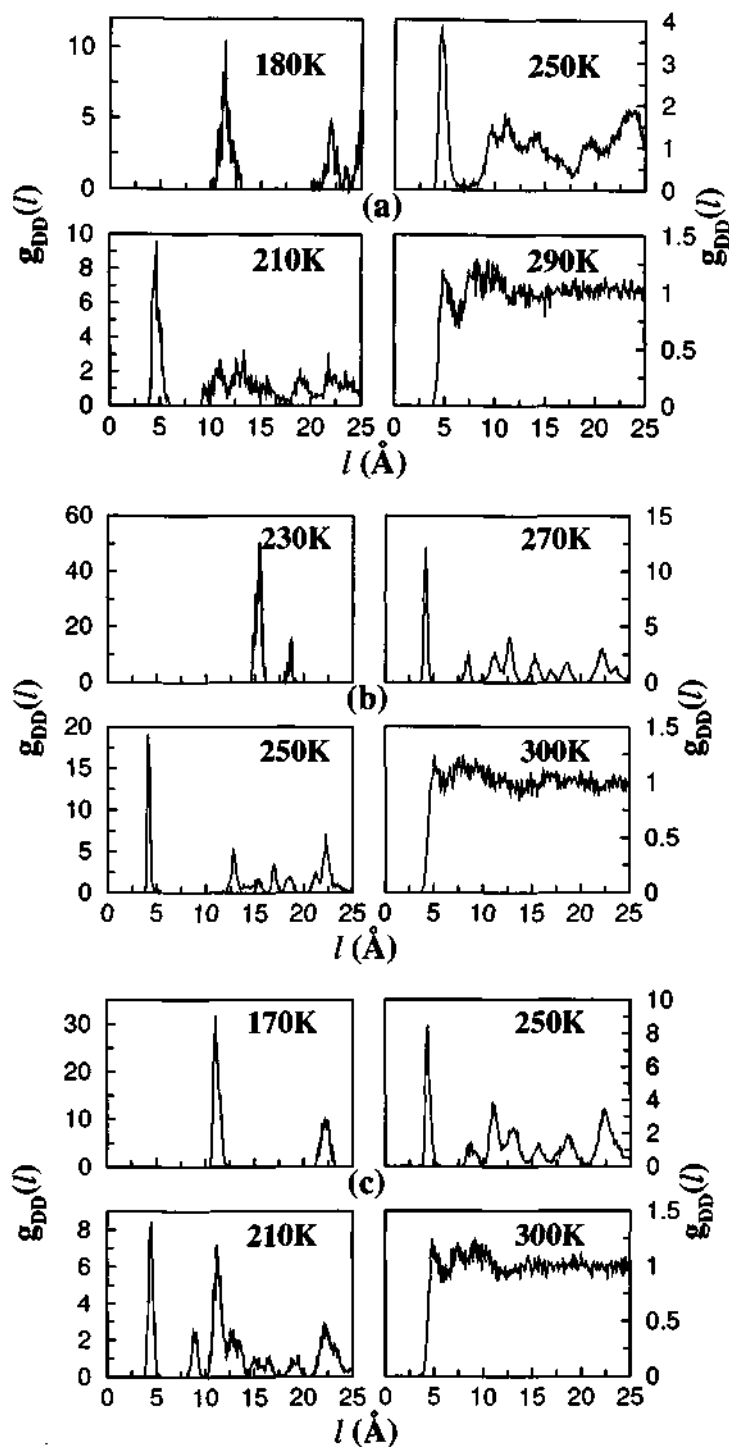


Figure 6.12: The two dimensional radial distribution function,  $g_{DD}(l)$ , for the center of mass of the rotated molecules present in the bottom layer is shown at different temperatures for (a) UCM (b) FCB, and (c) UCB. Here  $l$  is the two-dimensional distance between the centers of mass of the rotated molecules present in the bottom layer.

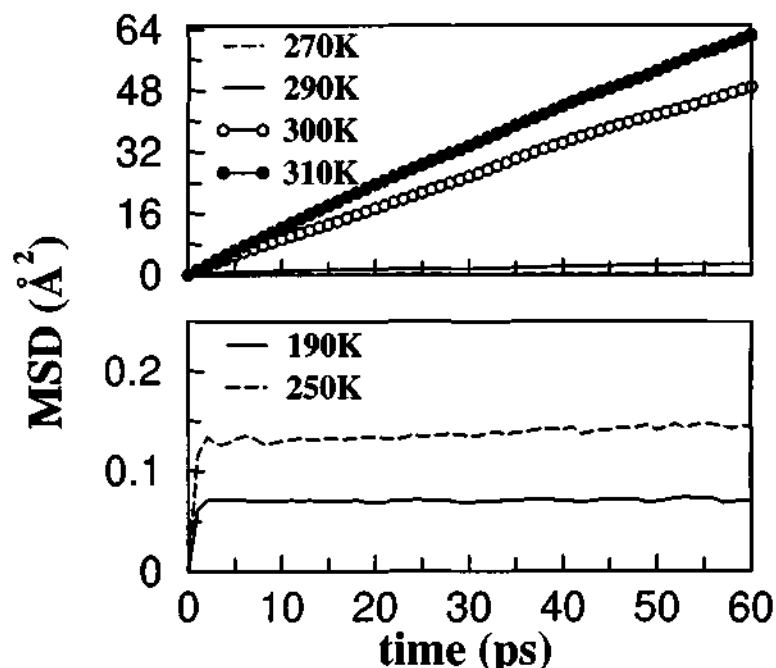


Figure 6.13: Mean square displacement of the center of mass of *n*-heptane molecules in the bottom layer of the fully commensurate bilayer (FCB) at different temperatures across the melting transition.

been obtained by calculating molecular displacements. In Figure 6.13, we show the mean square displacement of the center of mass of *n*-heptane molecules present in the bottom layer of FCB at different temperatures across the melting transition. It is clear that the molecules belonging to the first layer undergo significant displacement between 290K and 300K, which is precisely the temperature range in which we have observed changes in the energetics and structural quantities. This mobility transition thus adds further support to associate this temperature with melting.

## 6.4 Conclusions

We have employed constant temperature molecular dynamics simulations to understand the melting behavior of *n*-heptane bilayer films physisorbed on the basal plane of graphite. The calculations were performed for three different systems: an uniaxially commensurate monolayer (UCM), an uniaxially commensurate bilayer (UCB) and a fully commensurate bilayer (FCB). For FCB, the simulations were carried out at 35 (42 for UCM and 36 for



UCB) different temperatures with an interval of 5K. For bilayer systems, we have observed a layer-by-layer melting of the molecular film. The calculated intermolecular energies shows the FCB structure to be more stable than the UCB structure thus supporting the conclusions of x-ray and neutron scattering experiments [4]. In FCB, the intermolecular and the substrate energy of the bottom layer exhibit discontinuities in slope at 290 K, while such an effect was observed at 270 K and 250 K for the bottom layer of UCB and UCM, respectively. The enhancement in the temperature of melting of the bottom layer relative to bulk melting is in accordance with calorimetric and diffraction experiments [4, 28, 41]. The enhancement in the temperature of melting of the first adsorbed layer in the bilayer system has two contributions. (i) the increased in-plane density and (ii) the presence of an additional layer. We have explored their roles by performing simulations of a model system, that of an uniaxially commensurate bilayer. Our results suggest that the enhancement in the melting temperature of the bilayer system has significant contributions from both these effects. The possibility of a higher melting temperature in simulations relative to experiments could also come from any intrinsic deficiencies in the interaction potential, which could overstabilize the crystalline phase over the liquid. However, this can be ruled out as free energy calculations on crystalline *n*-octane using the same potential has yielded accurate reproduction (within 3 K) of the experimental melting curve [42].

The transition temperatures observed in our simulations are higher than what has been observed in experiments. This is likely due to the superheating of the crystalline phase due to the inevitably large heating rates (around  $10^{11}$  °/s) employed in simulations. Such an enhancement in the transition temperature obtained from simulations over that found in experiment has also been observed in temperature dependent MD simulations of other crystalline materials [43,44]. The difference between the transition temperatures obtained from experiments and simulations could also be due to the constant volume conditions employed in our work. The use of periodic boundary conditions necessitates that the simulation box contain an integral number of graphite unit cells, as the external potential

needs to be periodic. This demands that the simulations be carried out in the canonical ensemble (NVT). System size effects too could alter the transition temperatures. This needs to be studied further in future. For FCB, in the temperature range between 220K and 290K (190 K and 270 K for UCB and 165 K to 250 K for UCM), we find a fraction of molecules in the bottom layer to undergo rotation about their long-axis, preserving their *all-trans* character, in agreement with STM experiments. *These molecular rotations precede the melting of the film.* We have identified those rotated molecules and have determined their spatial correlations within the layer, in the temperature range of 220K and 290K (190 K and 270 K for FCB and 165 K to 250 K for UCM). The distribution of such rotated molecules in the bottom layer changes systematically from solid-like to liquid-like until melting when all correlations are lost.

Good agreement has been obtained with the experimental finding on the rotation of the molecular backbone for molecules in the first adsorbed layer in the FCB system. The simulation result of  $40^\circ$  is in excellent agreement with the neutron data of  $45^\circ$ . This rotation in the FCB system is likely to arise due to two reasons. (i) As suggested by Arnold *et al* [4], it could come about due to the compression of the lattice relative to the UCM system, and (ii) Since the experiments on the FCB system are conducted at a temperature between the bulk and monolayer melting points, sufficient number of molecules exhibit axial rotation, leading to an average angle of around 40 to  $45^\circ$ . The current MD results are thus able to offer a microscopic understanding of the neutron scattering data.

## Bibliography

- [1] M.A. Castro, S.M. Clarke, A. Inaba, T. Arnold and R.K. Thomas, *J. Phys. Chem. B* **102**, 10528 (1998).
- [2] J. Krim, J. Suzanne, H. Shechter, R. Wang, and H. Taub, *Surf. Sci.* **162**, 446 (1985).
- [3] T. Arnold, R.K. Thomas, M.A. Castro, S.M. Clarke, L. Messe and A. Inaba, *Phys. Chem. Chem. Phys.* **4**, 345 (2002).
- [4] T. Arnold, C.C. Dong, R.K. Thomas, M.A. Castro, A. Perdigon, S.M. Clarke and A. Inaba, *Phys. Chem. Chem. Phys.* **4**, 3430 (2002).
- [5] M.A. Castro, S.M. Clarke, A. Inaba, T. Arnold and R.K. Thomas, *Phys. Chem. Chem. Phys.* **1**, 5017 (1999).
- [6] A. Inaba, S.M. Clarke, T. Arnold and R.K. Thomas, *Chem. Phys. Lett.* **352**, 57 (2002).
- [7] M.A. Castro, S.M. Clarke, A. Inaba, R.K. Thomas and T. Arnold, *Phys. Chem. Chem. Phys.* **3**, 3774 (2001).
- [8] K. Morishige and T. Kato, *J. Chem. Phys.* **111**, 7095 (1999).
- [9] A.J. Groszek *Proc. Roy. Soc. Lond. A.* **314**, 473 (1970).
- [10] H.E. Kern and G.H. Findenegg, *J. Colloid Interface Sci.* **75**, 346 (1980).
- [11] G.H. Findenegg and M. Liphard, *Carbon* **25**, 119 (1987).

- 
- [12] J.P. Rabe, and S. Buchholz, *Science* **253**, 424 (1991).
- [13] L. Askadskaya and J.P. Rabe, *Phys. Rev. Lett.* **69**, 1395 (1992).
- [14] S.M. Clarke, *Current Opinion in Colloid and Interface Science* **6**, 118 (2001).
- [15] H. Taub, in *The time domain in surface and structural dynamics* (Vol. 228, NATO ASI Ser. C, ed. G.J. Long, and F. Grandjean) (Kluwer, Dordrecht, p. 486, 1988).
- [16] B. Boddenberg, G. Neue, and R. Grosse, *J. Chem. Phys.* **79**, 6418 (1983).
- [17] M.D. Alba, M.A. Castro, S.M. Clarke, and A.C. Perdigon, *Solid State Nucl. Magn. Reson.* **23**, 174 (2003).
- [18] S. Leggetter, and D.J. Tildesley, *Mol. Phys.* **68**, 519 (1989).
- [19] G.H. Peters and D.J. Tildesley, *Langmuir* **12**, 1557 (1996).
- [20] G.H. Peters, *Surf. Sci.* **347**, 169 (1996).
- [21] A. Cheng and M.L. Klein, *Langmuir* **8**, 2798 (1992).
- [22] F.Y. Hansen and H. Taub, *Phys. Rev. Lett.* **69**, 652 (1992).
- [23] K.W. Herwig, Z. Wu, P. Dai, H. Taub, and F.Y. Hansen, *J. Chem. Phys.* **107**, 5186 (1997).
- [24] F.Y. Hansen, J.C. Newton, and H. Taub, *J. Chem. Phys.* **98**, 4128 (1993).
- [25] B. Smit and R. Krishna, *Curr. Op. Solid St. Mat. Sci.* **5**, 455 (2001).
- [26] G. Sastre, C.R.A. Catlow, and A. Corma, *J. Phys. Chem. B* **106**, 956 (2002).
- [27] F.Y. Hansen, K.W. Herwig, B. Matthies, and H. Taub, *Phys. Rev. Lett.* **83**, 2362 (1999).

- [28] M.A. Castro, S.M. Clarke, A. Inaba, T. Arnold and R.K. Thomas *J. Phys. Chem. Solids* **60**, 1495 (1999).
- [29] M.A. Castro, S.M. Clarke, A. Inaba, and R.K. Thomas, *J. Phys. Chem. B* **101**, 8878 (1997).
- [30] M. Krishnan and S. Balasubramanian, *J. Chem. Phys.* **118**, 5082 (2003).
- [31] M. Krishnan and S. Balasubramanian, *Proc. Indian Acad. Sci. (Chem. Sci.)* **115**, 663 (2003).
- [32] W.A. Steele, *Surf. Sci.* **36**, 317 (1973).
- [33] G. Vidali and M.W. Cole, *Phys. Rev. B* **29**, 6736 (1984).
- [34] Y.P. Joshi and D.J. Tildesley, *Mol. Phys.* **55**, 999 (1985).
- [35] W. A. Steele, A. V. Vemov, and D. J. Tildesley, *Carbon* **25**, 7 (1987).
- [36] R. Hentschke, B.L. Schtirmann, and J.P. Rabe, *J. Chem. Phys.* **96**, 6213 (1992).
- [37] C.J. Mundy, S. Balasubramanian, K. Bagchi, J.I. Siepmann and M.L. Klein, *Farad. Discuss.* **104**, 17 (1996).
- [38] D.J. Tobias, K. Tu, and M.L. Klein, *J. Chim. Phys. PCB* **94**, 1482 (1997).
- [39] M. Krishnan and S. Balasubramanian, *J. Phys. Chem. B* **109**, 1936 (2005).
- [40] G.J. Martyna, M.L. Klein, and M. Tuckerman, *J. Chem. Phys.* **97**, 2635 (1992).
- [41] S.M. Clarke, A. Inaba, T. Arnold and R.K. Thomas, *J. Therm. Anal. Calorim.* **57**, 643 (1999).
- [42] J.M. Polson, D. Frenkel, *J. Chem. Phys.* **111**, 1501 (1999).
- [43] M. Sprik, U. Röthlisberger, and M.L. Klein, *Mol. Phys.* **97**, 355 (1999); *J. Phys. Chem. B* **101**, 2745 (1997).

## List of Publications

- Computer simulation study of water using a fluctuating charge model,  
M. Krishnan, A. Verma, and S. Balasubramanian  
**Proceedings of the Indian Academy of Sciences (Chemical Sciences)**, **113**, 579 (2001).
- An atomistic simulation study of a solid monolayer and trilayer of *n*-hexane on graphite,  
M. Krishnan, S. Balasubramanian, and S. Clarke  
**Journal of Chemical Physics**, **118**, 5082 (2003).
- Vibrational dynamics of solid poly(ethylene oxide)  
M. Krishnan and S. Balasubramanian  
**Physical Review B**, **68**, 064304-1, (2003).
- Structure of solid monolayers and multilayers of *n*-hexane on graphite  
M. Krishnan and S. Balasubramanian, and S. Clarke  
**Proceedings of Indian Academy of Sciences (Chemical Sciences)**, **115**, 663 (2003).
- Order-disorder transitions and melting in a helical polymer crystal:  
Molecular dynamics calculations of model poly(ethylene oxide)  
M. Krishnan and S. Balasubramanian  
**Chemical Physics Letters**, **385**, 351 (2004)
- *n*-Heptane under pressure: Structure and dynamics from molecular simulations  
M. Krishnan and S. Balasubramanian

**Journal of Physical Chemistry B 109, 1936 (2005) (Appeared with cover art)**

- Thermal evolution of conformation, structure, and dynamics in crystalline poly(ethylene glycol)  
M. Krishnan and S. Balasubramanian  
**Manuscript in preparation**
- Phase Behaviour of Ultrathin Crystalline *n*-Heptane films on Graphite: An Atomistic Simulation Study  
M. Krishnan and S. Balasubramanian  
**Physical Chemistry Chemical Physics 7, 2044 (2005)**

539.6

pos